SISSA
Scuola
Internazionale
Superiore di
Studi Avanzati

SISSA - ISAS
SCUOLA INTERANZIONALE SUPERIORE DI STUDI AVANZATI
INTERNATIONAL SCHOOL FOR ADVANCED STUDIES

Physics Area – PhD course in

Astrophysics and Cosmology

DOCTORAL THESIS

Evolution of rotating stars with PARSEC: implementation and comparison with observations

---

Candidate:
Guglielmo COSTA

Advisor:
Prof. Alessandro BRESSAN
Co-advisors:
Dr. Léo GIRARDI
Dr. Antonio LANZA

Academic Year 2018–2019

Abstract

The goal of this thesis is to study the effects of stellar rotation onto the evolution of stars. To this purpose, I have dedicated a good part of my PhD to study and implement the main rotation effects on our stellar evolutionary code PARSEC (PAdova tRieste Stellar Evolutionary Code). The first project in which I was involved was to investigate the possible concurrence between the convective core overshooting phenomenon and the rotation in intermediate-mass stars. For such study, I analyzed a sample of double-line eclipsing binaries (DLEBs, with very well determined masses radii and metallicities) by means of a Bayesian method and the new PARSEC v2.0 rotating tracks. This study allowed me to calibrate the overshooting efficiency in the code and to conclude that a constant efficiency of overshooting in concurrence with a star-to-star variation of the rotational mixing might be crucial in the interpretation of intermediate-mass stars observations.

The second project consisted of a study of the effects of rotation in the stellar photometry. As the rotation grows the star becomes more and more oblate, this induces a thermal imbalance between the poles and the equator that is known as the Von Zeipel effect. Rotating stars do not have a constant effective temperature along the surface and for higher rotational velocity such difference increases. Since the temperature is proportional to the emitted flux, a fast-rotating star will look very different if observed at the pole or at the equator (this is also called gravity darkening). In this work, we developed a tool to compute the rotating isochrones with the gravity darkening. This work is fundamental to interpret the observed stellar clusters CMD and their features that are emerging thanks to the recent excellent photometry provided by the *Hubble Space Telescope* (*HST*).

These two projects have been fundamental steps in the building of a new collection of tools to study stellar clusters populations. My third project was the first attempt to use these tools to analyze the Large Magellanic Cloud (LMC) stellar cluster NGC 1866. Instead of looking at individual features in the CMD, like the split main sequence (MS), eMSTO, and evolved stars, we seek to reinterpret the entire available data, in particular exploiting Cepheids that have accurate pulsational mass determinations. I found that four Cepheids out of five, belong to a young (of 176 ± 5 Myr) and slowly rotating ($\omega_{\rm i} < 0.3$) population, while the fifth belongs to an older population (of 288 ± 20 Myr) of rapidly rotating stars ($\omega_{\rm i} \sim 0.9$). Later, I fitted the observed CMD of the cluster with isochrones with selected ages and initial rotations obtained from the Cepheids analysis and corrected with the gravity darkening effect. I found that the two isochrones well fit the split-MS and the cluster turn-off. This study goes in

the direction to confirm that some young clusters like NGC 1866 harbour multiple populations, but gives also hints on its formation.

List of publications

In this Thesis I present the main results of my research during my Ph.D. In the following there is the list of paper published or submitted to refereed journals:

- **Costa G.**, Girardi L., Bressan A., Chen Y., Goudfrooij P., Marigo P., Rodrigues T. S., Lanza A. (2019), "Multiple stellar populations in NGC 1866. New clues from Cepheids and Colour Magnitude Diagram". Accepted in A&A. https://arxiv.org/abs/1909.01907.

- Girardi L., **Costa G.**, Chen Y., Goudfrooij P., Bressan A., Marigo P., Bellini A. (2019), "On the photometric signature of fast rotators". In: MNRAS 488, 696G. DOI: https://doi.org/10.1093/mnras/stz1767.

- **Costa G.**, Girardi L., Bressan A., Marigo P., Rodrigues T. S., Chen Y., Lanza A., Goudfrooij P. (2019), "Mixing by overshooting and rotation in intermediate-mass stars". In: MNRAS 485, 4641. DOI: https://doi.org/10.1093/mnras/stz728.

Here follows the list of works, developed during the PhD, but not included in this Thesis:

- Nataf D.M., Horiuchi S., **Costa G.**, Wyse R.F.G., Ting Y.S., Crocker R., Federath C., (2019), "The Predicted Properties of Helium-Enriched Globular Cluster Progenitors at High Redshift". In prep.

- Chen Y., Girardi L., Fu X., Bressan A., Aringer B., Dal Tio P., Pastorelli G., Marigo P., **Costa G.**, Zhang X., (2019), "YBC, a bolometric corrections database with variable extinction coefficients: an application to PARSEC isochrones". Submitted to A&A.

- Mirouh G.M., Angelou G.C., Reese D.R., **Costa G.**, (2019), "Mode Classification in Fast Rotating Stars using a Convolutional Neural Network". In: MNRAS 483L, 28M. DOI: https://doi.org/10.1093/mnrasl/sly212.

- Spera M., Mapelli M., Giacobbo N., Trani A., Bressan A., **Costa G.**, (2018), "Merging black hole binaries with the SEVN code". In: MNRAS 485,889S. DOI: https://doi.org/10.1093/mnras/stz359.

- Goudfrooij P., Girardi L., Bellini A., Bressan A., Correnti M., **Costa G.**, (2018), "The Minimum Mass of Rotating Main-sequence Stars and its Impact on the Nature of Extended Main-sequence Turnoffs in Intermediate-age Star Clusters in the Magellanic Clouds ". In: ApJ 864L, 3G. DOI: https://doi.org/10.3847/2041-8213/aada0f.

- **Costa G.**, Orlando S., Peres G., Argiroffi C., Bonito R. (2017), "Hydrodynamic modelling of accretion impacts in classical T Tauri stars: radiative heating of the pre-shock plasma". In: A&A 597, A1. DOI: https://doi.org/10.1051/0004-6361/201628554.

Acknowledgements

First of all, I would like to thank my supervisor Prof. Alessandro Bressan, who followed me constantly and actively during my PhD. I learned a lot from his knowledge, experience and enthusiasm on studying stellar astrophysics problems. A big thank goes also to Dr Léo Girardi and Dr Antonio Lanza for all the discussions and the work done together. Another thank goes to all the collaborators that allowed me to do great science during these years! They are Paola, Thaìse, Yang, Paul, Michela, Mario, Alessandro, Xiaoting, Giovanni and David.

I would like to thank all my doctoral colleagues for these four years together. I thank Chiara and Giulia, Riccardo, Anirban, Tommaso, Farida, Gabriele, Andrea and the others for the good time spent at SISSA.

Many thanks to all the staff of the SISSA astrophysics group and to the administrative staff for having created this very important reality which is SISSA.

I thank my group for playing great music thanks to our extraordinary lead guitarist Paolo, our talented singer Fiamma, our drummer Ivan for his perfect tempo and our skilled rhythm guitarist Ulisse. I really had fun with you guys!

I want to thank the SISSA Basketball Team, for all the time spent together in training and winning (sometimes) and losing (more often) championship matches. It was a lot of fun to play with all of you and join the post-game dinners!

A big thank you to my old friends from Palermo for all the time spent together in endless conversations about everything! Thank you, Renato, Nicolò, Salvo and Marcello! Now we are scattered all over the world, but one day we will be back in the same city.

I also want to thank my closest friends in Trieste, Rossana, Andrea, Simone, Francesco, Belen, Wendy, Vittoria and all the others (I'm sorry, you are too many). Trieste was a beautiful city thanks to you guys!

Finally, I wish to thank my parents and my sister for having always encouraged and supported me in my life and for allowing me to follow my dreams. Thanks.

Last but not least, a big thank to my girlfriend Chiara for all the love and the support she gave me during these four wonderful years! I love you so much.

Contents

List of Figures

List of Tables

List of Abbreviations

ACS	**A**dvanced **C**amera for **S**urveys
AGB	**A**symptotic **G**iant **B**ranch
BH	**B**lack **H**ole
CCD	**C**olor **C**olor **D**iagram
CHeB	**C**ore **He**lium **B**urning
cJPDF	**c**orrected **J**oint **P**robability **D**ensity **F**unction
CJPDF	**C**ombined **J**oint **P**robability **D**ensity **F**unction
CMD	**C**olor **M**agnitude **D**iagram
DLEB	**D**ouble-**L**ine **E**clipsing **B**inary
eMSTO	**e**xtended **M**ain **S**equence **T**urn **O**ff
EB	**E**clipsing **B**inary
EOS	**E**quation **O**f **S**tate
HB	**H**orizontal **B**ranch
HR	**H**ertzsprung-**R**ussell
IMF	**I**nitial **M**ass **F**unction
JPDF	**J**oint **P**robability **D**ensity **F**unction
LMC	**L**arge **M**agellanic **C**loud
LTE	**L**ocal **T**hermodynamic **E**quilibrium
MLT	**M**ixing **L**ength **T**heory
MS	**M**ain **S**equence
MW	**M**ilky **W**ay
PARSEC	**PA**dova-t**R**ieste **S**tellar **E**volution **C**ode
PDF	**P**robability **D**ensity **F**unction
PMS	**P**re-**M**ain **S**equence
RGB	**R**ed **G**iant **B**ranch
SMC	**S**mall **M**agellanic **C**loud
TAMS	**T**erminal **A**ge **M**ain **S**equence
TO	**T**urn **O**ff
WFC	**W**ild **F**ield **C**amera
WR	**W**olf **R**eyet
ZAHB	**Z**ero **A**ge **H**orizontal **B**ranch
ZAMS	**Z**ero **A**ge **M**ain **S**equence

Dedicated to my family

Chapter 1

Introduction

Stars have fascinated men since the earliest times of humanity, but only in the last century, have been discovered the main physical processes that power them and let them shine over time. This thanks to the efforts of many scientists and technological improvement.

1.1 Brief historical introduction on stellar structure and evolution

Studies on the star structure have started at the beginning of the 20th century. Emden (1902) showed that the sun (and than the stars) could be considered as a sphere of gas that obeys to the laws of the gas thermodynamics and to the hydrostatic equilibrium, giving the first clues on the stellar structure interiors. Later, the work by Hertzsprung (1911) and Russell (1914) have laid the foundations for the study of stellar evolution. They found separately that exists a correlation between the observed brightness and the spectral type of stars in plots that nowadays are called Hertzsprung-Russell (HR) diagrams. They discovered that the stars do not randomly populate the diagram, but populate well determined regions, such as the main sequence (MS). In the twenties, further steps were done in the comprehension of the internal structure of stars by the studies of Sir A. Eddington. He completed and elaborated a coherent theory of the internal structure of stars, by adding the equations of energy generation and transport to the previous system of equations solved by Emden (1902). Bethe (1939) found the basic nuclear reactions that power the stars during the MS. They are the famous proton-proton cycles that transform the Hydrogen into Helium and release energy. Thanks to this discovery, it was possible to relate the chemical evolution of the stellar matter to the evolution of the star itself.

A recent example of a HR diagram is shown in Figure 1.1. The plot shows stars magnitudes and colors in the solar neighborhood with an increasing distance from the sun, from the panel (a) to the (c) (Gaia Collaboration et al., 2018). It is clearly visible that the bulk of the stars are in the MS (with magnitude of $16 < M_G < 11$ and a color $0 < G_{BP} - G_{RP} < 5$). As we include more and more stars, the other regions of the diagram start to be populated, and the most apparent are the white dwarf sequence (less

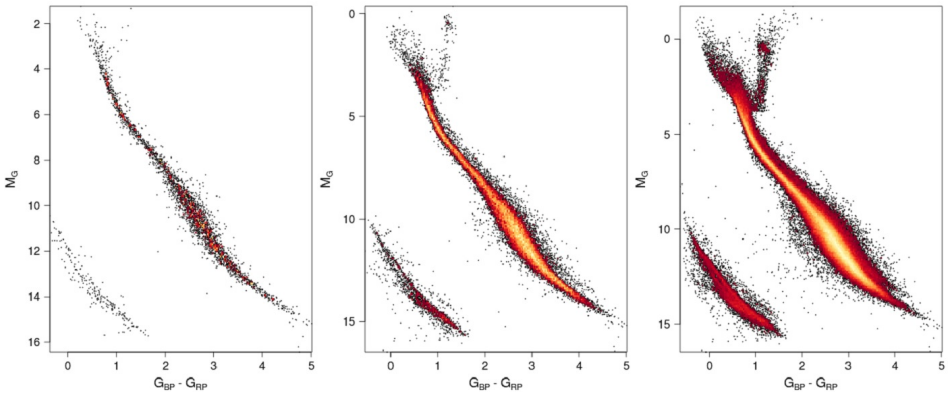

FIGURE 1.1: Color-magnitude diagram of stars in the solar neighborhood. In panel (a) there are 3724 stars at 25 pc, in panel (b) 29 683 stars at 50 pc; in panel (c) 212 728 stars at 100 pc from the sun. The colour scale represents the square root of the relative density of stars. The darker regions indicate lower density of stars. Image from the Gaia Collaboration et al. (2018).

bright, $16 < M_G < 11$ and bluer, $G_{BP} - G_{RP} < 2$, than the MS) and the red giant branch (RGB, with $M_G < 4$ and $G_{BP} - G_{RP} \sim 1.5$), phase in which the stars burn the Hydrogen in a thin shell above their Helium core.

Up to the first decades of the 20th century, all the calculations were performed by hand and, as stated by Schwarzschild, "a person can perform more than twenty integrations steps per day", so that "for a typical single integration consisting of, say, forty steps, less than two days are needed" (Rudolf Kippenhahn, Alfred Weigert, and Achim Weiss, 2012). A big step forward was done thanks to the incoming of the first computers. Already in the fifties, the first stellar evolution simulations have begun to appear in literature, such as the model of the Sun published by M. Schwarzschild, Howard, and Härm (1957). During the sixties, the innovative methods developed by Henyey, Forbes, and Gould (1964) allowed to numerically solve the equations of the internal star structure. Further improvements to these methodologies have been done by the pioneering work of R. Kippenhahn, A. Weigert, and Hofmeister (1967), that developed the precursor of the modern stellar evolution codes. Thanks to such efforts, great progress of knowledge has been achieved in many astrophysical fields. For instance, now it is well known that almost all the chemical elements in the universe have been created in stars or in processes that directly involve them, such as the dramatic (and beautiful) supernova explosions and the recently discovered merge of neutron stars.

All the new generation stellar evolution codes are based on the R. Kippenhahn, A. Weigert, and Hofmeister approach to model and solve the stellar problem. Some of them are GARSTEC (Achim Weiss and Schlattl, 2008), MESA (Paxton, Schwab, et al., 2018), GENEC (Eggenberger et al., 2008), FRANEC (Limongi and Chieffi, 2018), KEPLER (Heger, N. Langer, and Woosley, 2000), STERN (Brott, de Mink, et al., 2011) and PARSEC (A. Bressan, P. Marigo, et al., 2012). These codes are widely adopted to build sets of evolutionary tracks and isochrones, which are used to study many astrophysical problems such as, to understand the stars themselves, to

study the interaction star-planets and to get host star parameters for exoplanets (Maldonado, Affer, et al., 2015; Maldonado, Villaver, et al., 2019; Gallet and Delorme, 2019), to study dust formation (Nanni et al., 2019), to derive the main parameters of star clusters (Milone, Marino, D'Antona, Bedin, Piotto, et al., 2017; Gossage et al., 2018), to study the final fates of the stars and their yields (Limongi and Chieffi, 2018), to derive black hole mass when observing gravitational wave (Spera, Mapelli, and Alessandro Bressan, 2015; Spera, Mapelli, Giacobbo, et al., 2019), etc.

In the last decades, the comparisons between observations and models showed the necessity to include new physical phenomena in the evolutionary codes and, two of them are the core overshooting and the mass loss. Another phenomena that is nowadays under investigation and frequently included in the codes, is the rotation. In the past, it has been often considered to play only a second role on the stellar evolution, but recently it has been introduced as the possible explanation to many not yet fully understood phenomena. Such as, the abundance anomalies seen at the stellar surface (Mokiem, de Koter, Evans, et al., 2006; Mokiem, de Koter, J. S. Vink, et al., 2007; Hunter et al., 2009) or the split-MS and the extended MS turn-off (eMSTO) of many stellar clusters (Milone, Marino, D'Antona, Bedin, Piotto, et al., 2017; Cordoni et al., 2018).

1.2 Stellar rotation

It is a matter of fact that all the stars rotate, as any other object in the universe. From simple considerations, it easy to see that using the conservation of the angular momentum (i.e. $\Omega r^2 = \text{const.}$), a newborn star with a radius of $\sim 10^{11}$ cm formed from the collapse of a very slow rotating molecular cloud with a typical radius of about 0.1 pc (10^{17} cm), should be an extremely fast rotator.

The rotation of stars is a well known evidence since the early times of the twentieth century. But, even before, already Galileo knew that the Sun rotates (trough the observations of the sunspots). In the 1877, Abney supposed that maybe we can observe rotation in stars through the Doppler shift of the spectrum lines. But, only in 1909 Schlesinger was able to detect the shift and derive for the first time the rotational velocity of a star, that was δ Librae (Shajn and Struve, 1929). Recent theoretical and observational studies performed in the last two decades have shown that rotation plays a not negligible role in the evolution of stars, affecting every phase of stars, from the formation to the death. Rotating stars evolve differently with respect to the non-rotating ones. In general, they are more luminous and colder, the main sequence lifetimes are longer, the surfaces are enriched by products of the H-burning and, moreover, they build up bigger cores with a resulting differentiation of the final fates. This different evolution results from several effects induced by rotation. How pointed out by many authors (as R. Kippenhahn and Thomas, 1970; Endal and Sofia, 1976; J.-P. Zahn, 1992; Meynet and A. Maeder, 1997), these are

1. Centrifugal forces reduce the effective gravity at any point not on the axis of rotation;

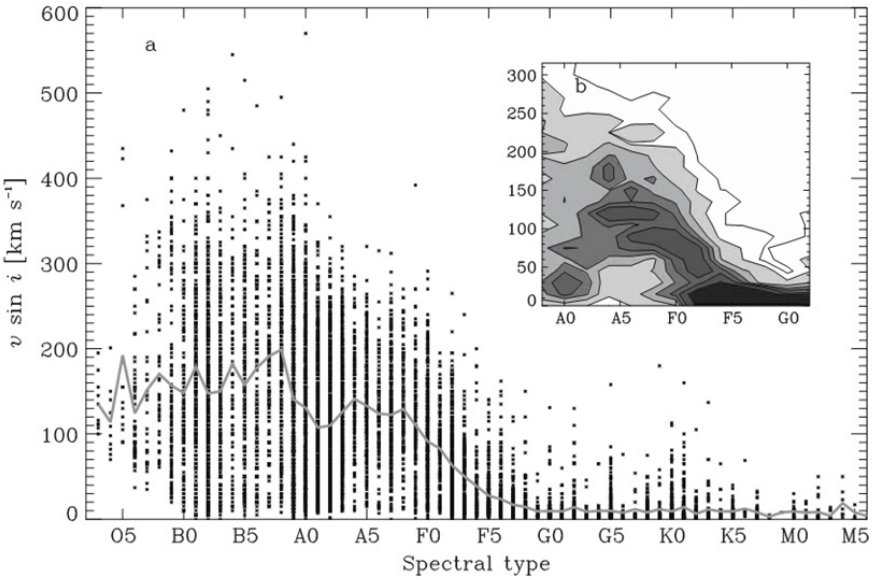

FIGURE 1.2: Distribution of $v \sin i$ as a function of the spectral type. The solid grey line is the variation of the average per spectral type. In the inset there is the density of points in the same diagram, and the darker tones indicate higher densities. Image from Royer (2009).

2. Since the centrifugal force is not, in general, parallel to the gravity, equipotential surfaces are no longer spheres;

3. Because the radiative flux varies with the local effective gravity (the so-called Von Zeipel effect von Zeipel, 1924), the radiative flux is not constant on an equipotential surface;

4. Rotation induces mixing processes.

Rotation has been observed in all the different types of stars and, for instance, Figure 1.2 shows the projected rotation velocity as a function of the stellar spectral type (Royer, 2009). The plot shows that all the stars in the sample are rotating, moreover it shows that there is an intriguing dichotomy between hot (from O5 to F5) and cool (from F5 to M5) stars. The mechanism beyond the difference between these two subgroups is not fully understood yet, but it is likely connected to the stars magnetic field and the coupling with the stellar winds. This shows that still much efforts must be done to improve our knowledge on stars.

1.3 Thesis outline

This Thesis is structured and organized as follows.

In Chapter 2, I briefly review the basic "classic" equations and methodologies adopted in our stellar evolutionary code PARSEC.

In Chapter 3, I discuss the fundamental assumptions to model stellar rotation in a 1D stellar evolutionary code, and I present the equations included in PARSEC to treat the structure and thermal distortion induced by rotation.

Chapter 4 is focused on the transport of angular momentum and the extra-mixing of chemical elements lead by rotational instability. It is also presented how the calibration of the rotations efficiency parameters is performed.

In Chapter 5, I use the new PARSEC v2.0 to investigate about the possible concurrence between the extra-mixing provided by the core overshooting and the one due to the rotational mixing. This Chapter is based on Guglielmo Costa, Léo Girardi, Alessandro Bressan, Paola Marigo, et al. (2019).

Chapter 6 is based on Léo Girardi et al. (2019), and it is focused on the photometric effects induced by the rotation. I describe how we compute and correct the stellar spectra as a function of the rotation rate and the inclination angle of the stellar rotation axes with the line of sight. These effects are inserted in our TRILEGAL code to compute isochrones and simulations.

In Chapter 7 I use all the developed tools to study the intermediate-age stellar cluster NGC 1866. In this study, I analyze a sample of well-studied Cepheids of the cluster to get their age and initial rotation rate. Then, I compare such results with the CMD of the cluster. This Chapter is based on Guglielmo Costa, Léo Girardi, Alessandro Bressan, Yang Chen, et al. (2019).

In Chapter 8, I summarized the main results of this Thesis and discuss the possible future developments of PARSEC and the next projects.

Chapter 2

Stellar structure

The theory of stellar evolution is the backbone of many theories that try to solve the Universe mysteries. One of them is the theory of stellar population, used to study the stellar clusters, that are the basilar components of galaxies. Thanks to these theories, we can estimate the ages and the composition of the stars in the clusters, the star formation rates and then the star formation histories, that are all fundamental ingredients to study galaxies and the whole Universe history. Continuously testing and improving the stellar evolution theory it is necessary because different physical prescriptions can change significantly the stellar models and thus, can deeply change the interpretations of the observed data and all the other studies based on it. Several physical phenomena take place in stars and the models should include atomic and nuclear physics , thermodynamics and matter-radiation interaction in a wide range of physical conditions, from tenuous gases to extremely high densities in degenerated stars cores.

In this Chapter, I introduce the basic physics that is implemented in our stellar evolutionary code PARSEC (the PAdova-tRieste Stellar Evolutionary Code; A. Bressan, P. Marigo, et al., 2012). In Section 2.1 I present the structure equations. I discuss how the equation of state and the opacity are treated within the code in Section 2.2. In Section 2.3, I discuss the mass loss prescriptions. In Section 2.4 I present the new scheme adopted for the mixing and the nuclear reactions network in the new version of PARSEC. Finally, in Section 2.5 I briefly introduce the methods and the boundary conditions adopted to solve the structure equation.

2.1 Equations of stellar structure

Following Rudolf Kippenhahn, Alfred Weigert, and Achim Weiss (2012), the *Lagrangian* formulation of the stellar structure equations is given below

$$\frac{\partial P}{\partial M} = -\frac{G\,M}{4\pi\,r^4}, \tag{2.1}$$

$$\frac{\partial r}{\partial M} = \frac{1}{4\pi\,r^2\rho}, \tag{2.2}$$

$$\frac{\partial L}{\partial M} = \epsilon_n - \epsilon_v + \epsilon_g, \tag{2.3}$$

$$\frac{\partial T}{\partial M} = -\frac{G\,M}{4\pi\,r^4}\,\frac{T}{P}\,\min\left[\nabla_{ad}, \nabla_{rad}\right]. \tag{2.4}$$

with

$$\nabla_{ad} = \frac{P\delta}{T\,\rho\,c_P}, \tag{2.5}$$

$$\nabla_{rad} = \frac{3}{16\pi\,acG}\,\frac{\kappa L\,P}{M\,T^4}, \tag{2.6}$$

where for each shell of the star (that are the equipotential surfaces), M is the independent variable and it is the mass enclosed by the shell of radius r, with a local pressure P,a local density ρ, a luminosity L and a temperature T. ϵ_n is the nuclear energy generation rate, ϵ_v is the neutrinos energy rate and ϵ_g is the gravitational energy rate. The ∇_{ad} and ∇_{rad} are the adiabatic and radiative gradients, $\delta = \left(\frac{\partial \ln \rho}{\partial \ln T}\right)_{P,\mu}$ is a thermo-dynamical derivative, c_P is the specific heat capacity at constant pressure, κ is the opacity of the material. Finally, $G = 6.6738 \times 10^{-11}\,\mathrm{m^3\,kg^{-1}\,s^{-2}}$ is the gravitational constant, $a = 7.5657 \times 10^{-16}\,\mathrm{J\,m^{-3}\,K^{-4}}$ is the radiation constant and $c = 2.9979 \times 10^{8}\,\mathrm{m\,s^{-1}}$ is the light velocity.

To close the system of equations (Eqs. 2.1 – Eqs. 2.4), we need to include the equation of the nuclear reactions, that gives the variation of the chemical elements with time. It can be generally written as

$$\frac{\partial X_i}{\partial t} = \frac{A_i}{\rho}\left(\sum r_{ij} - \sum r_{ik}\right), \qquad i = 1, \ldots, I, \tag{2.7}$$

where X_i is the mass fraction of the i-th element of the nuclear reactions network, and $\sum_i X_i = 1$ for each shell of the star. A_i is the atomic mass of the i-th element, r_{ij} and r_{ik} are the rates of the nuclear reactions that create and destroy the i-th element, respectively. I is the total number of elements considered in the nuclear network. In Section 2.4 is described in detail how the the nuclear network is handled within the code.

Eq. 2.5 and Eq. 2.6 are the temperature gradient in the case the energy is totally transported by convection or radiation, respectively. From the analysis of the *dynamical* instability, a layer of the star is stable if

$$\nabla_{rad} < \nabla_{ad} + \frac{\varphi}{\delta}\nabla_{\mu}, \tag{2.8}$$

where $\varphi = \left(\frac{\partial \ln \rho}{\partial \ln \mu}\right)_{P,T}$ is a thermo-dynamical derivative, and $\nabla_{\mu} = \frac{\partial \ln \mu}{\partial \ln P}$ is

the molecular weight gradient. This is the Ledoux criterion. In case of a chemical homogeneous region, $\nabla_\mu = 0$ and the stability criterion becomes

$$\nabla_{rad} < \nabla_{ad}. \tag{2.9}$$

This is the so-called Schwarzschild criterion.

In the following sections I describe the physics prescriptions adopted in PARSEC.

2.2 Equation of state and opacity

The set of structure equations is completed with the addition of the equation of state (EOS) of the stellar matter, that puts in relation the quantities T, ρ, P and the stellar matter composition X_i, and the opacities, κ, that is a function of ρ, T and X_i. These quantities are computed under the assumption of the local thermodynamic equilibrium (LTE).

The EOS are computed using the publicly available package FREEEOS and released by Irwin (2012). The package allows the computation of the thermodynamic quantities of interest (e.g. density, mean molecular weight, entropy, specific heats and their derivatives) in a wide ranges of temperatures and pressure. In PARSEC, the EOS can be computed *on-the-fly* or, alternatively, read by precomputed tables. Since the precomputed tables are sufficently accurated for most of the stellar tracks, this second method is the standard option in the code (A. Bressan, P. Marigo, et al., 2012). The tables are computed taking into account various chemical elements, from the Hydrogen to the Nickel, and different values of Z are considered for any distributions of heavy elements. In PARSEC we divide two different "regimes" for the stellar matter, when it is 'H-rich' and when it is 'H-free'. The two regimes consist in different EOS tables, that are 10 for the first H-burning phase, and 31 for the advanced burning phases. At each time-step, before solving the structure equations, PARSEC interpolates such tables to obtain the thermodynamic quantities for each mesh point of the star.

The opacity is a physical quantity that describes how the radiation intensity is dumped in the propagation path by the matter. Thus, it determines at which rate the light goes out from a star. The stellar opacities are mainly due to:

- electron scattering;
- free-free interactions;
- bound-free transitions, including H^- absorptions;
- bound-bound transitions;
- molecules band transitions.

In PARSEC, the standard procedure to treats opacities consists in an intepolation of pre-computed tables of Rosseland mean opacities, κ_{Ross}, function of density, of temperature and of the chemical composition. It is defined

as

$$\frac{1}{\kappa_{Ross}} = \frac{\int_0^\infty \frac{1}{\kappa_\nu} u_\nu d\nu}{\int_0^\infty u_\nu d\nu}, \tag{2.10}$$

where κ_ν is the absorption coefficient as a function of the frequency ν, u_ν is the radiation energy density. Such averaged value over the frequency is used to evaluate the global effect of the interaction between the radiation field and the stellar matter. The opacities tables covers a wide range of temperatures and densities, for each chemical abundance distributions (as done for the EOS A. Bressan, P. Marigo, et al., 2012). The tables are comptuded with two different codes for different temperature regimes. They are:

- the Opacity Project At Livermore (OPAL) code (Iglesias and Rogers, 1996) for the high temperature ($4.2 \leq \log T_{\rm eff} \leq 8.7$);
- the AESOPUS tool by P. Marigo and Aringer (2009) for temperatures in the range $3.2 \leq \log T_{\rm eff} \leq 4.1$;
- in the transition interval $4.0 \leq \log T_{\rm eff} \leq 4.1$ a linear interpolation between the opacity tables derived from the two codes is adopted.

In PARSEC are includeded also conductive opacities following Itoh et al. (2008). The tables are pre-loaded by PARSEC before the computation of each track, to follow in detail any significant change of the local opacity due to the variation of the local metal content due to mixing processes or dredge-up episodes. For each different partition of chemical elements (such as the solar-scaled mixture by Caffau et al. (2011) or the Large Magellanic Cloud partition computed for the calibration of rotation in Chapter 4), both the EOS and opacity tables should be recomputed before the computation of sets of tracks.

2.3 Mass loss

Another effect that is treated separately from the structure equations is the mass loss. The mass loss results from stellar winds driven by the radiation pressure, that pushes out the most external stellar matter. The main contribution to the total acceleration of the wind in due to the lines absorption of the stellar radiation. The momentum is mainly trasferred by UV photons in resonance lines of the Fe and the CNO elements (A. Maeder, 2009). Thus, mass loss plays a crucial role particularly in the massive stars, since they are more luminous of the low and intermediate mass stars. For a low mass star such the sun, the mass loss rate is $\dot{\rm M} = 10^{-14}\ M_\odot/{\rm yr}$, and the related timescale τ_{Mloss} is larger than the nuclear timescale τ_{nuc}, hence the evolution is not affected by the winds and the mass loss can be neglected in the models. The mass loss phenomenon starts to dominate the evolution for stars with an initial mass $M_{\rm i} \geq 30\ M_\odot$.

In PARSEC, the mass loss is activated for models with $M_{\rm i} > 12\ M_\odot$, and, there are implemented different prescriptions for the various phases of the stars. As summarized by Y. Chen, A. Bressan, et al. (2015), the adopted prescriptions are:

- from J. S. Vink, de Koter, and Lamers (2000) and Jorick S. Vink, de Koter, and Lamers (2001) are used for blue supergiant phase with $T_{\rm eff} \geq 12000$ K, with a metallicity dependence as $\dot{\rm M} \propto (Z/Z_{\odot})^{0.85}$ $M_{\odot}$ yr^{-1} is adopted;
- the (de Jager, Nieuwenhuijzen, and van der Hucht, 1988) formulations are used for red supergiant phase (so for $T_{\rm eff} <$ 12000 K), with the same metallicity dependence as for the Vink mass loss;
- for Wolf-Rayet (WR) stars, the Nugis and Lamers (2000) formalism is used, in which a metallicity dependence is also provided.

Once the $\dot{\rm M}$ is known from the previous relations, at the beginning of each time step, PARSEC compute the mass to be removed as:

$$M_{new} = M_{old} - \Delta M = M_{old} - \dot{\rm M}\,\Delta t, \tag{2.11}$$

where the M_{new} in the mass at the new timestep, M_{old} is the mass of the star at the previous timestep, ΔM is the mass lost and Δt is the time step in years. After, the mass lost is extracted by a simple removal of the external mesh points of the star. However, since the mass loss timescale is bigger than the thermal one (i.e. the Kelvin-Helmholtz timescale, τ_{KH}), the thermal structure is not changed by the mass loss, and is assumed to remain the same.

2.4 The new scheme for mixing and nuclear reactions

In the present release of PARSEC, there are two different schemes to treat the mixing of elements and the nuclear reactions. In the first one, adopted in the previous versions, the nuclear reactions network and the transport of elements are solved separately in two steps. Firstly, all the abundances are solved together with a semi-implicit extrapolation scheme, without any assumption for the nuclear equilibria. As clearly explained by P. Marigo, L. Girardi, C. Chiosi, et al. (2001), the choice of the semi-implicit method to solve the nuclear network, is motivated by the search for a convenient compromise between the higher accuracy typical of the explicit scheme, and the better stability of the implicit one. In general, implicit methods converge to the true equilibrium solutions of the nuclear network for relatively large time steps, whereas purely explicit methods would require extremely short time steps to both find the solution and maintain stability. The second step of this scheme, consists in the mixing of the elements. They can be transported by the microscopic diffusion in the stable zones of the star, or by the turbulent convection in the unstable regions. The microscopic diffusion is treated as an advective process and is modeled as described by Thoul, Bahcall, and Loeb (1994). While, the elements in the convective zones are "instantaneously" homogenized within the evolutionary time-step (Salasnich, Alessandro Bressan, and Cesare Chiosi, 1999).

The second method, implemented in the last version of PARSEC, consists in a diffusive scheme in which the nuclear reactions and the mixing are solved at the same time. In this scheme the microscopic diffusion is not inserted yet. The general equation that describes the change of a element i,

represented by the mass fraction X_i (Sackmann, Smith, and Despain, 1974) is given by

$$\frac{\partial Y_i}{\partial t} = \frac{1}{\rho r}\frac{\partial}{\partial r}\left(r^2 \rho D \frac{\partial Y_i}{\partial r}\right) \pm \sum_j Y_j \lambda_k(j) \pm \sum_{j \geq k} Y_j Y_k [jk], \tag{2.12}$$

where $Y_i = X_i / A_i$, D is diffusion coefficient in the unstable regions, and it is computed within the Mixing Length Theory (MLT) framework, thus, $D = D_{\rm MLT} = (1/3)\, v\, l$, where $l = \alpha_{\rm MLT} H_{\rm P}$ is the mixing length and v is the velocity. The second term of the right-hand part of the equation describes the local change of the i element caused by single body decays from i to k in case of negative sign and from j to i in case of positive sign. The third term describes the two body reactions, and for the reaction $j + k \rightarrow i + z$ is

$$Y_j Y_k [jk] = \frac{n_i \rho}{1 + \delta_{jk}} Y_j Y_k N_A \langle \sigma v \rangle_{jk}, \tag{2.13}$$

where n_i is the number density, $\delta_{jk} = 1$ if $j = k$, N_A is the Avogadro Number and $\langle \sigma v \rangle_{jk}$ is the reaction rate per particle pair. In the case of a triple body encounter (as in the triple He reaction), there is an other term such as $Y_j Y_k Y_l [jkl]$. To solve this system of equations, we adopt a full implicit method. It is known that this kind of treatment for the mixing, produces chemical profiles that fulfill the conditions imposed by the different timescales, namely the evolutionary, the convective and the nuclear. The latter timescale depends on the particular chemical element under consideration.

Both schemes for the treatment of the mixing and nuclear reactions, can still be activated for comparison purposes. For this work of Thesis, I adopt the second approach.

The nuclear reactions network has been also updated with respect to the previous releases of the code. Now it contains up to 33 isotopic elements from Hydrogen to Zinc, including the reverse reactions of the α-captures. In total there are 72 reactions. The rates and the Q values of each reaction are taken from the JINA REACLIB data base (Cyburt et al., 2010), with their April 6, 2015 recommendations. The electron screening factors are from Dewitt, Graboske, and Cooper (1973) and Graboske et al. (1973).

In the models computed in this work, I adopt the Schwarzchild criterion (Martin Schwarzschild, 1958) to define the convective unstable regions (Eq. 2.9), on top of which the overshooting phenomenon takes place. In the overshooting regions the velocity is computed with the ballistic approximation[1] (A. Maeder, 1975; A. G. Bressan, C. Chiosi, and Bertelli, 1981), also known as penetrative overshooting. In this scheme, the overshooting parameter (actually $\lambda_{\rm ov} \times H_{\rm P}$) is the mean free path that can be traveled by bubbles in the full convective region before dissolving (i.e. also *across* the border of the unstable region). Convective elements are accelerated in the unstable region and decelerated in the stable overshooting zone. The acceleration imparted to convective elements is derived in

[1] A treatment of convective overshooting similar to that described by Freytag, Ludwig, and Steffen (1996) is also implemented, but it is not used in this work.

the framework of the mixing length theory so that the corresponding velocity field can be obtained. For an easy comparison with other existing models in literature we keep track of the overshooting distance, i.e. the extension of the overshooting region above the Schwarzschild border $d_{\rm ov}$, during the evolution. For example, during H burning, we find that, approximately, $d_{\rm ov}/H_{\rm P} \simeq 0.5\,\lambda_{\rm ov}$, with a small dependence on the initial stellar mass. During the He-burning phase, we adopt the same prescription. However since as the helium burning proceeds the core grows giving rise to a distinct molecular weight barrier and associated mixing phenomena like semi-convection and breathing pulses of convection, the above simple scaling looses its validity. Further discussion on the method can be found in A. Bressan, Bertelli, and C. Chiosi (1986) where details on the core overshooting, during the central He burning phase, are also given.

In general, the mixing of the chemical elements in non-rotating stars, happens prevalently in the convective regions of the star. In the radiative zones there is no exchange of matter between different mass shells, if it is possible to neglect the microscopic diffusion (as in the case of the intermediate and massive stars).

2.5 Methods and boundary conditions

The equations of the stellar evolution cannot be solved in general analytically, even more because the EOS, the opacity and the nuclear reaction rates are given as data tables. Thus, we must rely on numerical solutions.

To numerically solve the structure equations (Eqs. 2.1 – Eqs. 2.4), we adopt the *Henyey* method (see Henyey, Wilets, et al., 1959; Henyey, Forbes, and Gould, 1964; R. Kippenhahn, A. Weigert, and Hofmeister, 1967; Rudolf Kippenhahn, Alfred Weigert, and Achim Weiss, 2012, for details) and the initial and the boundary conditions are described in the following.

The initial condition coincides with the structure of the star at the previous time-step. While, the boundary conditions are two: the one at the stellar center and the other at the stellar surface. At the center, the radius and the mass are null, so $r = 0$ and $M = 0$, but in order to obtain the central pressure P_c and the central density ρ, we need to know the behaviour of the four quantities (r, M, P and ρ) in the proximity of the center of the star. Thus, the above equations (Eqs. 2.1 – Eqs. 2.4) are approximated by expanding in powers of M, with $M \to 0$, and the four equations become

$$P = P_c - \frac{G}{2}\left(\frac{4\pi}{3}\right)^{\frac{1}{3}} \rho_c^{\frac{4}{3}} M^{\frac{2}{3}}, \tag{2.14}$$

$$r = \left(\frac{3M}{4\pi\rho_c}\right)^{\frac{1}{3}}, \tag{2.15}$$

$$L_c = \epsilon_c M, \tag{2.16}$$

$$T^4 - T_c^4 = -\frac{\kappa\epsilon_c}{2\,a\,c}\left(\frac{3}{4\pi}\right)^{\frac{1}{3}} \rho_c^{\frac{4}{3}} M^{\frac{2}{3}} \quad \text{(radiative case)} \tag{2.17}$$

$$\ln T - \ln T_c = -\left(\frac{\pi}{6}\right)^{\frac{1}{3}} \frac{G}{P_c}\rho_c^{\frac{4}{3}} M^{\frac{2}{3}} \nabla_{ad} \quad \text{(radiative case)}. \tag{2.18}$$

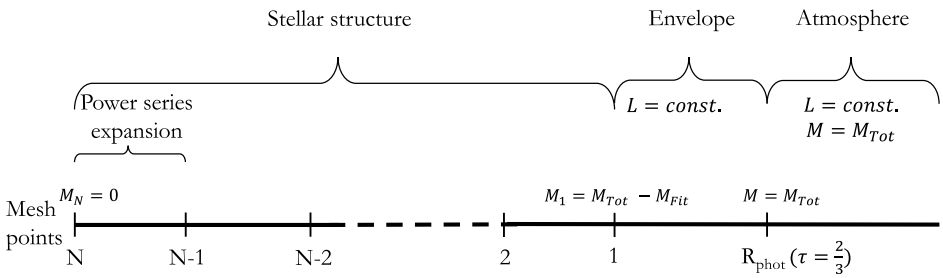

FIGURE 2.1: Sketch of the grid adopted in our models. The star interior is divided in N mesh points. The envelope is connected to the first point of the internal structure (M_1), and the atmosphere is integrated from $\tau = 2/3$ to infinite (see text for details).

where $\epsilon_c = (\epsilon_n - \epsilon_\nu + \epsilon_g)_c$ is the total energy rate at the center mesh point of the star. In PARSEC, the variation of the temperature is simplified in

$$T - T_c = \nabla(P - P_c) \quad \text{(in any case)}. \tag{2.19}$$

The boundary condition at the atmosphere is a bit more tricky, because in PARSEC the star is subdivided in three zones as shown in Figure 2.1 (following the R. Kippenhahn, A. Weigert, and Hofmeister, 1967, approach). The zones are:

1. **the inner structure**, described by the equations above mentioned (Eqs. 2.1 – Eqs. 2.4);
2. **the envelope**, in which there are no nuclear reactions, thus the luminosity is assumed constant;
3. **the atmosphere**, in which the mass is equal to the whole star mass.

The structure is connected to the envelope at the so-called fitting point. In turn, the envelope extends from the fitting point to the photosphere, in which the optical depth is $\tau = 2/3$. In the following sections I will describe with further details these two zones of the star.

In PARSEC, an adaptive mesh is used in the inner structure. The code adds or remove points in order to better follow the physical quantities and the chemical elements profiles in the structure. Thus, the number of points varies in different phases, for instance we have about 1500 points during hydrogen burning, 3000 during He burning and 5000 during the thermally pulsing AGB (TP-AGB) (A. Bressan, P. Marigo, et al., 2012).

2.5.1 The atmosphere

In PARSEC the external part of the star is divided in two, the envelope and the atmosphere. The latter one is a layer in which the mass, the luminosity and the radius are assumed constant. Then, to describe the remain physical quantities (i.e. the pressure and the temperature) we need only two equations. From the hydrostatic equilibrium we have that

$$\frac{dP}{dR} = -\rho\, g, \tag{2.20}$$

where ρ is the density in the atmosphere and g is the surface gravity of the star. Using the definition of the optical depth, namely $d\tau = \rho\kappa dr$, we obtain the first of the two equations to solve, it writes as

$$\frac{d\tau}{d\log P} = \frac{\kappa P}{g}\ln 10, \tag{2.21}$$

in which we used $d\log P = dP/P\ln 10$. The equation is integrated to obtain τ from the infinite ($r = \infty$) to $\tau = 2/3$, that is the definition of photosphere. At the infinite the pressure is only due to the radiation, thus $P(\infty) = P_{rad} = \frac{1}{3}aT^4$, where $a = 7.57 \times 10^{-15}$ erg cm^{-3} K^{-4} is the radiation density constant. For the atmosphere, the plane-parallel grey model is adopted, and the temperature stratification is given by a modified Eddington approximation for the radiative transport, that is

$$T^4(\tau) = \frac{3}{4}T^4_{eff}(\tau + q(\tau)), \tag{2.22}$$

where T_{eff} is the effective temperature of the star and $q(\tau)$ is the Hopf function. This is the second equation to solve to model the atmosphere.

2.5.2 The envelope

Among the inner structure and the atmosphere, there is the envelope. Its upper boundary is the point in which $\tau = 2/3$, i.e. the photosphere, while the lower boundary is the fitting point. This point is defined using the mass coordinate and can be regulated on the temperature of the meshpoint or can be set as a constant parameter. Usually, in PARSEC v1.2 (A. Bressan, P. Marigo, et al., 2012), it is set to $M/M_{Tot} = 1 - 10^{-5}$. Such a choice prevents to have temperatures high enough to ignite the nuclear reactions in this part of the star. Thus, the luminosity is constant, and the physical quantities to derive are only three (r, P, ρ). Since the mass varies so little in the envelope, we use the pressure P as independent variable, and the structure equations become

$$\frac{\partial \ln r}{\partial \ln P} = -\frac{Pr}{G\rho M} \tag{2.23}$$

$$\frac{\partial \ln M}{\partial \ln P} = -\frac{4\pi r^4 P}{GM^2} \tag{2.24}$$

$$\frac{\partial \ln T}{\partial \ln P} = \min[\nabla_{ad}, \nabla_{rad}] \tag{2.25}$$

The methods to treat the envelope and the atmosphere are fully described in (R. Kippenhahn, A. Weigert, and Hofmeister, 1967).

Chapter 3

Stellar rotation

In this chapter, I present the basic assumptions to model in a one dimensional (1D) scheme, the complex three dimensional (3D) effects induced by rotation in stars, in Section 3.1. Then, in Section 3.2 and 3.3 I discuss the isobars properties and derive the isobars shape as a function of the angular rotation rate, respectively. In Section 3.4, 3.5, 3.6 and 3.7 I derive the stellar structure equations for the rotating stars one by one, and I list them in Section 3.8. In Section 3.9 I derive the corrected equations for the boundary conditions for a rotating star. In Section 3.10 I show the derivation of the form factors, parameters that depends only on the rotation and that are used to correct the star structure equations. Finally, in Section 3.11 I discuss the Von Zeipel effect that strongly modifies the surface effective temperature of rotating stars.

3.1 Basic assumptions

R. Kippenhahn and Thomas (1970, here after KT) and later Endal and Sofia (1976) developed a methodology to include the geometric distortion of the star, due to the centrifugal forces, in the structure equations of stellar models. The main idea is to change the spherical stratification of the star with a deformed one, in case of rotation. Though to treat in a consistent way the effects of rotation would require a full 3D scheme, under the proper assumptions (and approximations), it is possible to model these effects in a 1D scheme. The four assumptions adopted in the KT scheme are:

1. The star is divided in shells, that are equipotential surfaces as in the non-rotating case, but no longer spherical;
2. In each shell, the angular velocity (Ω) has a cylindrical symmetry;
3. The Ω is constant along the colatitude (θ) of the shells;
4. The Roche approximation is used to compute the shape of the equipotentials.

Unfortunately, the feasibility of the scheme is limited to stars with a solid body rotation, since the combination of the second and the third assumptions imply that the only possible solution for the angular velocity distribution throughout the star is the solid body one. Thus, the scheme cannot be applied to differential rotating stars. Further steps to solve this problem have been done by J.-P. Zahn (1992) and Meynet and A. Maeder (1997). The first author investigated in detail on the interaction between the so-called meridional circulation (a macro-circulation of material in the star, see below for further details) and the turbulence in rotating stars. J.-P. Zahn (1992) proved that, in a internal star shell, the horizontal (tangential) turbulence is much stronger than the vertical (radial) one, thus Ω is "instantaneously" mixed along the shell (horizontally), but is not between two nearby shells (radially). The J.-P. Zahn (1992) interpretation supports the third assumption by KT, that is also called the internal "shellular" rotation law. In this scenario, the star shells are no longer equipotentials, at variance with the KT scheme, but isobars, surfaces in which the pressure, P, keeps a constant value.

Meynet and A. Maeder (1997) completed the puzzle to model differential rotating stars. They adopted the KT scheme, the shellular rotation law and dropped the second KT assumption, the cylindrical symmetry of the angular velocity. In this new scheme, each shell is defined by an isobar and it can rotate with its own Ω, constant along the colatitude, θ. From the practical point of view, the two schemes by KT and by Meynet and A. Maeder (1997) are the same.

The final set of assumptions let us to define and compute the shape of the isobars of the star, calculate the effective gravity and the other quantities related to the rotation. Remarkably, the adopted scheme allows us to keep the same form of the classical non-rotating stellar structure equations (the Eqs. 2.1 – 2.4). Only two "form factors" (f_P and f_T) are introduced in the structure equations to take into account the thermal and the mechanical distortion due to rotation. Obviously, since the physical quantities are not constant along the isobars, with the exception of the pressure and of the angular velocity, we must re-interprete the physical quantities that appear in the 1D structure equations (Eqs. 2.1 – 2.4). As described in the following, the quantities that appear in the new set of structure equation are proper averages along the isobars.

This scheme is currently adopted by most stellar evolutionary codes that treat rotation, such as MESA (Paxton, Bildsten, et al., 2011; Paxton, Cantiello, et al., 2013; Paxton, Marchant, et al., 2015; Paxton, Schwab, et al., 2018), GENEC (Eggenberger et al., 2008), FRANEC (Chieffi and Limongi, 2013; Chieffi and Limongi, 2017), KEPLER (Heger, N. Langer, and Woosley, 2000; Heger and N. Langer, 2000), STERN (Petrovic et al., 2005; Yoon and Langer, 2005; Brott, de Mink, et al., 2011), and now PARSEC v2.0.

In the next sections, following the description by Meynet and A. Maeder (1997) and A. Maeder (2009), I describe the derivation of the form factors and of the updated version of the structure equations.

3.2 Properties of the isobars

In a differentially rotating star, it is not possible to define the centrifugal forces from a potential, thus, it is a non-conservative case. However, in analogy with the conservative case, we can define the surface of a shell, Ψ, as follow

$$\Psi = \Phi - \frac{1}{2}\,\Omega^2\, r^2\, \sin^2\theta = constant \tag{3.1}$$

where $\Phi = -V$, V is the gravitational potential, r is the radius, Ω is the angular velocity of the shell and θ is the colatitude ($\theta = 0^\circ$ at the pole). The hydrostatic equilibrium implies that

$$\vec{\nabla} P = -\rho\, \vec{g}_{eff} \tag{3.2}$$

where ρ is the density and $\vec{g}_{eff}$ is the effective gravity that, in spherical coordinates, its components can be expressed as

$$g_{eff}(r) = \frac{\partial \Phi}{\partial r} + \Omega^2\, r\, \sin^2\theta \tag{3.3}$$

$$g_{eff}(\theta) = \frac{1}{r}\,\frac{\partial \Phi}{\partial \theta} + \Omega^2\, r\, \sin\theta\, \cos\theta. \tag{3.4}$$

The components of the gradient of Ψ in polar coordinates (r, θ) are

$$\frac{\partial \Psi}{\partial r} = \frac{\partial \Phi}{\partial r} + \Omega^2\, r\, \sin^2\theta + r^2\, \sin^2\theta\, \Omega\, \frac{\partial \Omega}{\partial r} \tag{3.5}$$

$$\frac{1}{r}\,\frac{\partial \Psi}{\partial \theta} = \frac{1}{r}\,\frac{\partial \Phi}{\partial \theta} + \Omega^2\, r\, \sin\theta\, \cos\theta + r^2\, \sin^2\theta\, \Omega\, \frac{1}{r}\,\frac{\partial \Omega}{\partial \theta}. \tag{3.6}$$

Comparing Eq. 3.5 to Eq. 3.3 and Eq. 3.6 to Eq. 3.4, one can write

$$\vec{g}_{eff} = \vec{\nabla}\Psi - r^2\, \sin^2\theta\, \Omega\, \vec{\nabla}\Omega. \tag{3.7}$$

From the above equation, it is clear that this is a non-conservative case and Ψ is not a potential. In this case the star is said to be *baroclinic*. On the contrary, the star is *barotropic*, and the isobars coincide with the equipotentials. This happens in the case of a solid body rotation.

We can rewrite the expression for the hydrostatic equilibrium (Eq. 3.2) as

$$\vec{\nabla} P = -\rho\, \left(\vec{\nabla}\Psi - r^2\, \sin^2\theta\, \Omega\, \vec{\nabla}\Omega\right). \tag{3.8}$$

Since Ω is constant on an isobar, the vector $\vec{\nabla}\Omega$ is parallel to the vector $\vec{\nabla} P$. So, this equation implies that the $\vec{\nabla}\Psi$ is parallel to $\vec{\nabla} P$ and hence, that the surfaces defined by $\Psi = const$ are the isobars. We can assume that

$$\vec{\nabla}\Omega = -\alpha\, \vec{\nabla}\Psi, \tag{3.9}$$

where $\alpha = \left|\frac{d\Omega}{d\Psi}\right|$ is a scalar quantity which depends only on Ψ. It is useful to defining the quantity dn as the average distance between two neighboring isobaric surfaces, $\Psi =$ constant and $\Psi + d\Psi =$ constant (thus, $dn \sim dr$).

Replacing $\vec{\nabla}\Omega$ in Eq. 3.7, we obtain that the modulus of the effective gravity is

$$g_{eff} = \left(1 - r^2 \sin^2\theta\, \Omega\alpha\right) \frac{d\Psi}{dn}. \tag{3.10}$$

This is a useful equation that will let us to rewrite the stellar structural equations accounting for the rotation distortions.

3.3 Surface shape of isobars

As suggested by KT, to calculate the surface of an isobar we adopt the Roche approximation. So, the gravitational potential associated to the mass enclosed by the radius, r, is not distorted by rotation and it is the same as if the whole mass is concentrated in the central point of the star. Using Eq. 3.1, we can reconstruct the shape of an isobar, adopting as constant value the gravity potential at the pole of the star. It remains constant and independent from the angular velocity[1], since the centrifugal forces are null. Then, the equation of an isobar can be expressed as

$$\frac{G\,M}{R} + \frac{1}{2}\,\Omega^2\,R^2\,\sin^2\theta = \frac{G\,M}{R_{pol}}, \tag{3.11}$$

where G is the gravitational constant, M is the mass enclosed by the isobar, $R = R(\theta)$ is the radius as a function of the colatitude, R_{pol} is the polar radius[2]. Rewriting the equation, we obtain

$$\frac{1}{2}\,\Omega^2\,R^3\,\sin^2\theta + G\,M\left(1 - \frac{R}{R_{pol}}\right) = 0. \tag{3.12}$$

At this point it is convenient a change of variables, namely $x = \frac{R(\theta)}{R_{pol}}$ that is the dimensionless spatial coordinate and $\omega = \frac{\Omega}{\Omega_c}$ that is the rotation rate, where Ω_c is the critical angular velocity or break-up velocity of the shell. The critical angular velocity is the angular velocity at which the centrifugal force balances the gravitational force at the equator. It can be easily obtained, and it writes as

$$\frac{G\,M}{R_{eq,crit}^2} = {\Omega_c}^2\,R_{eq,crit} \implies \Omega_c = \sqrt{\frac{G\,M}{R_{eq,crit}^3}} \tag{3.13}$$

where $R_{eq,crit}$ is the equatorial radius at the critical rotation. If we introduce Ω_c in Eq. 3.11, at the equator (hence with $\theta = 90°$)we obtain

$$\frac{G\,M}{R_{eq,crit}} + \frac{1}{2}\,\frac{G\,M}{R_{eq,crit}^3}\,R_{eq,crit}^2 = \frac{G\,M}{R_{pol}} \implies \frac{R_{eq,crit}}{R_{pol}} = \frac{3}{2} \tag{3.14}$$

[1] This is true within few percentage of variation in cases of high rotation, as demonstrated by Ekström, Meynet, et al. (2008).

[2] Obviously, $R_{pol} = R(\theta = 0°)$

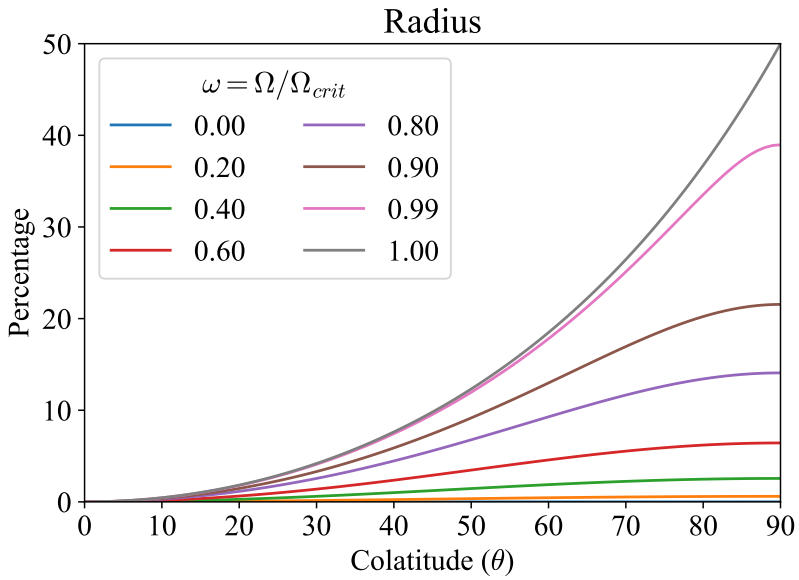

FIGURE 3.1: The ratio $x = R/R_{\rm pol}$ in percentage, as a function of the colatitude, θ. In different colors varying rotation rates, ω.

Substituting this last equation in Eq. 3.13, we obtain the definition of the critical angular velocity as a function of the polar radius, that is

$$\Omega_{\rm c} = \left(\frac{2}{3}\right)^{\frac{3}{2}} \sqrt{\frac{G\,M}{R^3_{pol}}}. \tag{3.15}$$

In this computations, we are assuming that R_{pol} is not changing in case of rotation. This is not always true, but it is a good approximation when we are not "near" the critical velocity. Ekström, Meynet, et al. (2008) found that $R_{pol}\,(\omega)$ can change of about the 5 per cent in case of maximal rotation.

Now, using $R = x\,R_{pol}$ and $\Omega = \omega\,\Omega_{\rm c} = \omega\,\left(\frac{2}{3}\right)^{\frac{3}{2}} \sqrt{\frac{G\,M}{R^3_{pol}}}$ in Eq. 3.12, we obtain

$$\frac{1}{2}\,\frac{8}{27}\,\frac{G\,M}{R^3_{pol}}\,\omega^2\,x^3\,R^3_{pol}\,\sin^2\theta + G\,M\,(1-x) = 0 \tag{3.16}$$

$$\frac{4}{27}\,\omega^2\,x^3\sin^2\theta - x + 1 = 0. \tag{3.17}$$

This last equation is a pure geometrical expression and the independent variables are the colatitude (with possible values between $0 \leq \theta \leq \pi/2$) and the angular rotation rate (ω, that rages between 0 and 1). Eq. 3.17 is an algebraic equation of the third degree, and exists only one physical root (among the three) that describe the surface of the star for a fixed rotation rate, ω. I solve the equation numerically with a simple Newton-Rapson method. The physical solution, $x(\theta)$ has values in the interval $1 < x(\theta) < 1.5$. Figure 3.2 shows the variation of the radius with respect to $R_{\rm pol}$ in percentage, as a function of the colatitude. In the case of critical rotation,

ω	R_{eq}/R_{pol}
0.00	1.000
0.10	1.002
0.20	1.006
0.30	1.014
0.40	1.026
0.50	1.042
0.60	1.064
0.70	1.095
0.80	1.141
0.90	1.216
0.95	1.281
0.99	1.390
1.00	1.500

TABLE 3.1: Values of the ratio $\frac{R_{eq}}{R_{pol}} = x(90^\circ)$ as a function of the rotation rate, ω.

the equatorial radius is the 50 per cent times larger than the polar one. Table 3.1 lists the values of the ratio $\frac{R_{eq}}{R_{pol}}$ as a function of different ω. From the values of $x(\theta)$ we can reconstruct the shape of the shell surface as a function of the θ, that is shown in Figure 3.6.

3.4 Hydro-static equilibrium equation

Once the shape of the shells is known, we can write the stellar structure equations on them. Following the method of KT, we define the "volumetric radius", r_P, as

$$V_P = \frac{4\pi}{3} r_P^3 \tag{3.18}$$

where V_p is the volume inside an isobar. As discussed in Sec. 3.1, if we want to write the stellar structural equations in one dimension, we need to re-interpret all the quantity that are not constant over an isobar. Hence, for any quantity, q, which is not constant,we take the averaged value over the isobar surface, that is defined by

$$\langle q \rangle = \frac{1}{S_P} \int_{\Psi=const} q \, d\sigma \tag{3.19}$$

where S_P is the surface of the isobar and $d\sigma$ is an element of the surface.

Combining Eq. 3.10 and the equation of hydro-static equilibrium (Eq. 3.8), we obtain

$$\frac{dP}{dn} = -\rho \left(1 - r^2 \sin^2\theta \, \Omega\alpha\right) \frac{d\Psi}{dn} \tag{3.20}$$

From the above equation, we notice that the quantity $\rho \left(1 - r^2 \sin^2\theta \Omega\alpha\right)$ is constant on an isobar.

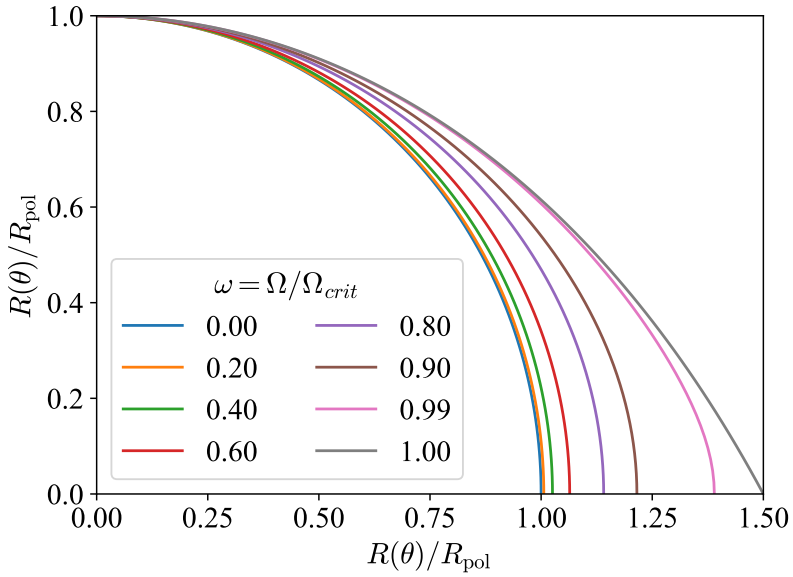

FIGURE 3.2: The shape of a rotating star with different ω in different colors.

To compute M_P, the mass inside the isobar, we use Eq. 3.10, and obtain

$$dM_P = \int_{\Psi=const} \rho \, dn \, d\sigma = d\Psi \, \rho \left(1 - r^2 \sin^2\theta \, \Omega\alpha\right) \int_{\Psi=const} \frac{1}{g_{eff}} \, d\sigma, \quad (3.21)$$

and using the definition in Eq. 3.19, we obtain

$$\frac{d\Psi}{dM_P} = \frac{1}{\rho \, \left(1 - r^2 \sin^2\theta \, \Omega\alpha\right) \langle g_{eff}^{-1} \rangle S_P}. \quad (3.22)$$

Using Eq. 3.20, the equation becomes

$$\frac{dP}{dM_P} = \frac{-1}{\langle g_{eff}^{-1} \rangle S_P}. \quad (3.23)$$

Finally, if we define a "form" factor as

$$f_P = \frac{4\pi \, r_P^4}{G \, M_P S_P} \frac{1}{\langle g_{eff}^{-1} \rangle}, \quad (3.24)$$

which is equal to 1 for a non-rotating star, we can rewrite the equation of hydro-static equilibrium in Lagrangian coordinates as

$$\frac{dP}{dM_P} = -\frac{G \, M_P}{4\pi \, r_P^4} f_P. \quad (3.25)$$

Apart from the "form" factor f_P, the equation maintains the same form as in the non-rotating scheme (see Eq. 2.1).

3.5 Continuity Equation

As done before, we can compute the equation of the mass conservation. Starting from the computation of the volume between two isobars, that is

$$dV_P = 4\pi\, r_P^2\, dr_P = \int_{\Psi=const} dn\, d\sigma, \tag{3.26}$$

and using Eq. 3.10 and Eq. 3.19, we obtain

$$dV_P = d\Psi\, S_P \left[\langle g_{eff}^{-1}\rangle - \langle g_{eff}^{-1}\, r^2 \sin^2\theta\rangle \Omega\, \alpha\right]. \tag{3.27}$$

This expression with Eq. 3.26 and Eq. 3.22, leads to

$$\frac{dr_P}{dM_P} = \frac{1}{4\pi\, r_P^2 \overline{\rho}}. \tag{3.28}$$

This equation has the same form of the continuity equation in the non-rotating case (Eq 2.2), with the exception of the meaning of the quantities. In particular, $\overline{\rho}$ is not equal to $\langle\rho\rangle$, that is the average density on an isobar, but is the average density in the element volume between two isobars. It is defined as

$$\overline{\rho} = \frac{\rho\left(1 - r^2\sin^2\theta\,\Omega\alpha\right)\langle g_{eff}^{-1}\rangle}{\langle g_{eff}^{-1}\rangle - \langle g_{eff}^{-1}\, r^2\sin^2\theta\rangle\Omega\,\alpha}. \tag{3.29}$$

Note that when mass steps are very small the difference between the two becomes negligible.

3.6 Conservation of energy

The net energy outflow dL_P from a shell comprised between two isobars is given by

$$dL_P = \int_{\Psi=const} \epsilon\,\rho\, dn\, d\sigma \tag{3.30}$$

where $\epsilon = \epsilon_n - \epsilon_\nu + \epsilon_g$ is the total rate of energy production in the shell, composed by the nuclear, neutrino losses and gravitational energy rates, respectively. Using Eq. 3.10 and Eq. 3.22 we obtain the equation of energy conservation, that can be expressed as

$$\frac{dL_P}{dM_P} = \frac{\langle\left(\epsilon_n - \epsilon_\nu + \epsilon_g\right)\, g_{eff}^{-1}\rangle}{\langle g_{eff}^{-1}\rangle}, \tag{3.31}$$

We can approximate these averages by

$$\frac{\langle\left(\epsilon_n - \epsilon_\nu + \epsilon_g\right)\, g_{eff}^{-1}\rangle}{\langle g_{eff}^{-1}\rangle} \approx \epsilon_n\left(\overline{\rho},\overline{T}\right) - \epsilon_\nu\left(\overline{\rho},\overline{T}\right) + \epsilon_g\left(\overline{\rho},\overline{T}\right), \tag{3.32}$$

where the $\overline{\rho}$ and $\overline{T}$ quantities are the average density and temperature in the element volume between two isobars, respectively. Since the above

approximation, we can write the equation of conservation of the energy as

$$\frac{dL_P}{dM_P} = \epsilon_n - \epsilon_v + \epsilon_g. \tag{3.33}$$

3.7 Transport of energy

3.7.1 Radiative equilibrium

Locally, the equation of vertical radiative transfer writes

$$F = -\frac{4a\,c\,T^3}{3\kappa\rho}\frac{dT}{dn} = -\frac{4a\,c\,T^3}{3\kappa\rho}\frac{dT}{dM_P}\rho\langle g_{eff}^{-1}\rangle S_P\, g_{eff}, \tag{3.34}$$

where κ is the opacity, a is the radiation constant and c the light velocity. In the previous passage we used the fact $\frac{dT}{dn} = \frac{dT}{dM_P}\frac{dM_P}{d\Psi}\frac{d\Psi}{dn}$ and Eq. 3.10, Eq. 3.22. Integrating over an isobar surface, we obtain

$$L_P = -\frac{4a\,c}{3}\langle g_{eff}^{-1}\rangle S_P^2\langle\frac{T^3\,g_{eff}}{\kappa}\frac{dT}{dM_P}\rangle, \tag{3.35}$$

which expresses the radiative transfer in rotating stars.

3.7.2 Convective transport

In a convective region at a given point on an isobar, the gradient of temperature is

$$\frac{d\,\ln T}{d\,\ln P} = \nabla_{ad}. \tag{3.36}$$

Taking the averages on an isobar and approximating, we can write

$$\langle\nabla_{ad}\rangle = \langle\frac{d\,\ln T}{d\,\ln P}\rangle \approx \frac{d\,\ln\overline{T}}{d\,\ln P} \tag{3.37}$$

Using Eq. 3.25, we can rewrite the equation obtaining

$$\frac{d\,\ln\overline{T}}{dP}\frac{dP}{dM_P}P = -\frac{G\,M_P}{4\pi\,r_P^4}f_P\nabla_{ad} \implies \frac{d\,\ln\overline{T}}{dM_P} = -\frac{G\,M_P}{4\pi\,r_P^4}\frac{1}{P}f_P\nabla_{ad} \tag{3.38}$$

3.7.3 Equation of energy transport

The equations of energy transport are written with these mean values of density and temperature, as done before, we can make the following approximations

$$\langle\frac{T^3 g_{eff}}{\kappa}\frac{dT}{dM_P}\rangle \approx \frac{\overline{T}^3\langle g_{eff}\rangle}{\kappa\left(\overline{\rho},\overline{T}\right)}\frac{d\overline{T}}{dM_P}, \tag{3.39}$$

This approximation and the previous used in Eq. 3.33 are not severe, since, as stated by Meynet and A. Maeder (1997), we are adopting the "shellular rotation law" and the strong horizontal turbulence responsible for the constancy of Ω on isobars will likely homogenize the chemical composition and reduce the differences in densities and temperatures on isobars.

Thus, Eq. 3.35 becomes

$$L_P = -\frac{4a\,c}{3}\langle g_{eff}^{-1}\rangle S_P^2 \frac{\overline{T}^3\langle g_{eff}\rangle}{\kappa\left(\overline{\rho},\overline{T}\right)}\frac{d\overline{T}}{dM_P}. \tag{3.40}$$

From Eq. 3.25 we obtain $dM_P = 4\pi r^4 dP/\left(GM_P f_P\right)$, and replacing it in Eq. 3.40 one finds

$$L_P = -\frac{4a\,c\,\overline{T}^3 G\,M_P}{3\kappa\left(\overline{\rho},\overline{T}\right)}\frac{S_P^2\langle g_{eff}^{-1}\rangle\langle g_{eff}\rangle}{4\pi r^4}\frac{d\overline{T}}{dP}f_P = -\frac{16\,\pi\,a\,c\,\overline{T}^3 G\,M_P}{3\kappa\left(\overline{\rho},\overline{T}\right)}\frac{d\overline{T}}{dP}\frac{f_P}{f_T}, \tag{3.41}$$

where

$$f_T = \left(\frac{4\pi r^2}{S_P}\right)^2 \frac{1}{\langle g_{eff}^{-1}\rangle\langle g_{eff}\rangle}, \tag{3.42}$$

is the second "form" factor. Rewriting Eq. 3.41 one obtains the radiative gradient for a rotating star, given by

$$\frac{d\,\ln\overline{T}}{d\,\ln P} = -\frac{3\kappa}{16\,\pi\,a\,c\,G}\frac{L_P\,P}{M_P\,\overline{T}^4}\frac{f_T}{f_P} = \nabla_{rad}\frac{f_T}{f_P}. \tag{3.43}$$

Directly follow that

$$\frac{d\,\ln\overline{T}}{dM_P} = -\frac{G\,M_P}{4\pi r_P^4}\frac{1}{P}f_P\nabla_{rad}\frac{f_T}{f_P}. \tag{3.44}$$

Applying the Schwarzschild criterion for convection one gets, from Eq. 3.38 and Eq. 3.44,

$$\frac{d\,\ln\overline{T}}{dM_P} = -\frac{G\,M_P}{4\pi r_P^4}\frac{1}{P}f_P\,\min\left[\nabla_{ad},\nabla_{rad}\frac{f_T}{f_P}\right]. \tag{3.45}$$

3.8 Equations of stellar structure with rotation

With these changes of variables and these approximations we recover the complete set of stellar structure equations with corrections for the rotating case:

$$\frac{\partial P}{\partial M_P} = -\frac{G\,M_P}{4\pi r_P^4}f_P, \tag{3.46}$$

$$\frac{\partial r_P}{\partial M_P} = \frac{1}{4\pi r_P^2\overline{\rho}}, \tag{3.47}$$

$$\frac{\partial L_P}{\partial M_P} = \epsilon_n - \epsilon_\nu + \epsilon_g, \tag{3.48}$$

$$\frac{\partial\,\ln\overline{T}}{\partial M_P} = -\frac{G\,M_P}{4\pi r_P^4}\frac{1}{P}f_P\,\min\left[\nabla_{ad},\frac{f_T}{f_P}\nabla_{rad}\right]. \tag{3.49}$$

with

$$\nabla_{ad} = \frac{P\delta}{\overline{T}\,\overline{\rho}c_P}, \tag{3.50}$$

$$\nabla_{rad} = \frac{3}{16\pi\, acG}\frac{\kappa L_P\, P}{M_P}, \tag{3.51}$$

$$f_P = \frac{4\pi\, r_P^4}{G\, M_P S_P}\frac{1}{\langle g_{eff}^{-1}\rangle}, \tag{3.52}$$

$$f_T = \left(\frac{4\pi\, r_P^2}{S_P}\right)^2 \frac{1}{\langle g_{eff}^{-1}\rangle\langle g_{eff}\rangle}, \tag{3.53}$$

where $\delta = \left(\frac{\partial \ln \rho}{\partial \ln T}\right)_{P,\mu}$ is a thermo-dynamical derivative. Quantities in the brackets, such as $\langle x\rangle$, are averaged on the isobar surface (Eq. 3.19), while $\overline{x}$ are averages in the volume separating two successive isobars. The index P refers to the isobar with a pressure equal to P. Partial derivatives have replaced total derivatives to allow for the fact that the quantities depend not only on mass but also on time. Eqs. 3.46 – 3.49 are used to model rotating star in hydrostatic equilibrium and, as anticipated before, they keep the same form of the classical structure equations (Eqs 2.1 – 2.4). The only difference is the introduction of the form factors f_P and f_T, to keep rotation into account.

3.9 Boundary conditions

As discussed in Section 2.5, in PARSEC the star is subdivided in three zones, the inner structure, the envelope and the atmosphere. The envelope equations are also corrected by the form factors, to take into account rotation, so the equations become

$$\frac{\partial \ln r_P}{\partial \ln P} = -\frac{P\, r_P}{\overline{\rho}\, G\, M_P}\frac{1}{f_P} \tag{3.54}$$

$$\frac{\partial \ln M_P}{\partial \ln P} = -\frac{4\pi r_P^4 P}{G\, M_P^2\, f_P} \tag{3.55}$$

$$\frac{\partial \ln \overline{T}}{\partial \ln P} = \min[\nabla_{ad}, \frac{f_T}{f_P}\nabla_{rad}] \tag{3.56}$$

The atmosphere is also deformed by rotation, and adopting the equation corrected by the form factors, we can derive the new equations, that are

$$\frac{d\tau}{d\log P} = \frac{S_P\langle g_{eff}^{-1}\rangle}{4\pi r_P^2}\kappa\, P \ln 10, \tag{3.57}$$

$$T^4(\tau) = \frac{3}{4}T_{eff}^4\left(\frac{S_P}{4\pi r_P^2}\, f_P\, \tau + q(\tau)\frac{g}{\langle g_{eff}\rangle}\right), \tag{3.58}$$

Where $g = \frac{G\, M_P}{r_P^2}$ is an average gravity. As concern the center boundary condition, we have that, in the center the radius is null so the angular momentum is null, however the condition for the angular velocity is $\left(\frac{d\Omega}{dr}\right)_c = 0$. Thus, even with rotation, we keep the same equations adopted for the classical non rotating case (i.e. Eqs. 2.21 and 2.22).

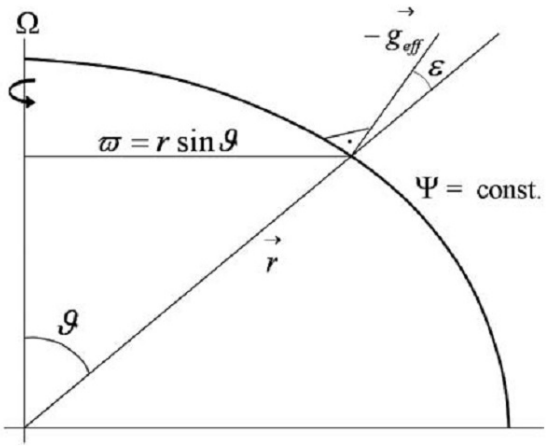

FIGURE 3.3: The angle ε is the angle between the vector radius and the effective gravity vector. From A. Maeder (2009).

3.10 Calculation of the form parameters

3.10.1 Surface of an isobar

In order to calculate the two form factors (given in Eq. 3.52 and Eq. 3.53), we need to know the values of the surface of an isobar, S_P, the averaged effective gravity, $\langle g_{eff} \rangle$, its inverse, $\langle g_{eff}^{-1} \rangle$, and the "volumetric" radius, r_P. Since we know the shape of the star ($x(\theta)$, solving Eq. 3.17), we can calculate the surface of the isobar by the integral

$$S_P = \int_0^{4\pi} d\sigma, \tag{3.59}$$

where $d\sigma$ is the element of the surface of a rotating star and is given by

$$d\sigma = \frac{R^2(\theta)\,\sin\theta\, d\theta\, d\varphi}{\cos\varepsilon} \tag{3.60}$$

where φ is the longitude angle, ε is the angle between the $\overline{g}_{eff}$ and $\overline{r}$, because generally in a rotating star the normal to the surface does not coincide with the radial direction (see Figure 3.3). The angle ε is small, it is zero only at pole and equator, and it is defined by

$$\cos\varepsilon = \frac{\overline{g}_{eff} \cdot \overline{r}}{|g_{eff}|\,|r|}. \tag{3.61}$$

Now, as done before, it is useful to rewrite the previous equation with the dimensionless variables; so, making simple passages, integrating over φ, and applying the substitution $R(\theta) = x(\theta)\, R_{pol}$, one obtains

$$S_P = 4\pi R_{pol}^2 \int_0^{\frac{\pi}{2}} \frac{x^2(\theta)\sin\theta}{\cos\varepsilon}\, d\theta = 4\pi R_{pol}^2\, S' \tag{3.62}$$

where we have defined $S' = S'(\omega) = \int_0^{\frac{\pi}{2}} \frac{x^2(\theta)\sin\theta}{\cos\varepsilon}\, d\theta$ as a dimensionless surface which is only function of ω.

To calculate the surface we need to know $\cos\varepsilon$ and the effective gravity vector, that is given by Eqs. 3.3 – 3.4. Using the unity vectors, $\hat{e}_r$ and $\hat{e}_\theta$, we can rewrite effective gravity vector as

$$\vec{g}_{eff} = \left[-\frac{G\,M_P}{R^2\,(\theta)} + \Omega^2\,R\,(\theta)\,\sin^2\theta\right]\,\hat{e}_r + \left[\Omega^2\,R\,(\theta)\,\sin\theta\,\cos\theta\right]\,\hat{e}_\theta. \quad (3.63)$$

The modulus is

$$|g_{eff}| = \left[\left(-\frac{G\,M_P}{R^2\,(\theta)} + \Omega^2\,R\,(\theta)\,\sin^2\theta\right)^2 + \left(\Omega^2\,R\,(\theta)\,\sin\theta\,\cos\theta\right)^2\right]^{\frac{1}{2}}. \quad (3.64)$$

By using $R\,(\theta) = x\,(\theta)\;R_{pol}$ and $\Omega^2 = \omega^2\,\Omega^2_{crit} = \omega^2\,\left(\frac{2}{3}\right)^3\,\frac{G\,M}{R^3_{pol}}$, we obtain

$$|g_{eff}| = \frac{G\,M_P}{R^2_{pol}}\left[\left(-\frac{1}{x^2} + \frac{8}{27}\,\omega^2\,x\,\sin^2\theta\right)^2 + \left(\frac{8}{27}\,\omega^2\,x\,\sin\theta\,\cos\theta\right)^2\right]^{\frac{1}{2}}. \quad (3.65)$$

For convenience, I define

$$\begin{aligned} A_{geff} &= -\frac{1}{x^2} + \frac{8}{27}\,\omega^2\,x\,\sin^2\theta \\ B_{geff} &= \frac{8}{27}\,\omega^2\,x\,\sin^2\theta\,\cos\theta \end{aligned} \quad (3.66)$$

and, using Eq. 3.65 with Eq. 3.61, one obtains

$$\cos\varepsilon = \frac{A_{geff}}{\left[\left(A_{geff}\right)^2 + \left(B_{geff}\right)^2\right]^{\frac{1}{2}}}. \quad (3.67)$$

It is worth noting that $\cos\varepsilon$ is a pure geometrical factor only function of ω and θ, and it is independent from M_P and R. We are now able to calculate the dimensionless surface, S', and the physical surface of an isobar using Eq. 3.62. Table 3.2 lists the S' values for different ω, and to obtain the total surface of a rotating shell, the corresponding value of the table should be multiplied by the non rotating spherical surface value, i.e $4\pi R^2_{pol}$.

3.10.2 Average effective gravity

Using the above formulation, the average of the effective gravity are given by

$$\langle g_{eff}\rangle = \frac{1}{S_P}\int_0^{4\pi} |g_{eff}|\,d\sigma = \frac{4\pi R^2_{pol}}{S_P}\int_0^{\frac{\pi}{2}} |g_{eff}|\,\frac{x^2\,(\theta)\sin\theta}{\cos\varepsilon}\,d\theta \quad (3.68)$$

Rewriting and using Eqs. 3.65 – 3.67, we obtain

$$\langle g_{eff}\rangle = \frac{G\,M_P}{R^2_{pol}}\langle g_{ad}\rangle, \quad (3.69)$$

where $\langle g_{ad} \rangle$ is the dimensionless average gravity, that using the definition in Eq. 3.66 is

$$\langle g_{ad} \rangle = \frac{1}{S'} \int_0^{\frac{\pi}{2}} \left[\left(A_{geff} \right)^2 + \left(B_{geff} \right)^2 \right]^{\frac{1}{2}} \frac{x^2(\theta) \sin\theta}{\cos\varepsilon} \, d\theta. \tag{3.70}$$

Doing the same for the average of the inverse effective gravity, one obtain

$$\langle g_{eff}^{-1} \rangle = \frac{1}{S_P} \int_0^{4\pi} \frac{1}{|g_{eff}|} \, d\sigma = \frac{4\pi R_{pol}^2}{S_P} \int_0^{\frac{\pi}{2}} \frac{1}{|g_{eff}|} \frac{x^2(\theta) \sin\theta}{\cos\varepsilon} \, d\theta. \tag{3.71}$$

Rewriting we obtain

$$\langle g_{eff}^{-1} \rangle = \frac{R_{pol}^2}{G M_P} \langle g_{ad}^{-1} \rangle, \tag{3.72}$$

where

$$\langle g_{ad}^{-1} \rangle = \frac{1}{S'} \int_0^{\frac{\pi}{2}} \left[\left(A_{geff} \right)^2 + \left(B_{geff} \right)^2 \right]^{-\frac{1}{2}} \frac{x^2(\theta) \sin\theta}{\cos\varepsilon} \, d\theta. \tag{3.73}$$

3.10.3 Computing the form parameters

We are now able to calculate the form factors using Eq. 3.52 and Eq. 3.53, but, as done for the other quantities, is useful to rewrite them using Eq. 3.62, Eq. 3.69 and Eq. 3.72. Thus, we obtain

$$f_P = \frac{4\pi r_P^4}{G M_P S_P} \frac{1}{\langle g_{eff}^{-1} \rangle} = \left(\frac{r_P}{R_{pol}} \right)^4 \frac{1}{S' \langle g_{ad}^{-1} \rangle}, \tag{3.74}$$

and

$$f_T = \left(\frac{4\pi r_P^2}{S_P} \right)^2 \frac{1}{\langle g_{eff}^{-1} \rangle \langle g_{eff} \rangle} = \left(\frac{r_P}{R_{pol}} \right)^4 \left(\frac{1}{S'} \right)^2 \frac{1}{\langle g_{ad}^{-1} \rangle \langle g_{ad} \rangle}. \tag{3.75}$$

It is evident that they are pure geometrical quantities, that depend only on the rotation rate, ω. Table 3.2 lists the values of the two "form" parameters for different ω.

3.10.4 Calculating volume inside the isobar

Since we know the shape of the surface of an isobar, namely the physical root obtained from Eq. 3.17 times the polar radius $R_{\rm pol}$, we can calculate the volume enclosed by it through a rotational integral (as shown in Figure 3.4)[3]. From the numerical integration we obtain the volume V of the isobar, hence, we can define the dimensionless volume as

$$V(\omega) = \frac{4}{3} \pi R_{pol}^3 \, V'(\omega), \tag{3.76}$$

that is only function of the rotation rate ω. The values obtained for different rotation rates are listed in Table 3.2. Combining Eq. 3.18 with the

[3] Among the various method, I used the Pappus-Guldino's formulas and the cylindrical shell method.

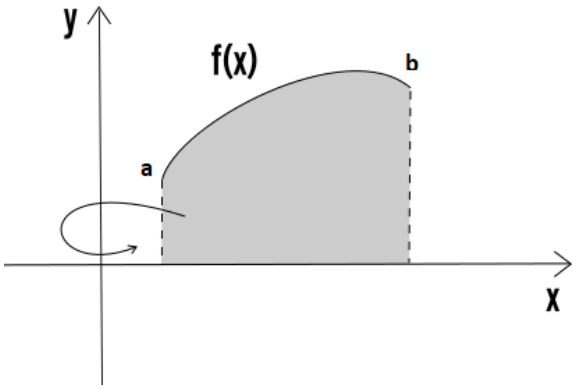

FIGURE 3.4: Schematic view of the rotation around y axis of a general function $f(x)$.

ω	S'	V'	f_T	f_P	$V'\omega^2$
0.00	1.000	1.000	1.000	1.000	0.000
0.20	1.008	1.012	1.000	0.992	0.040
0.40	1.034	1.051	0.999	0.966	0.168
0.50	1.056	1.084	0.997	0.943	0.271
0.60	1.086	1.130	0.992	0.912	0.407
0.70	1.127	1.193	0.982	0.869	0.585
0.80	1.186	1.285	0.960	0.804	0.823
0.90	1.282	1.434	0.900	0.694	1.162
0.95	1.363	1.558	0.821	0.593	1.406
0.99	1.485	1.733	0.622	0.413	1.698
1.00	1.580	1.826	0.000	0.000	1.826

TABLE 3.2: The dimensionless parameters as a function of the rotation rate $\omega = \Omega/\Omega_{crit}$. S' is the surface, V' is the volume, f_T and f_P are the "form" parameters and $V'\omega^2$ is defined in Eq. 3.79.

previous equation we obtain

$$V = \frac{4}{3}\pi r_P^3 = \frac{4}{3}\pi R_{pol}^3 V', \tag{3.77}$$

Thus

$$r_P = R_{pol}\left(V'\right)^{\frac{1}{3}}. \tag{3.78}$$

This relation connects the volumetric radius, used in the structural equations, with the polar one, that is constant as the rotation changes.

3.10.5 Re-computing the polar radius

The quantities that I computed so far, are useful to get the form parameters that enter in the equations of the structure as dimensionless corrections. However, at each time-step during a simulation, the code works with the averaged physical quantities, and to derive and update the form factors it is necessary to know the polar radius, R_{pol}. To find it, we need to have a relation that links the physical quantities to the dimensionless variables. We

find such relation combining the Eq. 3.14 and the Eq. 3.77, thus obtaining

$$V'\omega^2 = \frac{27}{8}\frac{\Omega^2 r_P^3}{G\,M_P}. \tag{3.79}$$

This is an interesting equation from which we can obtain the dimensionless values (in the left-hand term) from the physical variables that are used in the structure equations (in the right-hand term). Since the dimensionless volume, $V' = V'(\omega)$, is only a function of ω, the product $V'\omega^2$ is unique for each couple of V' and ω. In Table 3.2 are shown the $V'\omega$ values for different ω. At each time-step, for each shell identified by the mass M_P, enclosed in a volumetric radius r_P and that rotates with an angular velocity Ω, I obtain the rotation rate, ω, using the Eq. 3.79. Once ω is known, I can derive all the dimensionless quantities needed to evaluate the form factors and correct the structural equations.

I note that, the value $V'\omega^2$ is related to the useful quantity discussed by A. Maeder (2009) through the following relation

$$\frac{\Omega^2}{2\pi G\rho_M} = \frac{\Omega^2 V}{2\pi G M_P} = \frac{\omega^2\Omega_{crit}^2 V}{2\pi G M_P} = \tag{3.80}$$

$$= \frac{\omega^2}{2\pi G M_P}\frac{4}{3}\pi R_{pol}^3 V'\frac{8}{27}\frac{G\,M_P}{R_{pol}^3} = \frac{16}{81}\omega^2 V', \tag{3.81}$$

where $\rho_M = \frac{M_P}{V_P}$ is the average density on the volume of an isobar, $\frac{\Omega^2}{2\pi G\rho_M}$ is a dimensionless quantity, that is of the order of the ratio between the centrifugal acceleration and the gravity at the equator and it is a measure of the "strength" of the rotation. Table 3.2 lists the values obtained from our integration as a function of the rotation rate. This quantity is used to compute the effective mass, i.e. the mass which would produce the same gravity if there would be no centrifugal force, that is defined as

$$M_P^* = M_P\left(1 - \frac{\Omega^2}{2\pi G\rho_M}\right). \tag{3.82}$$

3.11 Von Zeipel effect and the surface temperature

The Von Zeipel theorem (von Zeipel, 1924) states that the emitted radiative flux of a rotating star is proportional to the local effective gravity. It writes

$$\vec{F}(\omega_s,\theta) = -\frac{L}{4\pi\,G\,M^*}\vec{g}_{eff}(\omega_s,\theta), \tag{3.83}$$

where ω_s is the surface angular velocity of the star, M^* is the star effective total mass, defined by Eq. 3.82 and $g_{eff}(\omega_s,\theta)$, is the surface effective gravity of the star. From the Von Zeipel theorem it is immediately clear that the flux emitted by a rotating star depends from both the rotation rate and the inclination angle of the rotation axes of the star with respect to the

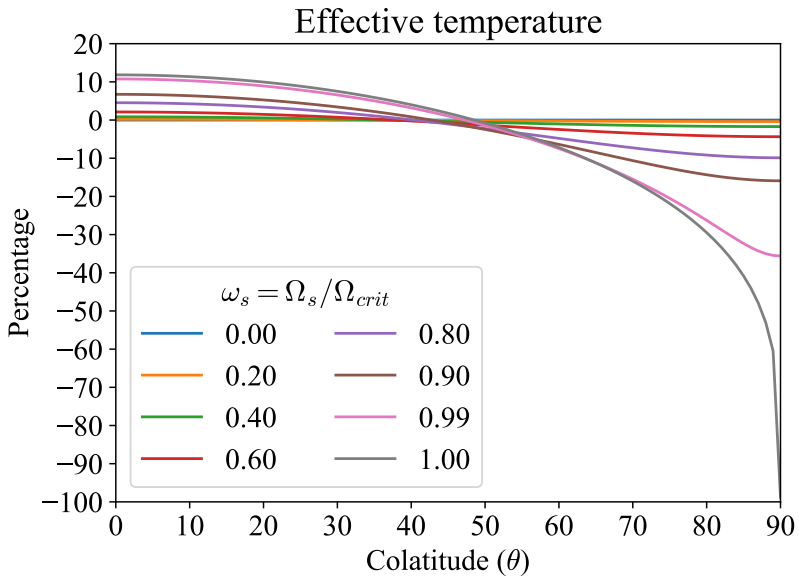

FIGURE 3.5: The ratio $T_{eff}(\omega)/T_{eff}(0)$ in percentage as a function of the colatitude θ for various rotation rates, in different colors. This is the gravity darkening due to the geometrical distortion of a rotating star.

line of sight. From the above equation we can derive effective temperature, that is

$$T_{eff}(\omega_s,\theta) = \left(\frac{L}{4\pi\,\sigma\,G\,M^*}\right)^{\frac{1}{4}} \left[g_{eff}\left(\omega_s,\theta\right)\right]^{\frac{1}{4}}. \tag{3.84}$$

Both g_{eff} and T_{eff} vary over the surface of a rotating star and influence the emergent spectrum of the star. It is convenient to derive the ratio between the effective temperature in case of rotation and the effective temperature at $\omega = 0$, $T_{eff}(0)$, that is constant along the surface, so

$$\frac{T^4_{eff}(\omega_s,\theta)}{T^4_{eff}(0)} = \frac{1}{\left(1-\frac{\omega_s^2}{2\pi G\rho_M}\right)} \frac{\left|g_{eff}\left(\omega_s,\theta\right)\right|}{\left|g_{eff}\left(0\right)\right|} \tag{3.85}$$

where $g_{eff}(0) = \frac{G\,M}{R^2_{pol}}$ is the classical formula for the gravity acceleration. Using Eq. 3.65 we obtain

$$\frac{T^4_{eff}\left(\omega_s,\theta\right)}{T^4_{eff}\left(0\right)} = \frac{\left[\left(A_{geff}\right)^2+\left(B_{geff}\right)^2\right]^{\frac{1}{2}}}{\left(1-\frac{\omega_s^2}{2\pi G\rho_M}\right)}, \tag{3.86}$$

where A_{geff} and B_{geff} are defined in Eqs. 3.66.

Figure 3.5 shows the percentage variation of the effective temperature, $T_{eff}(\omega_s,\theta)$, with respect to the $T_{\rm eff}(0)$ of the correspondent non rotating star. In case of rotation, the equatorial regions are fainter and cooler than the polar ones, which are brighter and hotter. As the rotation rate increases

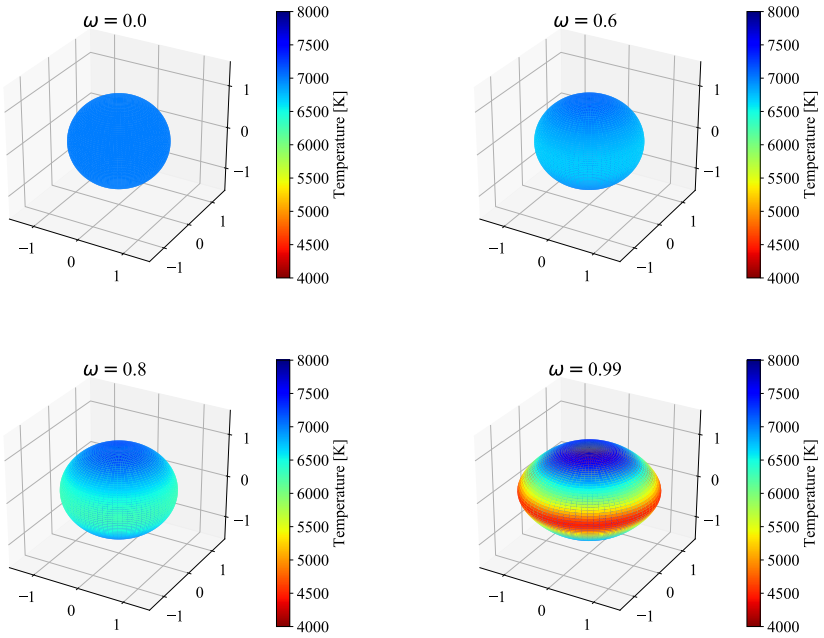

FIGURE 3.6: Reconstruction of the effective temperature on the star surface for different rotation rates, ω. In different colors the effective temperature. I adopted the Roche approximation to compute the surface shape and the Von Zeipel theorem to obtain the effective temperature. To note that in cases with rotation, the poles are hotter than the equatorial region of the star.

the differences become bigger. This effect is usually called the gravity darkening.

Adopting the Roche approximation and using the Von Zeipel theorem, we can reconstruct the surface of a rotating star and the distribution of the effective temperature along it. An example is shown in Figure 3.6 for different rotation rates, ω. In the computation I assumed that the non-rotating star (the top left-hand panel) has an effective temperature of 7000 K. As the rotation grows, the star becomes more and more oblate and the $T_{\rm eff}$ distribution changes with the colatitude, θ. In the case of critical rotation, the star has a equatorial radius the 50 per cent bigger than the polar one (as shown in Table 3.1) while the effective temperature at the pole is almost two times the $T_{\rm eff}$ at the equator.

It is worth to note that, recent interferometric observations of rapidly rotating stars (Domiciano de Souza et al., 2014) have found that if we model the gravity darkening as $F(\theta) \sim g_{eff}^{4\beta}$, then the coefficient is $\beta \leq 1/4$. And, in particular, Domiciano de Souza et al. (2014) found a decreasing trend of the exponent as the rotation rate grows. Theoretical studies by Espinosa Lara and Rieutord (2011) and Espinosa Lara and Rieutord (2013) are in line with the above results. They give a different analytical description for the gravity darkening, that is in agreement with 2D models of rotating stars performed with their 2D ESTER code. Adopting the Von Zeipel theorem takes to an over-estimate of the $T_{\rm eff}$ differences in case

of high rotation rates ($\omega \leq 0.6$). In Chapter 5, I will discuss with more details about the derivation of stellar spectra and photometry of rotating stars, also using the more accurate Espinosa Lara and Rieutord (2011) theoretical description of the gravitational darkening.

Chapter 4

Transport of angular momentum

In non rotating (classical) models, usually, the mixing of elements take place only in the convective regions of the star. The chemical elements in the radiative zones are not mixed (if the microscopic diffusion is neglected). On the other side, in rotating stars, the mixing takes place also in the radiative regions of the stars. Besides the geometrical distortion of the star structure, rotation induces instabilities that lead to a redistribution of the chemical elements and the angular momentum throughout the star. Depending on the rotation rate, this extra-mixing may strongly affect the evolution of the star. Thanks to several studies performed in the past decades on this subject, it is now well known that the two main rotation instabilities that cause the extra-mixing are:

- The meridional circulation, as known as the Eddington-Sweet circulation (Eddington, 1929; Sweet, 1950), is a macro motion of the stellar material from poles to the equator or the reverse, due to the thermal imbalance of a rotating star;
- The shear instability, due to the different rotation velocity of two nearby shells of the star, drives to turbulent mixing of the chemical elements between the layers.

Other physical instabilities are acting in rotating stars that lead to the transport of both the chemical elements and the angular momentum, but their contribution is of the second-order than the above mentioned two. The two cited rotation instabilities have a sort of hierarchical dependence, in fact, as stated by Meynet and A. Maeder (1997), rotation takes to the geometric distortion of the star that implies meridional circulation, which in turn induces the differential rotation which produces shear instabilities. Also, the mass loss plays an important role in the transport of the angular momentum since it is the main way in which single stars lose their momentum after the zero-age main sequence (ZAMS).

Depending on the initial rotation rate in the ZAMS, stars may evolve in a very different way. Mainly because, during the evolution, the rotation mixing provides fresh fuel to the burning cores of the stars and transports the processed material from the cores to the stellar surfaces.

This Chapter is divided as follows. I describe the meridional circulation in Section 4.1. In Section 4.2 I present the basic equation to treat the shear instability and in Section 4.3 the transport equation is given. In Section 4.4 I describe the prescriptions adopted to treat the mass loss enhancement due to rotation. Finally, in Section 4.5 I discuss the calibration of the mixing parameters.

4.1 Meridional circulation

The meridional circulation is a macro motion of material triggered by the thermal imbalance generated by the rotationally deformed geometry of the star. From the Von Zeipel theorem (Eq. 3.83, von Zeipel, 1924), we know that the radiative flux depends on the effective gravity, hence, a rotating star cannot be in hydrostatic and radiative equilibrium at the same time. The imbalance generated by the different effective gravity between the equator and the poles takes to this large scale motion of material (i.e. the Eddington–Sweet circulation). In the case of a solid body rotation, the matter in the deep radiative layers of the star rises at the pole and descends at the equator, as shown in Figure 4.1. While, in case of a differential rotating star, even two counter rotating circulation cells could appear, as shown in Figure 4.2. Figure 4.3 shows an example of the 3D structure of the circulation cells for a 20 $M_\odot$ differentially rotating star model. More detailed simulations of fast rotating stars, show that the circulation of the material may be more complicated than that shown in figures 4.1, 4.2, 4.3 (for instance see Espinosa Lara and Rieutord, 2013).

From the theory developed by J.-P. Zahn (1992), and improved by Andre Maeder and Jean-Paul Zahn (1998), the main quantity that characterizes the meridional circulation is the velocity, U, that can be decomposed into two components, the horizontal and the radial one. The latter is given by

$$U(r) = \frac{P}{\overline{\rho g}\, c_P\, \overline{T}\left[\nabla_{ad} - \nabla_{rad} + \left(\frac{\varphi}{\delta}\right)\nabla_\mu\right]} \left\{ \frac{L}{M^*}\left(E_\Omega + E_\mu\right) + \frac{c_P \overline{T}}{\delta}\frac{\partial \Theta}{\partial t} \right\}, \tag{4.1}$$

where the quantities ρ, g, T are averages on the isobars, L is the total luminosity that arises from an isobar, M^* is the effective mass defined by Eq. 3.82, c_P is the specific heat capacity at constant pressure, ∇_{ad} and ∇_{rad} are the adiabatic and radiative gradients, respectively, defined by Eqs. 3.50 and 3.51, $\nabla_\mu = \frac{d \ln \mu}{d \ln P}$ is the mean molecular weight gradient, $\delta = \left(\frac{\partial \ln \rho}{\partial \ln T}\right)_{P,\mu}$ and $\varphi = \left(\frac{\partial \ln \rho}{\partial \ln \mu}\right)_{P,T}$ are thermodynamic derivatives[1], $\Theta = \frac{\tilde{\rho}}{\overline{\rho}} = \frac{1}{3}\frac{r^2}{g}\frac{d\Omega^2}{dr}$ is the baroclinic equation, that is a measure of the differential rotation in the radial direction. In this definition, the density is expanded around its average on an isobar up to the second order of the Legendre polynomials, $P_2(\cos\theta)$[2]. In case of solid body rotation, the quantity Θ is null.

[1] These derivatives are defined from the general form of the equation of state, that is $\frac{d\rho}{\rho} = \alpha\frac{dP}{P} - \delta\frac{dT}{T} + \varphi\frac{d\mu}{\mu}$.

[2] The Legendre polynomials are a set of functions orthogonal each other, used to solve the Laplace equation ($\nabla^2\Phi = 0$) in spherical coordinates. The second order polynomial is $P_2(x) = \frac{1}{2}(3x^2 - 1)$.

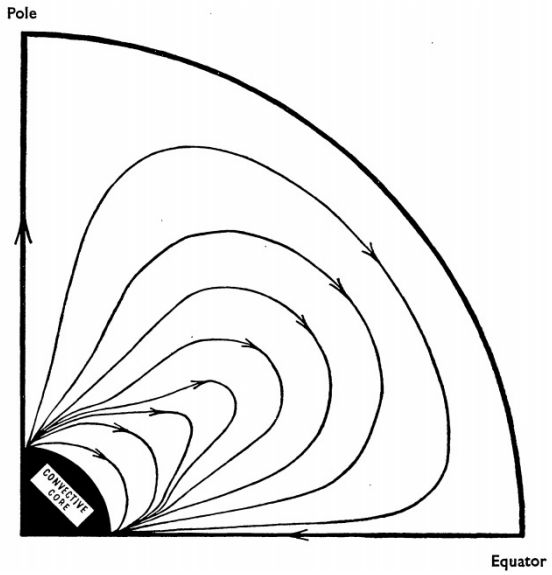

FIGURE 4.1: A schematic section of a rotating star in which the black lines represent the meridional circulation in the case of a solid body rotation. The black circle is the convective core of the star, while the white region of the sketch, including the lines of the circulation, is the radiative envelope of the star. The image has been taken and readapted from Sweet (1950).

E_Ω and E_μ are terms that depend on the Ω- and μ-distributions. The second one, the main molecular weight distribution, may act as a barrier and inhibit the circulation. We redirect the reader to A. Maeder (2009) to find the full expressions for the two term. Here we provide the expression of E_Ω in the case of a uniform rotation, that is

$$E_\Omega = 2\left[1 - \frac{\Omega^2}{2\pi G\overline{\rho}} - \frac{\overline{\epsilon}_n + \overline{\epsilon}_g}{\epsilon_m}\right]\frac{\widetilde{g}}{\overline{g}}, \tag{4.2}$$

where $\epsilon_m = L_P/M_P$ is the sum of the nuclear and gravitational energy produced within radius r_P, $\overline{\epsilon}_n$ is the averaged nuclear energy production rate, $\overline{\epsilon}_g$ is the gravitational energy rate, $\frac{\widetilde{g}}{\overline{g}}$ represents the fluctuations of the mean gravity on an isobar, and the ratio is of the order of $\frac{\Omega^2 r_0^3}{GM}$, where r_0 is the radius in which $P_2(\cos\theta) = 0$. An interesting quantity that appears in the E_Ω expression, is the Gratton-Opik term, $\left(1 - \frac{\Omega^2}{2\pi G\overline{\rho}}\right)$[3]. This term becomes important in the outer layers of the star, where the local density starts to be very small. In those regions, the ratio $\frac{\Omega^2}{2\pi G\overline{\rho}}$ may become bigger than 1, changing sign to the meridional circulation radial velocity. A positive value of $U(r)$ means a current that is going up along the polar axis and descend near the equatorial plane, as illustrated by the inner loop in Figure 4.2, thus transporting angular momentum inward. While, a negative value makes an inverse motion of the current that takes to an

[3]It is worth to note that, this term is different with respect to the one in the effective mass expression given in Eq. 3.82. In fact, here, the density is averaged in the volume between two isobars.

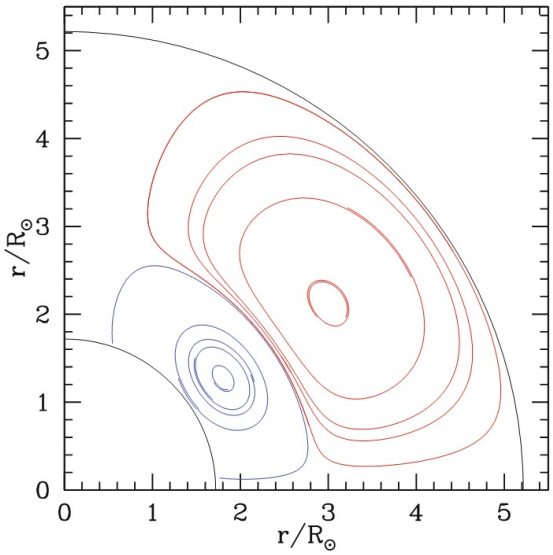

FIGURE 4.2: Circulation currents in a 20 $M_\odot$ differentially rotating star, in the middle of the H-burning (MS) phase. The initial rotation velocity is 300 km/s. The inner loop (the blue lines) is raising along the polar axis, while the outer loop (the red lines) is going up in the equatorial plane. The external cell is also called the Gratton Opik circulation cell. The figure has been taken and readapted from A. Maeder (2009).

outward transport of angular momentum, it corresponds to the external loop in Figure 4.2.

The horizontal component of the circulation, $U(\theta)$, can be derived from $U(\theta) = V(r)\frac{dP_2(\cos\theta)}{d\theta}$ and $V(r)$ can be obtained from

$$\frac{1}{r}\frac{d}{dr}\left[\rho\, r^2\, U(r)\right] - 6\rho\, V(r) = 0, \tag{4.3}$$

once $U(r)$ is known.

Since, numerical difficulties in the implementation and computation of the full equation for the velocity of the meridional circulation (Eq. 4.1), in PARSEC I have implemented three different simplified expressions for $U(r)$. These are:

- the classical expression for rigid rotation (Sweet, 1950; A. Maeder and Meynet, 2000; Rudolf Kippenhahn, Alfred Weigert, and Achim Weiss, 2012) reads as

$$U_{Kip} = \frac{8}{3}\,k^2\,\frac{L}{M_r g}\,\frac{\gamma-1}{\gamma}\,\frac{1}{\nabla_{ad}-\nabla}\left(1-\frac{\Omega^2}{2\pi G\rho}\right) \tag{4.4}$$

  where $k^2 = \frac{\Omega^2 r_p^3}{G\,M_r}$ is the local ratio of centrifugal force to gravity and γ is the ratio of the specific heats C_P/C_V. This expression is obtained assuming the conservative case of rotation (i.e. solid body rotation), it ignores the molecular weight barriers, and diverges at the surface of the star (A. Maeder and Meynet, 2000);

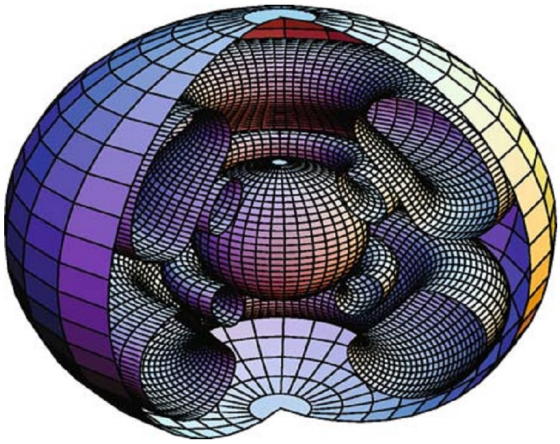

FIGURE 4.3: View of the different meridional circulation cells in a rotating 20 $M_\odot$ model, at the beginning of the MS with $v_{ini} = 300$ km s^{-1}. In the upper hemisphere on the right section, matter is turning counterclockwise along the outer stream line and clockwise along the inner one. The inner sphere is the convective core. Image from Meynet and A. Maeder (2002).

- The same expression as before, but corrected by a "stabilizing" circulation velocity due to the molecular weight barrier. Following Heger, N. Langer, and Woosley (2000) we have that

$$U_{Heg} = \max\{|U_{Kip}| - |V_\mu|, 0\}, \tag{4.5}$$

  where $V_\mu = \frac{H_P}{\tau_{KH}} \frac{\varphi \nabla_\mu}{\delta(\nabla - \nabla_{ad})}$ is the molecular weight current and τ_{KH} is the local Kelvin-Helmholtz timescale. This term stabilizes the current in the internal layers of the star in which there is a molecular weight gradient;

- An approximate form of the general expression in Eq. 4.1, in the case of stationary and uniform rotation, given by A. Maeder (2009) and Potter, Tout, and Eldridge (2012). It reads as

$$\begin{aligned} U_{Maed} = & \frac{P}{\overline{\rho g}\, c_P\, \overline{T}[\nabla_{ad} - \nabla_{rad} + (\frac{\varphi}{\delta})\nabla_\mu]} \frac{L}{M^*} \times \\ & \times \left[1 - \frac{\Omega^2}{2\pi G \overline{\rho}} - \frac{\overline{\epsilon}_n + \overline{\epsilon}_g}{\epsilon_m}\right] \frac{\Omega^2 r^3}{G M} \end{aligned} \tag{4.6}$$

  This formulation take into account for the molecular barrier, and does not diverge in the external layers of the star.

In this work, I adopted this latter prescription.

4.2 Shear instability

The shear instability starts to arise when two different layers in a stratified fluid, have different velocities. In the case of a rotating star, the differential rotation is generated by the meridional circulation, that transport

the angular momentum between the shells. The shear instability occurs according to the Richardson criterion, that reads as

$$Ri = \frac{N^2}{(dv/dr)^2} < Ri_c = \frac{1}{4}, \tag{4.7}$$

where $N^2 = \frac{g_{eff}\delta}{H_P}\left(\nabla_{ad} - \nabla_{rad} + \frac{\varphi}{\delta}\nabla_\mu\right)$ is the Brunt-Väisälä frequency, and v is the tangential rotation velocity. In case of shellular rotation the derivative becomes $\frac{dv}{dr} = r\sin\theta(\frac{d\Omega}{dr})$. In the Eq. 4.7, the criterion does not take into account of thermal effects and of the horizontal diffusion. Without the inclusion of the latter, the derived diffusion coefficient for the shear instability results totally suppressed in regions in which there is a μ-gradient. Talon and Jean-Paul Zahn (1997) showed that including the horizontal diffusion in the Richardson criterion, the effect of suppression by the μ-gradient is reduced, allowing the shear mixing in those regions. They provided the following expression to compute the diffusion coefficient of the shear instability in a 1D scheme

$$D_{\text{s.i.}} = \frac{8}{5}\frac{\text{Ri}_\text{c}\left(r\,d\Omega_r/dr\right)^2}{N_T^2/(K+D_h) + N_\mu^2/D_h}, \tag{4.8}$$

where the Brunt-Väisälä frequency has been split into two quantities, namely $N_T^2 = \left(g\delta/H_p\right)\left(\nabla_\text{ad} - \nabla_\text{rad}\right)$ and $N_\mu^2 = \left(g\varphi/H_p\right)\nabla_\mu$, Ri_c is the critical Richardson number, $K = 4acT^3/3C_pk\rho^2$ is the thermal diffusivity, $D_\text{h} \simeq |rU|$ is the coefficient of horizontal turbulence (J.-P. Zahn, 1992). In PARSEC, I introduced $D_\text{s.i.}$ following the Talon and Jean-Paul Zahn (1997) formulation to treat the shear mixing. Other formulation for the shear instability diffusion and for the horizontal turbulence diffusion coefficients can be found in literature (for instance see Heger, N. Langer, and Woosley, 2000; A. Maeder, 2009; Ekström, Georgy, et al., 2012; Potter, Tout, and Eldridge, 2012).

4.3 Mixing and transport of angular momentum

The transport of angular momentum due to rotation instabilities could be treated as an advective-diffusive process (Andre Maeder and Jean-Paul Zahn, 1998; Eggenberger et al., 2008; Potter, Tout, and Eldridge, 2012; Chieffi and Limongi, 2013). In this case, the equation for the transport is

$$\rho\, r^2\frac{dr^2\Omega}{dt} = \frac{1}{5}\frac{\partial}{\partial r}\left(\rho r^4 U(r)\Omega\right) + \frac{\partial}{\partial r}\left(\rho r^4 D_{s.i.}\frac{\partial\Omega}{\partial r}\right), \tag{4.9}$$

where Ω is the angular velocity, $U(r)$ is the radial component of the velocity of the meridional circulation, $D_{s.i.}$ is the shear instability diffusion coefficient given in Eq. 4.13. In the right side of this equation, the first term is related to the advection, due to the meridional circulation. While, the second term is the diffusion, that is due to the shear instability.

The advective-diffusive scheme is adopted by many stellar evolutionary codes, like GENEC (Eggenberger et al., 2008), ROSE (Potter, Tout, and Eldridge, 2012) and FRANEC (Chieffi and Limongi, 2013).

Another way to treat the angular momentum transport is with the pure diffusive scheme. This is a simplification of the more sophisticate advective-diffusive one. However, as shown by Chieffi and Limongi (2013), adopting the advection scheme, in most cases, the redistribution of angular momentum goes in the direction of flattening the Ω profile over time, as in the pure diffusive scheme. Moreover, Georgy, Ekström, et al. (2013) apply in GENEC the advection scheme only during the MS phase, since in later phases the advection has no time to efficiently transport the angular momentum, due to the shorter evolutionary time-scales. Hence, they use the pure diffusion approximation, for the more evolved phases of the star, gaining in computational simplicity and efficiency. This methodology to solve the angular momentum transport is adopted by various codes and, some of these are KEPLER (Heger, N. Langer, and Woosley, 2000), STERN (Yoon and Langer, 2005), MESA (Paxton, Smolec, et al., 2019), and now PARSEC v2.0. The pure diffusive equation for the angular momentum transport writes as

$$\rho\, r^2 \frac{dr^2\Omega}{dt} = \frac{\partial}{\partial r}\left(\rho r^4 D \frac{\partial \Omega}{\partial r}\right), \tag{4.10}$$

where the total diffusion coefficient D is given by the sum of different instabilities, namely

$$D = D_{\rm MLT} + D_{\rm s.i.} + D_{\rm m.c.}, \tag{4.11}$$

in which

1. $D_{\rm MLT}$ is the diffusion coefficient in the convective zones of the star. To computed it, in PARSEC, we adopt the mixing length theory (MLT) by Böhm-Vitense (1958). It is given by $D_{\rm MLT} = \frac{1}{3} v^*\, l_{\rm MLT}$, where v^* is the average velocity of the plasma bubbles that are rising or sinking in the convective regions, $l_{\rm MLT} = \alpha_{\rm MLT} H_{\rm P}$ is the mixing length, $\alpha_{\rm MLT}$ is the MLT parameter and $H_{\rm P}$ is the pressure scale height. The coefficient is non-zero only in the unstable zones of the star and in the overshooting regions.

2. $D_{\rm s.i.}$ is the diffusion coefficient due to the shear instability. We use the formulation by Talon and Jean-Paul Zahn (1997) given in Eq. 4.8.

3. $D_{\rm m.c.}$ is the diffusion coefficient due to the meridional circulation. We use the approximation provided by J.-P. Zahn (1992)

$$D_{\rm m.c.} \simeq \frac{|r\, U(r)|^2}{30 D_{\rm h}} \tag{4.12}$$

where $U(r)$ is the radial component of the meridional circulation velocity. This formulation for the meridional circulation diffusion coefficient is valid when the horizontal diffusion is much larger than the vertical one (i.e. $D_{\rm h} \gg D_{\rm s.i.}$), that is the "shellular" approximation law (see Sections 3.1 and 3.2). As discussed in Section 4.1, I have included three possible choices for $U(r)$ in the code, these are: (1) the simpler expression given by Rudolf Kippenhahn, Alfred

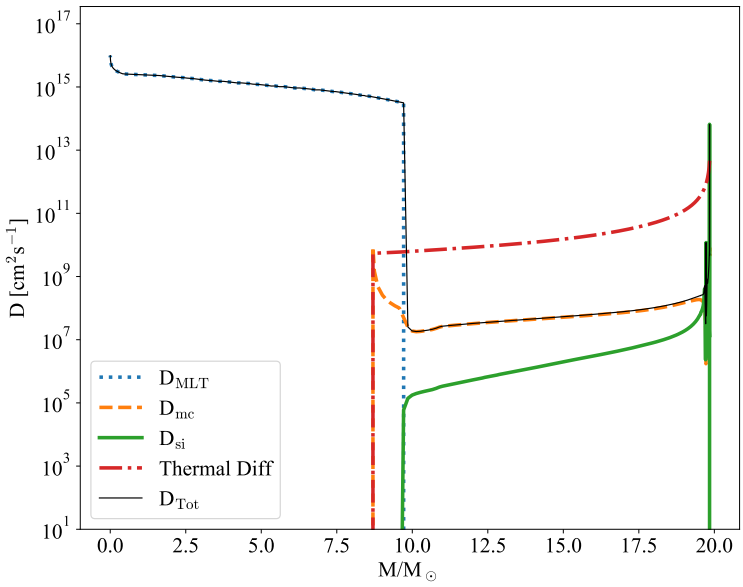

FIGURE 4.4: The diffusion coefficients in the interior of a star model of 20 $M_\odot$ in the MS. The model has an initial chemical composition of Hydrogen, Helium, and metals in mass fraction of X=0.728, Y=0.263 and Z=0.008, respectively. The current Hydrogen content is X=0.5. The blue dotted line indicate the convective coefficient, $D_{\rm MLT}$, the dashed orange line is the meridional circulation coefficient, the green solid line indicate the shear instability one, the dashed dotted line is the thermal diffusivity coefficient and the black thin solid line indicate the total diffusion coefficient.

Weigert, and Achim Weiss (2012) (Eq. 4.4); (2) the same expression corrected by a "stabilizing" circulation velocity due to the molecular weight barrier following Heger, N. Langer, and Woosley (2000) (Eq. 4.5); and (3) an approximate form of the more general expression of Andre Maeder and Jean-Paul Zahn (1998), for stationary and uniform rotation, given by A. Maeder (2009) and Potter, Tout, and Eldridge (2012) (Eq. 4.6). I adopt this latter prescription in the computation of the new sets of evolutionary tracks presented and used in this Thesis, i.e. $U(r) = U_{Maed}$.

Figure 4.4 shows the diffusion coefficients versus the mass of a 20 $M_\odot$ model when the star central Hydrogen content is 0.5 in mass fraction. In this phase, in the inner radiative region, the shear instabilities coefficient is few orders of magnitude lower than the meridional circulation one. While in the outer layer of the star, they have about the same order of magnitude. The convective diffusion coefficient is non zero only in the convective and in the overshooting regions of the star.

The mixing of the chemical elements is treated as discussed in Section 2.4, hence solving the system of equations given in Eq. 2.12. The extra

mixing induced by rotation instabilities is taken into account by expressing the total diffusion coefficient as a weighted sum of the different contributions:

$$D_{\rm tot} = D_{\rm MLT} + f_{\rm c} \times (D_{\rm s.i.} + D_{\rm m.c.}) \,. \tag{4.13}$$

Here, the rotation diffusion coefficients are scaled by a factor $f_{\rm c}$, used to calibrate the efficiency of the rotation extra mixing (the calibration of this parameter is discussed in a following Section).

It is worth mentioning that, a more complete treatment should account for interactions between the above mixing processes that could possibly affect their efficiency, as described e.g. in A. Maeder, Meynet, et al. (2013). These effects are generally not included in literature also because the total mixing coefficient already contains parameters that need to be calibrated on observations.

At each time step, we take care to conserve the angular momentum along the structure and in the atmosphere of the star, hence assuring the conservation of the total angular momentum with age. In this context, I recall that the parameter characterizing our evolutionary tracks regards the initial angular rotation rate, $\omega_{\rm i}$, that is the ratio between the surface angular velocity (Ω) and the star break-up angular velocity ($\Omega_{\rm crit}$), in the ZAMS of the star.

4.4 Mass loss

Another important effect in the angular momentum transport is the mass loss. In previous releases of PARSEC evolutionary tracks (without rotation), the mass loss was activated only for stars more massive than 12 $M_{\odot}$, which are the only ones to be significantly affected by this process during their main nuclear burning phases. However, in the case of rotating stars the mass loss must be taken into account also at lower masses, for the following reasons. Firstly, rotation takes to an enhancement of the mass loss due to the lower effective gravity, caused by the centrifugal forces. Secondly, the mass loss removes angular momentum from the star, assuring the stability of the angular momentum transport and of the evolution of the star. This is particularly true in cases of fast rotating stars (e.g. $\omega \geq 0.90$).

To include this effect in stellar models we used the prescription provided by Heger, N. Langer, and Woosley (2000), who modify the mass loss rate as follows

$$\dot{M}(\omega_S) = \dot{M}(\omega_S = 0) \left(\frac{1}{1 - v_S / v_{\rm S,crit}} \right)^{\xi}, \quad \text{with} \quad \xi = 0.43 \tag{4.14}$$

where ω_S is the surface rotation rate of the star, $\dot{M}(\omega_S = 0)$ is the mass loss rate in case of no rotation, computed using the prescriptions provided by de Jager, Nieuwenhuijzen, and van der Hucht (1988) for low-intermediate mass stars, and with the prescriptions described in Y. Chen, A. Bressan, et al. (2015) for massive stars. v_S is the surface tangential velocity of the star, and $v_{\rm S,crit}$ is the surface breakup velocity, that is

$$v^2_{\rm S,crit} = \frac{GM_*}{r_{Phot}} (1 - \Gamma_{\rm E}) \,, \tag{4.15}$$

where M_* is the total mass of the star, r_{Phot} is the photospheric radius of the star and Γ_E is the Eddington factor. During the evolution, stars with high initial rotation rates ($\omega_i \geq 0.90$) may reach the critical rotation (typically at the end of the MS). In that case, the surface effective gravity at the equator is zero due to the centrifugal forces, and the most external layers become detached from the star. This is usually called mechanical mass loss. As suggested by Georgy, Ekström, et al. (2013), we may expect that this phenomenon happens mainly in the equatorial region of the star, and the super-critical layers escape in such a way to maintain the surface at the critical velocity or slightly below it. The mass loss by winds (also called radiative mass loss) computed so far using Eq. 4.14, may not be enough to extract the momentum required for keeping the external shells below the critical velocity. To treat this, the code computes the mechanical mass loss starting from the angular momentum excess found in the the super-critical shells. This excess is the difference between the actual angular momentum of the super-critical shells and their critical one, defined as $L_c = \Omega_c\, I$, where I is the momentum of inertia of each shell. From the excess momentum we estimate the mass that should be removed to keep the star below its critical rotation. Because of numerical difficulties, we define a maximum angular rotation rate, that is $\omega_{\max} = 0.998$. After these calculations the code selects the largest mass loss between the two, and removes it from the star. We carefully treated the mass loss enhancement and the mechanical mass loss, taking particular care to the angular momentum conservation over time. At each time step, the sum of the current angular momentum of the star plus the total momentum lost by the wind is equal to the initial angular momentum given to the star. In this work, we do not take into account of longitudinal anisotropy of the wind and coupling with the magnetic field of the star. Other prescription for the mass loss enhancement by rotation are provided by A. Maeder and Meynet (2000) and Georgy, Meynet, and A. Maeder (2011) and Georgy, Ekström, et al. (2013).

4.5 Calibration of parameters

Current implementations of rotation require the use of two parameters to calibrate the diffusion coefficients in the mixing equations. They are f_μ and f_c, which control the molecular barrier "strength" and the chemical mixing efficiency, respectively (Heger, N. Langer, and Woosley, 2000; Yoon and Langer, 2005; Brott, de Mink, et al., 2011; Potter, Tout, and Eldridge, 2012; Chieffi and Limongi, 2013; Paxton, Cantiello, et al., 2013; Limongi and Chieffi, 2018). The f_c parameter, already introduced in Eq. 4.13, multiplies the rotational diffusion coefficients in the chemical diffusion equation. While, the f_μ parameter multiplies the molecular weight gradient, hence the effective molecular gradient becomes

$$\nabla_\mu^{\text{eff}} = f_\mu \times \nabla_\mu. \tag{4.16}$$

Figure 4.5 shows the effect of various combinations of the two calibration parameters, in a 20 $M_\odot$ star model, rotating with an initial rotation rate $\omega_i = 0.60$. In the HR diagram (the top panel) are clearly visible the effects

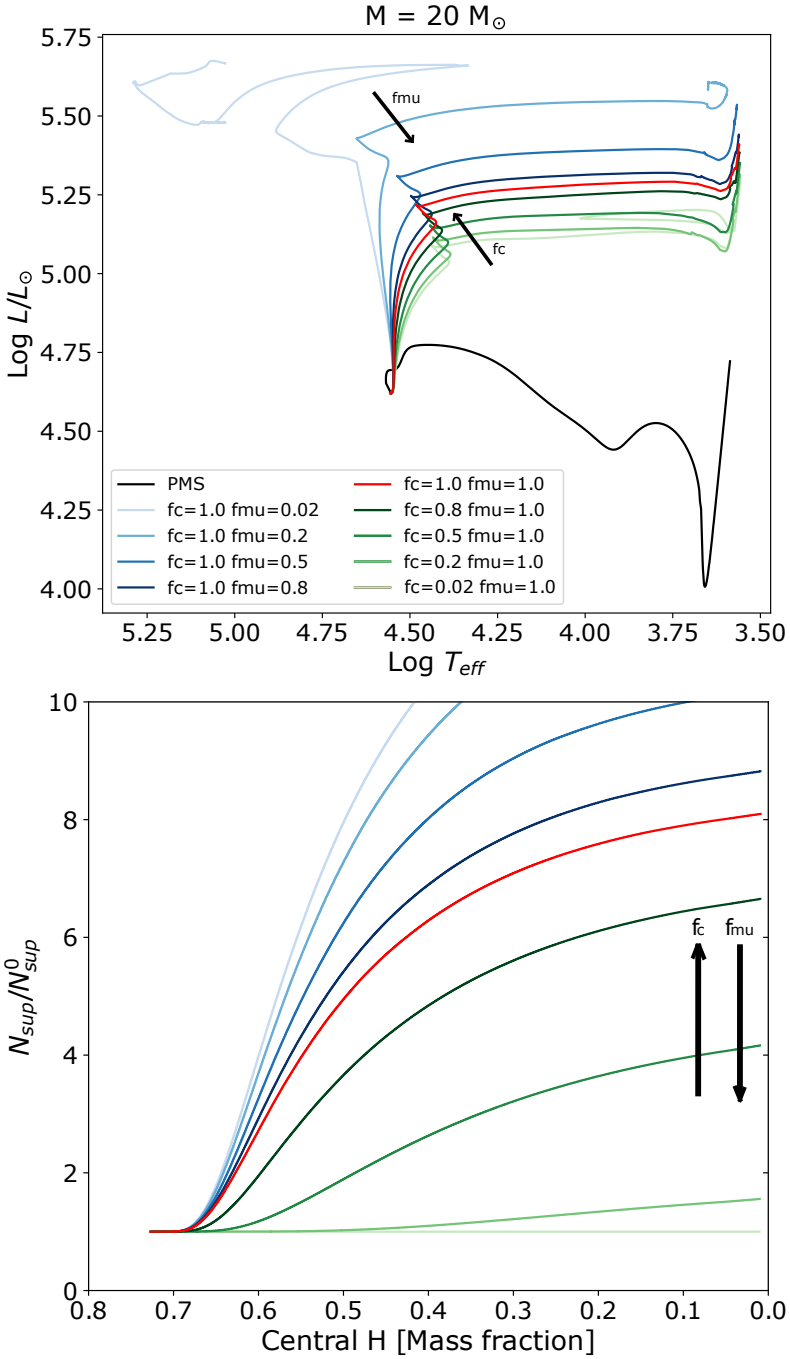

FIGURE 4.5: In the top panel is shown the evolutionary tracks of 20 $M_{\odot}$ models, with different combinations of the calibrating parameters, f_c and f_μ. The black solid line indicates the common PMS of the models. At the ZAMS the rotation rate is $\omega_i = 0.60$ for all the models. The blue lines indicate models with a fixed value for the f_c parameter, while the green lines indicate models with a fixed f_μ parameter. The black arrows indicate the direction of growing f_c and f_μ. In the bottom panel is shown the correspondent surface Nitrogen enrichment for each model. The color code is the same of the top panel.

TABLE 4.1: Hydrogen (X), helium (Y) and metals (Z) mass fractions adopted for the models of massive stars in the Galaxy (MW) and in the Large and Small Magellanic Clouds (LMC, SMC). From Brott, de Mink, et al. (2011).

	X	Y	Z
MW	0.7274	0.2638	0.0088
LMC	0.7391	0.2562	0.0047
SMC	0.7464	0.2515	0.0021

TABLE 4.2: Surface Nitrogen enrichment ratio measured at the main sequence termination, for different metallicities and masses, as predicted by PARSEC V2.0 with $f_c = 0.17$, $f_\mu = 0.45$. Comparison values are from Brott, de Mink, et al. (2011), for similar initial rotational velocities.

Mass [$M_\odot$]	$\frac{N_{sup}}{N^0_{sup}}$	
MW	PARSEC v2.0	Brott+11
12	3.87	3.25
15	4.66	2.65
30	13.31	13.55
LMC		
12	4.05	4.82
15	5.64	5.67
30	13.34	11.70
SMC		
12	5.52	6.27
15	6.82	9.39
30	13.93	16.16

of the two parameters in the evolution of the models. As the f_μ parameter grows, the mixing is more and more inhibited by the molecular weight gradient. High values of f_μ take the models to be less luminous, because the processed elements (mainly Helium) remain in the stellar cores, and the surface chemical abundances remain almost unchanged. On the contrary, high values of the f_c parameter lead to enhance the mixing. In general, an higher mixing takes the star to be more luminous and to build up bigger cores at the terminal age of the main sequence (TAMS), with effects on the evolved phases.

The calibration of the mixing efficiency due to rotation is still an open problem. There are different ways to find acceptable values of these two parameters, for instance, the method adopted by Heger, N. Langer, and Woosley (2000) consists in setting up the two parameters to reproduce the ratio between the surface Nitrogen abundance at the TAMS, and that at the ZAMS, for 10 – 20 $M_\odot$ stars of solar metallicity. An example of how the Nitrogen enrichment changes with different combination of the calibration parameters is shown in the bottom panel of Figure 4.5. The surface Nitrogen enrichment is probably one of the best observational probes of rotationally induced mixing in stars during the MS phase. This because, the Nitrogen – the main product of the CNO cycle during the MS – is not

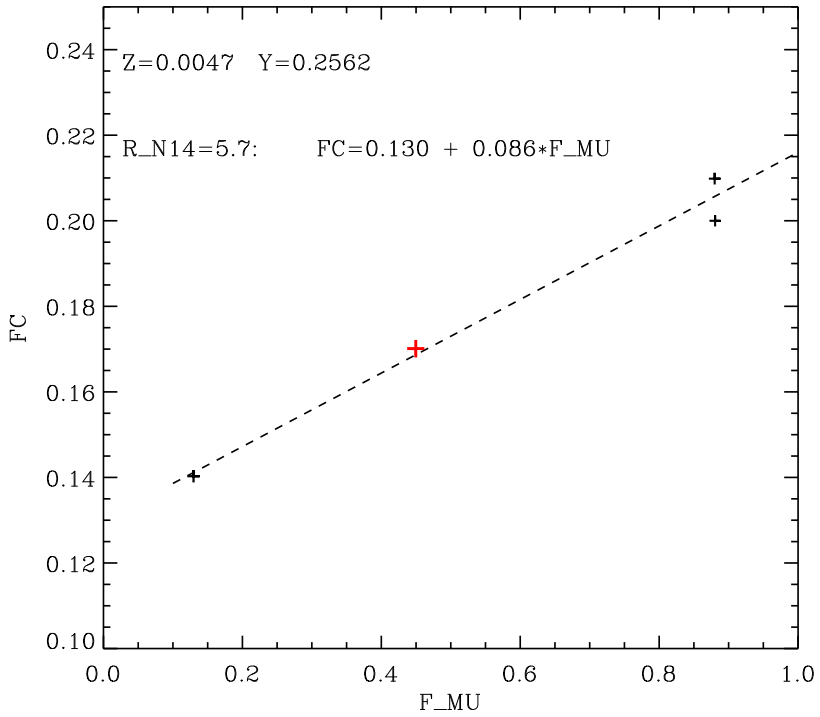

FIGURE 4.6: Relation between the two parameters. Each combination of the two values in the dashed line reproduces a ratio N surface enrichment of about 5,7, for the SMC 15 $M_{\odot}$ models. The red cross indicates the adopted values for the two parameters.

destroyed once created, at variance with other products of the Hydrogen burning. In fact, lighter elements as Lithium and Boron, are depleted at relatively low temperatures. The Nitrogen, once created, is then extracted from the cores and transported throughout the star by the rotation mixing. The ratio adopted by (Heger, N. Langer, and Woosley, 2000) was $N_{\rm sup}/N^0_{\rm sup} = 2-3$ for stars of 10 – 20 $M_{\odot}$ where $N_{\rm sup}$ is the surface Nitrogen at the end of the MS and $N^0_{\rm sup}$ is the surface Nitrogen in the ZAMS.

A second method was developed later by Brott, de Mink, et al. (2011) and Brott, Evans, et al. (2011), who used the observed Nitrogen surface abundances of a sample of stars from the LMC VLT-FLAMES survey to calibrate their models. Their first step was to adopt a suitable initial chemical composition to model the Small and Large Magellanic Clouds (SMC, LMC), to properly compare the surface abundances. Then, they calibrated the core overshooting parameter trying to reproduce the surface gravity and the projected rotation velocities ($V_{eq} \sin i$, where i is the inclination angle between the star rotation axes and the line of sight) of the observed data. Finally, they calibrate the parameters (f_{μ} and $f_{\rm c}$) aiming to reproduce the observed Nitrogen surface abundances and the projected rotational velocity of the selected fast rotating stars of their data sample. This method has been adopted in the recent work by (Limongi and Chieffi, 2018) to re-calibrate their stellar evolutionary code (FRANEC), that before was calibrated with the simpler Heger, N. Langer, and Woosley (2000) method.

In this Thesis, I calibrate the two mixing parameters by comparing the

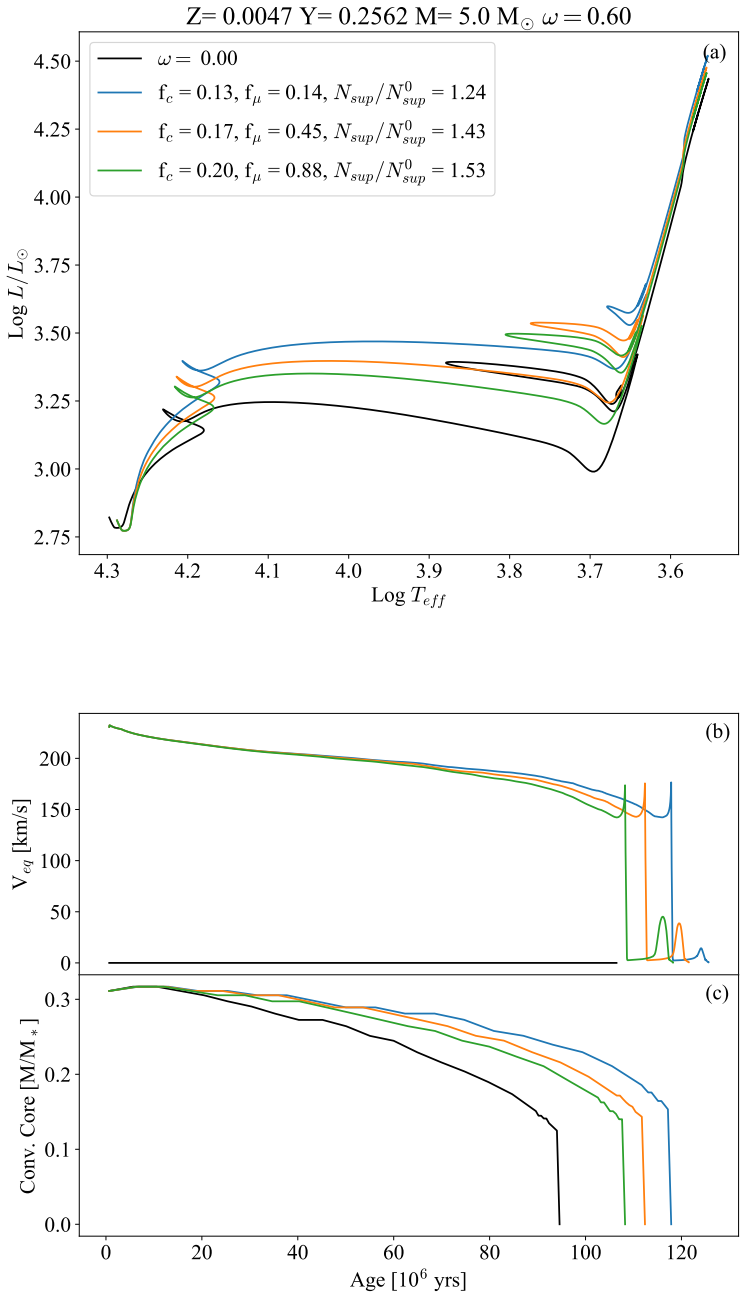

FIGURE 4.7: Panel (a): HR diagram of stellar models with different combination of the calibration parameters, with 5 $M_\odot$, the SMC composition (see Table 4.1) and with ω_i = 0.60. Panel (b): Equatorial rotation velocity as a function of the time. The color code is the same of the panel (a). Panel (c): Convective core extension (mass fraction) versus time. The colors are the same as in the above panels.

surface N enrichment ratio of massive stars found by Brott, de Mink, et al. (2011) with corresponding models. To be consistent in the comparison, I computed the models with a similar chemical abundances partition, and with the same initial metallicity, as reported in Brott, de Mink, et al. (2011) and listed in Table 4.1. Before the calibration of f_μ and f_c, I calibrate the overshooting parameter (λ_{ov}) using eclipsing binaries, and adopting the chosen value of $\lambda_{ov} = 0.4$. This is discussed in detail in Chapter 5. As a preliminary calibration, our best values for the two parameters are $f_c = 0.17$ and $f_\mu = 0.45$. Table 4.2 shows the surface Nitrogen enrichment ratios of our models compared with the values found by Brott, de Mink, et al. (2011), for models with similar rotation rates in the ZAMS.

It is worth noting, that different combination of the two parameters may give similar surface Nitrogen enrichment for a models with equal metallicity, mass and initial rotation rate. An example of such degeneracy is shown in Figure 4.6, in which the dashed line indicates the different combinations of the two parameters that give the same enrichment for a 15 $M_\odot$ model, with $\omega_i = 0.60$ and with the SMC chemical composition. However, I note that this degeneracy relation is not strictly unique, but it differs between models with different masses, metallicities and ω_i. The panel (a) of Figure 4.7 shows the HR diagram of three models of a 5 $M_\odot$ star with $\omega_i = 0.60$, with three different combinations of the mixing parameters chosen from the relation shown in Figure 4.6. The three models do not reproduce the same surface Nitrogen ratio, and noticeably they produce different blue loops extension. The blue loops extension looks to be strongly correlated to the core dimensions in the TAMS, as shown in the panel (c). Bigger cores takes to smaller loops. This Figure clearly shows that f_μ directly affects the growth of the core, while f_c affects the transport of elements in the radiative region, hence, the surface enrichment of the star. Panel (b) shows that, during the MS, the surface velocity of the star is not affected much by the different configurations of the two parameters. Panels (b) and (c) show also that, obviously, the MS lifetime depends on the efficiency of the mixing, because depending on that less or more fresh fuel (Hydrogen) is provided to the burning core.

Better calibration will be performed before the next release of the new sets of rotating tracks (Costa et al., in prep.), likely adopting the method by Brott, de Mink, et al. (2011).

4.6 Preliminary comparison with other authors

In this section, I make and discuss a preliminary comparison of our new rotating tracks with models computed with other authors. In the first part, I show the structure profile at different phases of 5, 13, 15 and 20 $M_\odot$ rotating PARSEC models. In the second part, I compare the HR diagram of models with masses of 13, 15 and 20 $M_\odot$ computed with PARSEC, GENEC[4] (Georgy, Ekström, et al., 2013) and FRANEC[5] (Chieffi and Limongi, 2017).

[4]Tracks taken from the SYCLIST online database at https://www.unige.ch/sciences/astro/evolution/en/database/syclist/

[5]Tracks taken from the ORFEO online database at http://orfeo.iaps.inaf.it/

4.6.1 Structure evolution and interior profile

During the MS, the rotational mixing – induced by the shear friction and the meridional circulation – provides fresh fuel to the burning core, and extracts the products of the H burning from the core, transporting them into the envelope, eventually up to the surface of the star. Figures 4.8, 4.9, 4.10 and 4.11 show the interior profiles of ^{1}H, ^{4}He and ^{14}N, and of selected quantities related to rotation, for rotating models with $\omega_{\rm i}$ = 0.60 and an initial mass of 5, 13, 15 and 20 $M_{\odot}$, respectively. From these plots it is clearly visible how the ^{1}H, ^{4}He and ^{14}N profiles are modified by rotation at different stages of the core H-burning. The profiles are smoothed by the rotational mixing, and in the left panels can be appreciated the ^{14}N surface enrichment in the TAMS. In all the models shown, at the end of the MS the stars have higher angular velocities in the cores than in the surfaces, in agreement with models computed with other codes, e.g. in the Figure 11.6 by A. Maeder (2009) and in the Figure 7 by (Limongi, 2017). As far as the diffusion coefficients are concerned, in all the models the meridional circulation is the dominant effect in the inner part of the star, while the shear instability is more efficient in the outer layers. This trend has been observed also in models computed with the FRANEC code (Limongi, 2017).

4.6.2 HR diagram comparison

Figure 4.12 shows the comparison of our new PARSEC tracks with the GENEC and FRANEC tracks in the top and bottom panels, respectively, for a 13 $M_{\odot}$ star, with $\omega_{\rm i}$ = 0.0, 0.6 and 0.9. In the top panel, the non rotating tracks show a similar core H-burning phase, they start from the same location in the diagram and then diverge during the evolution likely due to the different adopted mixing efficiency. At the terminal age MS (TAMS), the non rotating PARSEC model results to be slightly colder and more luminous than the GENEC one. This behaviour is due to the different mixing length and core overshooting parameters assumed in the two codes. In the GENEC models the mixing length parameter is $\alpha_{\rm MLT}$ = 1.6 and the core overshooting parameter is $\lambda_{\rm ov}$ = 0.1, while in the PARSEC models they are $\alpha_{\rm MLT}$ = 1.74 (A. Bressan, P. Marigo, et al., 2012, solar-model-calibrated mixing length by) and $\lambda_{\rm ov}$ = 0.4 (value taken across the convective border, that correspond to 0.2 in the GENEC code), as suggested by the analysis performed and described in Chap. 5 of this Thesis. An higher convective mixing efficiency leads the models to have longer MS lifetimes (as listed in Table 4.3) and to build up bigger He cores at the end of the H burning phase. These differences affect also the post-MS phases. As far as the rotating models are concerned, their starting positions on the HR diagram (the ZAMS) are very similar, and also the main rotating properties are in agreement between the models computed by the two codes (as shown in Table 4.3). During the evolution the models follow different path in the diagram, due to the different convective mixing (as discussed before) and also to the different rotational mixing efficiencies adopted in the two codes. By looking at the HR diagram at different MS times, it appears that the PARSEC models produce a more efficient rotational mixing than the GENEC models, and the tracks at the TAMS are more luminous

and colder with respect to the corresponding GENEC models. The last column of Table 4.3 shows the relative increment of the MS-lifetimes with respect the non-rotating case in percentage, for the models of each author. It is worth to be noted that GENEC treats the angular momentum transport with the advective-diffusive equation shown in Eq. 4.9, while in PARSEC is treated with a full-diffusive approach (Eq. 4.10). This makes the comparison of the rotational mixing efficiency more difficult since the calibrating parameters are not the same. In the bottom panel of Figure 4.12, I show the comparison with FRANEC tracks. While the non-rotating tracks are in good agreement, the FRANEC rotating tracks show a higher rotational mixing efficiency respect the PARSEC one. The FRANEC model with an initial equatorial velocity of 300 km/s corresponds to the PARSEC $\omega_i = 0.60$ model in the ZAMS (see in Table 4.3), but the higher rotational mixing adopted in FRANEC shifts the track to luminosities similar to the $\omega_i = 0.90$ PARSEC model.

In Figure 4.13 I compare the MS of 15 $M_\odot$ evolutionary tracks computed with PARSEC, GENEC and FRANEC. From these plots I find again that the non rotating PARSEC model has a more efficient mixing than the GENEC ones, but similar to the one of the FRANEC model. As far as the rotating models are concerned, I find that the mixing efficiency of PARSEC models is larger than that of GENEC ones but lower than that of the FRANEC models. The main rotational properties at the ZAMS of the models with different initial rotation rates are listed in the bottom part of Table 4.3. The MS-lifetimes and the relative increment with respect to the MS-lifetimes of the non rotating models are listed in the last two columns. Finally, Figure 4.14 shows the comparison of the MS of 20 $M_\odot$ tracks, computed with PARSEC and FRANEC. I find the same trend found for the lower masses. The main rotation properties and MS lifetimes are listed in Table 4.4.

A deeper and extended comparisons between our models and others computed with different codes will be performed and published with the next release of the new sets of rotating tracks (Costa et al., in prep.).

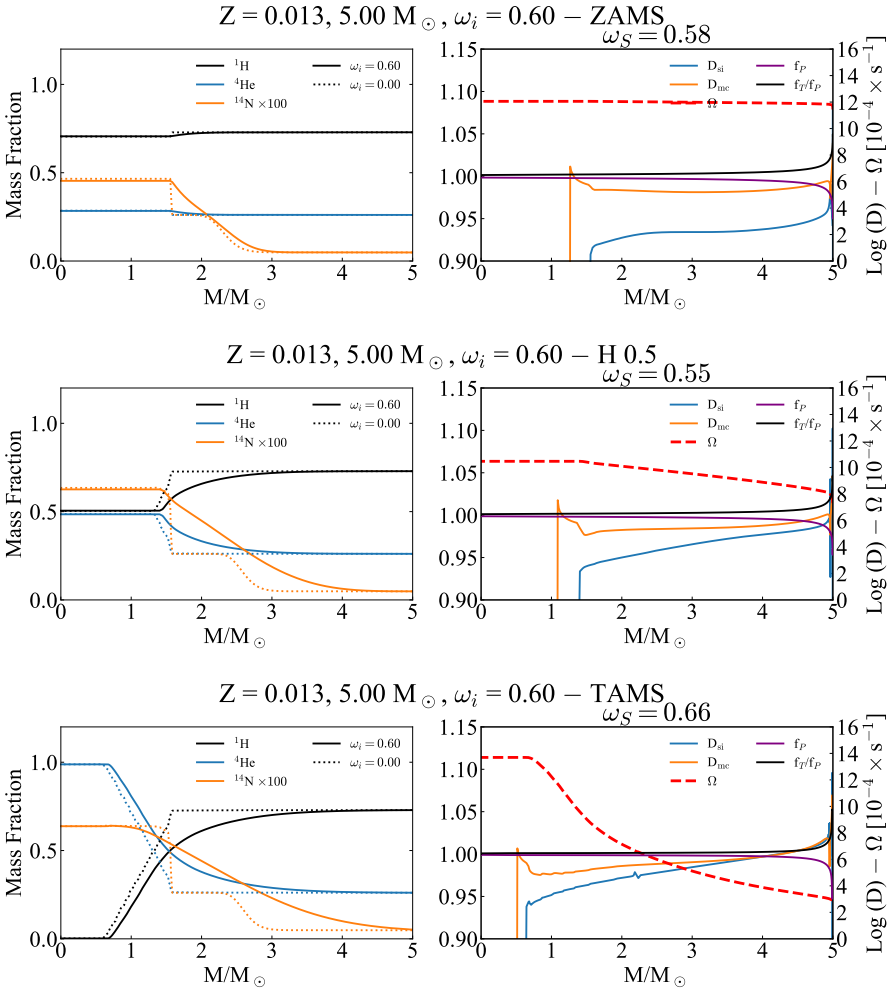

FIGURE 4.8: Left panels: interior profiles of ^{1}H, ^{4}He and ^{14}N in black, blue and orange lines, respectively, for 5 $M_{\odot}$ models. The continuous lines refer to the rotating models while the dotted to the non-rotating ones. Right panels: interior profiles of selected quantities of the rotating model at the correspondent phase indicated by the left panels. The shear instability and the meridional circulation diffusion coefficients are the blue and orange lines, respectively. The red dashed line indicates the angular velocity and, the purple and black lines indicates the f_P form parameter and the ratio f_T/f_P, respectively. From the top to the bottom, there are tree different MS phases. These are the ZAMS, the central H mass fraction $\sim$ 0.5 and the TAMS. For each phases ω_S indicate the actual surface rotation rate.

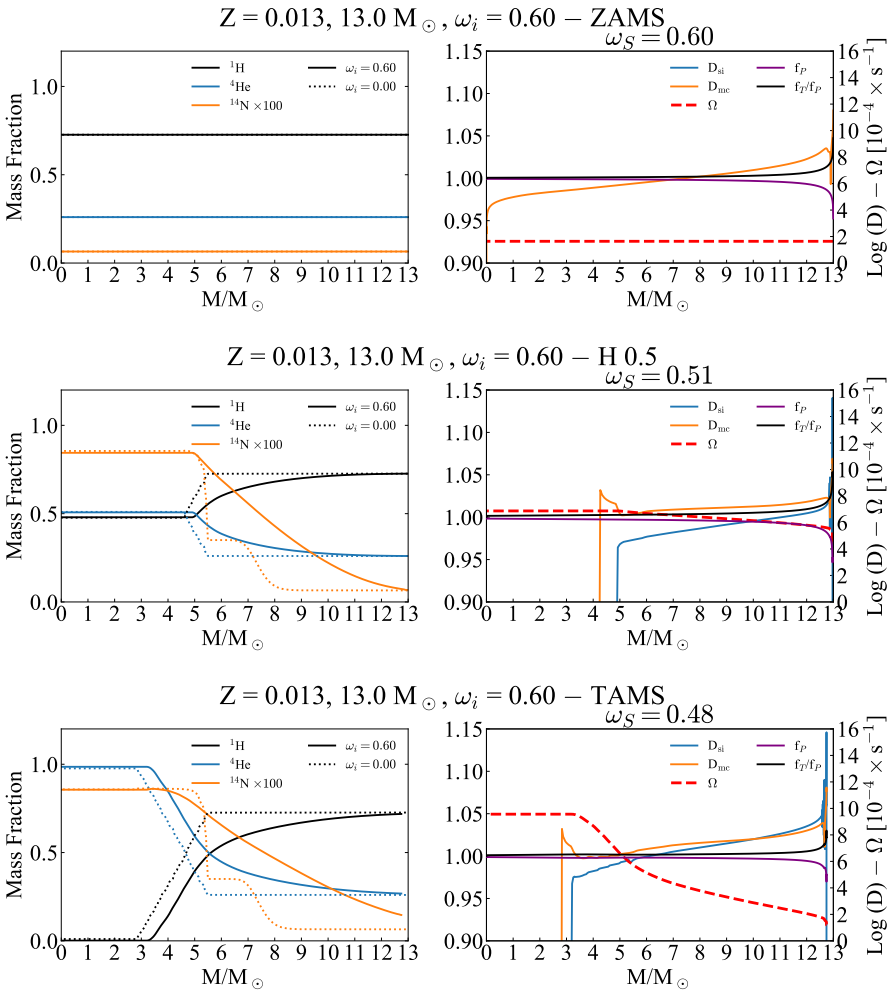

FIGURE 4.9: Same as in Figure 4.8, but for a 13 $M_{\odot}$ model.

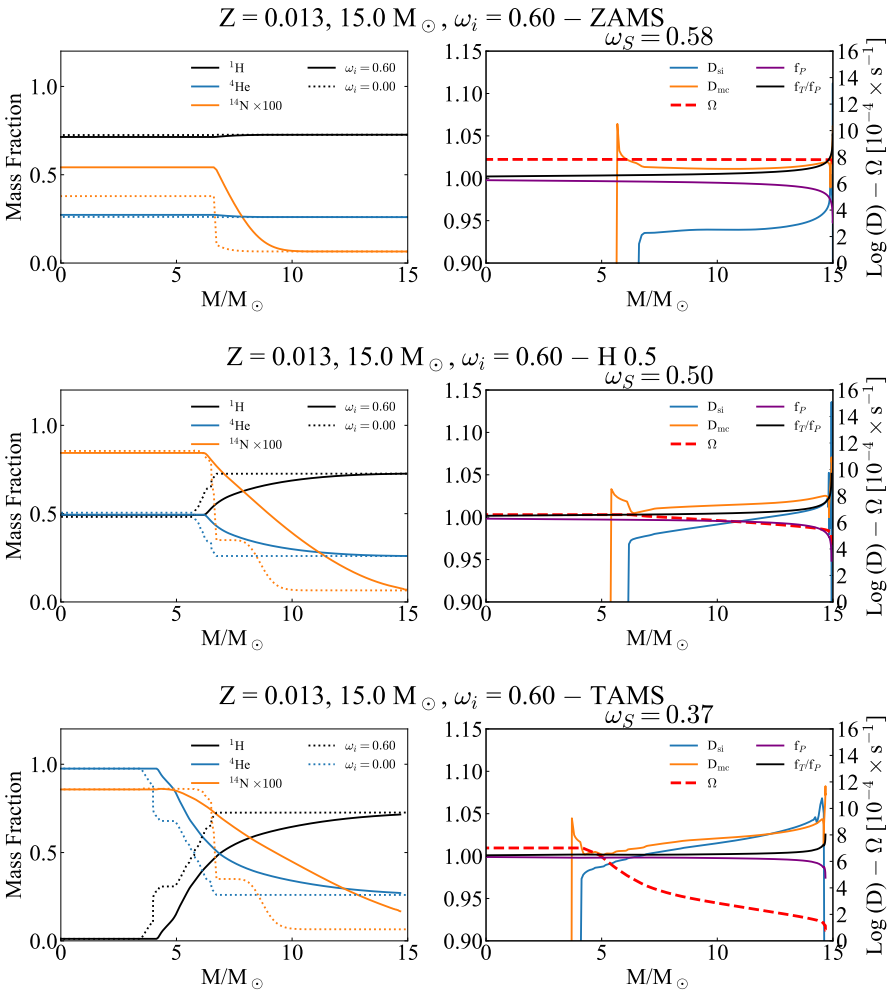

FIGURE 4.10: Same as in Figure 4.8, but for a 15 $M_{\odot}$ model.

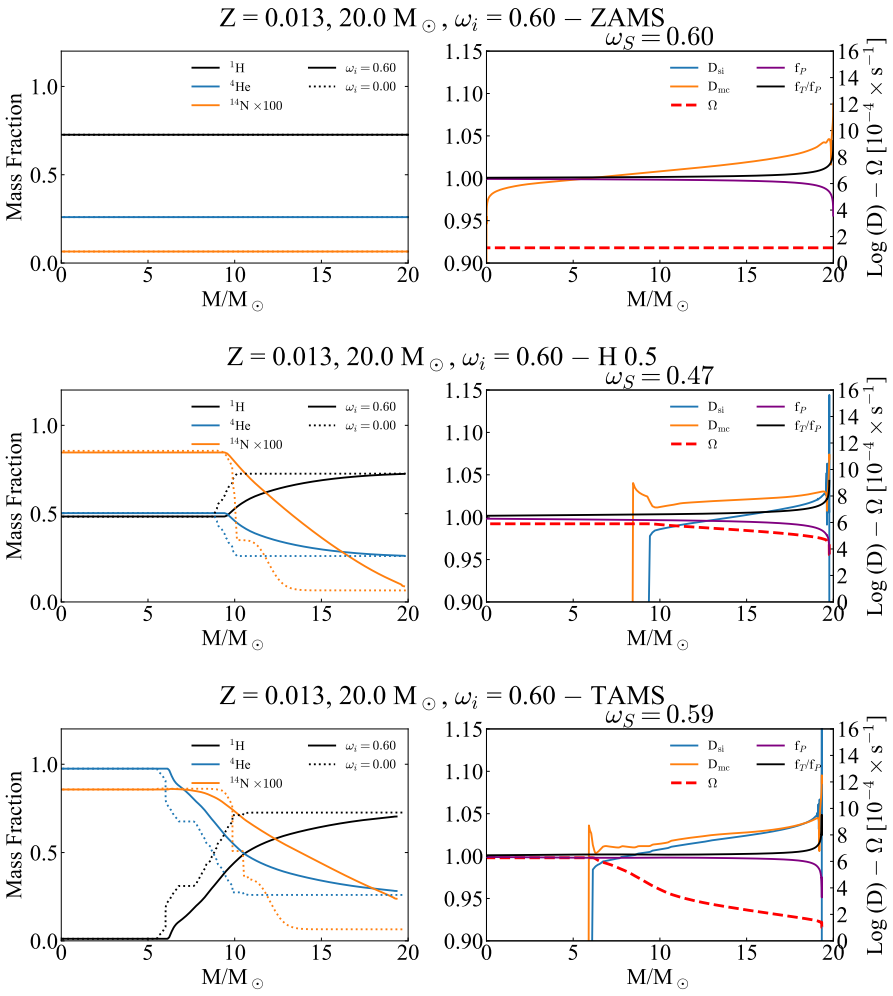

FIGURE 4.11: Same as in Figure 4.8, but for a 20 $M_{\odot}$ model.

CODE	Initial rotation [ω_i] - [Km/s]	Ang. Mom. [g cm^2 s^{-1}]	ω	Ω [s^{-1}]	V_{eq} [Km/s]	R [$R_\odot$]	R_{pol}/R_{eq}	R_{pol} [$R_\odot$]	MS-lifetimes [yr]	$\frac{\Delta MS-t}{MS-t(\omega=0)}$
				13 $M_\odot$						
PARSEC	0.00	0.00E+00	0.00	0.00E+00	0.00	4.25	1.00	4.25	1.61E+07	-
GENEC	0.00	0.00E+00	0.00	0.00E+00	0.00	4.14	1.00	4.14	1.36E+07	-
FRANEC	0.00 Km/s	0.00E+00	0.00	0.00E+00	0.00	4.19	1.00	-	1.60E+07	-
PARSEC	0.35	8.58E+51	0.35	4.82E-05	147.32	4.36	0.98	4.31	1.69E+07	5%
GENEC	0.35	8.76E+51	0.37	5.33E-05	158.00	4.22	0.98	4.16	1.60E+07	18%
FRANEC	150 Km/s	8.45E+51	0.35	4.91E-05	147.03	4.31	0.98	-	1.91E+07	20%
PARSEC	0.60	1.49E+52	0.60	8.35E-05	264.58	4.45	0.94	4.28	1.88E+07	17%
GENEC	0.60	1.51E+52	0.62	9.11E-05	281.00	4.33	0.93	4.13	1.67E+07	23%
FRANEC	300 Km/s	1.56E+52	0.60	7.92E-05	254.43	4.62	0.94	-	2.10E+07	32%
PARSEC	0.90	2.27E+52	0.90	1.29E-04	456.38	4.72	0.83	4.20	2.18E+07	35%
GENEC	0.90	2.28E+52	0.93	1.37E-04	487.00	4.72	0.80	4.11	1.72E+07	26%
				15 $M_\odot$						
PARSEC	0.00	0.00E+00	0.00	0.00E+00	0.00	4.60	1.00	4.60	1.28E+07	
GENEC	0.00	0.00E+00	0.00	0.00E+00	0.00	4.49	1.00	4.49	1.10E+07	
FRANEC	0 Km/s	0.00E+00	0.00	0.00E+00	0.00	4.54	1.00	-	1.30E+07	
PARSEC	0.35	1.13E+52	0.35	4.58E-05	151.82	4.74	0.98	4.68	1.37E+07	7%
GENEC	0.35	1.13E+52	0.36	4.95E-05	160.00	4.57	0.98	4.51	1.30E+07	18%
FRANEC	150 Km/s	1.03E+52	0.32	4.36E-05	140.79	4.64	0.98	-	1.55E+07	20%
PARSEC	0.60	1.97E+52	0.60	7.98E-05	273.27	4.79	0.94	4.60	1.53E+07	19%
GENEC	0.60	1.94E+52	0.60	8.34E-05	278.00	4.69	0.94	4.50	1.36E+07	24%
FRANEC	300 Km/s	1.99E+52	0.58	7.26E-05	251.19	4.98	0.95	-	1.65E+07	27%
PARSEC	0.90	3.00E+52	0.90	1.21E-04	468.77	5.13	0.83	4.58	1.76E+07	37%
GENEC	0.90	2.93E+52	0.92	1.31E-04	502.00	5.09	0.80	4.44	1.42E+07	28%

TABLE 4.3: Main properties of the 13 $M_\odot$ and 15 $M_\odot$ models at the ZAMS.

CODE	Initial rotation $[\omega_i]$ - [Km/s]	Ang. Mom. [g cm^2 s^{-1}]	ω	Ω [s^{-1}]	V_{eq} [Km/s]	R [$R_\odot$]	R_{pol}/R_{eq}	R_{pol} [$R_\odot$]	MS-lifetimes [yr]	$\frac{MS-t(\omega)}{MS-t(\omega=0)}$
					20 $M_\odot$					
PARSEC	0.00	0.00E+00	0.00	0.00E+00	0.00	5.38	1.00	5.38	8.93E+06	
FRANEC	0 Km/s	0.00E+00	0.00	0.00E+00	0.00	5.33	1.00	-	9.02E+06	
PARSEC	0.35	1.97E+52	0.35	4.19E-05	162.16	5.53	0.98	5.46	9.46E+06	6%
FRANEC	150 Km/s	1.80E+52	0.32	3.89E-05	147.70	5.46	0.98	-	1.09E+07	21%
PARSEC	0.60	3.42E+52	0.60	7.23E-05	290.87	5.65	0.94	5.44	1.05E+07	18 %
FRANEC	300 Km/s	3.46E+52	0.57	6.65E-05	268.21	5.81	0.95	-	1.15E+07	28%
PARSEC	0.90	5.21E+52	0.90	1.12E-04	502.52	5.95	0.83	5.31	1.22E+07	36 %

TABLE 4.4: Main properties of the 20 $M_\odot$ models at the ZAMS.

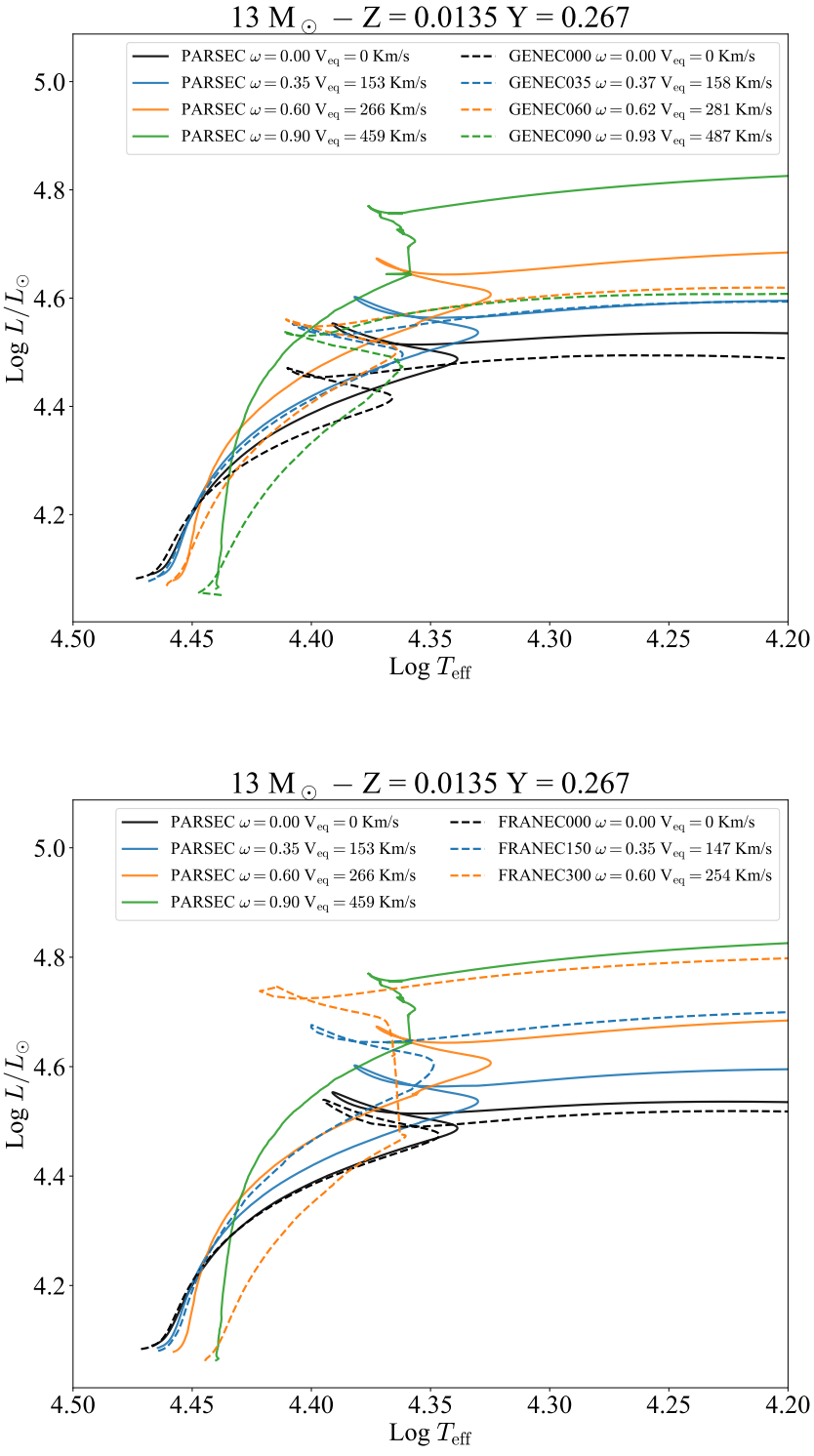

FIGURE 4.12: Top panel: Comparison in the HR diagram of tracks with a mass of 13 $M_\odot$ computed with the PARSEC and GENEC codes, in solid and dashed lines, respectively. The color code indicates different $\omega_{\rm i}$. Bottom panel: comparison between models computed with the PARSEC and FRANEC code.

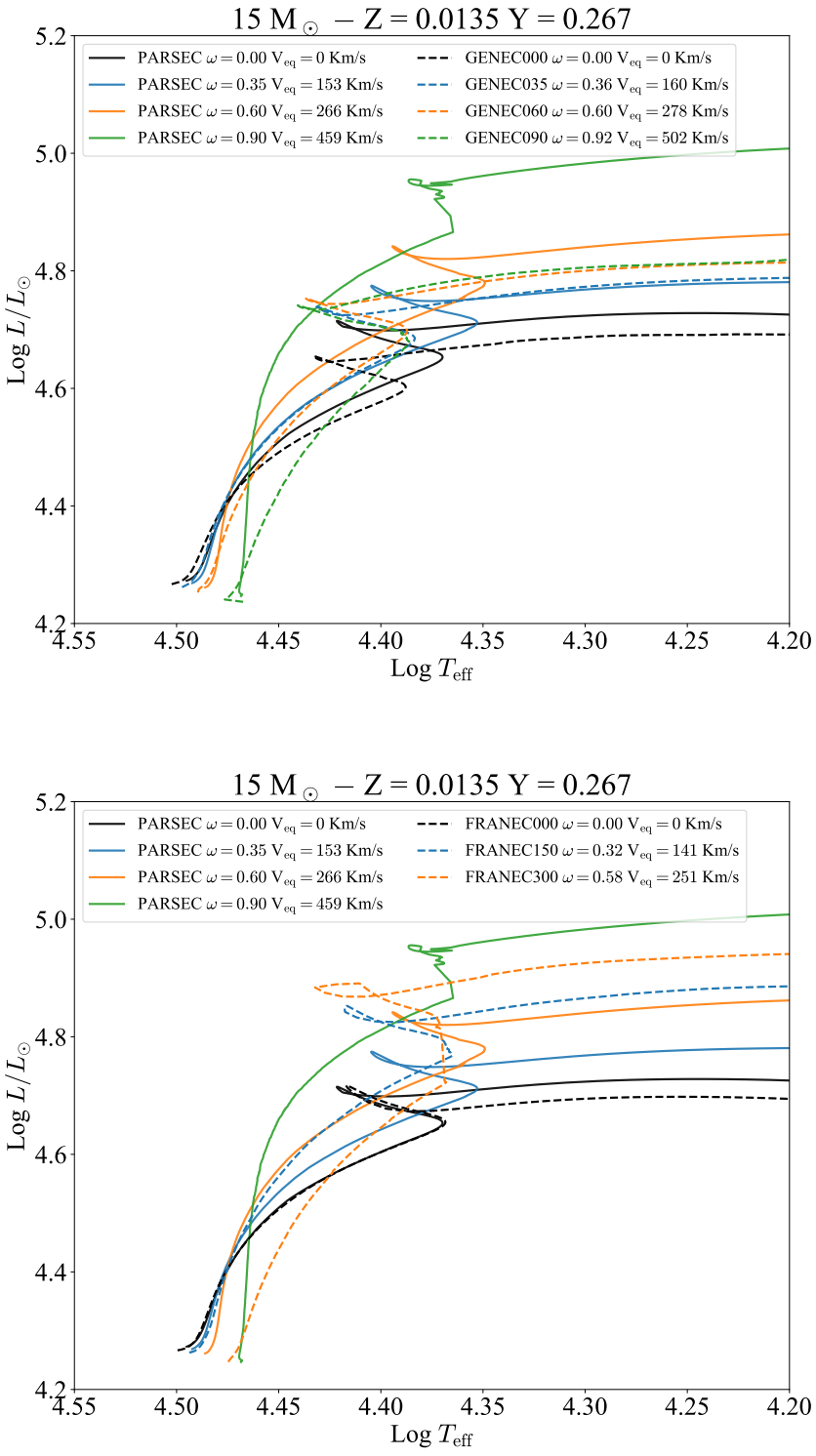

FIGURE 4.13: As in Figure 4.12, but for the 15 $M_\odot$ models.

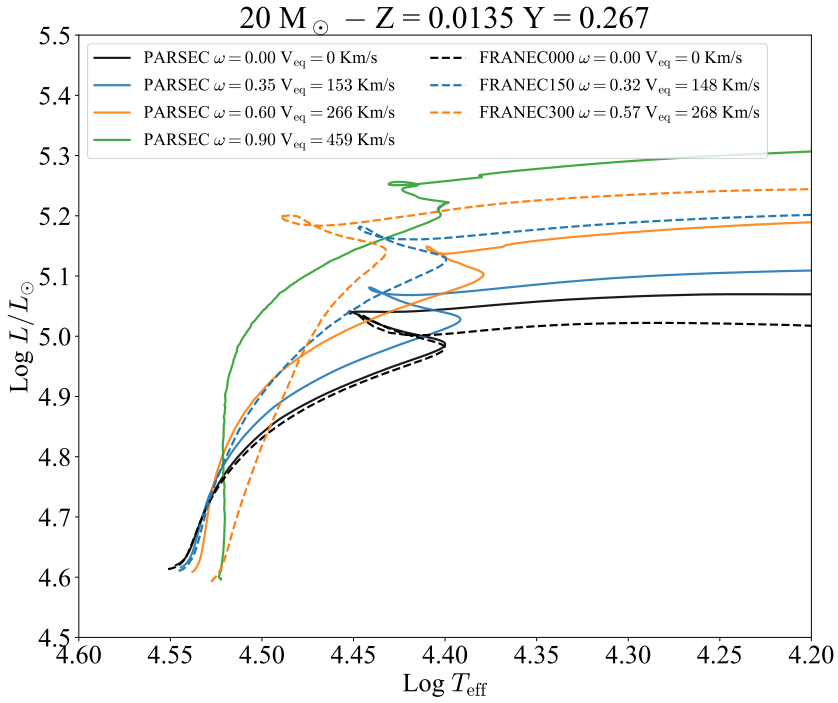

FIGURE 4.14: As in the bottom panels of Figure 4.12, but for the 20 $M_\odot$ models.

Chapter 5

Disentangling mixing by convective overshooting and by rotation

Chapter based on:
Costa G., Girardi L., Bressan A., Marigo P.,
Rodrigues T. S., Chen Y., Lanza A., Goudfrooij P.,
"'Overshooting and rotation in intermediate mass stars", 2019
MNRAS 485, 4641. DOI: https://doi.org/10.1093/mnras/stz728

In this Chapter, I investigate about the possible combined effect of core overshooting and rotation extra-mixing in intermediate-mass stars. For this purpose, I analyze Double-line eclipsing binaries (DLEBs) using a Bayesian method and new PARSEC tracks that account for both convective core overshooting and rotational mixing. The DLEBs are perfect laboratories to study the mixing in stars because thanks to their binary nature, we know with a very good precision their masses, luminosities and effective temperatures.

This Chapter is organized as follow. In Section 5.1 I introduce the contest about the main interpretative problems about the mixing in intermediate-mass stars. In Section 5.2 I describe the adopted DLEBs data sample and the general method used for the statistical analysis. In Section 5.3 I describe the physics adopted in PARSEC to allow to deal with mixing by rotation and overshooting. In Section 5.4 I perform the analysis using models with overshooting alone and I discuss the corresponding results. Since with overshooting alone I cannot fit the data with a fixed value of the overshooting parameter, I test the hypothesis, in Section 5.5, that rotation may cause the additional mixing required. I also derive a quantitative estimate of the initial rotational velocity required to fit the data. Discussion and conclusions are drawn in Section 5.6.

5.1 General background

Convection is one of the most uncertain processes in stars. In the context of 1D models of stellar evolution, the most widely used theory of convection is the Mixing Length Theory (MLT, Böhm-Vitense, 1958) described by the MLT parameter, $\alpha_{\rm MLT}$, which is the distance travelled by convective eddies before dissolving, in units of the pressure scale-height, $H_{\rm P}$. Additional prescriptions are needed to define the borders of convective zones (usually defined by the Schwarzschild or Ledoux criteria) and to treat the so-called overshooting process. The latter effect happens when a rising (sinking) eddy of plasma crosses the border of a convective zone due to its inertia, and is commonly described by the overshooting distance $d_{\rm ov}$, in $H_{\rm P}$ units. Changes in the $\alpha_{\rm MLT}$ and $d_{\rm ov}$ parameters will result in different evolutionary tracks, and different amounts of mixing of the chemical elements throughout the star, as it evolves. Hence, both effects can be calibrated to fit a variety of observations. The $\alpha_{\rm MLT}$ parameter is usually calibrated with the Sun, and a fixed value is commonly adopted in stellar evolution codes (Achim Weiss and Schlattl, 2008; Brott, de Mink, et al., 2011; A. Bressan, P. Marigo, et al., 2012; Choi et al., 2016; Spada et al., 2017; Hidalgo et al., 2018), although some codes use a slightly varying $\alpha_{\rm MLT}$ depending on the stellar mass (Ekström, Georgy, et al., 2012).

Different approaches are used to constrain the $d_{\rm ov}$ parameter, using various types of data, such as: color-magnitude diagrams of star clusters (e.g. Woo et al., 2003; Rosenfield et al., 2017), bump Cepheids (Keller and Wood, 2006), asteroseismology of either OB (Moravveji et al., 2015) or red clump (Bossini et al., 2017) stars, or detached double-lined eclipsing binaries (DLEBs; Stancliffe et al., 2015; A. Claret, 2016; Valle et al., 2016; A. Claret and G. Torres, 2017; Valle et al., 2017; J. Higl and A. Weiss, 2017; Antonio Claret and Guillermo Torres, 2018; Higl et al., 2018; Constantino and Baraffe, 2018). A series of works (e.g. Demarque et al., 2004; Pietrinferni et al., 2004; Mowlavi et al., 2012; A. Bressan, P. Marigo, et al., 2012) suggest that there is a transition regime of the overshooting process: its efficiency should grow from 0 for stars with radiative cores (initial mass $M_{\rm i} \sim 1 - 1.2\ M_{\odot}$), up to a constant value for stars with a mass $M_{\rm i} \geq 1.6 - 2\ M_{\odot}$. Stars in that constant range are considered to have a fully-efficient overshooting process. This suggestion is reinforced by A. Claret (2016), A. Claret and G. Torres (2017), and Antonio Claret and Guillermo Torres (2018), who analyze the properties of 38 DLEBs to calibrate the strength of core overshooting, finding a clear indication for a plateau in the overshooting efficiency for masses $M_{\rm i} > 2\ M_{\odot}$.

However, other studies using similar data, do not find the same plateau. In particular, Stancliffe et al. (2015) model 12 EBs from the sample of G. Torres, Andersen, and Giménez (2010), not finding any trend of the $d_{\rm ov}$ parameter with mass. J. Higl and A. Weiss (2017) studied a sample of stars mainly in the main sequence phase, finding no strict constrain on the overshooting value. In a sequence of papers regarding a few specific systems, Valle et al. (2016) and Valle et al. (2017) call attention to the increased errors when other variables, such as the initial Helium content, are fit together with the overshooting efficiency. More recently, Constantino and Baraffe (2018) analyze 8 binary systems selected from the 38 DLEBs in the

A. Claret (2016), A. Claret and G. Torres (2017), and Antonio Claret and Guillermo Torres (2018) sample, finding a large dispersion in the results, even concluding that DLEBs cannot be used to constrain overshooting. Therefore, the DLEB results are still controversial.

5.2 Data and methods

5.2.1 DLEB data

The stars used in this work are selected from the sample of detached double-lined eclipsing binaries studied by A. Claret (2016), A. Claret and G. Torres (2017), and Antonio Claret and Guillermo Torres (2018). The authors provide 38 DLEBs with very well determined masses and radii, with uncertainties below 3 per cent, and also precise values of effective temperatures, with uncertainties below 6 per cent and metallicity, with [Fe/H] absolute uncertainties below 0.2 dex. The stars are analyzed by means of stellar evolution models that account for different mixing efficiencies, caused by different values of the core overshooting parameter ($\lambda_{\rm ov}$, see Sec. 2.4), and by different initial rotational velocities. In both cases, various mixing efficiencies for models with a given mass and composition, correspond to different locations in the HR diagram and different evolutionary timescales. The DLEBs sample allow to precisely test stellar models by comparison with the predicted location of both components in the HR diagram at a common time, which is that of the individual binary system. The adopted methodological approach is described below.

5.2.2 The Bayesian method

Given a star with a set of measured data $\mathbf{y}$, the posterior probability distribution of their intrinsic quantities $\mathbf{x}$ can be expressed as

$$p(\mathbf{x}|\mathbf{y}) \sim p(\mathbf{y}|\mathbf{x})p(\mathbf{x}), \tag{5.1}$$

where the relationship between $\mathbf{y}$ and $\mathbf{x}$, $\mathbf{y} = \mathcal{I}(\mathbf{x})$, is given by a set of stellar models that spans the entire possible range of parameters; $p(\mathbf{y}|\mathbf{x})$ is the likelihood function, which is the probability of the observed data $\mathbf{y}$ given a set of model parameters $\mathbf{x}$; and $p(\mathbf{x})$ is the prior distribution, i. e., the distribution of how a given model parameter should behave. Assuming that the measured data can be described as a normal distributions, with mean y' and standard deviation $\sigma_{y'}$, the likelihood function is

$$p(\mathbf{y}'|\mathbf{x}) = \prod_i \frac{1}{\sqrt{2\pi}\sigma_{y'}} \times \exp\left(\frac{-(y'_i - y_i)^2}{2\sigma^2_{y_i}}\right). \tag{5.2}$$

For each component in the sample of the eclipsing binaries, I have as measured data

$$\mathbf{y} = \{M, R, T_{\rm eff}, [{\rm Fe/H}]\} \tag{5.3}$$

where the mass and radii come from the analysis of the light and velocity curve, whereas $T_{\rm eff}$ and [Fe/H] come from spectroscopic analysis of at least one of the components. I am interested in determine the following

parameters

$$\mathbf{x} = \{t, \lambda_{\rm ov}\} \tag{5.4}$$

that is, the stellar age (t) and overshooting parameter ($\lambda_{\rm ov}$). In this work, t is used only for a visual check of the best fitting isochrones, whereas $\lambda_{\rm ov}$ is the parameter I am actually looking for.

For the Bayesian analysis, I adopt:

1. a flat prior on age t, that is, all ages between a minimum and a maximum values of 5×10^7 yr and 13×10^9 yr are assumed to be equally likely;

2. similarly, a flat prior on the overshooting parameter $\lambda_{\rm ov}$, between the minimum and maximum values of 0 and 0.8;

3. an assumed mass distribution given by the initial mass function from Kroupa (2002).

We then implement this Bayesian method as an extension in the PARAM code - that is described in da Silva et al. (2006a) and T. S. Rodrigues et al. (2014a) and Thaíse S. Rodrigues et al. (2017) - to treat the binary measured data. As theoretical models, I use stellar evolutionary tracks and isochrones described in Section 5.4.1. Thus the code computes the joint probability density function JPDF($t, \lambda_{\rm ov}$, [Fe/H]) for each star in the sample, i.e., a 3D distribution map of t, $\lambda_{\rm ov}$, and [Fe/H].

Since I am dealing with binary systems, I have an additional powerful constraint: the age, t, and the metallicity, [Fe/H], should be the same for both components. Therefore I can compute the JPDFs separately for components 1 and 2, and hence combine the probabilities to get the constrained value of $\lambda_{\rm ov}$. The common way to proceed is to assume that the two stars have the same $\lambda_{\rm ov}$, either because they have almost the same mass or because the overshooting distance seems to saturate above a given initial mass, for stars with $M_{\rm i} > 1.6 - 2\ M_{\odot}$. In this way the combined JPDF is simply $\mathrm{CJPDF_{binary}} = \mathrm{JPDF_1} \times \mathrm{JPDF_2}$ (as done by Valle et al., 2017). Using the CJPDF is equivalent to take a sort of average between the two $\lambda_{\rm ov}$ of the two stars. However, I note that finding the trend of the overshooting as a function of the mass should be a result of the study, and not a bias introduced by the adopted methodology. To prevent this bias, I prefer to use a different procedure that, starting from the JPDF($\lambda_{\rm ov}$,t) of each component, allow me to account also for the common age of the system, as described in the following.

1. I first compute the marginalization of the $\mathrm{JPDF}_i(\lambda_{\rm ov},t)$ on age, i.e. the sum of all $\lambda_{\rm ov}$ values, obtaining the probability density function of the age ($\mathrm{PDF}_i(t)$) for both the stars.

2. Then, I obtain the *corrected* JPDF of one star as the product $\mathrm{cJPDF}_i(\lambda_{\rm ov},t)$ = $\mathrm{JPDF}_i(\lambda_{\rm ov},t) \times \mathrm{PDF}_j(t)$, where i and $j \neq i$ refer to any two components.

In this way, I obtain the new corrected cJPDFs of the two stars, by using only the common age of the binary system without any prior on the overshooting parameter. I assume that the best values for the age and

the overshooting parameter for each component is the mode of the corresponding marginalized distributions. The credible interval (CI) associated to the best value is calculated as the shortest interval including the 68 per cent of each marginalized distribution, as suggested by T. S. Rodrigues et al. (2014a).

I remark that the present approach is fundamentally different from the method recently applied by Constantino and Baraffe (2018). Mine is a fully Bayesian approach that weights every small piece of the derived isochrones according to its likelihood, eventually giving little weight not only to the stellar models which are far from the properties of the observed stars, but also to isochrones sections corresponding to fast evolutionary stages. This does not happen in the Constantino and Baraffe (2018) method, which give equal weight to all models crossing the 1σ region of the observed values – which may explain the larger error bars they derive.

Before discussing the results obtained with this method, I introduce the adopted evolutionary models computed with the new PARSEC in the next Section.

5.3 PARSEC version 2.0: The input physics

There are three major differences in the code with respect to the previous version (PARSECv1.2, extensively described in A. Bressan, P. Marigo, et al., 2012; Y. Chen, L. Girardi, et al., 2014; Y. Chen, A. Bressan, et al., 2015; Tang et al., 2014; Fu et al., 2018). The first two concern the nuclear reaction network and the mixing treatment. As described in Section 2.4, the elements in the turbulent regions are mixed by solving a system of diffusion equations coupled with the nuclear reaction rates for each chemical element. In this analysis, I adopted a nuclear reaction network that contains up to 30 isotopic elements from Hydrogen to Silicon, solved with a fully implicit method. The method is much faster than the previously adopted one (semi-explicit scheme). As mentioned above, the current analysis makes use of PARSEC models with rotation, that is the third major update. Its implementation is described in detail in Chapters 3 and 4.

A few models before the ZAMS, the code computes the rotation rate Ω that corresponds to a given $\omega_{\rm i}$, and assigns this angular velocity uniformly throughout the star. This ingestion of initial angular momentum is completed before 1 per cent of hydrogen has been burned in the core. Afterwards, the current rotational velocity at the surface generally decreases as the star ages. The core overshooting is calibrated using the $\lambda_{\rm ov}$ parameter (see Section 2.4 for further details).

5.4 The effect of core overshooting alone

I first assume that the core overshooting is the only responsible of the eventual extra mixing in intermediate mass stars. The analysis of the data is performed using the corresponding non-rotating stellar evolutionary tracks with varying overshooting parameter.

TABLE 5.1: X, Y and Z mass fractions adopted for the models, and the correspondent [Fe/H] values.

X	Y	Z	[Fe/H]
0.746	0.252	0.002	−0.89
0.740	0.256	0.004	−0.58
0.729	0.263	0.008	−0.27
0.713	0.273	0.014	−0.02
0.696	0.284	0.020	+0.14

5.4.1 Evolutionary tracks and isochrones at varying overshooting parameter

For this purpose I computed different sets of evolutionary tracks, with a range of masses between 1 and 5 $M_\odot$ with the following values for the overshooting efficiency: λ_{ov} = 0, 0.1, 0.2, 0.3, 0.4, 0.5, 0.6, 0.7, 0.8. I adopt scaled-solar mixtures based on Caffau et al. (2011) solar composition, with initial metal content Z = 0.002, 0.004, 0.008, 0.014, 0.020 and initial helium content given by $Y = \frac{\Delta Y}{\Delta Z} Z + Y_P = 1.78 \times Z + 0.2485$ (Table 5.1), as obtained from the solar calibration performed by A. Bressan, P. Marigo, et al. (2012). The corresponding values of [Fe/H] can be obtained using the relation [Fe/H] $\simeq$ [M/H] = $\log((Z/X)/0.0207)$ (A. Bressan, P. Marigo, et al., 2012) and are listed in Table 5.1. Finer grids of evolutionary track in the parameters are obtained by interpolation. Tracks are interpolated within "equivalent mass intervals" in which the evolution is similar, following the scheme described in Bertelli et al. (2008) for the case of grids of models computed at varying metal and helium content. I refer to that paper for a detailed explanation – just recalling that, in our case, the varying helium content is replaced by a varying λ_{ov} (or ω_i with a fixed λ_{ov}, later in Sec. 5.5). Just to give a general idea of how this works, let us mention, as an example, that all tracks which develop a convective core in the MS and a degenerate core after the MS, define one of "equivalent interval of mass", even if their minimum and maximum masses, M_1 and M_2, occur at different values for different [Fe/H] and λ_{ov}. Tracks for intermediate values of [Fe/H] and λ_{ov} are interpolated, inside the mass range defined to be equivalent, by using the mass fraction inside this range, $(M - M_1)/(M_2 - M_1)$, as the independent variable. The interpolation between any two tracks then uses the concept of "equivalent evolutionary sections" within the tracks: all stellar quantities are interpolated between pairs of evolutionary stages considered to be equivalent, using the age fraction inside these intervals as the independent variable. The whole process ensures a smooth interpolation between tracks. Interpolations performed for a given age then provide well-behaved isochrones. I also check that, by removing intermediate values of λ_{ov} from the interpolations, grids of interpolated tracks can be built for the same λ_{ov}, that look very similar to the actually-computed ones. This gives me confidence that the present grid of computed λ_{ov} values is sufficient for my goals.

I recall that mass loss is not taken into account, since I am dealing only with low and intermediate-mass stars in the stages well below the tip of

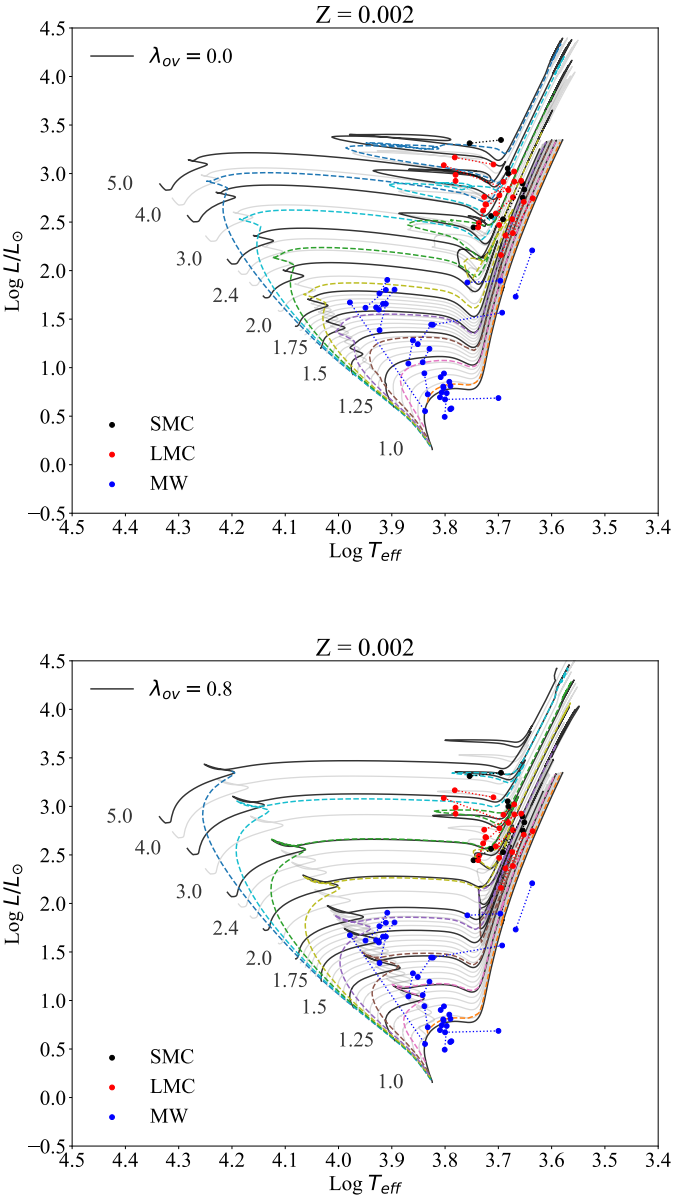

FIGURE 5.1: Overview of the data and models used in this work. The points linked by dotted lines are the stars in binaries, grouped into three broad metallicity bins (SMC, LMC, and MW, with black, red and blue points respectively). Tracks and isochrones are over-plotted with $Z = 0.002$, for the extreme values of overshooting available: in the top panel $\lambda_{ov} = 0.0$, in the bottom panel $\lambda_{ov} = 0.8$. Tracks (the black and gray solid lines) cover the mass range from 1 to 5 $M_\odot$. The isochrones illustrated with dashed lines are equally spaced in $\log t$, covering the age range from 10^8 (upper blue dashed line) to 10^{10} yr (bottom red dashed line).

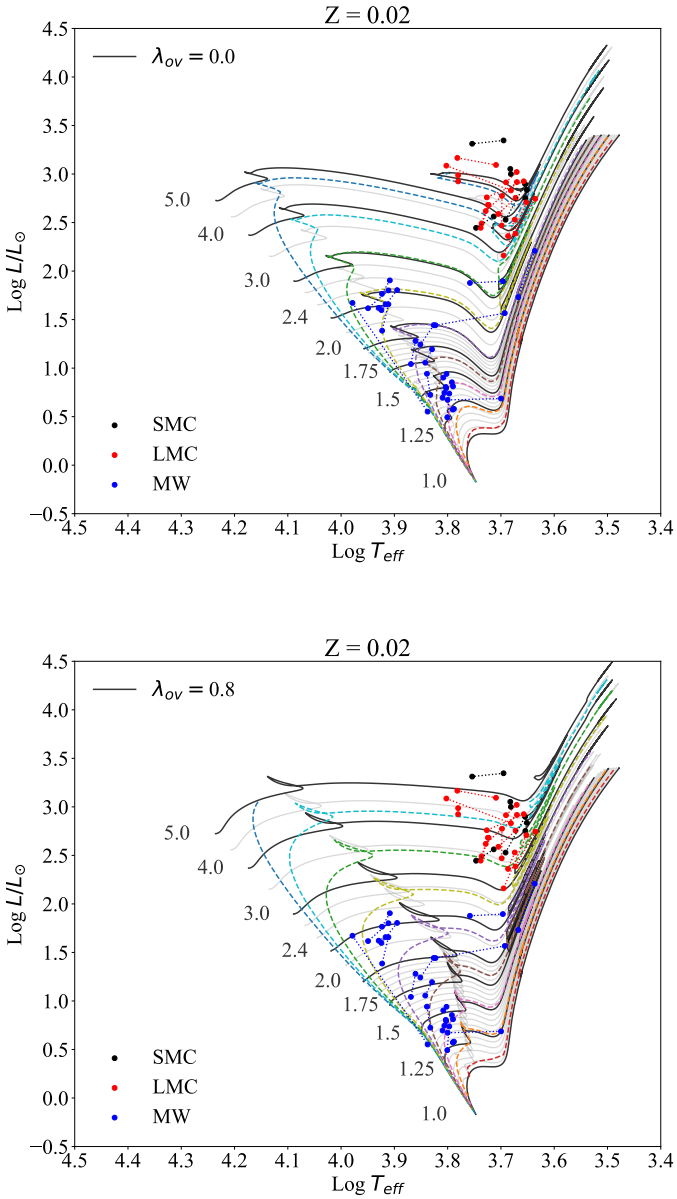

FIGURE 5.2: As in Figure 5.1, but for tracks and isochrones computed with Z = 0.02.

the RGB, for which no significant mass loss is expected to take place. Finally, I stress that a unique solar-model-calibrated mixing length parameter $\alpha_{\rm MLT}$ = 1.74 is adopted for all the computed evolutionary tracks, as in A. Bressan, P. Marigo, et al. (2012). Following their approach, we do not include the microscopic diffusion in stars that develop a convective core, hence in which the core overshooting process takes place. Since I am interested in studying such stars, even our 1 $M_{\odot}$ models are computed without the microscopic diffusion. I redirect the reader to A. Bressan, P. Marigo, et al. (2012) and Stancliffe et al. (2016) for a detailed comparison between models of low mass stars with and without the microscopic diffusion.

5.4.2 Interpretation with models with overshooting

The HR diagrams of Figures 5.1 and 5.2 compare the observed data with some of the new tracks with variable overshooting parameter, and the derived isochrones at a few selected ages. They show that the range of parameters adopted for the models is wide enough to represent all the observed binary components.

After interpolating tracks for all the intermediate values of the two parameters Z and $\lambda_{\rm ov}$, I used the corresponding isochrones to obtain the 3D JPDF of age, $\lambda_{\rm ov}$, and [Fe/H] (as discussed in Section 5.2.2 for each star.

After verifying that the JPDFs dependence on [Fe/H] has negligible effects on the results, I further decide to marginalize the 3D JPDFs on the metallicity so obtaining a 2D JPDF on age and $\lambda_{\rm ov}$. Two examples of the resulting 2D JPDF are shown in Figure 5.3, specifically for the systems α Aurigae and TZ Fornacis.

To allow an easy comparison with previous studies (e.g. Valle et al., 2017) I first show the results obtained using the method of the combined JPDFs (CJPDFs$_{\rm binary}$), as described in Section 5.2.2. This method assumes not only that the binary stars must have the same age, but also that the agent of the extra mixing is the same. While the first assumption does not require further justification, the second condition is adopted because I am considering overshooting as the only source of extra mixing, and I will exclude from our discussion systems with mass ratios significantly different from unity, because overshooting may have a dependence on the stellar mass below a certain threshold mass.

The two plots show the superposition of three different JPDFs: one for the primary, one for the secondary, and the combined one. These three JPDFs are normalized to their respective peak values. The colored regions delimit JPDF contours levels of 50 per cent (the darker), 10 per cent (the intermediate) and 1 per cent (the lighter) of the correspondent maximum density value. I stress that the values of these levels are arbitrarily chosen and do not correspond to the 2D credible intervals.

To assign best values and the correspondent credible intervals, I proceed as described in Section 5.2.2. Each map is marginalized in the two parameters to obtain two 1D probability distributions, one in age t and the other in $\lambda_{\rm ov}$. The best values are the peak values (the mode) of the 1D marginalized distributions, while, the credible interval of each parameter corresponds to the smallest interval around its mode corresponding to a

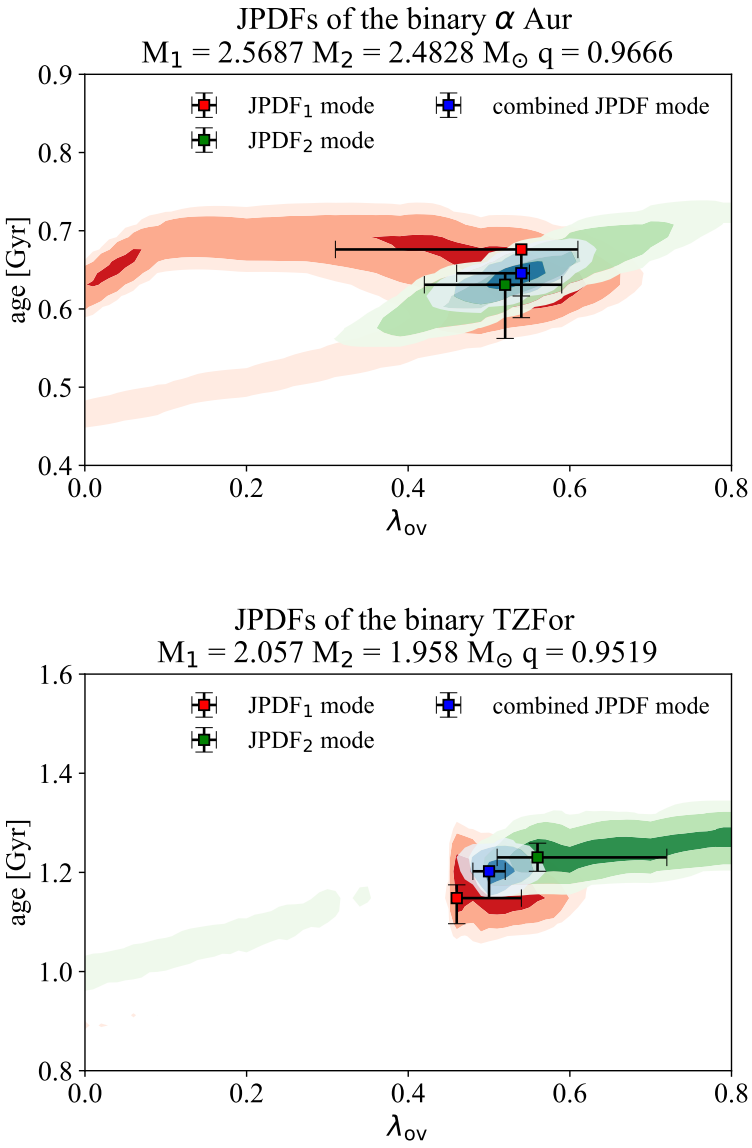

FIGURE 5.3: Two-dimensional JPDF maps as a function of the age, t, and the overshooting parameter, λ_{ov}, of the selected binary systems α Aurigae (top panel) and Z Fornacis (bottom panel). The red (green) contours correspond to the primary (companion) star of the system, and the blue one is the CPDF. The squares indicate the mode values of the corresponding colored probability maps, with their related CIs.

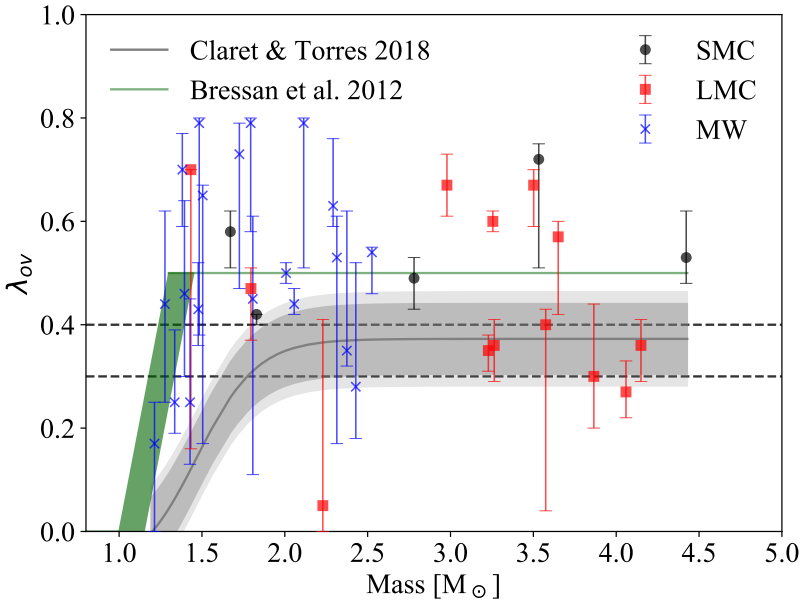

FIGURE 5.4: Resulting overshooting parameter λ_{ov} as a function of the stellar mass for the 38 DLEBs, obtained from the combined JPDF method. The best values (the modes) and the corresponding 68 per cent credible intervals and are colored with the same color code used in Figure 5.1, to divide stars of different galaxies. The black dashed lines are drown for an easier reading. The gray line is the fit curve of the f_{ov} parameter found by Antonio Claret and Guillermo Torres (2018) with the errors (gray areas) scaled by a multiplicative factor. The green line and area, describe the λ_{ov} parameter used in A. Bressan, P. Marigo, et al. (2012). See the text for more details.

probability of 68 per cent. The best values are represented by squares with the same darker color of the corresponding 2D distribution.

The values of the λ_{ov} and age parameters I derive for α Aurigae and TZ Fornacis are listed in Table 5.2. Here, I show the parameters for the distributions of the individual components (superscript 1 and 2) and for the combined distribution (superscript C).

Applying the same method to all the binary systems in the sample, I obtain the results shown in Figure 5.4, in which the λ_{ov} parameters of the combined distributions (CJPDFs) are plotted as a function of the *average mass* of each binary system.

The plot also shows the results found by Antonio Claret and Guillermo Torres (2018) represented by their fit curve (their equation 2, the gray line). Their fit describes the overshooting efficiency by means of the parameter, f_{ov}, that enters the velocity scale-height in the overshooting region. To plot this curve in Figure 5.4, I first express their fit as a function of λ_{ov} using their relation between f_{ov} and their overshooting distance parameter ($\alpha_{ov} = d_{ov}/H_P$), $\alpha_{ov}/f_{ov} \sim$ 11.36 (A. Claret and G. Torres, 2017), and then I use my finding that $d_{ov}/H_P \simeq 0.5\lambda_{ov}$. The uncertainties introduced by

TABLE 5.2: Resulting values of age and λ_{ov} for two selected binary systems.

Systems	α Aurigae	TZ Fornacis
M_1 [$M_\odot$]	2.5687±0.0074	2.057±0.001
M_2 [$M_\odot$]	2.4828±0.0067	1.958±0.001
JPDFs mode values		
${\lambda_{ov}}^1$	$0.54^{+0.07}_{-0.23}$	$0.46^{+0.08}_{-0.00}$
${\lambda_{ov}}^2$	$0.52^{+0.07}_{-0.10}$	$0.56^{+0.16}_{-0.05}$
${\lambda_{ov}}^C$	$0.54^{+0.01}_{-0.08}$	$0.51^{+0.01}_{-0.03}$
Age^1 [Gyr]	$0.676^{+0.001}_{-0.087}$	$1.15^{+0.03}_{-0.05}$
Age^2 [Gyr]	$0.631^{+0.015}_{-0.069}$	$1.23^{+0.03}_{-0.03}$
Age^C [Gyr]	$0.646^{+0.001}_{-0.029}$	$1.20^{+0.00}_{-0.05}$
Corrected JPDFs mode values		
${\lambda_{ov}}^1$	$0.55^{+0.07}_{-0.16}$	$0.46^{+0.07}_{-0.00}$
${\lambda_{ov}}^2$	$0.54^{+0.06}_{-0.09}$	$0.55^{+0.10}_{-0.06}$
Age^1 [Gyr]	$0.65^{+0.02}_{-0.04}$	$1.23^{+0.00}_{-0.06}$
Age^2 [Gyr]	$0.65^{+0.02}_{-0.04}$	$1.23^{+0.00}_{-0.06}$

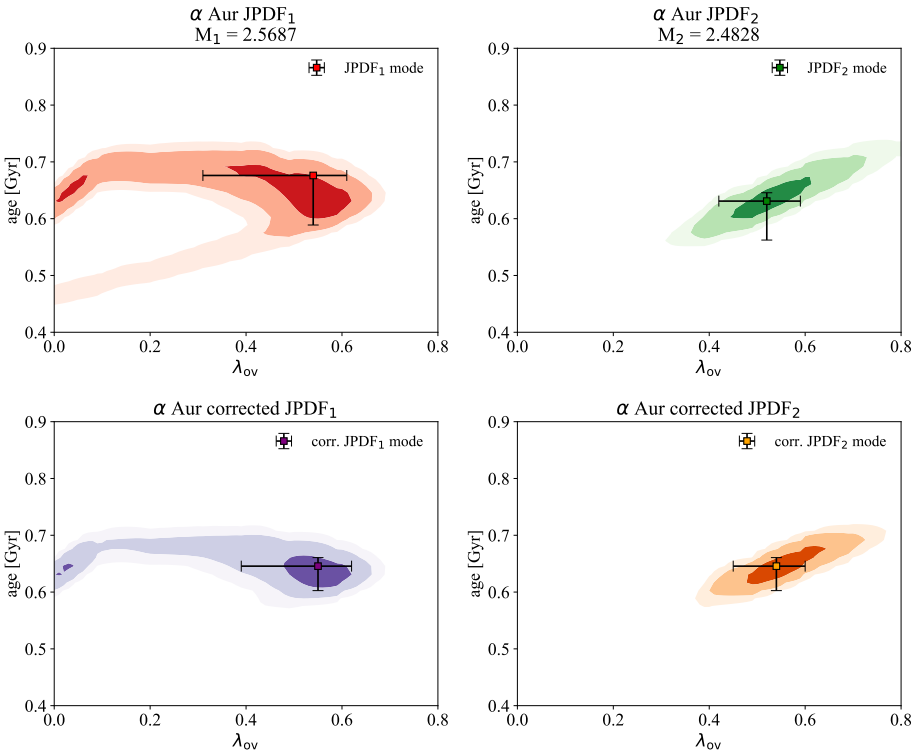

FIGURE 5.5: Selected JPDFs as a function of the age, t, and the overshooting parameter, λ_{ov}, for the two stars of the binary system α Aurigae. In the top panels there are two single star JPDFs, as in Figure 5.3. In the bottom panels there are new corrected JPDFs that constrain the age of the system, as described in the text. The purple (orange) contours represent the primary (companion) star corrected JPDF. The points indicate the maximum of the marginalize distribution with their corresponding CIs.

this scaling process are well below the errors of the data. The darker and lighter gray areas describe the error bars of 0.003 and 0.004 (Antonio Claret and Guillermo Torres, 2018), respectively, multiplied by the same factors. The green area and the green line are the overshooting parameter adopted in A. Bressan, P. Marigo, et al. (2012). The overshooting parameter, which represents the extra mixing probed by our analysis, may depend on the initial mass, as found by other studies. From the comparison, I may identify two overshooting regimes in the plot: the growing one, in which overshooting increases from its null efficiency at about $M_i = 1\ M_\odot$, up to a mass of $\sim 1.5\ M_\odot$; and then the constant one, for larger masses, that indicates a regime of full efficiency. However, the big errors obtained in the low mass range do not let us to clearly identify the growing region. This growing efficiency with mass is commonly adopted by model builders (e.g. Demarque et al., 2004; Pietrinferni et al., 2004; Mowlavi et al., 2012; A. Bressan, P. Marigo, et al., 2012). The average scale of overshooting determined by this procedure, in the constant region, is $\lambda_{ov} = 0.5$.

However, the striking characteristics of the plot in Figure 5.4 is that the overshooting parameter, in the full efficiency regime, shows a large dispersion that is, in many cases, larger than the associated uncertainty. More specifically, this analysis of stars in binary systems suggests that the overshooting parameter for masses above about $M_i = 1.5\ M_\odot$ has a minimum value of $\lambda_{ov} = 0.3 - 0.4$ but, at the same initial mass there can be values as large as the maximum value adopted in the models, $\lambda_{ov} = 0.8$. This dispersion is difficult to explain in the framework of the commonly used models of the overshooting process which, in this regime, adopt a fixed efficiency. Furthermore, this results is also at variance with my previous assumption that justifies the combined JPDF, i.e. that the overshooting parameter is fixed in the full efficiency regime. It is easy to repeat the analysis by relaxing this assumption and using only the condition on the age, as described in Section 5.2.2.

In Figure 5.5 I show, as an example, how the JPDF contours maps change when I adopt this new method for the α Aurigae system. In the top panels I show the single star JPDFs obtained from the PARAM code, before applying the condition on the age. In the bottom panels I show the corrected JPDFs (cJPDFs) resulting from the application of the common age constraint. These corrected distributions have independent λ_{ov} parameters but share the same age distribution. The best values of the corrected JPDF distributions for α Aurigae and TZ Fornacis are shown in the bottom part of Table 5.2.

To show the effect of this new method I repeat the statistical analysis for all the stars of the sample, and plot the λ_{ov} parameter as a function of the mass in Figure 5.6. The latter is similar to Figure 5.4, but in this case each star has its own mass and λ_{ov} parameter. The dispersion of the points is similar to the one obtained with the CJPDFs method, and again, there are several cases in which the values of λ_{ov} are not unique in a given mass bin, in particular looking at masses larger than $\sim 1.5\ M_\odot$. The credible intervals, in Figure 5.6,are slightly larger than those plotted in Figure 5.4.

As a further check I perform another analysis assuming a constant value of [Fe/H] for the stars belonging to the same galaxies. This allow me to check how the metallicity affects the observed dispersion in

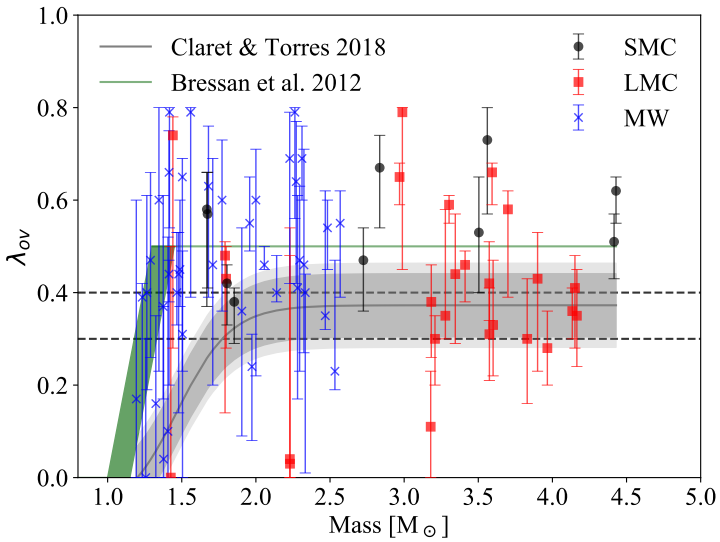

FIGURE 5.6: Same as in Figure 5.4, but with the new method to constrain the age of the system. Thus, the overshooting parameter λ_{ov} is shown as a function of the stellar mass for each star of our sample.

λ_{ov}. Averaging the observed values of stars in different groups I obtain [Fe/H] = -0.89 ± 0.15, -0.48 ± 0.1, -0.14 ± 0.1, for the stars belonging to the SMC, LMC and MW, respectively. The results of the analysis performed with mean [Fe/H] values are shown in Figure 5.7. The plot is not significantly different from the former one. Some stars have different values of λ_{ov}, but the global trend remains very similar.

I note that, in all cases, the error bars at the lower mass end are larger than those associated to the higher masses. This is likely due to the fact that the lower mass sample contains several stars that are still on the early main sequence where the effects of overshooting are less evident and thus the models degenerate more.

In summary this analysis shows the following results:

1. In the mass range below 1.5 $M_\odot$, the λ_{ov} distribution populates all values explored in the analysis (from $\lambda_{ov} = 0.0$ to $\lambda_{ov} = 0.8$), and it is not possible to find a clear trend as a function of the mass.

2. In the mass range above 2 $M_\odot$, the λ_{ov} parameter shows a large scatter, even for similar initial masses. For these stars I find an average value of $\lambda_{ov} \sim 0.45$.

3. In this latter range, there is also an evident lack of points below $\lambda_{ov} \sim 0.3 - 0.4$, in agreement with the Antonio Claret and Guillermo Torres (2018) distribution. The only points to populate this region (in Figure 5.6) are the two components of OGLE-LMC-ECL-25658 at $M_i \simeq 2.23$, for which the derived λ_{ov} present extremely large error bars, and the secondary of OGLE-051019.64-685812.3, with $M_i =$

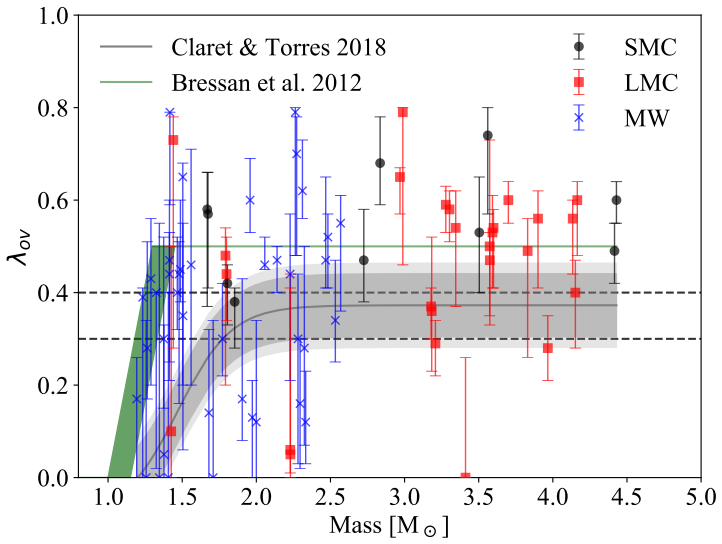

FIGURE 5.7: Same as in Figure 5.6, but results from the statistical analysis using the averaged metallicity for stars of the three different galaxies.

3.179 ± 0.028 and $\lambda_{ov} = 0.11^{0.12}_{0.11}$, which is only marginally inconsistent with the $\lambda_{ov} > 0.3$ limit. In contrast, the sample presents 52 other stars with $M_i \geq 1.5\ M_\odot$ and derived $\lambda_{ov} > 0.3$.

The dispersion I find is certainly larger than that obtained by A. Claret and G. Torres (2017) and Antonio Claret and Guillermo Torres (2018) who analyzed the same data with different models and a different procedure. However it is important to note that, in their analysis, they allow the Mixing Length Parameter, α_{MLT}, to change and their best fits are characterized by a significant star to star variation in the adopted α_{MLT}. This likely absorbs some of the scatter that I find in my results with a fixed α_{MLT}. A star to star scatter of the α_{MLT} is surprising and at variance with common findings from both observational and theoretical sides (Achim Weiss and Schlattl, 2008; Ekström, Georgy, et al., 2012; Magic, Achim Weiss, and Asplund, 2015; Arnett et al., 2018). On the other hand, a large scatter of λ_{ov} at the same initial mass is difficult to explain within the current convection theories that adopt fixed values for the mixing parameters (including the MLT).

I speculate here that, the observed scatter above the minimum threshold, suggested by my analysis, is a signature of an additional source of extra mixing on top of that caused by core overshooting. The most natural candidate is stellar rotation because it is known to be a source of extra mixing and it has a stochastic nature since stars with similar masses may rotate at different speeds. In the next section I will explore the additional effect of rotation.

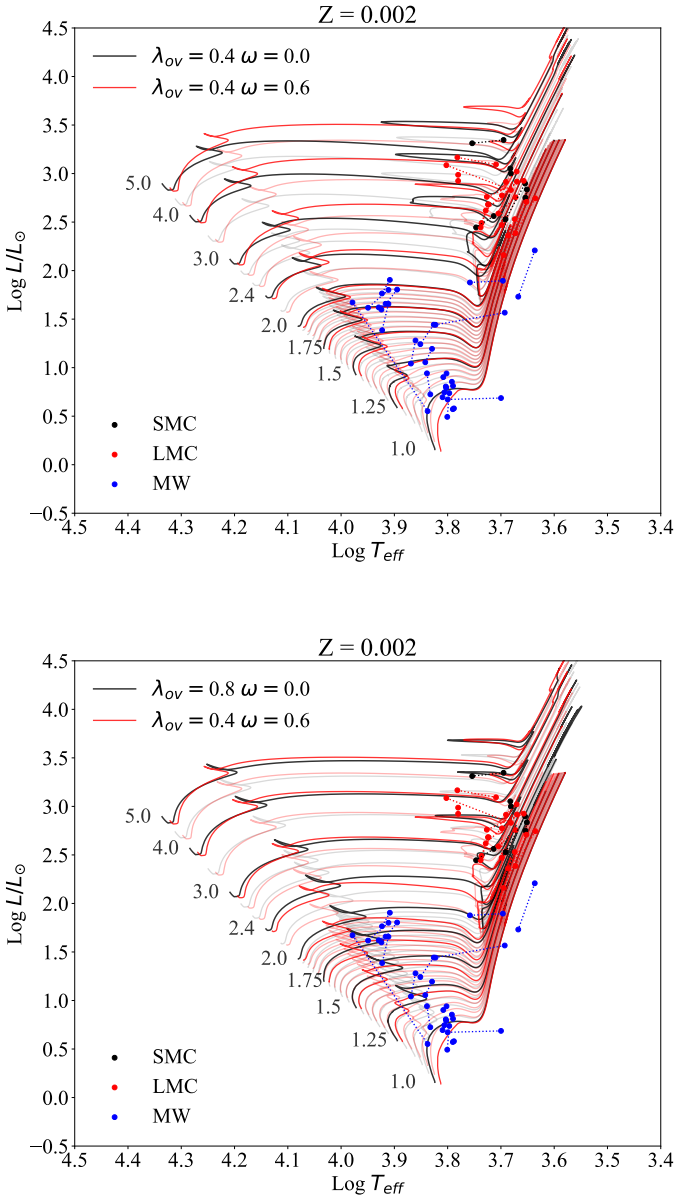

FIGURE 5.8: Overview of the data and evolutionary tracks with rotation used in this work. The points united by the dotted lines are the stars in binaries, grouped as in Figure 5.1. In the top panel, tracks with fixed $\lambda_{ov} = 0.4$ without rotation (in black), and with rotation, with $\omega_i = 0.6$ (in red) are over-plotted, for Z = 0.002. In the bottom column, tracks with $\lambda_{ov} = 0.4$ and $\omega_i = 0.6$ (in red), are over-plotted with tracks with $\lambda_{ov} = 0.8$ without rotation (in black). All the sets of tracks cover the mass range from 1 to 5 $M_\odot$. All intermediate values of ω_i and Z are available. I recall that tracks with rotation and $M_i < 1.9\ M_\odot$ are not used in the analysis.

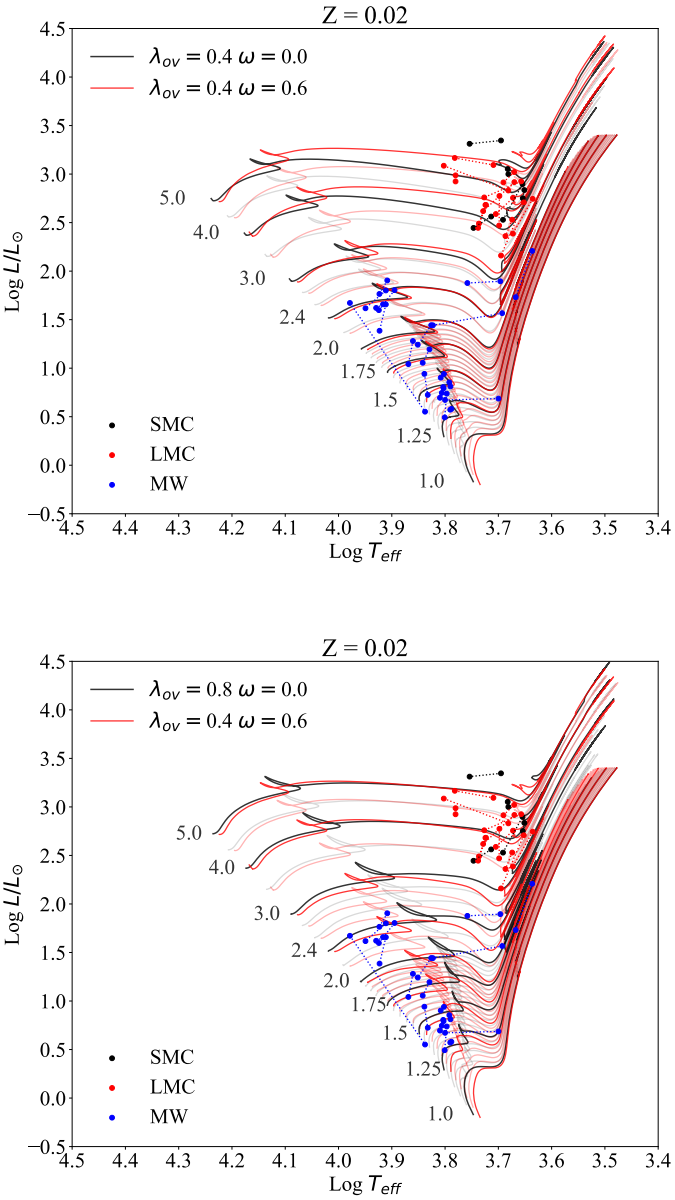

FIGURE 5.9: Overview of the data and evolutionary tracks with rotation used in this work as in Figure 5.8 but with Z = 0.02.

5.5 Effects of rotation

In the previous section I have shown that the values of λ_{ov} in Figures 5.4, 5.6 and 5.7, are suggestive of a minimum overshooting parameter between 0.3 and 0.4, for stars with $M_i \geq 1.5\ M_\odot$. I have also stated that the excess mixing clearly shown by data above this overshooting threshold, could be due to another effect that I speculate to be the rotational mixing. Here, I check this hypothesis by means of the new rotation models of PARSEC. However, I restrict the study to stars with mass greater than 1.9 $M_\odot$ because, being in advanced phases of evolution, they should have experienced the induced mixing by rotation during the previous hydrogen-burning phase. Some of these stars are in the core He-burning (CHeB) and, as mentioned in Sec. 5.3, the overshooting is treated in the same way as in the H-burning phase. Nevertheless, the core overshooting process in this phase is less critical, since what matters is the core mass at which stars enter into the CHeB phase, which is determined by the overshooting on the main sequence. Moreover, since they should be slow rotators now, they should not be significantly affected by geometrical distortions and their position in the HR diagram should not depend on the inclination of their rotation axes with respect to the line of sight.[1]

5.5.1 Evolutionary models with rotation

To study the combined effect of overshooting and rotation, I have computed sets of models with masses between 1 $M_\odot$ and 5 $M_\odot$, with a fixed overshooting efficiency of $\lambda_{ov} = 0.4$. This value of λ_{ov} is only a preliminary choice dictated, on one side, by the paucity of stars below this value (see e.g. Figure 5.6) and, on the other, by the large values derived for a few objects in the previous analysis. Concerning rotation (described in detail in Chapters 3 and 4), I explore a wide range of initial rotation rate parameter $\omega_i = 0.0, 0.1, 0.2, 0.3, 0.4, 0.5, 0.6, 0.65, 0.70, 0.75, 0.80$, at the ZAMS. All the other stellar evolution parameters are kept unchanged. As in the previous analysis, the grids of stellar tracks are interpolated to produce finer grids of tracks as a function of [Fe/H] and ω_i. Selected sets of tracks with different values of ω_i and overshooting are shown in Figures 5.8 and 5.9. In the top panels of the two Figures, I show the tracks with constant value of $\lambda_{ov} = 0.4$ with and without rotation, over-plotted to the data. The selected rotation rate is $\omega_i = 0.6$. In the bottom panels, I compare tracks with large overshooting, $\lambda_{ov} = 0.8$ and without rotation, with tracks with $\lambda_{ov} = 0.4$ and with $\omega_i = 0.6$. These Figures allow to make an immediate comparison between the effects of large overshooting and those of mild overshooting and rotation. For example I note that, for the above parameters, the non rotating tracks of $M_i = 5\ M_\odot$ and $M_i = 4\ M_\odot$ run almost superimposed in the HR diagram to their corresponding models with mild overshooting and rotation. This already suggests that objects for which I have determined a large overshooting parameter without rotation, could be simply explained by mild overshooting and additional rotational mixing. In support of this suggestion I show, in Figures 5.10 and 5.11, the evolution of

[1] This was verified a posteriori, see for instance the cases of α Aurigae and TZ Fornacis commented in Sect. 5.6.

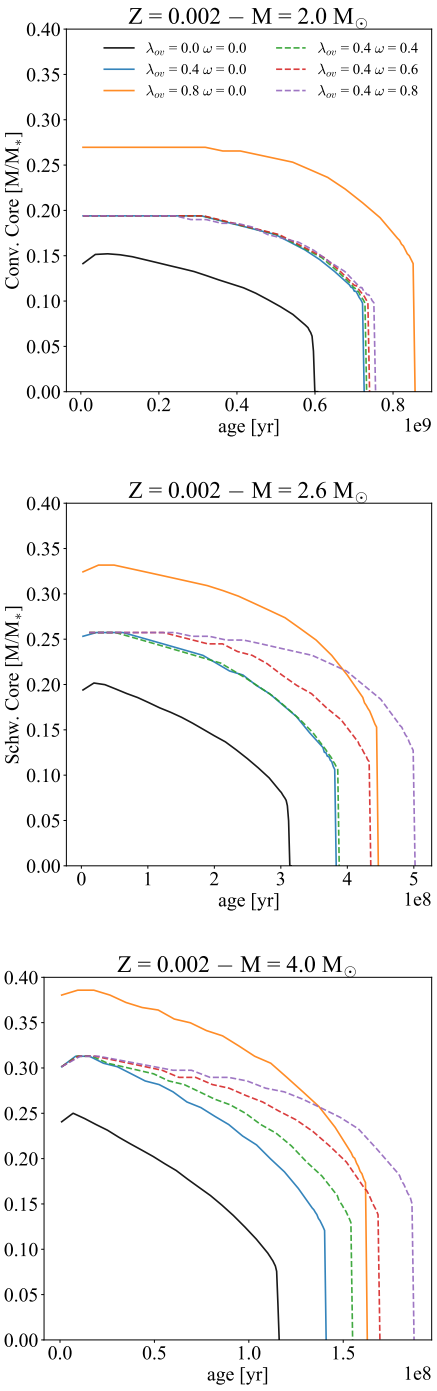

FIGURE 5.10: Comparison between the convective core extension (mass fraction) versus time (year) of different models. The solid lines are models with varying overshooting parameter (λ_{ov} = 0.0, 0.4, 0.8) and no rotation, while the dashed lines are models with a fixed overshooting parameter (λ_{ov}= 0.4) and varying rotation (ω_i = 0.4, 0.6, 0.8). In the top, mid and bottom panels there are models with masses of 2, 2.6 and 4 $M_\odot$, respectively.

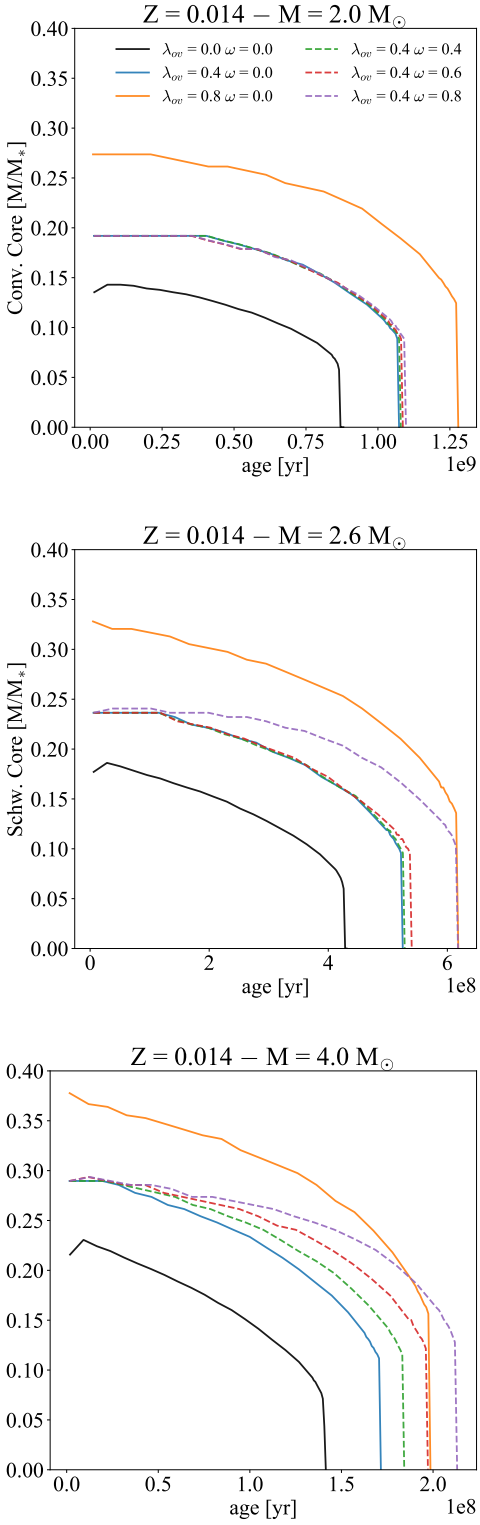

FIGURE 5.11: Same as in Figure 5.10 but with models with a metallicity content of Z = 0.014.

the border of the convective core (in mass fraction) during the Hydrogen burning phase, for the models with 2, 2.6 and 4 $M_{\odot}$, and for two metallicities (Z = 0.002 and 0.014). In each panel there are three models with core overshooting and no rotation (the solid lines), and three models with fixed λ_{ov} parameter (λ_{ov} = 0.4) and different rotation rates (ω_i, the dashed lines), as indicated in the figure. I note that the sizes of the cores of the models with fixed overshooting (λ_{ov} = 0.4) and varying initial rotational velocities decrease more slowly that of the corresponding model without rotation. This effect is more pronounced for larger rotational velocities and for larger masses. It also depends slightly on the metallicity. For both the metallicities, in the case of M_i = 4 $M_{\odot}$, the final core of the fastest rotating model becomes larger than that of the non rotating model with λ_{ov} = 0.8. This effect is due to the increase of the mean molecular weight induced by rotational mixing, that directly affects the stellar luminosity. This effect is less evident in models with masses below about 2 $M_{\odot}$, that instead, are more sensitive to the overshooting process. Eventually larger rotation rates are needed to obtain bigger effects. In the case of Z = 0.014 and M_i = 2 $M_{\odot}$, the age differences (Δage) are still appreciable. In particular, at the end of the main sequence, the Δage between the model with λ_{ov} = 0.4 and without rotation, and the model with λ_{ov} = 0.4 and ω_i = 0.8 is $\sim$ 24 Myr.

These facts are in line with the choice to restrict this study to stars with mass greater than 1.9 $M_{\odot}$. In the next Section I show the results of the statistical analysis performed with the new models with rotation, in this mass range.

5.5.2 Results

In Section 5.4.2 I applied the Bayesian analysis to obtain the JPDF of age and λ_{ov} parameters for the components of our binary systems. Here I repeat the same procedure to the models with fixed overshooting, λ_{ov} = 0.4, and variable rotation parameter, ω_i. Moreover, I limit the analysis to initial masses $M_i \geq 1.9\ M_{\odot}$ because our goal is to study the effects of rotation in the mass range where overshooting has eventually reached its maximum efficiency. This simplifies the problem because it allows me to work with only two independent parameters, age and ω_i, since λ_{ov} is fixed. The result of this analysis is displayed in Figure 5.12. In the figure I plot for each component the derived mode and credible intervals (CIs) of the initial ω_i as a function of the initial mass. In this analysis I have adopted the observed values of [Fe/H]. A similar plot, but made adopting the average value of [Fe/H] for each group of binary stars depending on the parent galaxy, is shown in Figure 5.13. To better compare the results obtained adopting variable overshooting in one case and fixed overshooting plus rotation in the other case, I also list in Table 5.3 the derived parameters for the analyzed binary components, in the two cases. I note that, independently from the method used to determine the metallicity, rotation is actually able to explain the varying extra mixing observed in stars with similar masses. The results show a certain degree of stochasticity that now can be simply explained by different initial rotational rates, from very small to

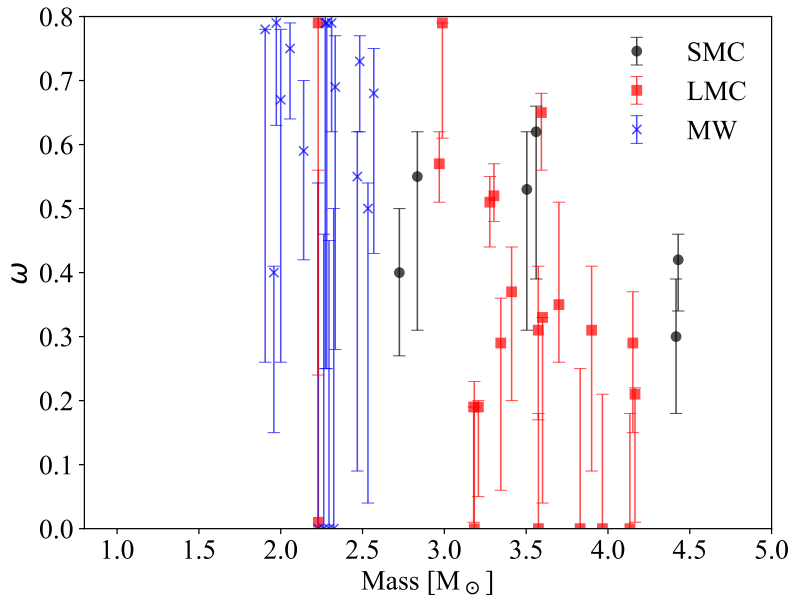

FIGURE 5.12: Resulting initial angular rotation rate, ω_i, as a function of the initial stellar mass for the stars with $M_i \geq 2.0\ M_\odot$, with the correspondent 68 credible interval bars. The color code and the symbols are as in Figure 5.4. Results from the analysis performed with the observed [Fe/H] values.

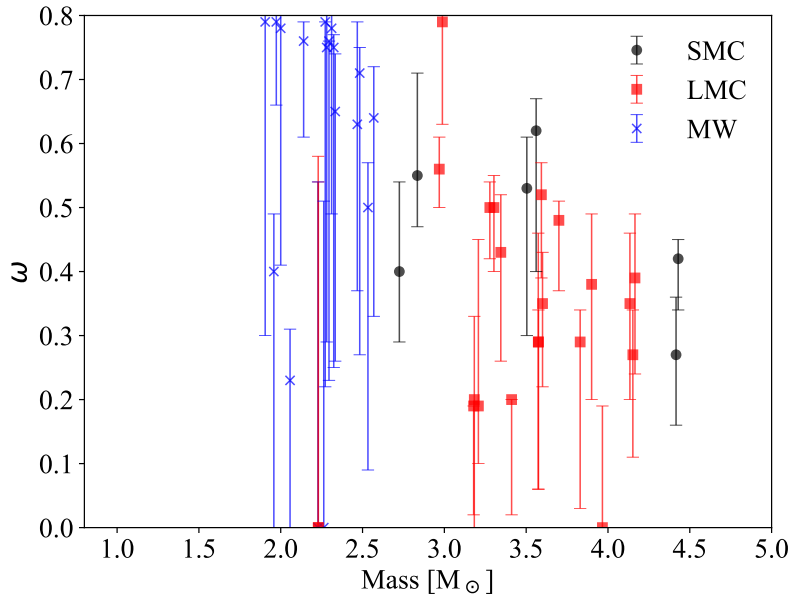

FIGURE 5.13: Same as in Figure 5.12, but in this case the analysis has been performed with the averaged [Fe/H] for stars of each galaxy.

quite large values. I remind that in objects with very small initial rotational rates the extra mixing is produced only by mild core overshooting (λ_{ov} = 0.4). On the other hand, objects that in the previous analysis required a high overshooting mixing, are now well fitted by high rotational rates on top of the same amount of overshooting (λ_{ov} = 0.4).

Concerning the ages, the other parameter derived from this analysis, I note that they are almost independent of the adopted mixing scheme used in the models to match the stellar properties (see Table 5.3). The largest difference in the ages is $|\delta_{Age}/Age_{\omega}| \sim 12$ per cent, for the system TZ Fornacis (without taking into account of OGLE-LMC-ECL-25658 and OGLE-051019.64-685812.3 systems, which are evident outliers) but, in general the average difference is below ~ 5 per cent. Thus, the two different mixing schemes are actually able to reproduce the same radius, $T_{\rm eff}$, mass and age of an observed star indicating that, at the end, they produce the same global mixing.

5.6 Discussion and Conclusions

In this Chapter, I analyze the concurrence between convective core overshooting and rotation in low and intermediate mass stars. Both processes may cause extended extra mixing in the central regions of the stars. There is a large debate in literature concerning the efficiency of these two processes. While overshooting is widely recognized as an important process affecting the evolution of all stars with sizable convective cores (as well the ages assigned to all stellar populations up to ages of a few Gyr), rotation has been considered relatively less important, at least for low and intermediate-mass stars. There is growing evidence, however, that fast rotators are reasonably common and may significantly affect the CMDs of young and intermediate-age clusters in the Magellanic Clouds and in the Galaxy (see e.g. Brandt and Huang, 2015b; Marino, Milone, et al., 2018; Marino, Przybilla, et al., 2018). Here, I aim at shedding light on the relative importance of these two processes by analyzing a sample of well studied double lined eclipsing binaries. The accurate determinations of their masses, radii, luminosities, effective temperatures and metallicities, together with the constraint imposed by the common ages of the systems, provide a unique opportunity to test stellar evolution models with different mixing schemes. For this purpose I consider the two most common extra mixing schemes, overshooting and rotational mixing. I adopt a Bayesian approach that allows to properly weight all the models with stellar properties close to the observed ones, and to derive the PDFs and credible intervals for the model parameters.

In the first part of this analysis (Section 5.4), I consider the hypothesis that only overshooting is responsible of the extra mixing and I try to reproduce the observed data by varying the overshooting efficiency parameter, λ_{ov}, in the models. Because of the significant scatter and the error bars, I do not find a clear trend of the λ_{ov} parameter, but I may expect that it grows from zero to its full efficiency regime in the mass domain between 1 and $\sim$1.5 $M_{\odot}$ and, thereafter, it remains constant, up to about $M_{\rm i} \sim 5\ M_{\odot}$. Furthermore, the analysis clearly shows that, above

TABLE 5.3: Resulting values of the Overshooting parameter and the age of the system, for the two type of analysis. First analysis: interpretation with only the overshooting parameter, λ_{ov}. Second analysis: interpretation with a fixed value of the overshooting parameter, λ_{ov} = 0.4, and variable rotation. For each binary system component is listed the observed values of Mass and [Fe/H] (from A. Claret and G. Torres, 2017; Antonio Claret and Guillermo Torres, 2018), and the computed best values of the λ_{ov} and age parameters (for the two analysis) with their correspondent errors. In the last column there is the relative absolute difference (in percentage) between the age parameters found in the two different analysis.

			Variable Overshooting		Fixed Overshooting and Rotation		
Binary Name	Mass [$M_\odot$]	[Fe/H]	λ_{ov}	Age$_{\lambda_{ov}}$ [Gyr]	ω_i	Age$_\omega$ [Gyr]	$\lvert\delta$ Age/Age$_\omega\rvert$ [%]
SMC-108.1-14904	4.429 ± 0.037	-0.80 ± 0.15	$0.62^{+0.02}_{-0.09}$	$0.132^{+0.000}_{-0.009}$	$0.42^{+0.04}_{-0.08}$	$0.135^{+0.000}_{-0.009}$	2.3
...	4.416 ± 0.041	...	$0.51^{+0.06}_{-0.08}$	...	$0.30^{+0.09}_{-0.12}$	...	...
OGLE-LMC-ECL-CEP-0227	4.165 ± 0.032	-	$0.35^{+0.10}_{-0.11}$	$0.141^{+0.021}_{-0.003}$	$0.21^{+0.01}_{-0.20}$	$0.145^{+0.003}_{-0.003}$	2.2
...	4.134 ± 0.037	-	$0.36^{+0.05}_{-0.06}$	...	$0.00^{+0.18}_{-0.00}$	...	...
OGLE-LMC-ECL-06575	4.152 ± 0.030	-0.45 ± 0.10	$0.41^{+0.07}_{-0.13}$	$0.151^{+0.004}_{-0.013}$	$0.29^{+0.08}_{-0.14}$	$0.159^{+0.004}_{-0.007}$	4.5
...	3.966 ± 0.032	...	$0.28^{+0.08}_{-0.08}$	...	$0.00^{+0.21}_{-0.00}$	...	...
OGLE-LMC-ECL-CEP-2532	3.900 ± 0.100	-	$0.43^{+0.10}_{-0.20}$	$0.170^{+0.008}_{-0.025}$	$0.31^{+0.10}_{-0.22}$	$0.178^{+0.008}_{-0.012}$	4.5
...	3.830 ± 0.100	-	$0.30^{+0.14}_{-0.13}$	...	$0.00^{+0.25}_{-0.00}$	...	...
LMC-562.05-9009	3.700 ± 0.030	-	$0.58^{+0.04}_{-0.19}$	$0.195^{+0.014}_{-0.009}$	$0.35^{+0.16}_{-0.09}$	$0.200^{+0.019}_{-0.005}$	2.3
...	3.600 ± 0.030	-	$0.33^{+0.14}_{-0.11}$	...	$0.33^{+0.00}_{-0.29}$	...	...
OGLE-LMC-ECL-26122	3.593 ± 0.055	-0.15 ± 0.10	$0.66^{+0.02}_{-0.07}$	$0.263^{+0.006}_{-0.018}$	$0.65^{+0.03}_{-0.09}$	$0.282^{+0.000}_{-0.036}$	6.7
...	3.411 ± 0.047	...	$0.46^{+0.04}_{-0.07}$	...	$0.37^{+0.07}_{-0.17}$	...	...
OGLE-LMC-ECL-01866	3.574 ± 0.038	-0.70 ± 0.10	$0.42^{+0.09}_{-0.08}$	$0.200^{+0.009}_{-0.005}$	$0.31^{+0.10}_{-0.14}$	$0.209^{+0.020}_{-0.005}$	4.5
...	3.575 ± 0.028	...	$0.31^{+0.10}_{-0.10}$	...	$0.00^{+0.18}_{-0.00}$	...	...
OGLE-SMC-113.3-4007	3.561 ± 0.025	-	$0.73^{+0.07}_{-0.16}$	$0.214^{+0.010}_{-0.010}$	$0.62^{+0.04}_{-0.23}$	$0.234^{+0.035}_{-0.021}$	8.8
...	3.504 ± 0.028	-	$0.53^{+0.12}_{-0.13}$	...	$0.53^{+0.09}_{-0.22}$	...	...

TABLE 5.3: (Continued)

			Variable Overshooting		Fixed Overshooting and Rotation		
Binary Name	Mass [$M_\odot$]	[Fe/H]	λ_{ov}	Age$_{\lambda_{ov}}$ [Gyr]	ω_i	Age$_\omega$ [Gyr]	$\lvert\delta$ Age/Age$_\omega\rvert$ [%]
OGLE-LMC-ECL-10567	3.345 ± 0.040	-0.81 ± 0.20	$0.44^{+0.13}_{-0.15}$	$0.246^{+0.018}_{-0.011}$	$0.29^{+0.07}_{-0.23}$	$0.246^{+0.018}_{-0.006}$	0.0
...	3.183 ± 0.038	...	$0.38^{+0.08}_{-0.12}$	...	$0.00^{+0.23}_{-0.00}$	...	...
OGLE-LMC-ECL-09144	3.303 ± 0.028	-0.23 ± 0.10	$0.59^{+0.03}_{-0.03}$	$0.302^{+0.000}_{-0.014}$	$0.52^{+0.05}_{-0.04}$	$0.302^{+0.007}_{-0.007}$	0.0
...	3.208 ± 0.026	...	$0.30^{+0.03}_{-0.13}$	...	$0.19^{+0.01}_{-0.14}$	...	...
OGLE-051019.64-685812.3	3.278 ± 0.032	-	$0.35^{+0.23}_{-0.05}$	$0.240^{+0.036}_{-0.026}$	$0.51^{+0.04}_{-0.07}$	$0.302^{+0.029}_{-0.007}$	21
...	3.179 ± 0.028	-	$0.11^{+0.12}_{-0.11}$	...	$0.19^{+0.00}_{-0.18}$	...	...
OGLE-LMC-ECL-09660	2.988 ± 0.018	-0.44 ± 0.10	$0.79^{+0.01}_{-0.34}$	$0.372^{+0.000}_{-0.017}$	$0.79^{+0.00}_{-0.18}$	$0.389^{+0.028}_{-0.018}$	4.5
...	2.969 ± 0.020	...	$0.65^{+0.02}_{-0.08}$	...	$0.57^{+0.05}_{-0.06}$	...	...
SMC-101.8-14077	2.835 ± 0.055	-1.01 ± 0.15	$0.67^{+0.06}_{-0.14}$	$0.380^{+0.000}_{-0.034}$	$0.55^{+0.07}_{-0.24}$	$0.372^{+0.009}_{-0.025}$	2.3
...	2.725 ± 0.034	...	$0.47^{+0.07}_{-0.11}$	...	$0.40^{+0.10}_{-0.13}$	...	...
α Aur	2.569 ± 0.007	-0.04 ± 0.06	$0.55^{+0.07}_{-0.16}$	$0.646^{+0.015}_{-0.043}$	$0.68^{+0.07}_{-0.25}$	$0.646^{+0.000}_{-0.083}$	0.0
...	2.483 ± 0.007	...	$0.54^{+0.06}_{-0.09}$	...	$0.73^{+0.04}_{-0.11}$	...	...
WXCep	2.533 ± 0.050	-	$0.23^{+0.24}_{-0.04}$	$0.562^{+0.013}_{-0.049}$	$0.50^{+0.04}_{-0.46}$	$0.550^{+0.000}_{-0.060}$	2.3
...	2.324 ± 0.045	-	$0.46^{+0.25}_{-0.19}$	...	$0.00^{+0.50}_{-0.00}$	...	...
V1031Ori	2.468 ± 0.018	-	$0.35^{+0.27}_{-0.03}$	$0.631^{+0.015}_{-0.042}$	$0.55^{+0.07}_{-0.46}$	$0.617^{+0.000}_{-0.041}$	2.3
...	2.281 ± 0.016	-	$0.41^{+0.20}_{-0.24}$	...	$0.79^{+0.00}_{-0.54}$	...	...
V364Lac	2.333 ± 0.014	-	$0.35^{+0.14}_{-0.28}$	$0.646^{+0.000}_{-0.070}$	$0.69^{+0.08}_{-0.41}$	$0.631^{+0.030}_{-0.014}$	2.3
...	2.295 ± 0.024	-	$0.47^{+0.15}_{-0.25}$	...	$0.00^{+0.45}_{-0.00}$	...	...
SZCen	2.311 ± 0.026	-	$0.70^{+0.07}_{-0.09}$	$0.708^{+0.017}_{-0.047}$	$0.79^{+0.01}_{-0.17}$	$0.692^{+0.016}_{-0.031}$	2.3
...	2.272 ± 0.021	-	$0.62^{+0.15}_{-0.20}$	...	$0.79^{+0.01}_{-0.54}$	...	...
OGLE-LMC-ECL-25658	2.230 ± 0.019	-0.63 ± 0.10	$0.03^{+0.51}_{-0.03}$	$0.676^{+0.100}_{-0.060}$	$0.01^{+0.55}_{-0.01}$	$0.631^{+0.163}_{-0.000}$	7.1
...	2.229 ± 0.019	...	$0.04^{+0.44}_{-0.04}$	...	$0.79^{+0.01}_{-0.55}$	...	...

TABLE 5.3: (Continued)

			Variable Overshooting		Fixed Overshooting and Rotation		
Binary Name	Mass [$M_\odot$]	[Fe/H]	λ_{ov}	Age$_{\lambda_{ov}}$ [Gyr]	ω_i	Age$_\omega$ [Gyr]	$\lvert\delta$ Age/Age$_\omega\rvert$ [%]
V885Cyg	2.228 ± 0.026	-	$0.70^{+0.09}_{-0.28}$	$0.759^{+0.054}_{-0.034}$	$0.00^{+0.54}_{-0.00}$	$0.708^{+0.033}_{-0.016}$	7.2
...	2.000 ± 0.029	-	$0.60^{+0.12}_{-0.37}$	...	$0.67^{+0.11}_{-0.41}$	...	...
AIHya	2.140 ± 0.038	-	$0.40^{+0.09}_{-0.01}$	$1.047^{+0.024}_{-0.047}$	$0.59^{+0.11}_{-0.17}$	$1.023^{+0.024}_{-0.023}$	2.3
...	1.973 ± 0.036	-	$0.24^{+0.07}_{-0.16}$	...	$0.79^{+0.01}_{-0.16}$	...	...
AYCam	1.905 ± 0.040	-	$0.36^{+0.18}_{-0.27}$	$1.097^{+0.026}_{-0.142}$	$0.78^{+0.00}_{-0.52}$	$1.047^{+0.101}_{-0.024}$	4.7
...	1.709 ± 0.036	-	$0.46^{+0.23}_{-0.26}$	...	-	...	...
SMC-130.5-04296	1.854 ± 0.025	-0.88 ± 0.15	$0.38^{+0.03}_{-0.11}$	$1.047^{+0.024}_{-0.047}$	-	-	-
...	1.805 ± 0.027	...	$0.42^{+0.03}_{-0.09}$	...	-	-	-
OGLE-LMC-ECL-03160	1.799 ± 0.028	-0.48 ± 0.20	$0.40^{+0.10}_{-0.11}$	$1.122^{+0.053}_{-0.099}$	-	-	-
...	1.792 ± 0.027	...	$0.48^{+0.03}_{-0.34}$	...	-	-	-
EICep	1.772 ± 0.007	-	$0.60^{+0.13}_{-0.24}$	$1.514^{+0.000}_{-0.133}$	-	-	-
...	1.680 ± 0.006	-	$0.63^{+0.13}_{-0.24}$	...	-	-	-
SMC-126.1-00210	1.674 ± 0.037	-0.86 ± 0.15	$0.57^{+0.11}_{-0.13}$	$1.380^{+0.133}_{-0.092}$	-	-	-
...	1.669 ± 0.039	...	$0.58^{+0.08}_{-0.21}$	...	-	-	-
HD187669	1.505 ± 0.004	-0.25 ± 0.10	$0.31^{+0.18}_{-0.31}$	$2.455^{+0.057}_{-0.164}$	-	-	-
...	1.504 ± 0.004	...	$0.65^{+0.02}_{-0.45}$	...	-	-	-
OGLE-LMC-ECL-15260	1.426 ± 0.022	-0.47 ± 0.15	$0.00^{+0.50}_{-0.00}$	$2.291^{+0.164}_{-0.103}$	-	-	-
...	1.440 ± 0.024	...	$0.74^{+0.04}_{-0.46}$	...	-	-	-
AIPhe	1.234 ± 0.005	-0.14 ± 0.10	$0.39^{+0.03}_{-0.39}$	$4.677^{+0.2204}_{-0.2106}$	-	-	-
...	1.193 ± 0.004	...	$0.17^{+0.43}_{-0.17}$	...	-	-	-
YZCas	2.263 ± 0.012	0.01 ± 0.11	$0.80^{+0.00}_{-0.24}$	$0.575^{+0.000}_{-0.038}$	-	-	-
...	1.325 ± 0.007	...	$0.16^{+0.19}_{-0.16}$	...	-	-	-

TABLE 5.3: (Continued)

			Variable Overshooting		Fixed Overshooting and Rotation		
Binary Name	Mass [$M_\odot$]	[Fe/H]	λ_{ov}	Age$_{\lambda_{ov}}$ [Gyr]	ω_i	Age$_\omega$ [Gyr]	$\lvert\delta$ Age/Age$_\omega\rvert$ [%]
TZFor	2.057 ± 0.001	0.01 ± 0.04	$0.46^{+0.07}_{-0.00}$	$1.230^{+0.000}_{-0.055}$	$0.75^{+0.04}_{-0.11}$	$1.097^{+0.026}_{-0.025}$	12
...	1.958 ± 0.001	...	$0.55^{+0.10}_{-0.06}$	...	$0.40^{+0.01}_{-0.25}$	...	...
V442Cyg	1.560 ± 0.024	-	$0.80^{+0.00}_{-0.41}$	$1.738^{+0.041}_{-0.189}$	-	-	-
...	1.407 ± 0.023	-	$0.10^{+0.42}_{-0.10}$	...	-	-	-
GXGem	1.488 ± 0.011	-0.12 ± 0.10	$0.45^{+0.15}_{-0.08}$	$2.630^{+0.000}_{-0.339}$	-	-	-
...	1.467 ± 0.010	...	$0.40^{+0.13}_{-0.07}$	...	-	-	-
BWAqr	1.479 ± 0.019	-0.07 ± 0.11	$0.44^{+0.09}_{-0.30}$	$2.455^{+0.176}_{-0.111}$	-	-	-
...	1.377 ± 0.021	...	$0.04^{+0.33}_{-0.04}$	...	-	-	-
AQSer	1.417 ± 0.021	-	$0.80^{+0.00}_{-0.26}$	$2.884^{+0.067}_{-0.254}$	-	-	-
...	1.346 ± 0.024	-	$0.60^{+0.20}_{-0.37}$	...	-	-	-
BFDra	1.414 ± 0.003	-0.03 ± 0.15	$0.66^{+0.09}_{-0.28}$	$2.818^{+0.202}_{-0.127}$	-	-	-
...	1.375 ± 0.003	...	$0.50^{+0.11}_{-0.33}$	...	-	-	-
BKPeg	1.414 ± 0.007	-0.12 ± 0.07	$0.44^{+0.03}_{-0.24}$	$2.754^{+0.064}_{-0.124}$	-	-	-
...	1.257 ± 0.005	...	$0.00^{+0.30}_{-0.00}$	...	-	-	-
COAnd	1.2892 ± 0.0073	$+0.01 \pm 0.15$	$0.47^{+0.19}_{-0.21}$	$3.981^{+0.000}_{-0.514}$	-	-	-
...	1.2643 ± 0.0073	...	$0.40^{+0.21}_{-0.21}$	...	-	-	-

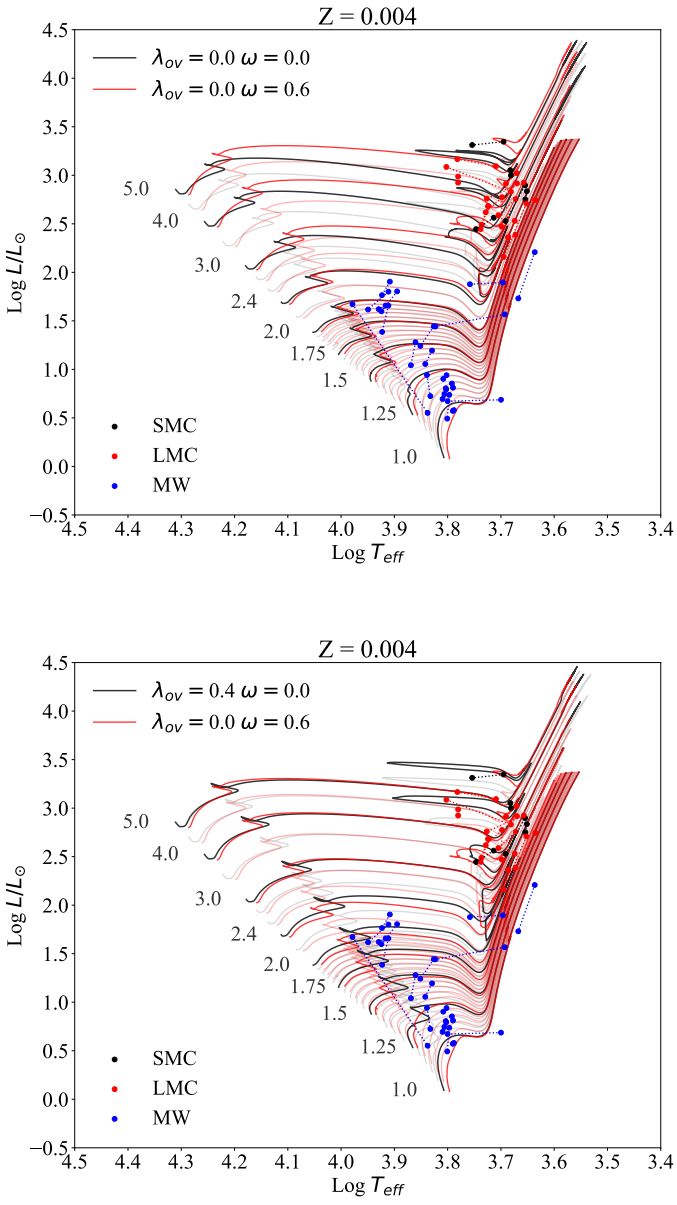

FIGURE 5.14: Same as in Figure 5.8. But on the top panel, tracks with fixed $\lambda_{ov} = 0.0$ and without rotation (in black), and with rotation of $\omega_i = 0.6$ (red lines). On the bottop panel, tracks with $\lambda_{ov} = 0.4$ without rotation (in black), and tracks with $\lambda_{ov} = 0.0$ and rotation, with $\omega_i = 0.6$, in red. All the sets of tracks cover the mass range from 1 to 5 $M_\odot$, with Z = 0.004.

$M_i \sim 1.5\ M_\odot$, the overshooting parameter is generally confined between $\lambda_{ov} \geq 0.3 - 0.4$ and $\lambda_{ov} \leq 0.8$. Such a large scatter of the extra mixing is difficult to explain in the framework of the usually adopted models of convection that instead predict a constant efficiency for a given mass. In other words, the result of the analysis would require an overshooting parameter with a large stochastic variation in the range of intermediate mass stars. I infer, from the distribution of the λ_{ov} parameter as a function of the initial mass depicted in Figure 5.6, that there may be an concurrence between overshooting, that sets a constant minimum threshold extra mixing, and a further effect, that adds extra mixing in a stochastic way. This could be obtained by changing other stellar parameters, such as the adopted Mixing Length Parameter (A. Claret, 2016; A. Claret and G. Torres, 2017; Antonio Claret and Guillermo Torres, 2018), the Helium content (Valle et al., 2017) and even the inclusion of some mechanisms which may distort the observed luminosities and effective temperatures like stellar spots (see e.g. J. Higl and A. Weiss, 2017).

I suggest, instead, that rotation provides a more reasonable explanation for this stochastic extra mixing. In the second part of the analysis, I explore this hypothesis with models with fixed overshooting parameter and at varying initial rotation rates. The results, shown in Figure 5.12, indicate that initial rotation rates in the interval $0 \leq \omega_i \leq 0.8$, combined with a mild overshooting distance of $\lambda_{ov} = 0.4$, may easily reproduce all the observed data above $M_i \sim 1.9\ M_\odot$. I stress that most of the stars in the sample, that are in this mass range, are now observed in an evolved phase and as slow rotators, thus they are not affected by other effects such as gravity darkening.

It is also possible to check if rotation is the only agent of extra mixing. To this purpose I compute sets of models with no overshooting and variable rotation rate. The right panel of Figure 5.14 shows a comparison between tracks with a mild overshooting ($\lambda_{ov} = 0.4$) and without rotation, and tracks with no overshooting and with rotation ($\omega = 0.6$). I note that, irrespective of the mixing scheme adopted, models with initial mass between 2.8 $M_\odot$ and 5.0 $M_\odot$ cross the Hertzsprung gap at the same luminosity, indicating a similar global mixing during the main sequence. Thus, in order to reproduce a minimum extra mixing corresponding to $\lambda_{ov} = 0.4$, the threshold value in Figure 5.6, *all* objects with initial mass $M_i \geq 1.9\ M_\odot$ should have been fast rotators in the early main sequence, with at least $\omega_i \geq 0.6$. While such a possibility cannot be excluded for binary stars, I recall that most of our components reside in detached systems (A. Claret, 2016). Thus this possibility is unlikely given that many single stars in this mass range are observed to possess small initial rotational velocities (Goudfrooij et al., 2018).

I conclude our discussion by considering in more detail the case of α Aurigae and of TZ Fornacis, two of the best studied objects in our sample. Observed quantities of individual components (Guillermo Torres et al., 2015; Gallenne et al., 2016), in particular rotational velocities, can be compared to the predictions of our analysis. To this purpose I compute evolutionary tracks with initial parameters appropriated for the binary components that result from the analysis performed with fixed overshooting and variable rotation. The comparisons with α Aurigae and with

TZ Fornacis are shown in Figures 5.15 and 5.16. All the models are computed with $\lambda_{ov} = 0.4$. As far as the initial rotational velocities are concerned, I adopt $\omega_{\alpha A1} = 0.68$ for the primary star of α Aurigae and $\omega_{\alpha A2} = 0.73$ for the secondary, while for TZ Fornacis I adopt $\omega_{TZ1} = 0.75$ and $\omega_{TZ2} = 0.40$ for primary and secondary, respectively (Table 5.3). I note that, since I am dealing with evolved stars, fully accounting for geometrical distortions will not significantly affect our results. Indeed, the adopted initial values of ω_i imply a values smaller than 0.5 for the present secondary of α Aurigae, which translate into deviations from sphericity, $1 - R_{eq}/R_{pol}$, smaller than 4 per cent, and a maximum temperature excursion of 240 K from equator to the pole. For TZ Fornacis the secondary have a present $\omega = 0.32$, which implies $1 - R_{eq}/R_{pol} = 1.5$ per cent and 100 K of T_{eff} excursion. Other stars in the $M_i > 1.9\ M_\odot$ sample present even smaller deviations since they correspond to more evolved stars. A more detailed investigation of individual objects with high rotational rates, including less evolved stars with $M_i < 1.9\ M_\odot$, should take into account geometric distortion and gravity darkening effects, and they are pursued in the following Chapter.

The top panels in Figure 5.15 and 5.16 show the evolution of stellar radius, plotted as a function of the effective temperature. For the primary component of α Aurigae, it is difficult to distinguish if the star is on the ascent of the Red Giant Branch or on the Helium Burning phase. However, an inspection of the evolutionary track together with the uncertainties in the best fit parameters indicate that the star is in the Helium-burning phase. The plots also indicates that its companion is at the end of the Hertzsprung gap. As for the TZ Fornacis system, I find that the primary component is in the He-burning phase, while the secondary, for the adopted best fit value of ω_i and accounting for the uncertainties in the radius, effective temperature and age, turns out to be just at the beginning of the post-main sequence. In the bottom panels, I show the comparison between the tangential velocities of the models and the observed values of the projected velocity. Given that the latter values constitute only lower limits to the real equatorial velocities, I see that the analysis provides initial rotational velocities in good agreement with the observations.

Of particular interest are the secondary components of the two systems because they are in the sub-giant phase, and still, keep the memory of the initial rotation rate. The best fit of α Aurigae predicts a current surface equatorial velocity of $V_{eq}(\alpha A_2) \sim 66\ km\,s^{-1}$ while the observed value is $V \sin i\ (\alpha A_2) = 35\ km\,s^{-1}$. At face value it implies an inclination angle of the star pole with respect to the line of sight of $i \sim 32^\circ$. My models with rotation indicate that in order to to obtain $V_{eq}(\alpha A_2) > 40\ km\,s^{-1}$ an initial rotation rate of $\omega_i > 0.5$ should have been necessary. The result of this analysis, based only on spectro-photometric properties of the components without any prior information on the rotational velocity, and suggesting that the secondary component of α Aurigae was a fast rotator with $\omega_i \sim 0.73$, is thus reinforced by the independent observation of its current rotational velocity. For the secondary component of TZ Fornacis, the best fit predicts a current equatorial velocity of $V_{eq}(TZF_2) \sim 53\ km\,s^{-1}$. The observed value is $V \sin i\ (TZF_2) = 46\ km\,s^{-1}$ implying an inclination angle

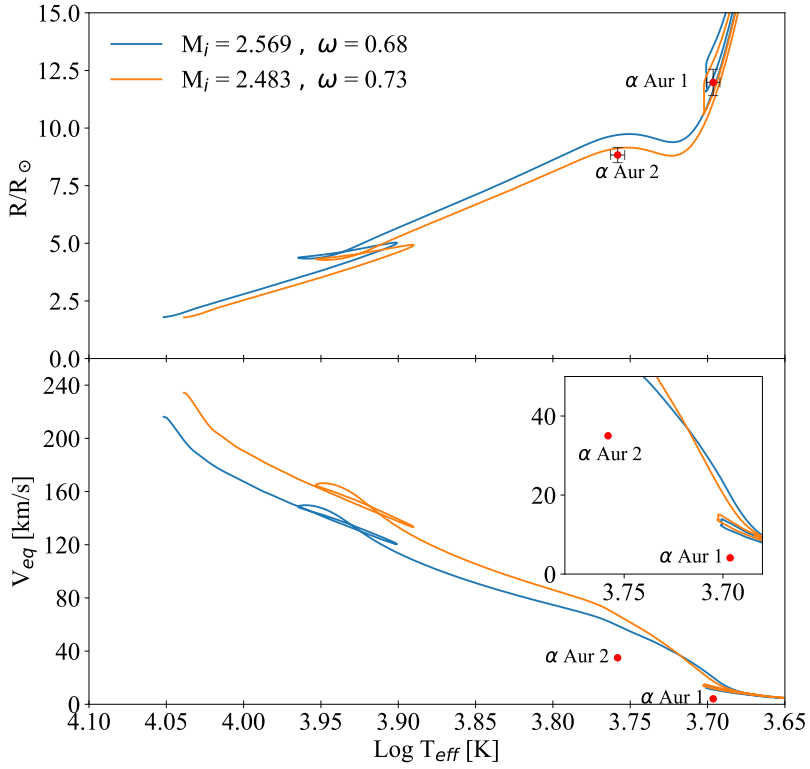

FIGURE 5.15: Comparison between the observed quantities (red points) and evolutionary tracks (continuous lines) for the α Aurigae system. The top panel shows the Radius vs. the logarithm of $T_{\rm eff}$. The bottom panel presents the equatorial tangential velocities of the stars vs. $T_{\rm eff}$. Blue and orange lines are the tracks aimed to represent the primary and secondary components, respectively.

$i \sim 60°$. Thus, also the secondary star of TZ Fornacis provides direct independent evidence that the initial rotation rate of the secondary component was not negligible (see also Higl et al., 2018), even if not as high as that of α Aur$_2$.

It is worth noticing that the predicted current equatorial velocity for TZ For$_2$ is near the minimum of its possible value. Using an overshooting distance significantly larger than $\lambda_{\rm ov} = 0.4$, would result in a lower initial $\omega_{\rm i}$, thus producing a tension with the current observed value. This is already suggested by the plot in Figure 5.6. Thus the test of TZ For$_2$ strongly supports my independent finding that the threshold efficiency of the overshooting process is $\lambda_{\rm ov} \sim 0.4$.

Finally, I can conclude that this study provides an insight on the extra mixing processes in stars, and gives strong suggestions that there is a concurrence between the overshooting effect and rotation in low-intermediate mass stars.

In summary I conclude that the spectro-photometric properties of detached double-lined eclipsing binaries are well reproduced by assuming

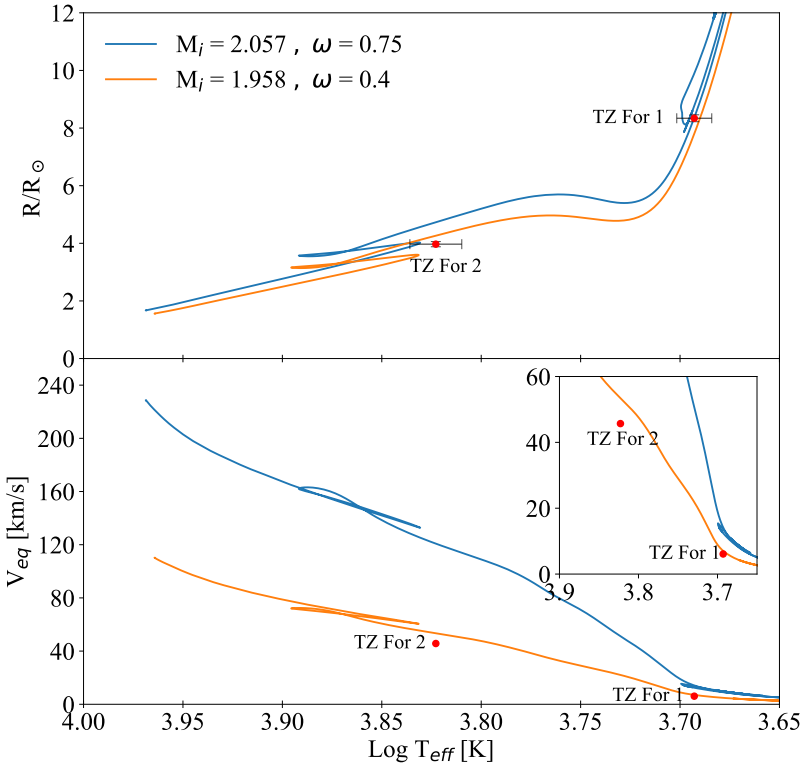

FIGURE 5.16: Comparison between the observed quantities and evolutionary tracks as in Figure 5.15, but for the TZ Fornacis system.

a threshold core overshooting distance, in the A. G. Bressan, C. Chiosi, and Bertelli (1981) scheme, of $\lambda_{ov} \sim 0.4$ with an additional effect of rotation that, by its nature, introduces a significant star to star variation of the global mixing.

Chapter 6

Analysing photometric signatures of fast rotators in color-magnitude diagram of star clusters

Chapter based on:
Girardi L., Costa G., Chen Y., Goudfrooij P.,
Bressan A., Marigo P., Bellini A.
"On the photometric signature of fast rotators", 2019
MNRAS 488, 696G. DOI: https://doi.org/10.1093/mnras/stz1767

In this Chapter, I discuss and study how the rotation impacts on the observables of stars. In particular, we evaluate the distinctive spectra and distributions in colour-magnitude and colour-colour diagrams that follow from the presence of a substantial range in effective temperatures across the surface of fast rotators. This because, rapidly rotating stars have been recently recognized as having a major role in the interpretation of colour-magnitude diagrams of young and intermediate-age star clusters in the Magellanic Clouds and in the Milky Way.

The calculations are inserted in a formalism similar to the one usually adopted for non-rotating stars, which allows us to derive tables of bolometric corrections as a function not only of a reference effective temperature, surface gravity and metallicity, but also of the rotational speed with respect to the break-up value, ω, and the inclination angle, i.

In Section 6.2, we describe the input data, methods for the spectral computations and the formalism for the inclusion of such tables into isochrones and stellar population codes. Some properties of the derived spectra and colour-colour relations are illustrated in Section 6.3, together with a couple of practical applications/considerations which are independent of stellar evolutionary models. Section 6.4 presents a few final comments and conclusions.

6.1 Introduction

The existence of rapidly rotating stars has been known for long, especially in the form of Be stars and among field A-type stars in the Milky Way (Royer, 2009; van Belle, 2012, and references therein). However, it was only recently recognized that they could be playing a very important role in determining the photometric properties of other commonly-studied stars, namely those born in populous star clusters in the Magellanic Clouds and in Milky Way open clusters. Indeed, fast rotators have been identified spectroscopically in both the Large Magellanic Cloud clusters NGC 1866 and NGC 1818 (Dupree et al., 2017; Marino, Przybilla, et al., 2018, respectively) and in the Galactic open cluster M 11 (Marino, Milone, et al., 2018), and seem to be linked to the presence of extended main sequence turn-offs (see e.g. Brandt and Huang, 2015b) and/or split main sequences (e.g. Milone, Marino, D'Antona, Bedin, Da Costa, et al., 2016; Milone, Marino, D'Antona, Bedin, Piotto, et al., 2017) in these objects. Since the same clusters have often been used to calibrate non-rotating stellar models, the neglect of rotation might have had important consequences. For instance, it might have caused systematic errors in the age estimates of well-studied clusters (Brandt and Huang, 2015a; Gossage et al., 2018), and an overestimation of the amount of convective core overshooting needed to reproduce the luminosity of post-main sequence stars (as shown in Chapter 5).

With this in mind, it is very important that we expand the previous sets of stellar models by including the effects of rotation, in a way suitable to the study of such clusters, as well as to the multitude of field stars which likely started their nuclear-burning lives as fast rotators. In the present work, we make a step in this direction, by evaluating the distinctive spectra and distributions in colour-colour space that follow from the presence of a substantial range in effective temperatures across the surface of fast rotators. We recall that similar computations have been performed a few times in the past literature. While many authors have concentrated their efforts on detailed calculations of changes in line profiles and equivalent widths in order to inform spectroscopic studies (e.g. Slettebak, Kuzma, and Collins, 1980; Frémat et al., 2005), the works by A. Maeder and Peytremann (1972), Collins and Sonneborn (1977), Pérez Hernández et al. (1999) and Lovekin, Deupree, and Short (2006) are especially insightful about the effects of rotation on the photometry.

Our calculations are intended to complement the libraries of evolutionary models for rotating stars based on PARSEC v2.0. As a library of models intended for stellar population studies, they cover the widest possible range of parameters – including the mean effective temperature and surface gravity, metallicity, angular velocity and inclination – and photometric systems as well. As will be shown later, these new computations are necessary for a proper evaluation of the effects – or signatures – of rotation in the present databases of very accurate HST multi-band photometry of Magellanic Cloud clusters.

6.2 Computing the spectra

6.2.1 The special case of non-rotating stars

Before we deal with rotating stars, it is convenient to recall the formalism and assumptions involved in the computation of synthetic spectra of non-rotating, perfectly spherical stars.

The energy a stellar surface element of area $\mathrm{d}A$, observed at an inclination angle θ, emits per unit time $\mathrm{d}t'$ and wavelength $\mathrm{d}\lambda$, over an element of solid angle $\mathrm{d}\omega'$, is

$$\mathrm{d}E_\lambda = I_\lambda \mathrm{d}A \cos\theta \mathrm{d}t \mathrm{d}\lambda \mathrm{d}\omega' \tag{6.1}$$

where I_λ is the specific intensity. In a plane-parallel atmosphere, I_λ depends only on θ, and integration over the all solid angles provides the astrophysical net flux

$$\begin{aligned} F_\lambda &= \int_{4\pi} I_\lambda(cos\theta) \cos\theta \mathrm{d}\omega' \\ &= \int_0^{2\pi} \int_0^{\pi/2} I_\lambda(\cos\theta) \cos\theta \sin\theta \mathrm{d}\theta \mathrm{d}\phi \end{aligned} \tag{6.2}$$

where the final integral was limited to the interval $[0, \pi/2]$, because there is no incoming radiation from outside the star. The equation can be simplified further, with the definition of $\mu = \cos\theta$:

$$F_\lambda = 2\pi \int_0^1 I_\lambda(\mu) \mu \mathrm{d}\mu \,. \tag{6.3}$$

This latter equation is actually used to compute F_λ once I_λ is given for several values of μ, in a plane-parallel atmosphere calculation. F_λ respects the Stefan-Boltzmann law

$$\int_0^\infty F_\lambda \mathrm{d}\lambda = F_{\mathrm{bol}} = \sigma {T_{\mathrm{eff}}}^4 \,. \tag{6.4}$$

The same symmetry that allows us to convert Eq. (6.2) into Eq. (6.3), leads to another important consequence: For a sphere of constant T_{eff} observed from a given line-of-sight, the I_λ integrated over all surface elements in a half sphere, is proportional to the I_λ of an element area averaged over all outgoing lines-of-sight, or, more precisely

$$\int_{\mathrm{half-sphere}} I_\lambda(\cos\theta) \cos\theta \mathrm{d}A = R^2 F_\lambda \tag{6.5}$$

which in practice allow us to avoid integrating the flux over the stellar surface. The monochromatic stellar luminosity becomes

$$L_\lambda = 4\pi R^2 F_\lambda, \tag{6.6}$$

and the flux observed at a distance d of the star simply scales from the flux outgoing from a small piece of its surface:

$$F_\lambda^{\text{observed}} = \left(\frac{R}{d}\right)^2 F_\lambda^{\text{stellarsurface}} \tag{6.7}$$

where $F_\lambda^{\text{stellarsurface}}$ comes from Eq. (6.3).

Equations (6.3) to (6.7) are at the basis of the synthetic photometry method, and the definition of bolometric corrections (see L. Girardi, Bertelli, et al., 2002).

6.2.2 The case of rotating stars

For rotating stars there is no spherical symmetry, and the simplification that leads from Eq. (6.2) to Eq. (6.5) does not apply. The outcoming flux has to be computed explicitly from integration over the visible surface of the star.

To describe this surface, let us adopt the spherical coordinates (x, θ, ϕ), with $\theta = 0$ aligned with the rotation axis. For convenience, the stellar radius can be scaled to its polar value, i.e. $x = R(\theta)/R_{\text{pol}}$. For a star of mass M rotating at an angular velocity Ω, in the Roche approximation, the isobar that defines the surface of radius R as a function of the polar angle θ is given by Eq. 3.11, which can be converted in Eq. 3.17. Then, it is solved numerically to give $x(\theta)$, for any value of the angular velocity with respect to its critical break-up value, $\omega = \Omega/\Omega_c$, where $\Omega_c = (2/3)^{3/2}\sqrt{GM/{R_{\text{pol}}}^3}$. The local effective surface gravity, g_{eff}, follows from computing the gravity and centrifugal forces at $x(\theta)$, and can also be easily expressed in terms of its value at the stellar pole, $g_{\text{pol}} = GM/{R_{\text{pol}}}^2$ (as shown in Section 3.10). In addition, the surface radiative flux, hence the local ${T_{\text{eff}}}^4(\theta)$, scales with g_{eff} as:

$$T_{\text{eff}} \propto f(\theta, \omega)\, {g_{\text{eff}}}^{1/4} \tag{6.8}$$

in which $f(\theta, \omega)$ is either equal to 1 as in von Zeipel (1924)'s theorem (see Section 3.11 for detail), or the term coming from the solution of equation (24) in Espinosa Lara and Rieutord (2011). We adopt the latter formalism in this work. Unless all stellar quantities are specified (including M and R_{pol}), this equation tell us how T_{eff} varies across the surface, but not its absolute value. To fix the T_{eff} scale, we define the parameter $T_{\text{eff}0}$, which is the T_{eff} value that a non-rotating star of the same R_{pol} should have to produce the same luminosity:

$$T_{\text{eff}0} = \left(\frac{1}{4\pi {R_{\text{pol}}}^2} \int_{\text{surface}} {T_{\text{eff}}}^4(\theta) \mathrm{d}A\right)^{1/4}. \tag{6.9}$$

The right-hand side can be computed without actually specifying R_{pol}, and its result is used to re-scale the entire $T_{\text{eff}}(\theta)$ relation up/down to a given $T_{\text{eff}0}$.

These approximations and definitions suffice to give us all quantities of interest – namely $x(\theta)$ $T_{\text{eff}}(\theta)$, and $g_{\text{eff}}(\theta)$ – as a function of our selected stellar input parameters, ω, $T_{\text{eff}0}$, and g_{pol}. Another important variable is

ϵ, defined as the angle between the radial vector and the normal to the surface (see Figure 3.3). For a "flattened" rotating star, ϵ is positive for $\theta < 90^\circ$, then rapidly falls to null at the equator, then becomes negative for $90^\circ < \theta < 180^\circ$. These quantities are illustrated in Fig. 6.1, for a few values of ω and for $T_{\rm eff0} = 7500$ K. It can be noticed that the deviations from spherical symmetry (or, equivalently, from the polar values) are quite modest for all $\omega < 0.5$, but increase dramatically as ω approaches 1. With the coordinate system (x, θ, ϕ) attached to the rotating star, we can now move the observer from the pole to the equator, defining a new angle i, which could be called "viewing angle", but in reality it is the "inclination angle" that a rotating star would have as seen on the sky ($i = 0^\circ$ when observing from above the pole, $i = 90^\circ$ when observing from the equator). In addition, let us define a quantity $F_\lambda^{\rm rot}$ that is similar to the F_λ of Eq. (6.7) – in the sense that it could be used to compute the flux coming from distant rotating stars by means of:

$$F_\lambda^{\rm rot,observed}(i) = \left(\frac{R_{\rm pol}}{d}\right)^2 F_\lambda^{\rm rot}(i) \tag{6.10}$$

Since the radius varies with θ, in this later equation we have adopted the polar radius as the reference one. With this definition, we can write the analogous of Eq. (6.5) for a rotating star:

$$\begin{aligned} F_\lambda^{\rm rot}(i) &= \frac{1}{{R_{\rm pol}}^2}\int_{\rm surface} I_\lambda(\cos\xi)\cos\xi {\rm d}A \\ &= \frac{1}{{R_{\rm pol}}^2}\int_0^{2\pi}\int_0^{\pi} I_\lambda(\mu')\mu'(x^2/\cos\epsilon)\sin\theta {\rm d}\theta{\rm d}\phi\,, \end{aligned} \tag{6.11}$$

where:

- ${\rm d}A = (x^2/\cos\epsilon)\sin\theta\,{\rm d}\theta{\rm d}\phi$ is the element of surface area for the coordinates (θ, ϕ). Compared to the spherical case of Eq. (6.5), it has two new multiplicative factors: x^2 takes into account the increase in area due to the variation in $x(\theta)$, while $(1/\cos\epsilon)$ takes into account the increase in area because the surface elements are inclined with respect to the radial vector.

- ξ is the angle between the normal to the surface $\vec{g}$ and the direction of the observer $\vec{i}$. The cosine of this angle, μ', is now used to select the proper I_λ at every position, and to compute the projected area with respect to the observer (which is ${\rm d}A\mu'$). Therefore, μ' replaces the former μ used for spherical stars.

- As with the non-rotating case, the integration is performed only for surface elements in the visible part of the star, i.e. those with μ' between 1 and 0.

- Since the total stellar surface also scales with ${R_{\rm pol}}^2$, Eq. (6.11) can be computed without actually specifying $R_{\rm pol}$. Moreover, since the $T_{\rm eff}$ scale has been rescaled to produce a given $T_{\rm eff0}$ value, the total stellar

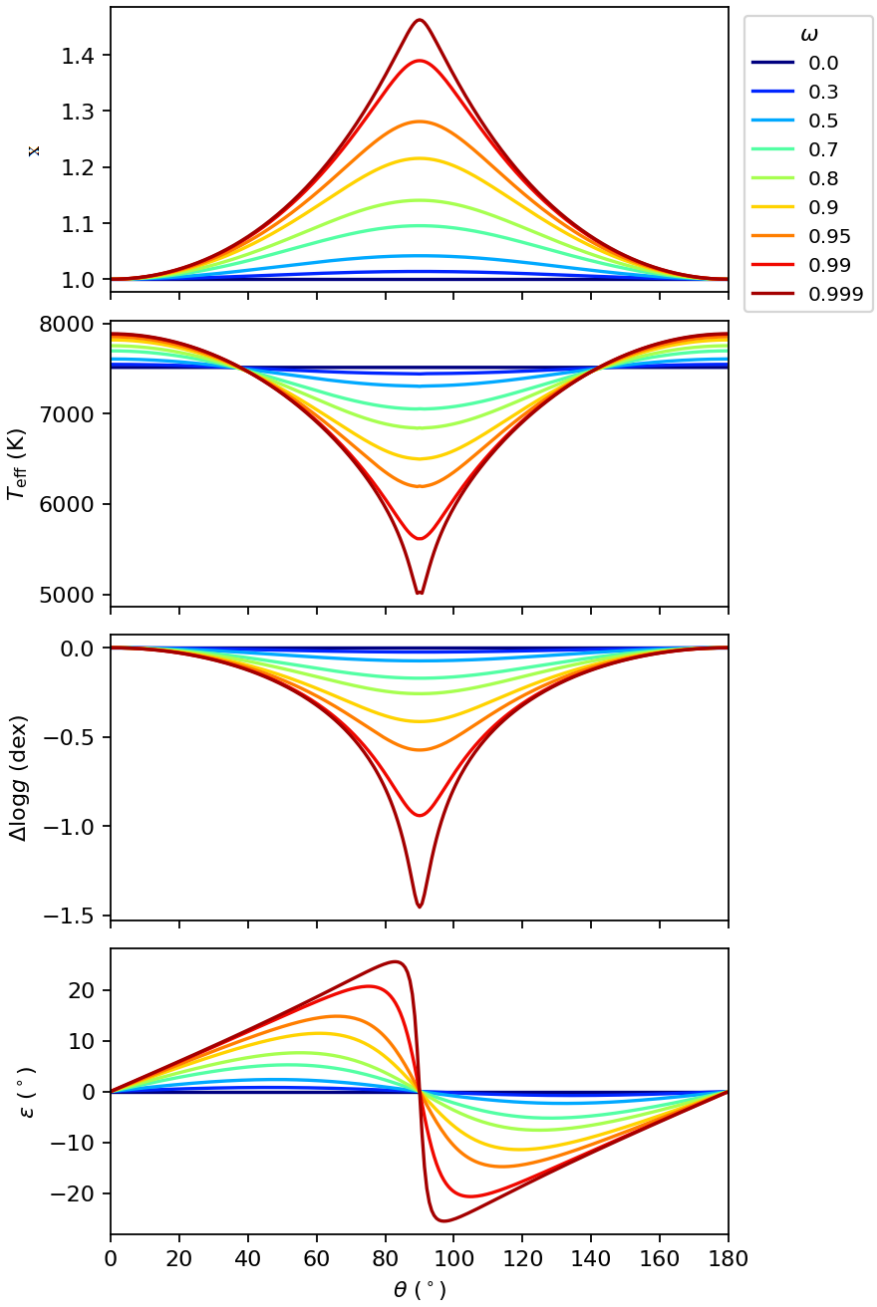

FIGURE 6.1: The variation of stellar surface quantities with the angle θ, for stars with $T_{\rm eff0} = 7500$ K and several values of ω. Panels from top to bottom show the stellar radius scaled to its polar value, the local effective temperature, the surface gravity with respect to its polar value, and the angle ϵ between the radius and the normal to the surface.

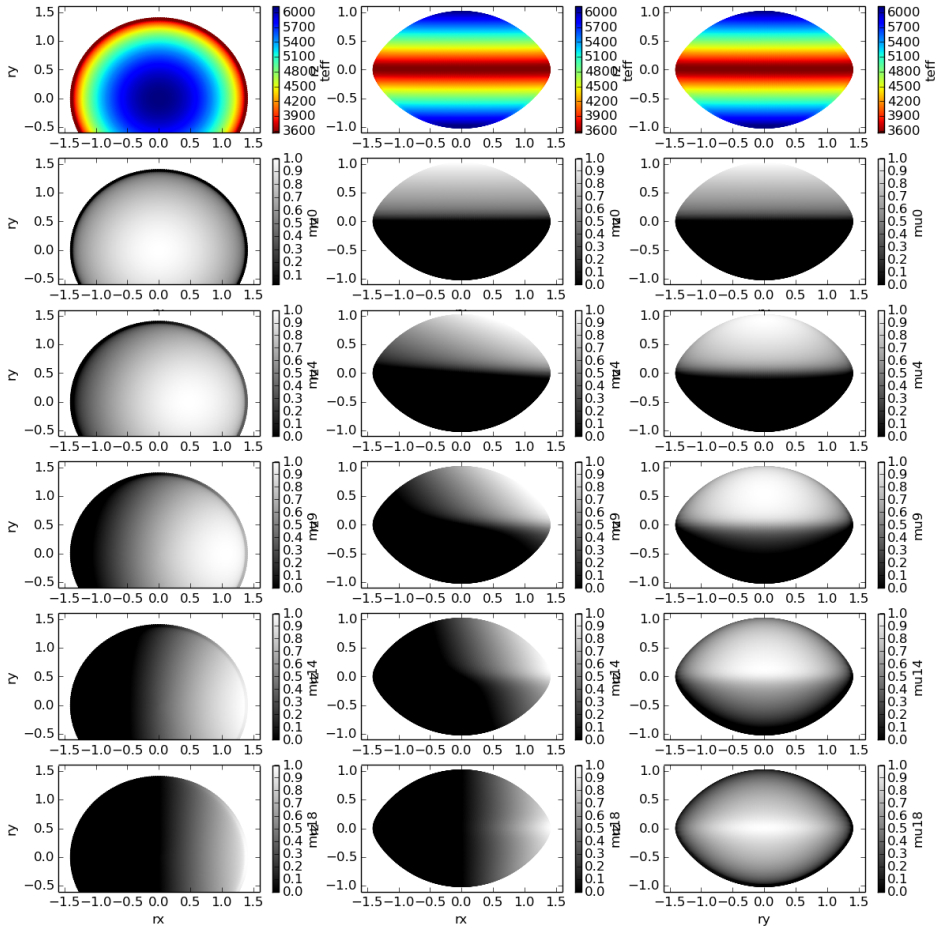

FIGURE 6.2: A star with $T_{\mathrm{eff}0} = 5000$ K, $\omega = 0.99$, in a Cartesian system where z coincides with the rotation axis. Columns at the left, centre, and right show it as seen from above, side, and front ($z > 0, y > 0, x > 0$, respectively). Top row: the surface T_{eff}. The other rows instead show the values of $\mu' = \cos\xi$ (limited to values between 1 and 0) for observers positioned at several angles, from the pole to the equator ($i = 0$ to $i = 90°$, in the sequence from top to bottom). They roughly indicate the level at which every point of the surface will be visible to these observers.

luminosity relates simply to the $(R_{\rm pol}, T_{\rm eff0})$ properties of our choice:

$$\begin{aligned} L &= \int_0^\infty L_\lambda {\rm d}\lambda = \int_{\rm surface} \int_0^\infty F_\lambda {\rm d}\lambda {\rm d}A \\ &= \int_{\rm surface} \sigma {T_{\rm eff}}^4(\theta) {\rm d}A = 4\pi {R_{\rm pol}}^2 \sigma T_{\rm eff0}^4 \end{aligned} \tag{6.12}$$

In practice, we compute Eq. (6.11) numerically, by dividing the stellar surface into several thousands of pieces of size $\Delta\theta \times \Delta\phi$ not larger than a few square degrees each. All quantities are evaluated at every point of the stellar surface, with μ' values being re-evaluated for every inclination angle i. Fig. 6.2 shows how these computer-generated rotating stars look like in Cartesian coordinates, by means of maps of $T_{\rm eff}$ and μ'.

Finally, several $F_\lambda^{\rm rot}(i)$ are shown in the left panels of Fig. 6.3 for a rapidly-rotating star of $\omega = 0.99$, and compared to similar quantities obtained for a spherical non-rotating star of same $T_{\rm eff0}$. It is evident that the star seen from the pole will be much brighter, and bluer, than when seen from the equator. The right panels allow us to appreciate these differences in a magnitude-like scale, by plotting the quantity

$$\Delta BC_\lambda = -2.5 \log \frac{F_\lambda^{\rm rot}(\omega, i)}{F_\lambda(\omega = 0)}, \tag{6.13}$$

where $F_\lambda(\omega = 0)$ is the flux of the reference non-rotating star.

6.2.3 Consistency and accuracy checks

Given the non-standard procedure adopted to compute these spectra, we perform a series of consistency and accuracy checks. First, we verify that our code recovers the F_λ provided by Castelli and Kurucz (2003), for the case of $\omega = 0$, for a wide range of $T_{\rm eff}$ (or, equivalently, $T_{\rm eff0}$) values, and for any value of i. Then, we modify the code so that we use the geometry from the rotating star, but the $I_\lambda(T_{\rm eff0})$ everywhere. In this case, $F_\lambda^{\rm rot}(i)$ simply decreases with the projected area, as expected.

Finally, the normalization of $F_\lambda^{\rm rot}(i)$ can be verified by comparing two quantities: The first is the mean $\overline{F_\lambda^{\rm rot}(i)}$, that is, the average flux seen from random positions uniformly distributed on the sky:

$$\overline{F_\lambda^{\rm rot}(i)} = \frac{1}{4\pi} \int_{\rm sphere} F_\lambda^{\rm rot}(i) {\rm d}\omega' = \frac{1}{2} \int_0^{\pi/2} F_\lambda^{\rm rot}(i) \sin i {\rm d}i \tag{6.14}$$

(where we use the north-south symmetry of the star to simplify the integral). The second is the average $F_\lambda(\theta)$ over the stellar surface:

$$\frac{1}{A} \int_{\rm surface} F_\lambda(\theta) {\rm d}A = \frac{\sigma {T_{\rm eff}}^4}{4\pi R_{\rm pol}^2}. \tag{6.15}$$

We perform these integrals numerically and find them to be nearly identical, provided that Eq. (6.14) is computed with steps $\Delta i < 5^\circ$. The outcoming average spectra are shown with gray lines in Fig. 6.3. It is interesting to note that the mean $\overline{F_\lambda^{\rm rot}(i)}$ in general presents an excess flux at

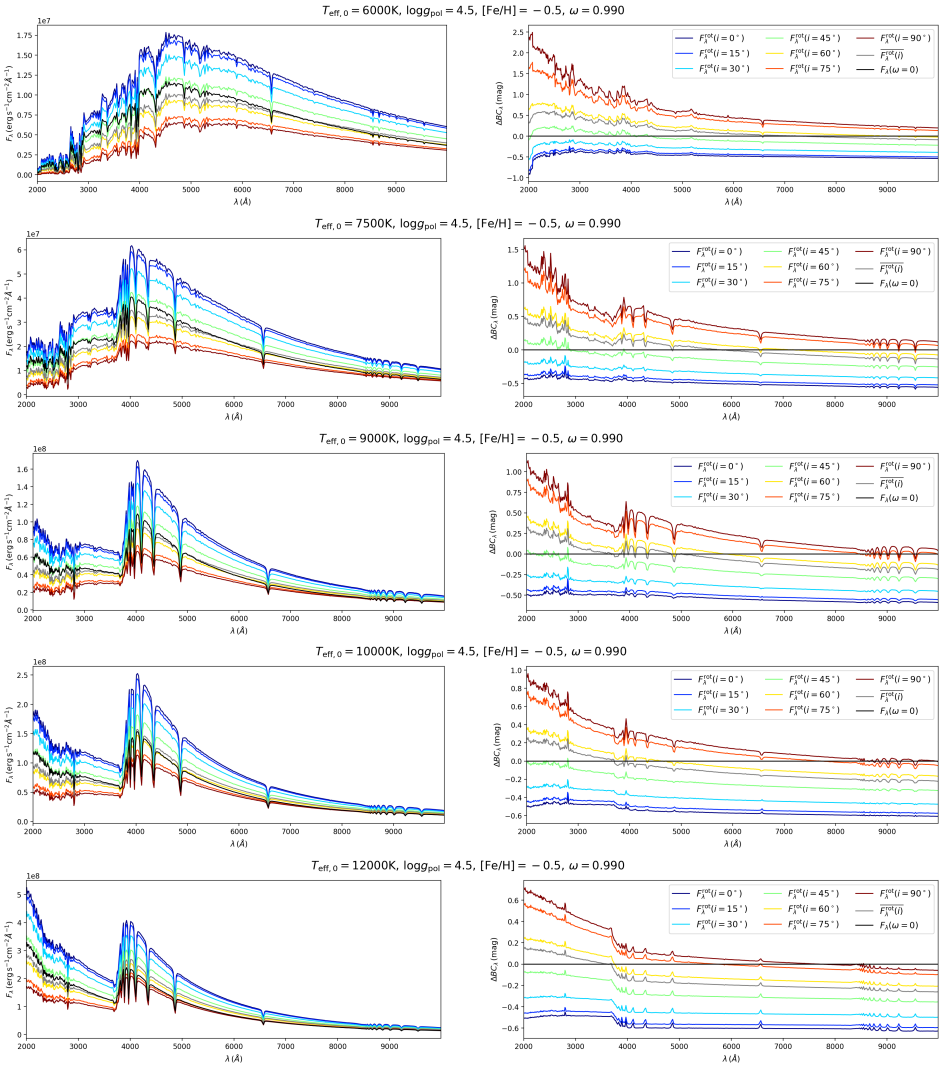

FIGURE 6.3: Left panels: $F_\lambda^{\rm rot}(i)$ computed for a sequence of stars of increasing $T_{\rm eff0}$ (from 6000 to 12000 K, from top to bottom panels), and for a fixed $\omega = 0.99$, $\log g_{\rm P}$, and [Fe/H] $= -0.5$ dex. Coloured lines show the F_λ observed from various angles from the pole ($i = 0$, bluer) to the equator ($i = 90°$, redder). The gray line is the mean F_λ averaged from all possible lines-of-sight, $\overline{F_\lambda^{\rm rot}(i)}$ (Section 6.2.3). Finally, the dark line is the F_λ computed for the non-rotating star of same $T_{\rm eff0}$. Right panels: The same models but now plotting, in a magnitude scale, the relative flux of the rotating models compared to the reference non-rotating star – that is, plotting $\Delta BC_\lambda = -2.5\log[F_\lambda(\omega = 0.99)/F_\lambda(\omega = 0)]$.

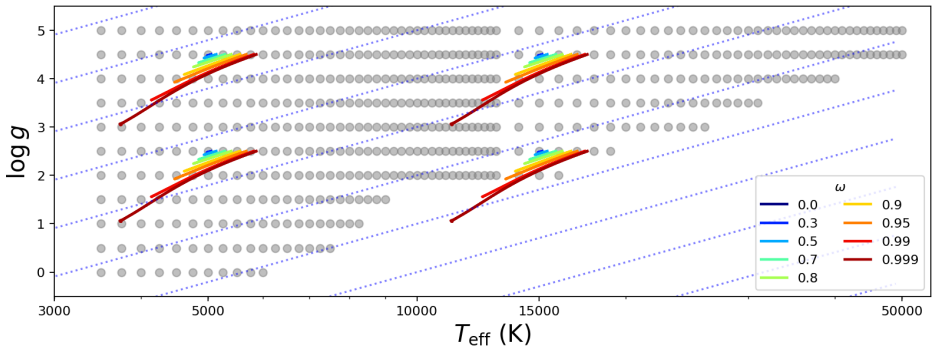

FIGURE 6.4: $T_{\rm eff}$ and $\log g$ values for which I_λ is available, from the Castelli and Kurucz (2003) models of solar metallicity at `kurucz.harvard.edu/grids/gridp00/ip00k0.pck19` (gray dots). We superpose the $T_{\rm eff}$-$\log g_{\rm eff}$ lines spanned by the surface of rotating star models of $T_{\rm eff0} = [5000, 15000]$ K and $\log g_{\rm pol} = [4.5, 2.5]$, at increasing ω (from blue to red lines, as in the legend). For the sake of comparison, the dotted lines illustrate the slope expected from von Zeipel (1924)'s law, $\beta = 0.25$, which coincides with the slope found in our models at the limit of small ω. As a consequence of using Espinosa Lara and Rieutord (2011) formalism for gravity darkening, our models with high ω present variable slopes, with mean values approaching $\beta \simeq 0.14$ at $\omega > 0.99$.

UV wavelengths, with respect to the reference non-rotating star of same $T_{\rm eff0}$, caused by the presence of a hot pole. Nonetheless, the integral of these spectra over λ turns out to be the same, and they both respect the Stefan-Boltzmann law for the temperature $T_{\rm eff0}$.

6.2.4 Limitations

Our calculations reflect a number of approximations in the modeling of rotating stars. The most fundamental ones consist in using the Roche model to compute the stellar geometry, and the Espinosa Lara and Rieutord (2011) approximation to derive the surface distribution of $T_{\rm eff}$. A number of works reveal that these are quite good approximations, able to describe both the general behaviour of 2D stellar models, and present observations of rapidly rotating stars (van Belle, 2012; Espinosa Lara and Rieutord, 2011; A. Claret, 2016). In particular, the Espinosa Lara and Rieutord (2011) model represents a clear improvement over the classical von Zeipel (1924) formula, in which $T_{\rm eff} \propto {g_{\rm eff}}^\beta$ with $\beta = 0.25$. Indeed, Espinosa Lara and Rieutord (2011) models produce β values variable across the stellar surface, with mean values closer to the expected (and observed; see van Belle, 2012) $\beta \sim 0.14 - 0.18$ for stars with ω close to 1. These slopes can be appreciated in the $T_{\rm eff}$ versus $\log g$ diagram of Fig. 6.4.

Another approximation consists in the adoption of the plane parallel model atmospheres, which is quite a reasonable assumption for relatively hot dwarfs. Fortunately, our models are not aimed to describe cool stars with extended atmospheres and convective envelopes, where the validity of these assumptions could be easily questioned.

Apart from the physical assumptions, our calculations are limited by the available libraries of I_λ, which may not cover the entire possible range of $T_{\rm eff}$ and $\log g$ values found in rotating stars. This is illustrated in Fig. 6.4, which shows the coverage offered by Castelli and Kurucz (2003) models. Similar grids are available for metallicity values, [Fe/H], going from $+0.5$ to -2 dex. Interpolation inside these grids can provide us with any I_λ comprised in the $T_{\rm eff}$ interval from 3500 to 50000 K, and with $\log g$ spanning from 5 down to a minimum value which gets larger for higher $T_{\rm eff}$. The same plot shows four families of rotating star models at varying ω, for $T_{\rm eff0} = [5000, 15000]$ K and $\log g_{\rm pol} = [4.5, 2.5]$. It is easy to see that models with large ω may exceed the range of validity of the Castelli and Kurucz (2003) tables. Two particular cases are worth considering:

1. When regions close to the stellar equator assume $\log g_{\rm eff}$ values smaller than those included in the table, as in the case of the $T_{\rm eff0} = 15000$ K, $\log g_P = 3.5$ modes with $\omega > 0.99$. We decide to use the smallest available value of $\log g$ in these cases, instead of the correct value, simply because the I_λ change slowly with surface gravity. We check this with a more extreme experiment, performed for rapidly rotating stars ($\omega = 0.99$) of $\log g_{\rm pol} = 4.5$ and 3.5: first we compute the $F_\lambda^{\rm rot}(i)$ using the correct calculation of $\log g_{\rm eff}(\theta)$, and then we do the same by setting $\log g$ equal to the polar value everywhere; the resulting $F_\lambda^{\rm rot}(i)$ change by just $\leq 5\%$ at most. This experiment seems to justify the approach of adopting the I_λ tables of smaller $\log g$ values, whenever necessary. In addition, we have to consider that this approximation will only affect hot stars of $\log g_{\rm pol} \leq 3.5$ and $\omega \geq 0.9$, which will be very rare (if not absent) in real simulations, since rotation slows down significantly as dwarfs evolve into giants.

2. Rapidly rotating stars may also exceed the $T_{\rm eff}$ range of the tables, as it would be the case, for instance, for models with $T_{\rm eff0} \leq 4000$ K and $\omega > 0.99$, and those with $T_{\rm eff0}$ approaching the upper limit of 50000 K. In these cases, we simply do not compute the $F_\lambda^{\rm rot}(i)$. This is probably less of a problem for cool stars, which are observed not to be fast rotators anyway. Rapidly rotating stars with $T_{\rm eff0}$ exceeding 30000 K, instead, will not be considered in the present work.

Another limitation is that we presently do not take into account the broadening of absorption lines by the Doppler effect in rapidly rotating stars. Even if consideration of this effect is relatively simple, the main reasons for this choice are: (1) the computational speed gained by simply adding spectra in bins of $T_{\rm eff}$, $\log g$, and μ' – i.e. without additional bins in radial velocity space; (2) the advantage of producing results independent of the actual stellar radius, i.e., as a function of ω only; and (3) the fact that we are presently interested in the flux changes expected in *broad* filters, generally with widths $\Delta\lambda > 500$ Å, and without sharp edges in the vicinity of strong absorption lines. In comparison, rapidly rotating stars generally have $v \sin i \leq 400$ km s^{-1} (see e.g. Royer, 2009) which would translate into a maximum line broadening of ~ 8 Å in the V band. It is obvious that the Doppler broadening of absorption lines will have to be considered, in addition to our present results, whenever one deals with photometric filters narrower than about ~ 200 Å.

6.2.5 BC tables for rotating stars

Setting the equations for $F_\lambda^{\rm rot}(i)$ as we have done, we can easily derive bolometric corrections BC_{S_λ}, that will allow us to transform the bolometric magnitudes, $M_{\rm bol} = -2.5\log(L/L_\odot) + M_{\rm bol,\odot}$, into absolute magnitudes as a function of i, $M_{S_\lambda} = M_{\rm bol} - BC_{S_\lambda}$, for any filter transmission curve S_λ (cf. Eq. (7) in L. Girardi, Bertelli, et al., 2002):

$$\begin{aligned} BC_{S_\lambda} &= M_{\rm bol,\odot} - 2.5\log\left[4\pi(10\,{\rm pc})^2\sigma T_{\rm eff0}^4/L_\odot\right] \\ &\quad +2.5\log\left(\frac{\int_{\lambda_1}^{\lambda_2}\lambda F_\lambda^{\rm rot}(i)10^{-0.4A_\lambda}S_\lambda {\rm d}\lambda}{\int_{\lambda_1}^{\lambda_2}\lambda f_\lambda^0 S_\lambda {\rm d}\lambda}\right) - m_{S_\lambda}^0 \,. \end{aligned} \quad (6.16)$$

This equation is generic and could be applied for any set of $F_\lambda^{\rm rot}(i)$ and interstellar extinction curves A_λ. For the moment, we simplify the analysis by setting $A_\lambda = 0$.

Then, it is a matter of fact that we have already large tabulations of the BCs for non-rotating stars, as a function of $T_{\rm eff}$, $\log g$, and [Fe/H] (e.g. L. Girardi, Bertelli, et al., 2002; L. Girardi, Dalcanton, et al., 2008). These grids work quite well in predicting the multi-band photometry of single stars, and some of them exist in different versions – for instance, with an improved spectral resolution, or with chemical abundances better matching the stars observed in different galactic samples, etc. Therefore, one may find it convenient to work with the "changes in BC caused by the rotation", rather than with the absolute BCs themselves. For that, we can simply tabulate the

$$\Delta BC_{S_\lambda}(i,\omega,T_{\rm eff0},\log g_{\rm pol}) = 2.5\log\left(\frac{\int_{\lambda_1}^{\lambda_2}\lambda F_\lambda^{\rm rot}(i,\omega,T_{\rm eff0})S_\lambda {\rm d}\lambda}{\int_{\lambda_1}^{\lambda_2}\lambda F_\lambda(T_{\rm eff0},\log g_{\rm pol})S_\lambda {\rm d}\lambda}\right) \quad (6.17)$$

and apply them to derive the changes in the magnitudes of rotating stars, as a function of $(i,\omega,T_{\rm eff0},\log g_{\rm pol})$. With this approach, we can use the $\Delta BC_{S_\lambda}(i,\omega,T_{\rm eff0},\log g_{\rm pol})$ computed for limited grids – for instance, including just scaled-solar surface chemical compositions, and just a handful of metallicity values – for a wide variety of rotating stars. This is the approach we will follow in future applications. A suitable set of ΔBC_{S_λ} tables are being inserted in the TRILEGAL code (see L. Girardi, Groenewegen, et al., 2005; P. Marigo, L. Girardi, A. Bressan, et al., 2017) for the production of isochrones and simulated stellar populations in many different photometric systems. They are also part of the YBC database of BCs and interpolating routines (`http://stev.oapd.inaf.it/YBC/`;Chen et al., in prep).

6.3 Results and applications

6.3.1 General behaviour of the spectra and colours

The $F_\lambda^{\rm rot}(i)$ we derive consist essentially in linear combinations of stellar spectra covering a limited range in $T_{\rm eff}$, with minor effects coming from the

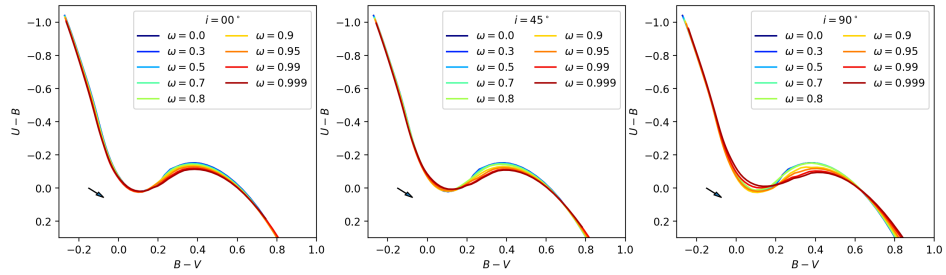

FIGURE 6.5: The $U-B$ versus $B-V$ diagram for our dwarf models of $\log g_{\rm pol} = 4.5$ and [Fe/H] $= -0.5$ dex (continuous coloured lines), for several values of ω and for three different inclinations going from the pole-on ($i = 0°$) to equator-on ($i = 90°$) configurations.

coverage of a limited range in $\log g$. Therefore, they evidently resemble the spectra of non-rotating stars of the same $T_{\rm eff0}$, with the presence of either excess flux in the bluer part of the spectrum coming from the hot pole, or "depleted flux" caused by the cool equator. For stars in which both the pole and equator are clearly visible, the departures from the spectral shape of non-rotating stars will be the largest. The situation resembles the apparent spectrum of unresolved binaries, which often appear as outliers in colour-colour diagrams, with respect to single stars, due to the different $T_{\rm eff}$ of the two components.

That said, the colour changes expected for rotating stars are very small compared to those possible for binaries. They become more evident exactly at the $T_{\rm eff}$ and wavelength ranges in which the spectral features change more rapidly with $T_{\rm eff}$. One such situation is around the well-known S-shaped curve drawn by single stars in the $U-B$ versus $B-V$ colour-colour diagram (hereafter CCD), which is caused by the appearance of a prominent Balmer jump in main sequence stars with $T_{\rm eff} \geq 7000$ K.

Figure 6.5 illustrates the $U-B$ versus $B-V$ diagram for a subset of our models. As can be seen, fast rotators are observed to "spread" aside the S-curve of non-rotating stars, but much more prominently for pole-on stars than for equator-on. This is because, when clearly observed, the hot pole quickly dominates the emitted flux (since $F_\lambda \propto T_{\rm eff}{}^4$), making the star to resemble a non-rotating, hotter star. For rapidly rotating stars seen at high inclinations, the S-curve is still very evident, but appears smoother than the classical one. Only models with $\omega \geq 0.9$ appear more than 0.01 mag away from the $\omega = 0$ sequence.

6.3.2 Comparison with other approaches

Detailed modeling of gravity darkening in rotating stars is not a novelty (see for instance Aufdenberg et al., 2006; Lovekin, Deupree, and Short, 2006; Espinosa Lara and Rieutord, 2011; Espinosa Lara and Rieutord, 2013; A. Claret, 2016), but few are the *extended grids* of rotating models aimed at performing population synthesis of such stars, hence considering wide ranges of stellar parameters such as $T_{\rm eff0}$, $\log g_{\rm pol}$, ω, and i, as well as appropriate interpolation and simulation tools.

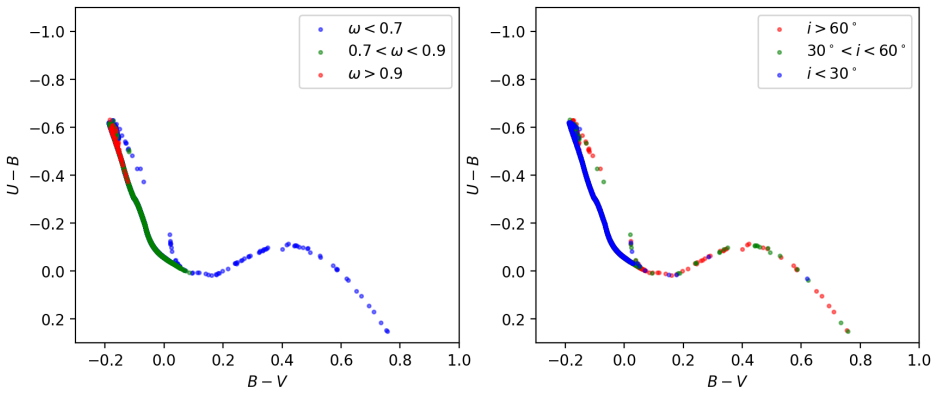

FIGURE 6.6: The $U - B$ versus $B - V$ diagram for a $Z = 0.006$, 10^8-yr old cluster simulated with the SYCLIST code (Georgy, Granada, et al., 2014), containing 10^4 stars with a uniform distribution of initial ω observed at random orientations. The left-hand panel colour-code the stars according to their present ω, whereas the right-hand does the same according to i.

The currently most popular set of such tools is SYCLIST from Georgy, Granada, et al. (2014). They follow a different approach to simulate the photometry of rotating stars: They first derive the apparent luminosity and effective temperature of the star at several i, which they refer to as $L_{\rm MES}$ and $T_{\rm effMES}$, and then convert these quantities into absolute magnitudes and colours by means of tables of colour-$T_{\rm eff}$ calibration and BC tables. Their procedure includes corrections for the limb darkening, and is consistent from the point of view of the energetics. However, they do not explicitly compute the apparent spectra at several i, and use colour-$T_{\rm eff}$ calibration and BC tables that were derived for non-rotating stars. As a consequence, their rotating models cannot present the small deviations from the colour-colour relations of non-rotating stars that ours do. This can be appreciated in Fig. 6.6, which illustrates the $U - B$ versus $B - V$ diagram of a star cluster simulated with SYCLIST and including a significant star-to-star spread in both ω and i, yet describing a very narrow S curve.

This is an important point, since present-day HST photometry of Magellanic Cloud star clusters with broad turn-offs and/or split main sequences, and suspected to contain rapidly rotating stars, include highly-precise multiband photometry of a few clusters (see e.g. Milone, Marino, D'Antona, Bedin, Da Costa, et al., 2016; Milone, Marino, D'Antona, Bedin, Piotto, et al., 2017; Goudfrooij et al., 2018). The analysis of their colour-colour plots can benefit from considering the expected deviations from the standard colour-colour relations.

Recently, also the MIST project has made available models with rotation and applied them to the detailed modeling of star clusters (Gossage et al., 2018). From the details provided in Paxton, Smolec, et al. (2019), we can conclude that their photometry is computed using essentially the same method as in SYCLIST, that is by first computing projected values of L and $T_{\rm eff}$ at several i, and then applying bolometric corrections as a

function of these $T_{\rm eff}$s.

6.3.3 An example: fast rotators in NGC 1866

As discussed above, present models introduce a new aspect that can be explored in the identification and study of fast rotators, namely that such stars should follow colour-colour relations slightly different from those of non-rotating stars. The effect should be present independently of evolutionary aspects – at least in less evolved stars in which the initial rotation has not slowed down significantly.

Let us look at one of the best known examples of star clusters containing both fast and slow rotators in their main sequence: the $\sim$200-Myr old LMC star cluster NGC 1866. A careful study by Milone, Marino, D'Antona, Bedin, Piotto, et al. (2017) revealed a clearly double main sequence in the F336W$-$F814W versus F814W CMD of this cluster, in the magnitude range $19 \leq$ F814W ≤ 21. Comparison with SYCLIST models suggested that the blue main sequence (bMS) is caused by slow rotators, while the red sequence (rMS) is caused by stars rotating as fast as $\omega = 0.9$. A third, even redder sequence, is also present and likely caused by the presence of approximately equal-mass binaries. Other aspects of these sequences are surprising, as discussed in Milone, Marino, D'Antona, Bedin, Piotto, et al. (2017): although the ratio between bMS and rMS varies with magnitude and spatial position in the cluster, nearly 2/3 of the observed stars were found in the rMS, hence suggesting an extremely high fraction of very fast rotators in this cluster.

The HST data for this cluster has been reduced independently by us (F336W, F438W, F555W, and F814W passbands; see Goudfrooij et al., 2018). Fig. 6.7 shows the F555W versus F336W$-$F814W CMD for this cluster. With its long wavelength baseline, the F336W$-$F814W colour allows to spread the main sequence features the most. Only stars with photometric errors smaller than 0.05 mag in all passbands are plotted. For comparison, we over-plot PARSECisochrones (see Chapter 5) computed both without rotation ($\omega_{\rm i} = 0$), and with fast rotation (i.e. for an initial value of $\omega_{\rm i} = 0.9$). The isochrones have been assigned magnitudes directly applying the BCs we derived in this work (Eq. (6.16)). The $\omega_{\rm i} = 0.9$ isochrones are plotted for the two extreme values of i (0° and 90°), as well as for their mean properties when observed at random orientations. Compared to the models presented in Chapter 5, the present ones are calculated with an updated version of the PARSEC which takes into account the mass loss enhancement due to the rotation, following the prescriptions by Heger, N. Langer, and Woosley (2000), described in Section 4.4. The updated code, the new tracks and isochrones and the comparison with other codes, will be presented in the following Chapter 7. Here, suffice it to recall that the tracks and isochrones include the changes in ω with respect to its initial value $\omega_{\rm i}$. For stars of intermediate mass, ω generally increases as the core contracts towards the end of the main sequence, and then sharply decreases as the star evolves into a red giant – as can be seen in the figure for the $\omega_{\rm i} = 0.9$ case. However, in the magnitude interval where the bMS and rMS are well delineated, the value of ω is essentially identical to ω_i.

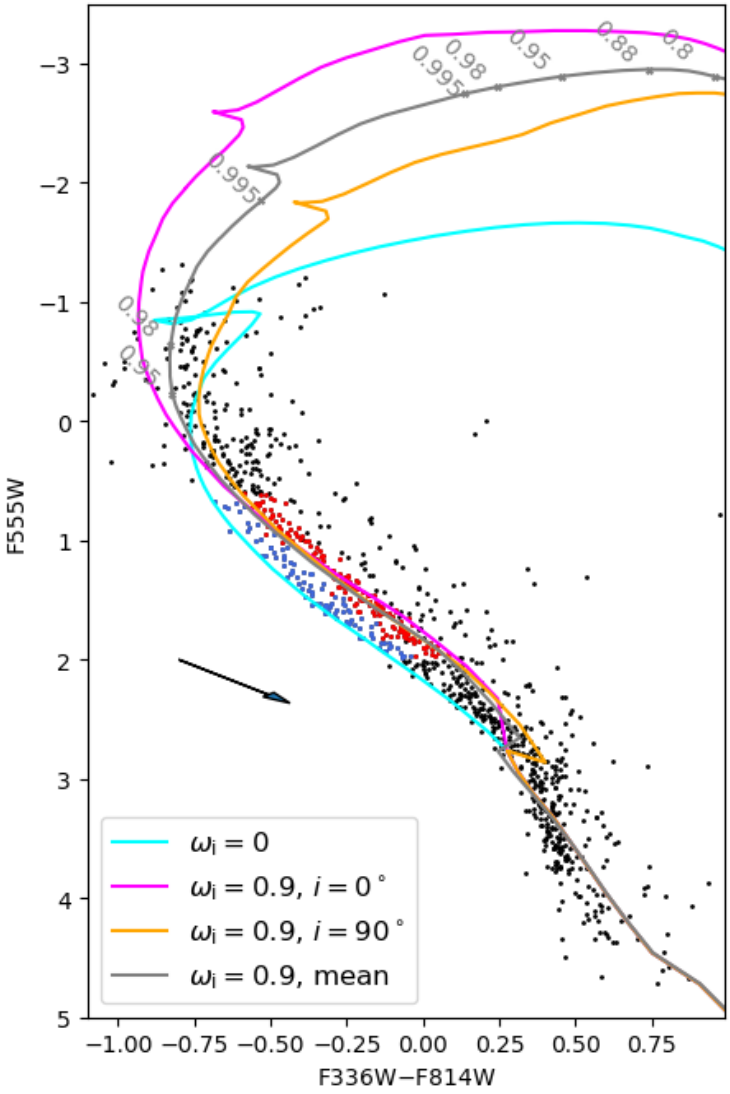

FIGURE 6.7: HST photometry of the main sequence of NGC 1866, corrected for a true distance modulus of $(m-M)_0 = 18.43$ mag and a foreground extinction of $A_V = 0.28$ mag (see Goudfrooij et al., 2018). This particular CMD presents a striking split main sequence, presumably caused by the presence of both slow rotators (in blue) and fast rotators (in red). They correspond to the bMS and rMS in Milone, Marino, D'Antona, Bedin, Piotto, et al. (2017), respectively. The continuous lines are PARSEC 250-Myr old isochrones of metallicity $Z = 0.006$, computed with initial values of $\omega_i = 0$ (cyan) and $\omega_i = 0.9$ (magenta, orange and gray, for $i = 0^\circ$, $i = 90^\circ$, and for the mean of stars observed at random orientations, respectively). Stars in the lower main sequence, with masses smaller than $1.8\ M_\odot$, are all computed with $\omega_i = 0$.The arrow illustrates the reddening vector corresponding to $A_V = 0.1$ mag. Dots and labels along the $\omega_i = 0.9$ mean isochrone are indicating the changes in the actual ω values as stars move away from their zero age main sequence.

Essentially, the plot in Fig. 6.7 reproduces the initial suggestion by Milone, Marino, D'Antona, Bedin, Piotto, et al. (2017), that the two components of the cluster split main sequence indicate two very different rotational velocities: a bMS with $\omega = 0$ and a rMS with $\omega = 0.9$. In the latter case, i values ranging from 0° to 90° cause a spread in colour–magnitude space that runs almost parallel to the main sequence, hence it does not cause significant broadening of the isochrones unless in its evolved part, close to and above the turn-off.

However, our spectral models tell more about these different main sequences, than can be presumed from the CMD alone: they tell that the fast rotators should present slightly different colour-colour sequences than the slow rotators. Therefore, in Fig. 6.8 we present the colours F336W−F438W versus F555W−F814W CCD, derived by the combination of WFC3/UVIS and ACS/WFC photometry. This colour-colour combination captures the best sensitivity we have to changes in the stellar $T_{\rm eff}$, in the current HST data for NGC 1866: indeed, while the colour F336W−F438W should be more sensitive to size of the Balmer jump developing at $T_{\rm eff} \geq 7000$ K, F555W−F814W measures the more gradual change in the slope of the red part of the spectra, over a much wider range of $T_{\rm eff}$. This colour combination also presents the S-shaped sequence characteristic of the classic $U - B$ versus $B - V$ plot, already shown in Fig. 6.5.

It turns out that the bMS and rMS merge into a single, indistinguishable sequence in this CCD, as illustrated in the top panels of Fig. 6.8. The relative mean shift between these two sequences, as measured at intermediate colours (F336W−F438W between -0.3 and -0.1) amounts to 0.01 mag at most.

Let us then interpret the CCD, according to our models. As illustrated in the middle and bottom panels of Fig. 6.8, the only models to present significant displacements from the reference stellar locus defined by slow rotators, are those with $\omega > 0.95$ and observed nearly equator-on ($i = 90^\circ$). Therefore, observing such a narrow CCD sequence means that either the fraction of fast rotators with $\omega > 0.95$ is negligible, or that these fast rotators are all observed nearly pole-on. This limit on the fraction of very fast rotators seems in agreement with the Milone, Marino, D'Antona, Bedin, Piotto, et al. (2017) initial interpretation, which attributed $\omega = 0$ for the bMS, and $\omega = 0.9$ for the rMS.

Remarkably, the *combined* constraints from the CMD and CCDs of NGC 1866 point to a significant fraction of fast rotators with velocities close to the critical value (more specifically, close to $\omega = 0.9$), but at the same time apparently excluding the values immediately close to it (i.e. excluding the interval with $\omega > 0.95$, unless for $i \sim 0^\circ$). If we assume that fast rotators follow a random distribution of inclination angles, this points to a convergence of fast rotators to a very narrow range of ω, which is intriguing to say the least, considering that we are dealing with main sequence stars which did not have their radii expanded by evolutionary effects – hence their initial rotation was not expected to have slow down significantly. It suggests a careful analysis of the data using both evolutionary tracks and population synthesis tools, taking into consideration the additional geometric effects described in this work. These steps will be performed in the following Chapter.

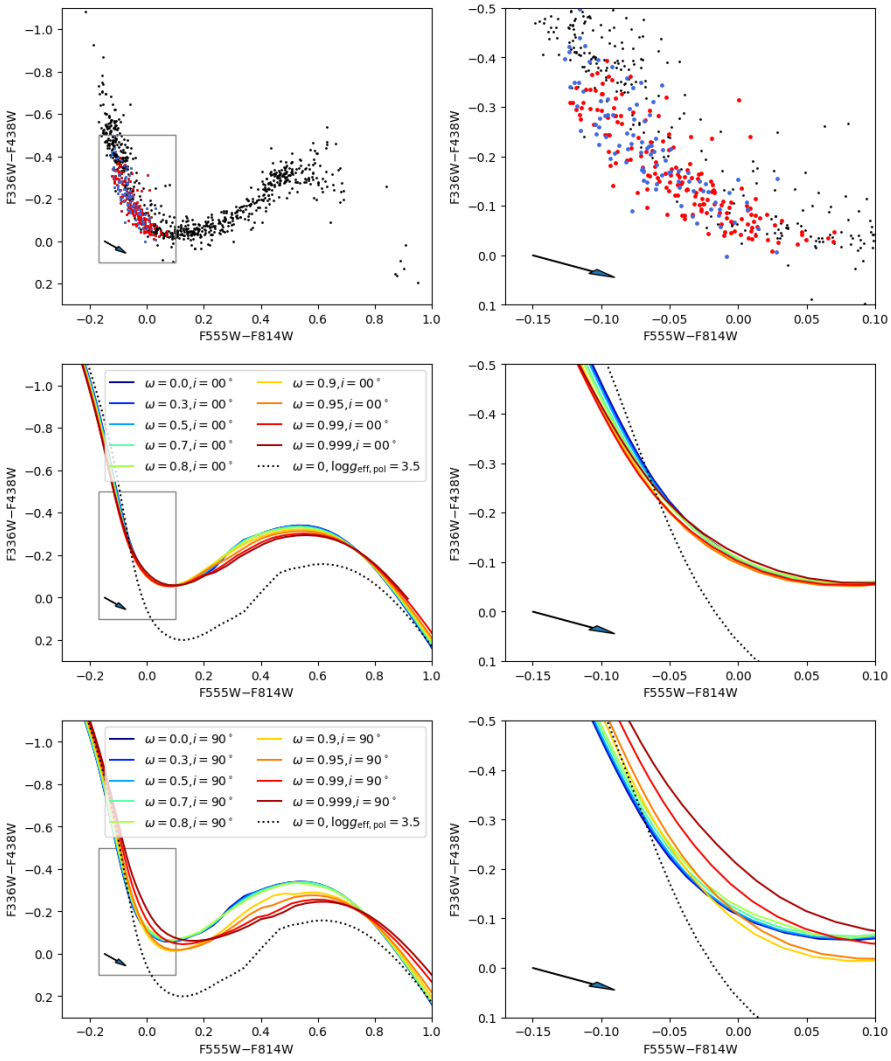

FIGURE 6.8: The potential effect of rotation in present CCDs from HST data. The top panels show the photometry of NGC 1866 (Fig. 6.7 and Goudfrooij et al., 2018)) corrected by a foreground extinction of $A_V = 0.28$ mag, in the F555W−F814W versus F336W−F438W diagram, around its characteristic S-shaped feature. Again, suspected slow and fast rotators in the cluster main sequence are marked in blue and red, respectively. The right panel zooms in the region occupied by bMS and rMS stars (gray box in left panel), revealing that there is no evident offset between the two groups of stars in the CCD. The central and bottom rows show the same diagrams as derived from our models for different values of ω: the middle row is for $i = 0°$, the bottom row for $i = 90°$. All the sequences drawn with continuous lines are for dwarfs with $\log g_{\rm pol} = 4.5$. To illustrate the dependence on surface gravity, the dotted line shows a single sequence of non-rotation models with $\log g_{\rm pol} = 3.5$. In all panels, the arrow indicates the reddening vector corresponding to $A_V = 0.1$ mag, for comparison.

Although the NGC 1866 observations are particularly intriguing, several other young LMC clusters also show a similarly bifurcated upper MS (see, e.g., M. Correnti et al., 2017; Milone, Marino, Di Criscienzo, et al., 2018). On the other hand, in the CMD of the NGC 1831 cluster in Goudfrooij et al. (2018), the upper MS is far less bimodal in appearance, suggesting a more uniform distribution of ω at the older age of NGC 1831 ($\sim$700 Myr). These aspects will be discussed in more detail in a forthcoming paper (M. Correnti et al., in prep). In all cases, it will be interesting to check whether colour-colour diagrams for these clusters – whenever available and of sufficient quality – provide additional constraints to the distributions of rotational velocities and stellar inclinations.

6.4 Conclusions

In the present Chapter, we propose a formalism for the inclusion of geometric effects and gravity darkening in models for the synthetic photometry of rotating stars. We compute the outcoming flux and bolometric corrections expected for stars spanning a very large range in mean effective temperature, surface gravity at the pole, metallicity, rotational velocity, and observed inclination. Although the computations are illustrated just for a few filters, they are available for over 50 photometric systems covering all major instrumentation and surveys, hence extending the database of such calculations for non-rotating stars in the PARSECdatabase of isochrones (see `http://stev.oapd.inaf.it/cmd`). The next step is to actually apply these models to a new family of PARSEC evolutionary models with rotation, hence closing the loop. A first study will be presented in the following Chapter.

Our models inevitably rely in some approximations (e.g. the Roche model, the Espinosa Lara and Rieutord 2011 formula, the plane-parallel atmospheres) which can be improved as more realistic grids of rotating models are built. Despite these approximations, the present approach at least opens the way for a systematic consideration of the possible colour-colour effects in population synthesis models, which is still missing in the study of both Magellanic Cloud and Galactic open clusters. We demonstrate that our models predict small, but non-negligible deviations of the fast rotators from the colour-colour relations of non-rotating stars. Identifying these deviations in the highly-precise HST photometry of star clusters might be perfectly possible, especially for very fast rotators seen nearly equator-on. This was illustrated by comparing our predicted colour-colour relations with those observed in the main sequence of the LMC cluster NGC 1866, which is thought to contain a sequence of rapidly-rotating stars. Our models suggest an upper limit of $\omega = 0.95$ to the rotational velocity of this sequence or, alternatively, that any stars rotating faster than such a limit are seen nearly pole-on.

That said, the predicted deviations from the colour-colour relations of non-rotating stars might be identifiable also in other future databases of high-precision photometry, other than the HST one, at least for stars very close to their critical break-up rotation. The basic observational requirement is having photometry with an accuracy of $\sim$ 0.01 mag in several

filters spanning the maximum possible wavelength range – and possibly including at least one filter blueward of the Balmer jump, as illustrated in this work. The future combination of very large databases accurate to the millimagnitude level, such as Gaia + LSST + Euclid + WFIRST, might provide such an interesting database for looking for very fast rotators in the Milky Way. Of course, such a search might deal with a number of complications, such as the intrinsic colour-colour spread caused by star-to-star variations in metallicity and extinction, and the more subtle problem of distinguishing unresolved binaries from rotating stars. Therefore, searches of these photometric effects should better start in star clusters, to minimize metallicity and extinction variations.

Chapter 7

Rotational properties of multiple stellar populations in star clusters: the case of NGC 1866

Chapter based on:
Costa G., Girardi L., Bressan A., Chen Y.,
Goudfrooij P., Marigo P., Rodrigues T. S., Lanza A.
"Multiple stellar populations in NGC 1866. New clues from Cepheids and Colour Magnitude Diagram". Accepted in A&A.
https://arxiv.org/abs/1909.01907

In this Chapter, I perform a comprehensive study of the stellar populations in the young Large Magellanic Cloud (LMC) cluster NGC 1866. I combine the analysis of its best studied Cepheids with that of a very accurate color-magnitude diagram (CMD) obtained from the most recent Hubble Space Telescope (*HST*) photometry. I use a Bayesian method based on new PARSEC stellar evolutionary tracks with overshooting and rotation to obtain ages and initial rotation velocities of five well studied Cepheids of the cluster.

This Chapter is organized as follows: In Section 7.2 I present the NGC 1866 data set and the Cepheid sample. In this section I also summarize the statistical methods used. In Section 7.3 I give a brief description of the new physics adopted in PARSEC and I present the new evolutionary tracks and isochrone grids. In Section 7.4, I present the results obtained from the Cepheids analysis, and compare the observed CMD with selected isochrones. Finally, in section 7.5 I discuss the results and draw the conclusions.

7.1 Introduction

NGC 1866 is one of the most populous young clusters in the Magellanic Clouds. Its location in the Northern outskirts of the LMC disk, little affected by interstellar dust and field stars, makes it one of the most interesting clusters for testing intermediate-age stellar populations and, in particular, stellar evolutionary models with masses close to its turn-off mass of $4-5\ M_{\odot}$. It contains not only a large number of evolved stars, but also a extremely high number of Cepheid variables (more than 20, Musella et al., 2016). Early studies of its CMD (Brocato, Castellani, and Piersimoni, 1994; Testa et al., 1999; Barmina, L. Girardi, and C. Chiosi, 2002) were concentrated on discussing the efficiency of convective core overshooting in intermediate-mass stars. More recently, the excellent photometry provided by the *Hubble Space Telescope* (*HST*), revealed new surprises, such as the presence of extended main-sequence turn-offs (eMSTO) and a split main sequence. The interpretation of these features are still under debate in the community, but similar features are observed also in other clusters, such as NGC 1844, NGC 1856 and NGC 1755 (Matteo Correnti et al., 2015; D'Antona et al., 2015; Milone, Marino, D'Antona, Bedin, Da Costa, et al., 2016; N. Bastian et al., 2017).

A recent study by Milone, Marino, D'Antona, Bedin, Piotto, et al. (2017) demonstrated that these features are real, and can result from an unexpectedly high presence of fast rotators in the cluster. Fast rotators were also detected directly, around the cluster turn-off, by spectroscopic measurements of line broadening (Dupree et al., 2017).

Fast rotation is believed to contribute to the eMSTOs in clusters up to much larger ages, until about 2 Gyr (Cordoni et al., 2018). There is however intense debate on whether such populous young and intermediate age clusters also harbour multiple stellar populations, formed at different ages (spanning more than a few Myr), and/or with different initial chemical compositions (Niederhofer et al., 2017; Nate Bastian and Lardo, 2018; Martocchia et al., 2018).

In the present work, I aim at reinterpreting the available data for NGC 1866, in the light of new PARSEC stellar models including rotation. Instead of looking at individual features in the CMD, like the split main sequence (MS), eMSTO, and evolved stars, I seek to reinterpret the entire available data, in particular exploiting Cepheids that have accurate pulsational mass determinations.

7.2 Data and methods

7.2.1 The NGC 1866 photometry

The NGC 1866 photometric data have been acquired through the Ultraviolet and Visual Channel of the Wide Field Camera 3 (UVIS/WFC3) and the Advanced Camera for Surveys of the Wide Field Camera (ACS/WFC) on board of the *Hubble Space Telescope* (*HST*). The cluster was observed in the four passband filters F336W, F438W (from WFC3), F555W, and F814W (from ACS). The data have been taken in programs GO-14204

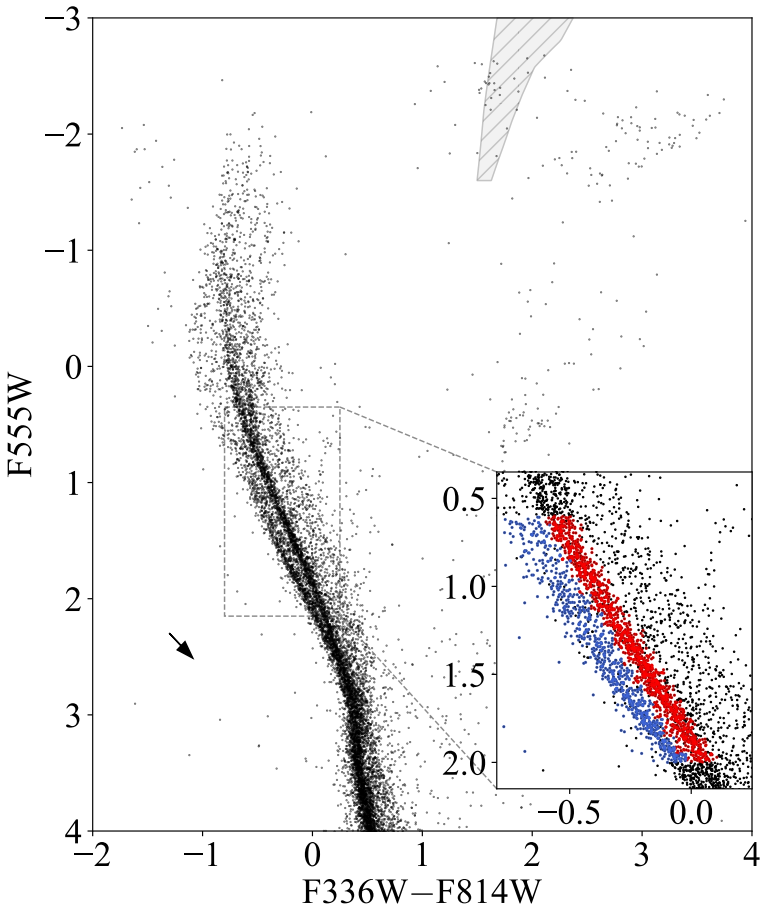

FIGURE 7.1: The F555W versus F336W − F814 CMD for all the selected stars of the cluster (see text), corrected for the effective magnitude zeropoints for each band, for a true distance modulus of $(m - M)_0 = 18.43$ mag and a foreground extinction of $A_V = 0.28$ mag (Goudfrooij et al., 2018). The black arrow indicates a reddening vector corresponding to $A_V = 0.1$ mag for reference. The gray shaded region indicates the Cepheids instability strip. The luminosity and the effective temperature of the red and blue strip are taken from Marconi, Fiorentino, and Caputo (2004) and have been colored with the new YBC bolometric database available at http://stev.oapd.inaf.it/YBC/ (Y. Chen and L. A. . Girardi, submitted to A&A). The diagram clearly shows the MS split and the extended MS turn off. The inset shows a zoom of the MS in which the two main sequences are selected and coloured for indicating the bMS (in blue) and the rMS (in red, Milone, Marino, D'Antona, Bedin, Piotto, et al., 2017).

TABLE 7.1: Structural parameters of the Cepheids sample, from Marconi, Molinaro, et al. (2013). [Fe/H] data from Lemasle et al. (2017).

Name	Mass [$M_\odot$]	log L [$L_\odot$]	$T_{\rm eff}$[K]	[Fe/H]
HV 12197	4.6 ± 0.2	3.045 ± 0.012	5950 ± 12	-0.36 ± 0.03
HV 12198	4.2 ± 0.1	3.10 ± 0.01	6050 ± 12	-0.36 ± 0.03
HV 12199	3.5 ± 0.1	2.91 ± 0.01	6125 ± 12	-0.36 ± 0.03
We 2	4.31 ± 0.15	3.00 ± 0.01	5925 ± 12	-0.36 ± 0.03
V6	4.0 ± 0.1	3.03 ± 0.01	6300 ± 12	-0.36 ± 0.03

(PI: A. P. Milone) and GO-14069 (PI: N. Bastian), then, have been downloaded from the *HST* archive and reduced as described in Goudfrooij et al. (2018). The catalog comprises $\sim 2 \times 10^4$ objects. Fig. 7.1 shows the F555W versus F336W $-$ F814W color-magnitude diagram (CMD). As already done in Chapter 6, we use of a broad wavelength baseline as colour, to stretch out the MS and better identify its features, that in this case are: the split-MS and the eMSTO. The inset shows a zoom of the MS region with a subdivision of selected stars with photometric errors smaller than 0.05 mag in all filters, for the blue sequence (bMS) and the red one (rMS) shown in blue and red points, respectively.

As already mentioned, the split-MS is a real feature of the cluster and seems to be present in many young-intermediate star clusters. The case of NCG 1866 has been studied recently by many authors (e.g. Milone, Marino, D'Antona, Bedin, Piotto, et al., 2017; Goudfrooij et al., 2018), and the common findings are that both rotation and different ages are required to explain the double MS and the eMSTO at the same time. Rotation or the spread in age alone are not able to reproduce consistently the data. Different authors found slightly different values for the metal content in the cluster. Lemasle et al. (2017) in their spectroscopic analysis of a sample of Cepheids in the cluster, found a very homogeneous chemical composition of [Fe/H] = -0.36 ± 0.03 dex, in agreement with previous measurement of the red giant branch stars by Mucciarelli et al. (2011). The MS presents a third main feature: its extension as a broad strip towards redder colours and brighter magnitudes (the dark points in the inset of Fig. 7.1). This feature corresponds to the well-known sequence of nearly-equal mass binaries, which in practice spreads a fraction of the stars from the bMS and rMS, up to a maximum upward excursion of 0.75 mag (see Haffner and Heckmann, 1937).

7.2.2 Cepheids data

In this work, I adopt two complementary approaches to study NCG 1866. Firstly, I analyze a sample of five Cepheids of the cluster, selected and studied by Marconi, Molinaro, et al. (2013), with a Bayesian statistical method. Later, I will fit the cluster features (the MS split and the eMSTO) with new PARSEC isochrones described in Sec. 7.3.2 and 7.3.3.

The use of Cepheids is convenient for several reasons. First, these stars are characterized by pulsational instabilities that have been extensively

studied in the past decades, and the physical mechanisms behind their periodical nature are well known. Thanks to very accurate pulsational models it is possible to derive their intrinsic stellar properties (in particular, the pulsational mass, the luminosity, the photospheric radius and the $T_{\rm eff}$) with a very good precision. Another reason concerns the rotation properties. Since evolved single stars are in general slow rotators, their surfaces are not significantly distorted by the centrifugal forces. Hence, the difference in temperature between the poles and the equator is negligible, and their position in the HR diagram does not depend on the inclination of the rotation axis with respect to the line of sight. As shown in Figure 6.1 of Chapter 6, non negligible effects of the rotation in the stellar geometry start to arise for $\omega > 0.5$, where $\omega = \Omega/\Omega_{\rm c}$ and $\Omega_{\rm c}$ is the angular velocity of rotational break-up.

Table 7.1 lists the intrinsic properties given by the Marconi, Molinaro, et al. (2013) analysis, performed by a data fitting procedure with non-linear convective pulsation models. Their models are computed taking into account a mild core overshooting. Their data are multi-filter photometric light curves and radial velocity measurements for the selected Cepheids. The table is complemented with the mean metal content derived by Lemasle et al. (2017) for several Cepheids of NGC 1866.

The data in Table 7.1 show that four Cepheids have a mass slightly greater than 4 $M_{\odot}$, and one has a mass of $M = 3.5\ M_{\odot}$. Assuming that all the stars belong to the same stellar population, it is surprising to see such a large range of masses for evolved stars, taking into account the associated small errors in the pulsational mass determination. One possible solution is that HV12199, the star with lower mass, lost part of its mass during its previous evolution (Marconi, Molinaro, et al., 2013). However this is difficult to explain in the framework of a common mass-loss rate formulation for the red giant stars. Alternatively, Cepheid HV12199 could be the result of a particular binary evolution history. However this would require a fine tuning for HV12199 to loose only a small fraction (about 0.5 $M_{\odot}$) of its external envelope that, for an evolved star of 4 $M_{\odot}$, is of about 3 $M_{\odot}$. Another possibility is that HV12199 really belongs to a population older than the other Cepheids and hence it has a lower post main sequence mass. I will investigate this possibility in more detail in the following sections.

7.2.3 The Bayesian statistical analysis

The Cepheids data are analyzed by means of new stellar evolutionary models[1], using a full Bayesian statistical analysis. I use the PARAM code (da Silva et al., 2006b; T. S. Rodrigues et al., 2014b; Thaíse S. Rodrigues et al., 2017) to obtain the posterior joint probability density functions (JPDFs) that depend only on three parameters, that are the metallicity [Fe/H], the age, and the initial rotation rate, $\omega_{\rm i}$, of the stars. As prior functions I adopt:

1. a flat prior on age, that is, all ages between minimum and maximum values of 3.0×10^7 yr and 9.8×10^8 yr are assumed to be equally likely;

[1] That will be presented in the next section.

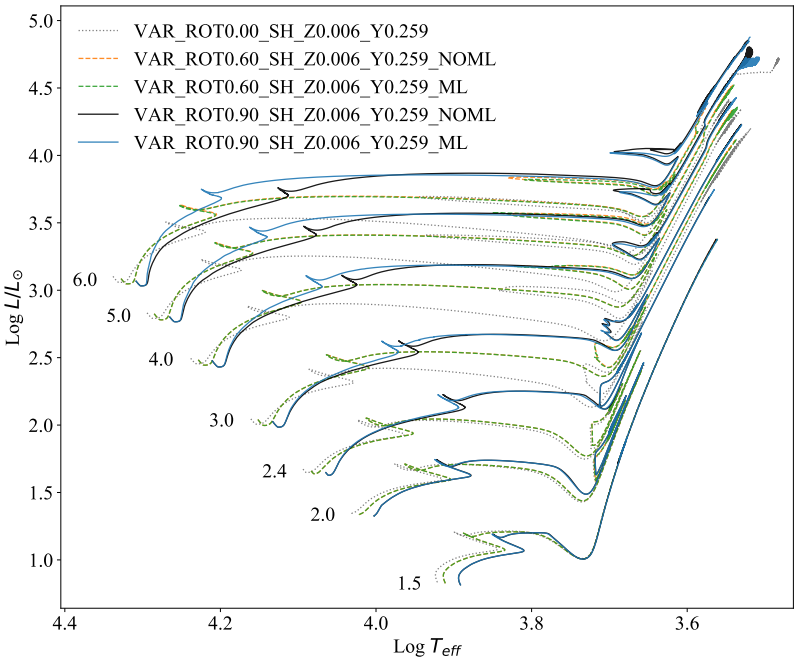

FIGURE 7.2: Comparison between sets of tracks computed with and without mass loss, for different initial rotation velocities. The dotted gray line indicates the sets without rotation. The dashed lines are the models with $\omega_i = 0.60$ and the solid lines indicate tracks with $\omega_i = 0.90$.

2. similarly, a flat prior on the initial angular rotation rate parameter ω_i, between values of 0 and 0.95;

3. a mass distribution given by the initial mass function from Kroupa (2002).

In Section 7.4 I will present the results of the analysis for each star, and I will discuss about the possible belonging to the same stellar population of the Cepheids, hence assuming a common age and metallicity content. In that case, I combine the different JPDFs to obtain the *corrected* JPDF (cJPDF). The cJPDF of each star will share the age and the metal content with the other without having any constraints on their initial rotation rates, ω_i. In Chapter 5 there is a detailed description of the statistical method, and how the computation of the cJPDFs is done.

7.3 The PARSEC models with rotation

7.3.1 New prescriptions

In this analysis, I use the PARSEC V2.0 to compute models of rotating stars. The detailed descriptions of these features can be found in Chapter 2, 3 and 4. Here, I use the most recent nuclear reaction network implemented

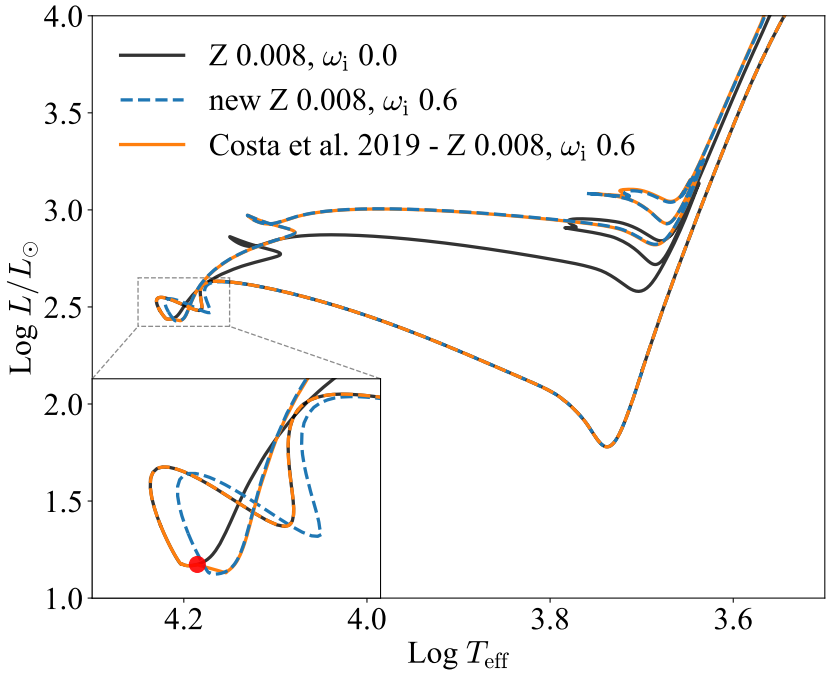

FIGURE 7.3: Comparison between tracks of a 4 $M_\odot$ star. The black line is the non-rotating model, while the dashed blue and the solid orange lines are the new and old rotating tracks, respectively. In the inset is shown a zoom of the ZAMS region to emphasize the differences between the old and the new method of introduction of the angular velocity (see text).

in PARSEC, that now consists of 33 isotopic elements, from Hydrogen to Zinc, and in total there are 72 reactions.

Since in this work I compute rotating tracks with $\omega_i > 0.90$, I take into account for the mass loss also for models less massive than 12 $M_\odot$. The implementation of this effect in PARSEC, is fully described in Chapter 4. Figure 7.2 shows a comparison between sets of tracks with and without the inclusion of the mass loss, for ω_i = 0.60 and 0.90. For stars below about 2.4 $M_\odot$, the tracks show no differences in the HR diagram, while for models with masses above that value, the differences between the two sets start to be significant. For these models, the presence or not of the mass loss does not seem to affect the extension of the blue loops.

At variance with the work presented in Chapter 5, I adopt a new strategy to assign the initial angular rotation rate to the star. In the former method the initial rotation rate is assigned when the star reaches the zero age main sequence (ZAMS) in a single time-step. With the new method the angular velocity is increased in time, starting from few time-steps before the ZAMS (about 40 time-steps, corresponding to $\sim$ 2 Myr in case of a 4 $M_\odot$ star with $\omega_i = 0.60$). If the desired ω_i is reached before the ZAMS, I do not allow ω to grow above that value. After that the ZAMS is reached, this condition is relaxed, and the angular velocity is let free to evolve. This new approach allows to have tracks that smoothly reach

the new 'rotating' ZAMS without big jumps between the not rotating pre-main sequence (PMS) and the rotating MS. This is shown in Fig. 7.3 for a 4 $M_{\odot}$ star. With the new method a 4 $M_{\odot}$ star at the "rotating" ZAMS with $\omega_{\rm i}$ = 0.60 has ingested an angular momentum that differs less than the 0.3 per cent with respect to the previous method. The following evolution is not affected by this different approach.

7.3.2 Evolutionary tracks and isochrones

The new sets of evolutionary tracks are computed with a mass range spanning from 1.5 $M_{\odot}$ to 7 $M_{\odot}$. I used solar-scaled mixtures based on Caffau et al. (2011) solar composition, with values of initial metal content Z = 0.004, 0.006, 0.008, 0.01, and with the respective values of helium content being Y = 0.256, 0.259, 0.263, 0.267. These values and the adopted fixed mixing length parameter, $\alpha_{\rm MLT}$ = 1.74, have been obtained from the solar calibration performed by A. Bressan, P. Marigo, et al. (2012). The magnetic braking and the surface magnetic effects are not taken into account in this work.

For each metallicity set, I computed tracks with varying initial rotation rate values, that are $\omega_{\rm i}$ = 0, 0.30, 0.60, 0.80, 0.90, 0.95. All the tracks are computed with a fixed core overshooting efficiency parameter, $\lambda_{\rm ov}$ = 0.4, as suggested by the analysis performed in Chapter 5. As discussed before, the evolutionary tracks are computed with mass loss to handle cases with high rotation rate ($\omega > 0.80$). The mass loss will not influence the MS evolution in case of low mass and slow rotation rates. For instance, in case of a 1.5 $M_{\odot}$ star with $\omega_{\rm i}$ = 0.30, the mass at the base of the red giant phase is 0.01 per cent smaller than its initial mass (I find similar values regardless the metallicities considered). Fig. 7.4 shows a comparison between models computed with different initial rotation rates, for models with selected masses and metallicity. Depending on the mass, the effect of rotation is slightly different. In the case of low mass stars (1.5 $M_{\odot}$), the prevailing effect induced by rotation is the geometrical distortion, that depending on the ω, takes the track to run in the HR diagram at lower temperatures (during the MS) with respect to the non-rotating case. In the giant phase, the surface angular velocity of the star drops down, due to the conservation of the angular momentum, and the rotating track runs almost superimposed to the non-rotating one. In the case of intermediate mass stars, the mixing induced by rotation starts to play a more and more important role as the mass and the rotation rate increase. The rotational mixing, acting in the radiative regions of the stars, provides fresh fuel to the burning core and transports the processed material to the stellar surface. The extra-mixing causes the stars to be more luminous and to build up bigger He-cores at the end of the MS than the correspondent non-rotating models. Thus, the tracks of rotating stars run on the Hertzsprung gap at higher luminosities than non-rotating ones, mimicking luminosities of more massive non-rotating stars. Rotating stars live longer in the MS phase and for instance, in the case of a 6 $M_{\odot}$ star model (with Z = 0.004), the MS lifetimes are 62, 74, 82 and 89 Myr for $\omega_{\rm i}$ = 0.0, 0.60, 0.80 and 0.95, respectively.

The core He-burning (CHeB) phase is also influenced by the rotation, for both the different mass of the Helium core (built during the MS phase)

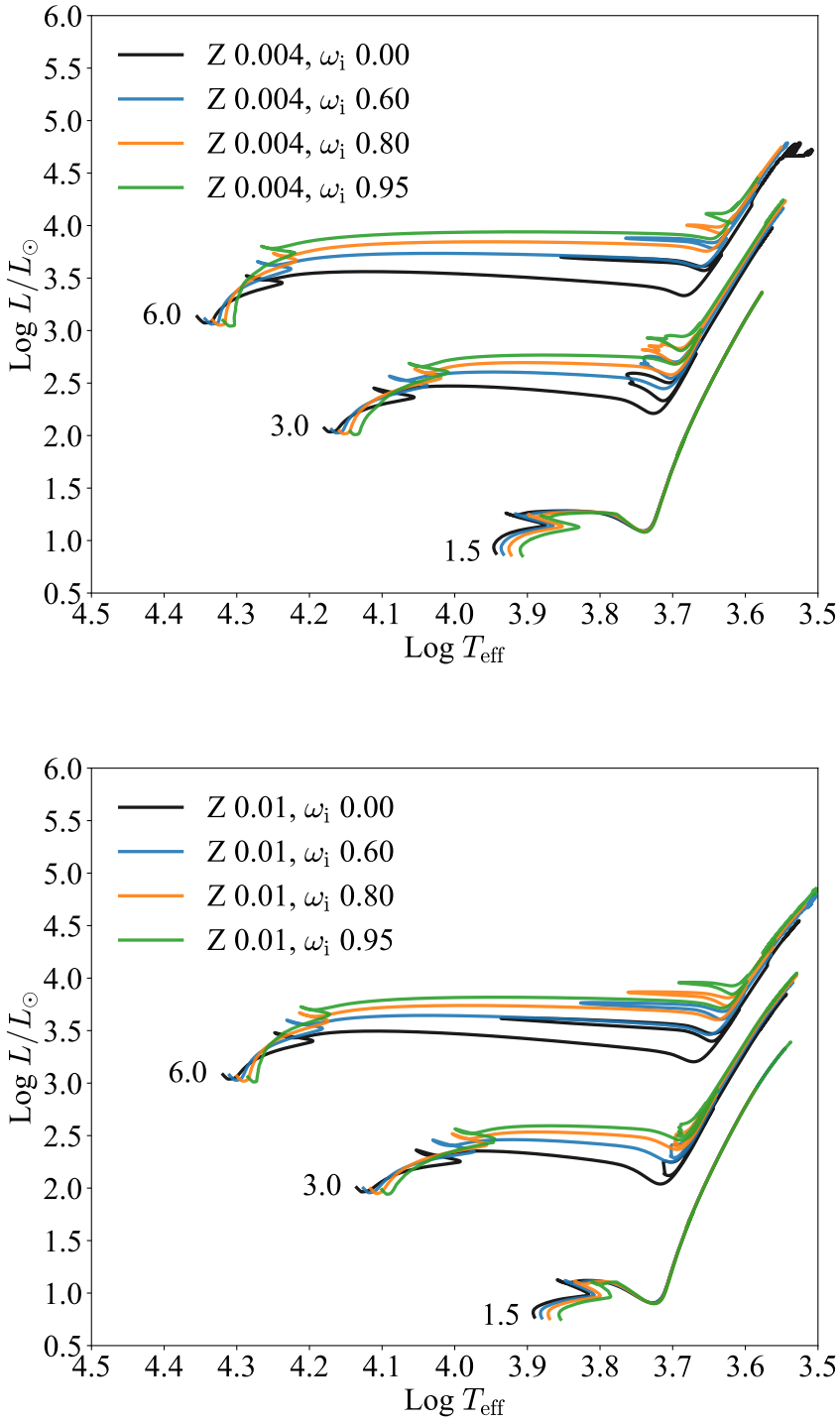

FIGURE 7.4: Selected evolutionary tracks from our sets. In different colours different rotation rates (ω_i = 0.0, 0.60, 0.80, 0.90), for three different masses (1.5, 3 and 6 $M_\odot$). In the top panel there are tracks with a selected metallicity of Z = 0.004, while in the bottom panel there are tracks with Z = 0.01.

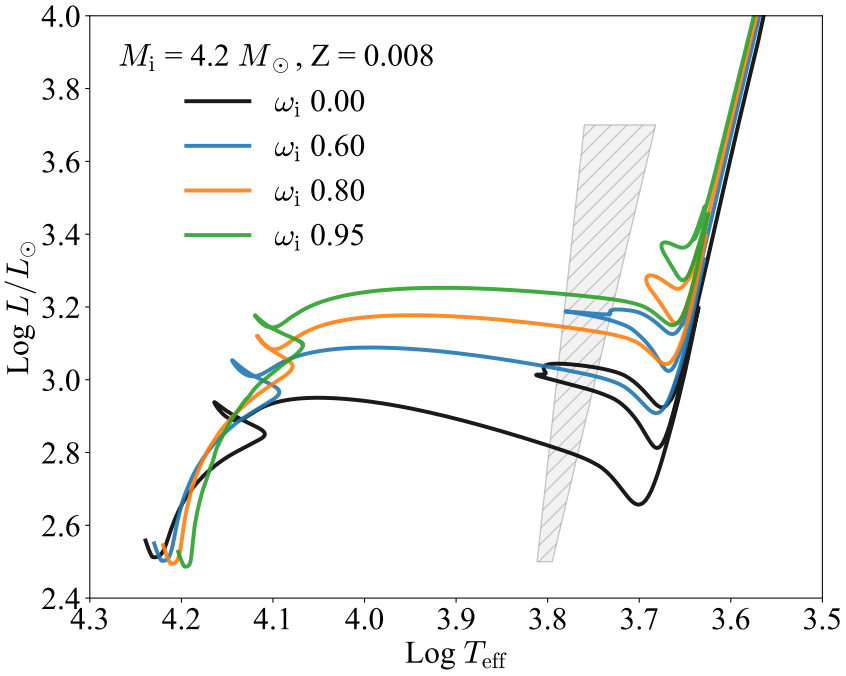

FIGURE 7.5: Evolutionary tracks of a 4.2 $M_\odot$ star with different initial rotation rates, ω_i, in different colours. The grey shaded area indicates the Cepheids instability strip (Marconi, Fiorentino, and Caputo, 2004).

and the enhanced mixing acting during the phase. I note that from the models, the position and the extension of the blue loops – typical features of intermediate mass stars during the CHeB phase – in the HR diagram is affected by rotation. As ω_i increases, the blue loops become less extended and the CHeB lifetimes decreased. In particular, for the case of the 6 $M_\odot$ star model (with Z = 0.004), the CHeB lifetimes are 6, 5, 4 and 3 Myr for ω_i = 0.0, 0.60, 0.80 and 0.95, respectively. The extension of the blue loop due to different rotations plays a crucial role in determining the number of Cepheids in the CHeB phase. In Figure 7.5 I show selected tracks of a 4.2 $M_\odot$ star, with different rotation rates and with Z = 0.008. The chosen mass is the average mass of the stars in Table 7.1 excluding HV12199. The gray shaded area in the plot indicates the Cepheids instability strip, and it can be easily seen how the blue loops of the tracks cross only once or multiple times the strip, depending on the ω_i. From the comparison, I may already expect that the number of Cepheids belonging to initially slow rotating populations, with a turn-off mass and a metallicity similar to those selected for the plot, should be higher than the number of Cepheids that belong to an initially fast rotating population. This argument will be further discussed in Sec. 7.5.

In order to obtain finer grids of tracks to perform our analysis, the sets are interpolated in metallicity, mass, and ω_i. In Chapter 5 and references therein there are details on the method of interpolation. This method let us to obtain well-behaved isochrones. Figures 7.6 and 7.7 show an example

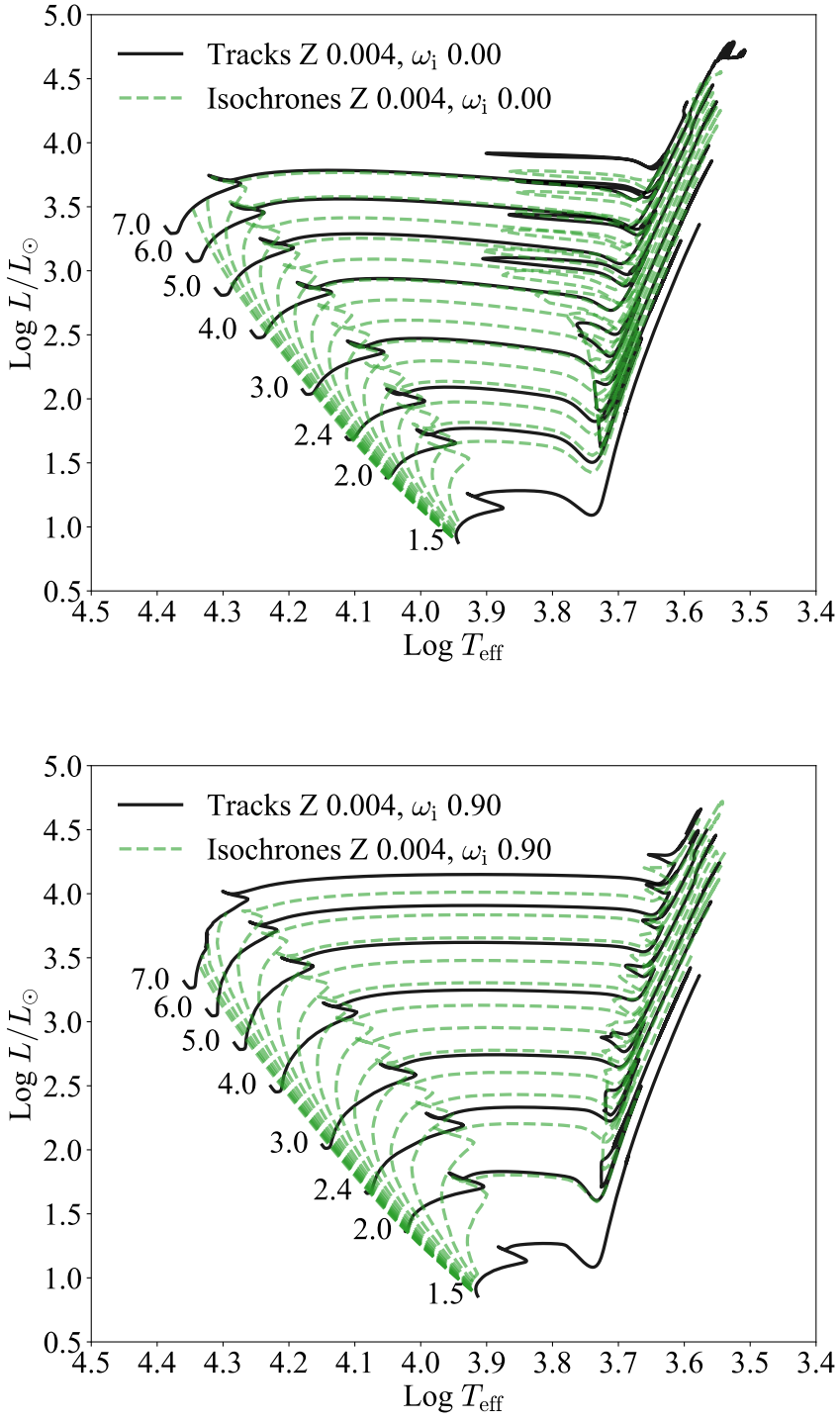

FIGURE 7.6: Selected evolutionary tracks (black solid lines) over-plotted with the correspondent isochrones (green dashed lines) used in this work. The top panel shows tracks with ω_i = 0.0, while the bottom panel with ω_i = 0.90. The tracks are computed with Z = 0.004. Tracks cover the mass range from 1.5 to 7 $M_\odot$. The isochrones are equally spaced in log t and cover the age range from 30 to 980 Myr.

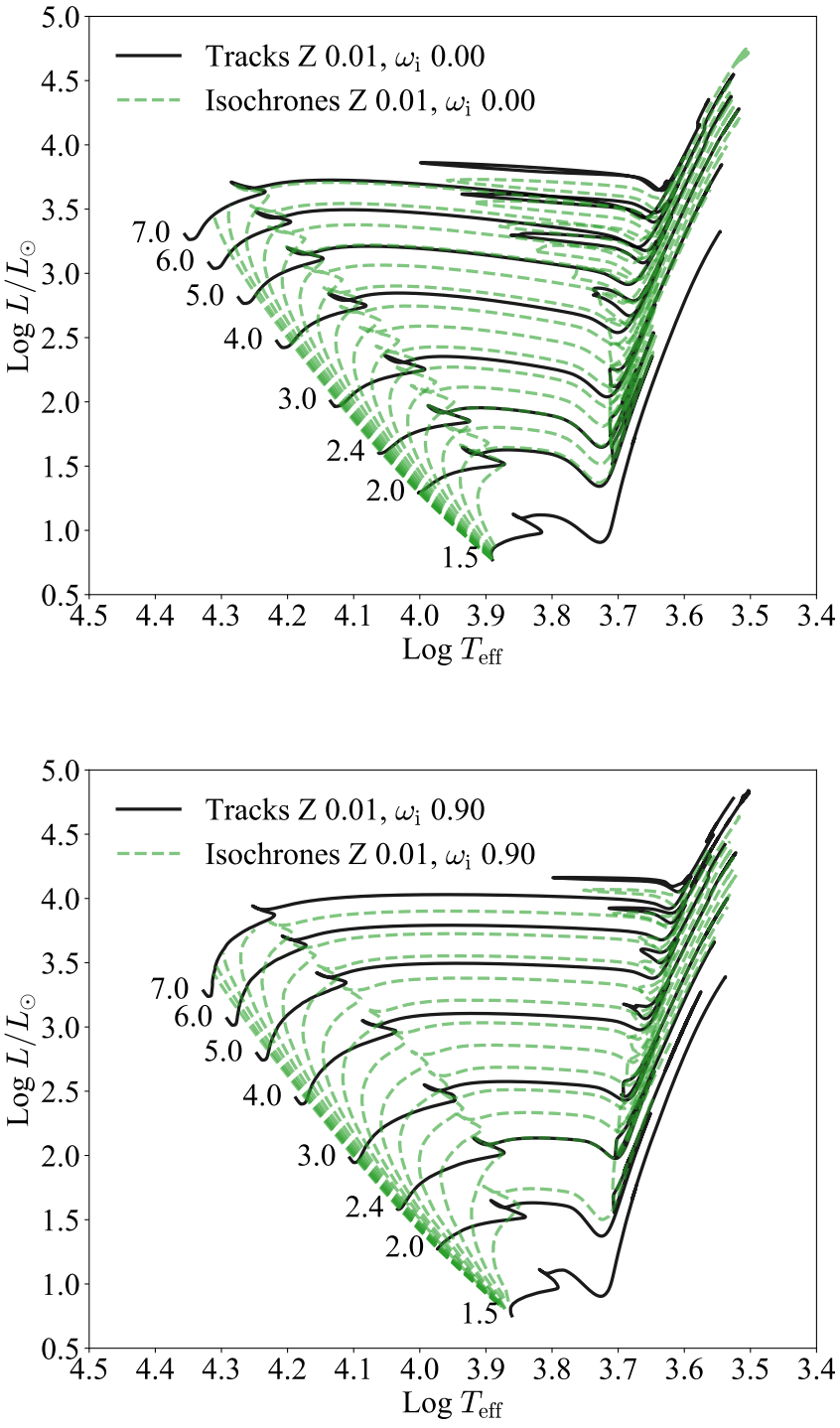

FIGURE 7.7: As in Figure 7.6 but with Z = 0.01.

of HR diagrams of four selected evolutionary tracks sets over-plotted with the correspondent isochrones selected in age. These sets of tracks are used as inputs for the Bayesian analysis.

7.3.3 Gravity Darkening and Color-Magnitude Diagram

As discussed before, rotation induces a distortion of the star shells, which become more and more oblate as the ω increases. At the critical velocity, Ω_c, the equatorial radius of the star is 1.5 times bigger than the polar one. This effect is due to centrifugal forces that reduce the effective gravity along the surface, depending on the co-latitude angle, θ (with $\theta = 0^\circ$ aligned with the rotation axis). Since the local effective temperature is proportional to the local effective gravity, the $T_{\rm eff}(\theta)$ of a rotating star is not constant along the surface. This effect is known as gravity darkening and was firstly described by von Zeipel (1924). It is discussed in detail in Chapter 3 and 6. Such dependence of the $T_{\rm eff}$ on the co-latitude, introduces a new variable in the computation of the total flux emitted by a star, i.e. the inclination angle, i, of the star rotation axis with respect to the observer line of sight.

To compute the isochrones in the HST/WFC3 photometric system I use the TRILEGAL code (L. Girardi, Groenewegen, et al., 2005; P. Marigo, L. Girardi, A. Bressan, et al., 2017), that has been recently updated as discussed in Chapter 6 and in the work by Y. Chen and L. A. . Girardi (submitted to A&A), to include the effects of the gravity darkening on rotating stars. The equations of Espinosa Lara and Rieutord (2011) are adopted to calculate the emitted flux depending on the current surface ω and inclination angle of the star. The new tables of bolometric corrections (BC) used by TRILEGAL, are part of the YBC database and interpolating routines by Y. Chen and L. A. . Girardi (submitted to A&A). An online version of the tool can be found at `http://stev.oapd.inaf.it/YBC/`. Figure 7.8 shows an example of selected isochrones with different initial angular velocity and with two different ages (100 Myr and 300 Myr). The plot shows the effect of the gravity darkening depending on different rotations. The most evident feature is the very different brightness and color shown by highly rotating stars in the turn off. If stars in a cluster do not have a preferred angle of inclination, but a distribution of various inclination, high rotating stars could populate such region of the HR diagram creating the eMSTO, which is a feature commonly observed in young to intermediate-age star clusters (Milone, Marino, D'Antona, Bedin, Piotto, et al., 2017). The possible alignment of stellar spins in a cluster (Corsaro et al., 2017) is still controversial (Mosser et al., 2018).

7.4 Results

7.4.1 Bayesian analysis

The results from the PARAM code are three dimensional (3D) JPDFs of age, ω_i and [Fe/H] for each Cepheid. The JPDFs are returned by our Bayesian analysis, that is performed adopting the value of σ of each parameter given in Table 7.1, for each star.

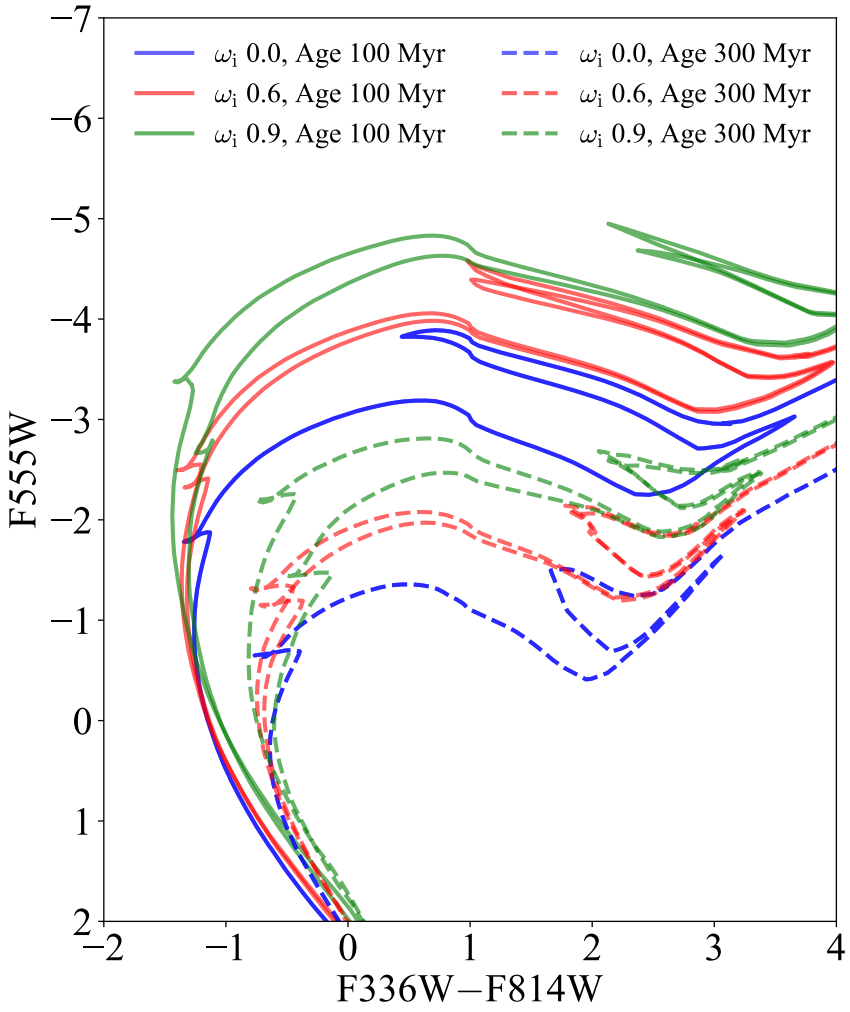

FIGURE 7.8: F555W versus F336W - F814W CMD, display of the effects of gravity darkening on isochrones with different combinations of rotation rates and ages. The solid lines are isochrones with the selected age of 100 Myr, while the dashed ones are with about 300 Myr. The blue, red, green lines correspond to ω_i = 0.00, 0.60 and 0.90, respectively. The metallicity is Z = 0.006 for all the isochrones. The cases for the inclination angles are two, pole on ($i = 0°$) and edge on (i = 90°), that are the brightest and faintest isochrones, respectively.

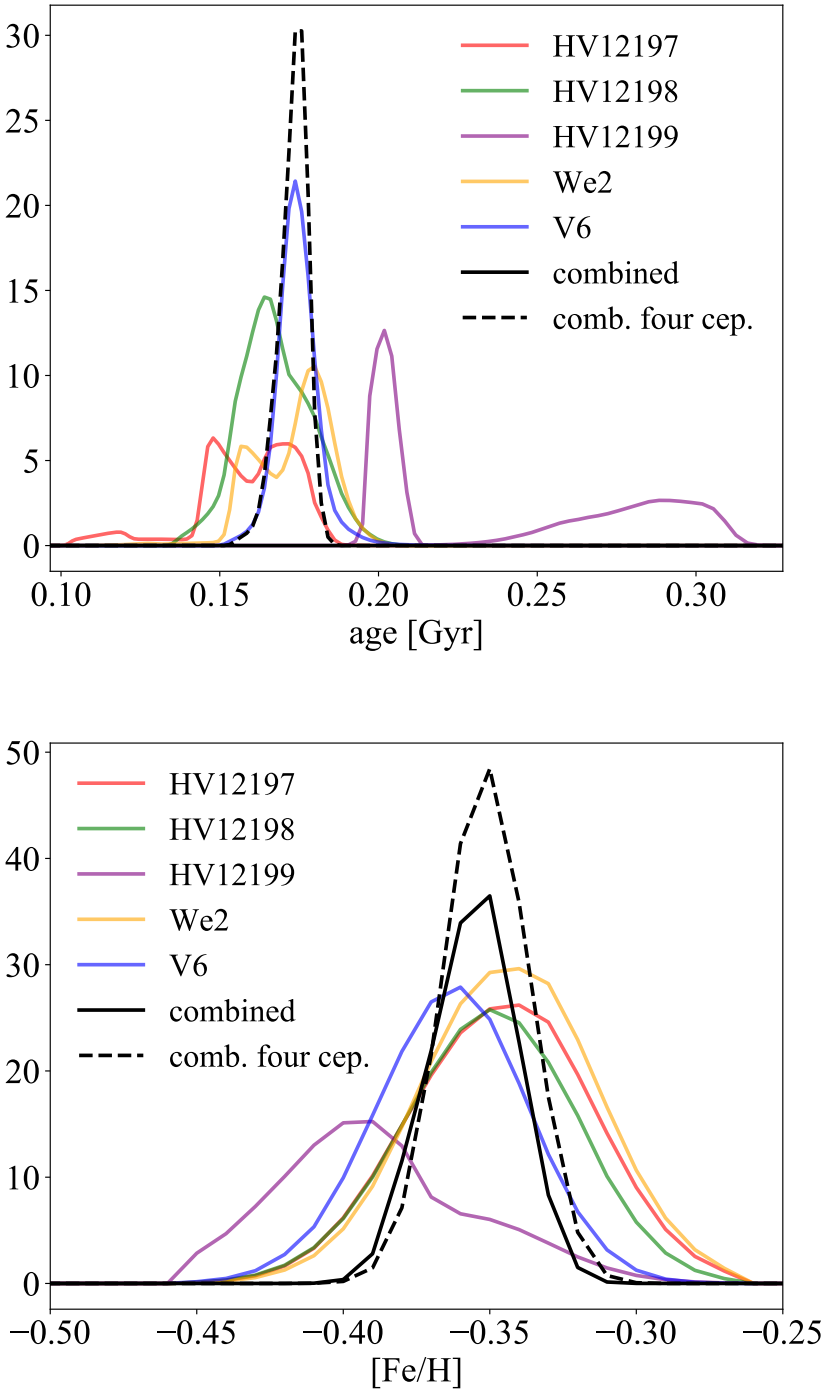

FIGURE 7.9: Marginalized JPDFs on age (top panel) and on metallicity (bottom panel) of each Cepheid. The solid black line is the combined PDF of all stars, while the dashed one is the CPDF of four stars (as described in the text).

Our first step is to check if the stars belong to the same population, hence I look at their metallicity and age marginalized 1D-PDFs. Figure 7.9 shows the 1D-PDFs of age and metallicity of the stars in the top and bottom panels, respectively. The PDFs show a good agreement in both age and metallicity distributions, with the only exception of the Cepheid HV12199. This star deviates from the trend of the others, and it seems to be older and metal poorer. Even more, I note that its 1D-PDF in age is clearly bimodal. As already anticipated (see Sec. 7.2), HV12199 is the less massive star in the sample by Marconi, Molinaro, et al. (2013), and it was found to be slightly more luminous than the luminosity predicted by the theoretical mass-luminosity relation (MLR) used as comparison in their work (see their Figure 10). They ascribed such over-luminosity to possible effects induced by mass loss. Assuming that all stars belong to the same population, i.e. same age and metallicity for all the stars, I may compute the combined PDFs (1D-CPDF) in age and metallicity with the product of the five 1D-PDFs. It is immediately apparent in the left-hand panel, that the combined distribution in the case of the age is flat and almost zero at all ages. In other words, there are no models that can fit at once HV12199 and the other four Cepheids. On the contrary if I exclude HV12199, the combined 1D-CPDF shows a well defined age peaking at 176 Myr, as can be seen from the left panel of Figure 7.9. These four stars, that are younger than the ages provided by the 1D-PDFs of HV12199, will be referred to in the followings as the young Cepheid population. As far as the metallicity is concerned, both the combined PDFs (computed with all the five stars, and the one computed excluding HV12199) peak at about $[\mathrm{Fe/H}] = -0.35$, indicating that the observed data are less sensitive to differences in the metal content. This preliminary analysis already suggests that the Cepheid HV12199 may belong to a different population.

I now marginalize the 3D-JPDFs with respect to the metallicity, in order to obtain the 2D-JPDFs on age and rotation. Then, I constrain the 2D-JPDFs of the young Cepheid population to follow their combined 4-star CPDF age distribution shown in the left panel of Figure 7.9. An example of the resulting 2D *corrected* JPDF of the Cepheid HV12198 is shown in the bottom-left panel of Figure 7.10. The coloured contours indicate arbitrarily chosen levels of the cJPDF, that are 50 per cent (the darker), 10 per cent (the intermediate) and 1 per cent (the lighter) of the maximum value of the cJPDF. The top-left and bottom-right panels show the 1D marginalized PDFs on ω_{i} and age, respectively. As suggested by T. S. Rodrigues et al. (2014b), I choose the peaks of the marginalized 1D PDFs (the mode, indicated by the dotted lines) as best values and I select the smallest interval around the mode that contains the 68 per cent of the distributions as the credible intervals (CIs, indicated by the shaded areas). The best value and the CIs are represented by the square and the black error bars in the 2D JPDF plot (the bottom-left panel). I remind that the selected best value is not the peak of the 2D JPDF, however this point is inside the chosen CIs in each distribution. The only difference between the age PDF shown in the bottom-right panel and the combined four stars age distribution shown in Figure 7.9, is that the first PDF has been obtained from the 2D *corrected* JPDF after the normalization to its maximum. Hence, while the absolute

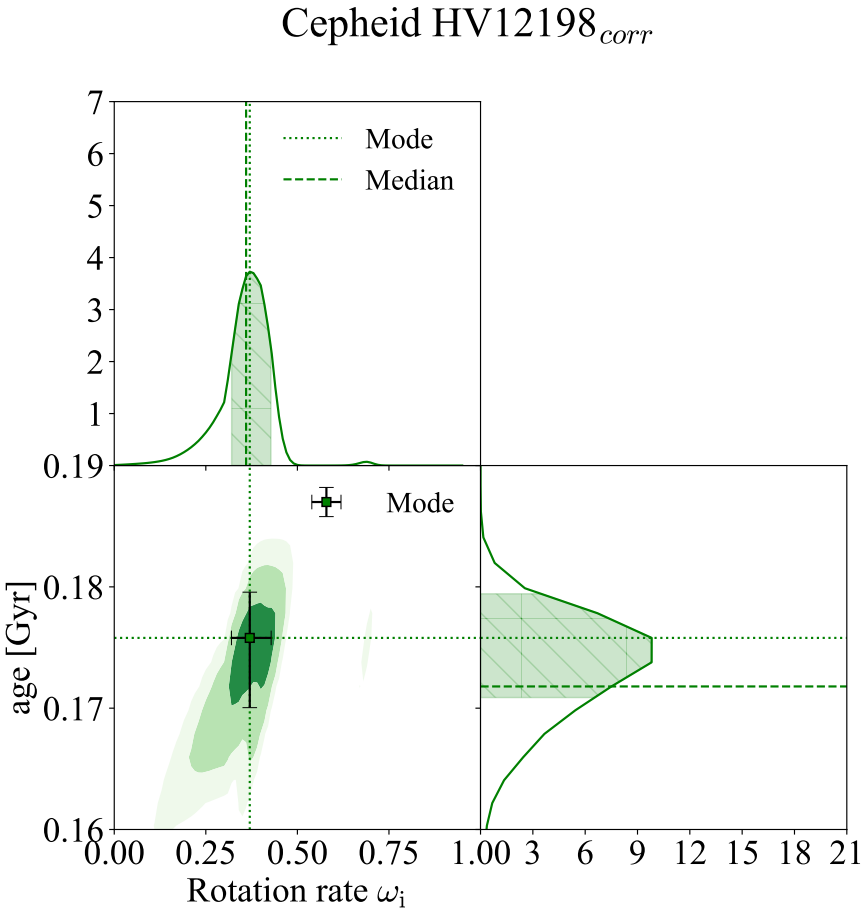

FIGURE 7.10: An example of selected 2D-cJPDF as a function of age and ω_i for the Cepheid HV12198. In the left-hand bottom panel is shown the JPDF, while in the left-hand upper and right-hand lower panels show the marginalized 1D-PDF of ω_i and age, respectively. The square and the error bars in the left-hand bottom panel indicate the mode and the CIs. The coloured contours indicate different levels of the JPDF as indicated in the text. The dashed and dotted lines are the mode and the median of the distributions. The shaded areas in the marginalized plots indicate the 68 per cent CI of the two PDFs.

TABLE 7.2: Resulting values of the initial angular rotation rates and the age for each Cepheid.

Cepheid Name	$\omega_{\rm i}$	Age [Myr]	[Fe/H]
HV12197	$0.00^{+0.24}_{-0.00}$	148^{+26}_{-3}	$-0.34^{+0.02}_{-0.04}$
HV12197$_{corr}$	$0.31^{+0.05}_{-0.16}$	176^{+4}_{-6}	$-0.35^{+0.01}_{-0.02}$
HV12198	$0.37^{+0.07}_{-0.20}$	164^{+14}_{-9}	$-0.35^{+0.03}_{-0.03}$
HV12198$_{corr}$	$0.37^{+0.06}_{-0.05}$	176^{+4}_{-6}	$-0.35^{+0.01}_{-0.02}$
We2	$0.00^{+0.24}_{-0.00}$	180^{+5}_{-19}	$-0.34^{+0.02}_{-0.04}$
We2$_{corr}$	$0.20^{+0.09}_{-0.12}$	176^{+4}_{-6}	$-0.35^{+0.01}_{-0.02}$
V6	$0.20^{+0.10}_{-0.10}$	174^{+6}_{-6}	$-0.36^{+0.02}_{-0.03}$
V6$_{corr}$	$0.18^{+0.11}_{-0.08}$	176^{+4}_{-6}	$-0.35^{+0.01}_{-0.02}$
HV12199$_{\rm CS-1}$	$0.13^{+0.03}_{-0.09}$	202^{+3}_{-5}	$-0.40^{+0.01}_{-0.03}$
HV12199$_{\rm CS-2}$	$0.89^{+0.06}_{-0.06}$	288^{+17}_{-23}	$-0.36^{+0.02}_{-0.04}$

values are different, the shape, the derived best value and the credible intervals of the two distributions are exactly the same.

Table 7.2 lists the resulting best values and the correspondent CIs for the selected Cepheid, both for the non-corrected and the corrected JPDFs (except for the star HV12199, that will be further discussed below). The common age of the four Cepheids obtained is 176^{+4}_{-6} Myr, and the common metallicity is [Fe/H] = $-0.35^{+0.01}_{-0.02}$. I remark that these four young Cepheids have slow initial rotation rates (even taking into account the CIs). Figures 7.11 and 7.12 show the comparison between the Cepheids data and selected isochrones in age, $\omega_{\rm i}$, metal content and mass (values and CIs listed in Table 7.2). Each panel shows the best fitting isochrone for the different stars, excluding HV12199, adopting the best value of [Fe/H] found in the analysis. The plot shows that the four Cepheids are all in the Core Helium Burning (CHeB) phase. It is worth noting that the obtained small rotation rates are also in agreement with the ability of the corresponding models to produce more extended blue loops that can reach and cross the instability strip, as discussed in Sec. 7.3.2 and illustrated in Figure 7.5.

As far as the star HV12199 is concerned, in Figure 7.13 I show the 2D-JPDF, obviously not constrained by a common age. The 2D distribution displays two well-detached regions (or classes) of solutions, which are analyzed separately. The first one (from now on CS-1) peaks at slow initial rotation rates with an age of about 200 Myr and metallicity of -0.40 dex ($Z \sim 0.006$). The second region, instead, is centered at high $\omega_{\rm i}$ and older ages ($\sim$290 Myr), with a metallicity of [Fe/H] = -0.36. I will refer to this solution as CS-2. The best values of the two classes and their correspondent CIs are shown in the lower section of Table 7.2. Both solutions give ages different from the common age found for the young Cepheid population, in particular, the second case ($\sim$ 290 Myr). As concern the metallicities, CS-1 peaks at a lower [Fe/H] with respect to the common metallic content, while CS-2 is in agreement within the CIs.

In Figure 7.14 I compare the location of HV12199 in the HR diagram with the isochrones corresponding to the two different classes of solutions. The left-hand panel shows the isochrones selected for the CS-1 case, while

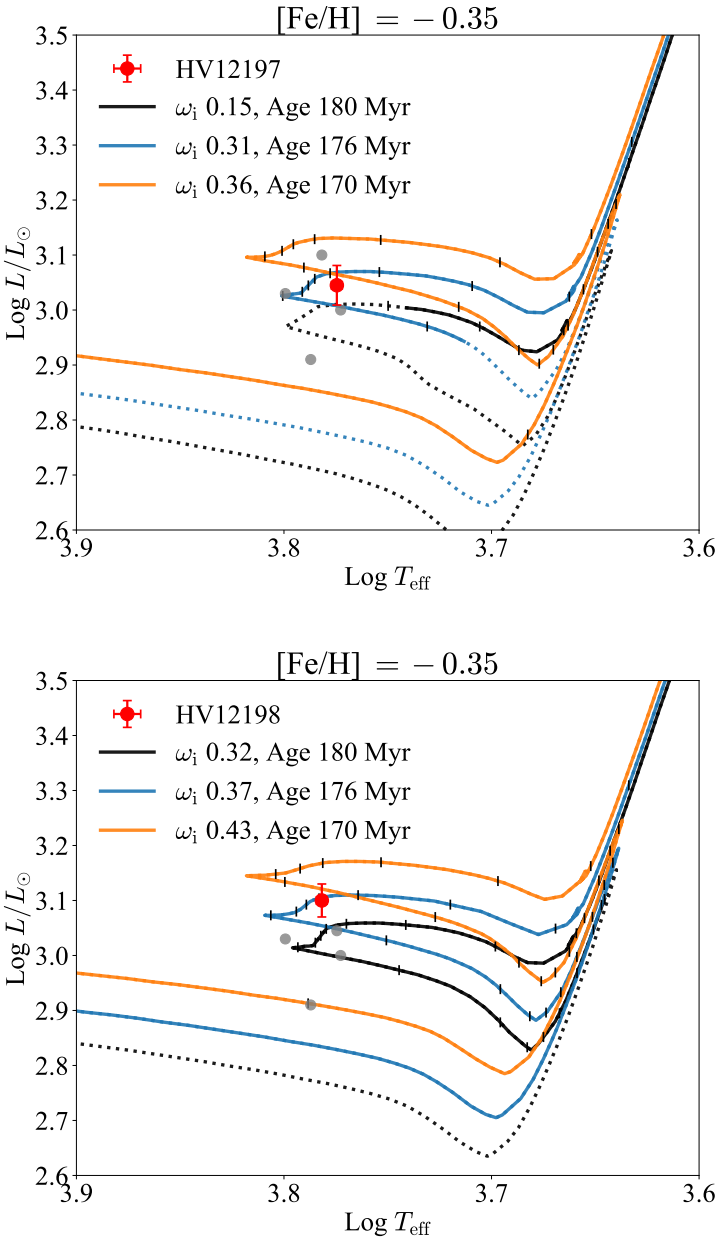

FIGURE 7.11: Comparison between the Cepheids (HV12197 and HV12198) data and isochrones selected from the best values obtained from the Bayesian analysis. In each panel the red point with the error bars is the selected Cepheid, while the gray points are the other stars. The error bars are plotted using 3 σ. The blue isochrone represents the best fitted values from the analysis, with age and ω_i indicated in Table 7.2. The black and orange lines are the most and less luminous isochrones within the CIs, respectively. The continuous lines indicate the mass within 3σ of the errors in Table 7.1, while the dotted lines indicate the part of isochrones with a mass that is outside the 3σ interval. To highlight the different evolutionary speed along isochrones, we plot black vertical markers at intervals of $\Delta M = 0.01\ M_\odot$.

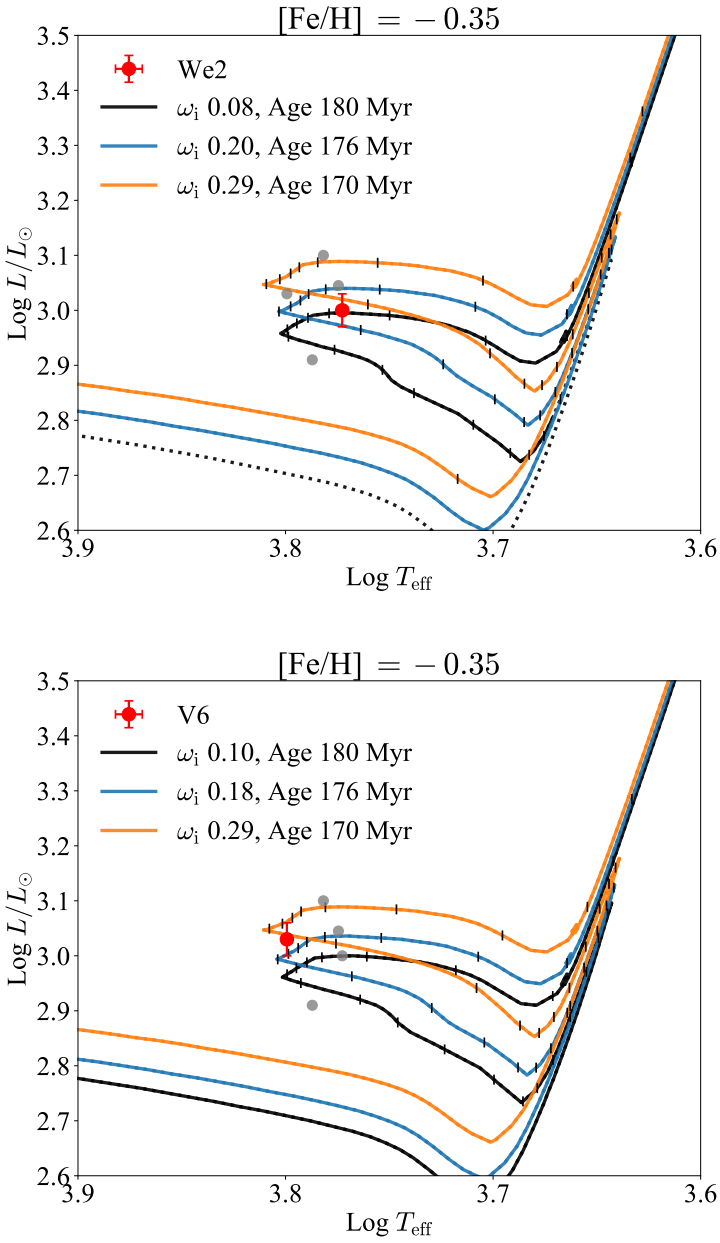

FIGURE 7.12: Same as in Figure 7.11, but for Cepheids We2 and V6.

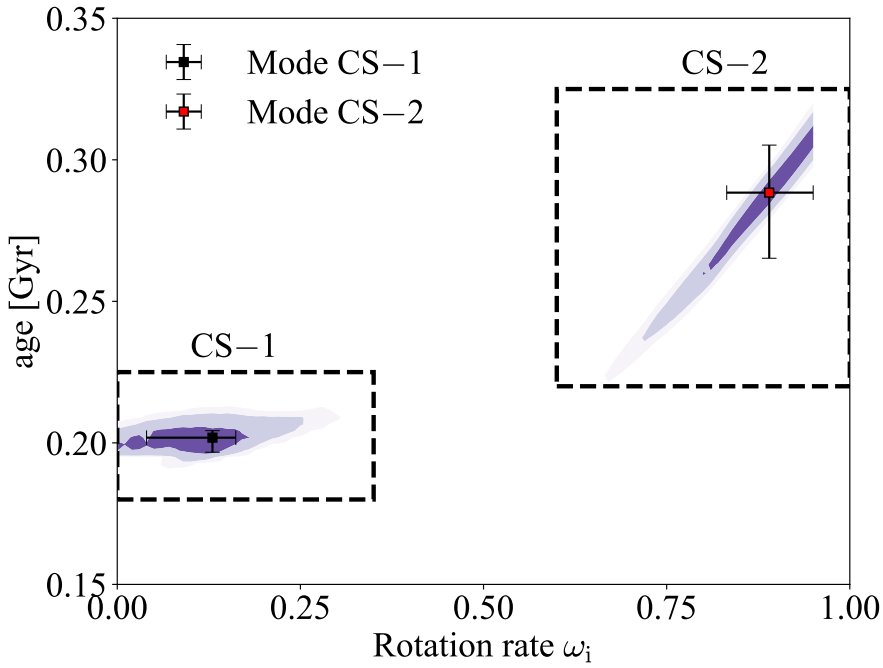

FIGURE 7.13: 2D-JPDF as a function of age and initial rotation rate for the Cepheid HV12199. The contours are coloured for different levels of the JPDF as in Figure 7.10. The squares and the error bars indicates the two mode values of the two classes of solutions.

the right-hand panel shows the isochrones selected for the CS-2 case. The isochrones are selected using the best value of [Fe/H] for each solution. In the CS-1 case HV12199 is in the CHeB phase while, the CS-2 case favours a position in the Hertzsprung Gap phase. Such analysis explains why in Figure 7.13, and in the left-hand panel of Figure 7.9, the second solution (CS-2, with higher ω_i, cluster metallicity and older ages) is less likely than the first one (CS-1, with lower ω_i, lower metallicity and younger ages). Indeed intermediate-mass stars spend the bulk of their post main sequence lifetime in the CHeB phase. The other advanced evolutionary phases are much shorter. In particular a 4 $M_\odot$ star spends only a few 10^5 years on the Hertzsprung Gap phase, which is about a factor ten shorter than the time spent on the CHeB phase. I note however that, in our Bayesian analysis we explore a parameter space of intervals of 3-σ for each value given in Table 7.1 and, if restrict the computation to only 1-σ around the observed values, the CS-1 solution disappears leaving only the CS-2 solution.

This said, I will keep both solutions and discuss now the fit of the CMD data.

7.4.2 Colour Magnitude Diagram

In this Section I analyze the observed CMD of NGC 1866 in the light of our previous results. In particular I compare isochrones with ages, metallicities and initial rotation rates derived from the analysis of the Cepheids

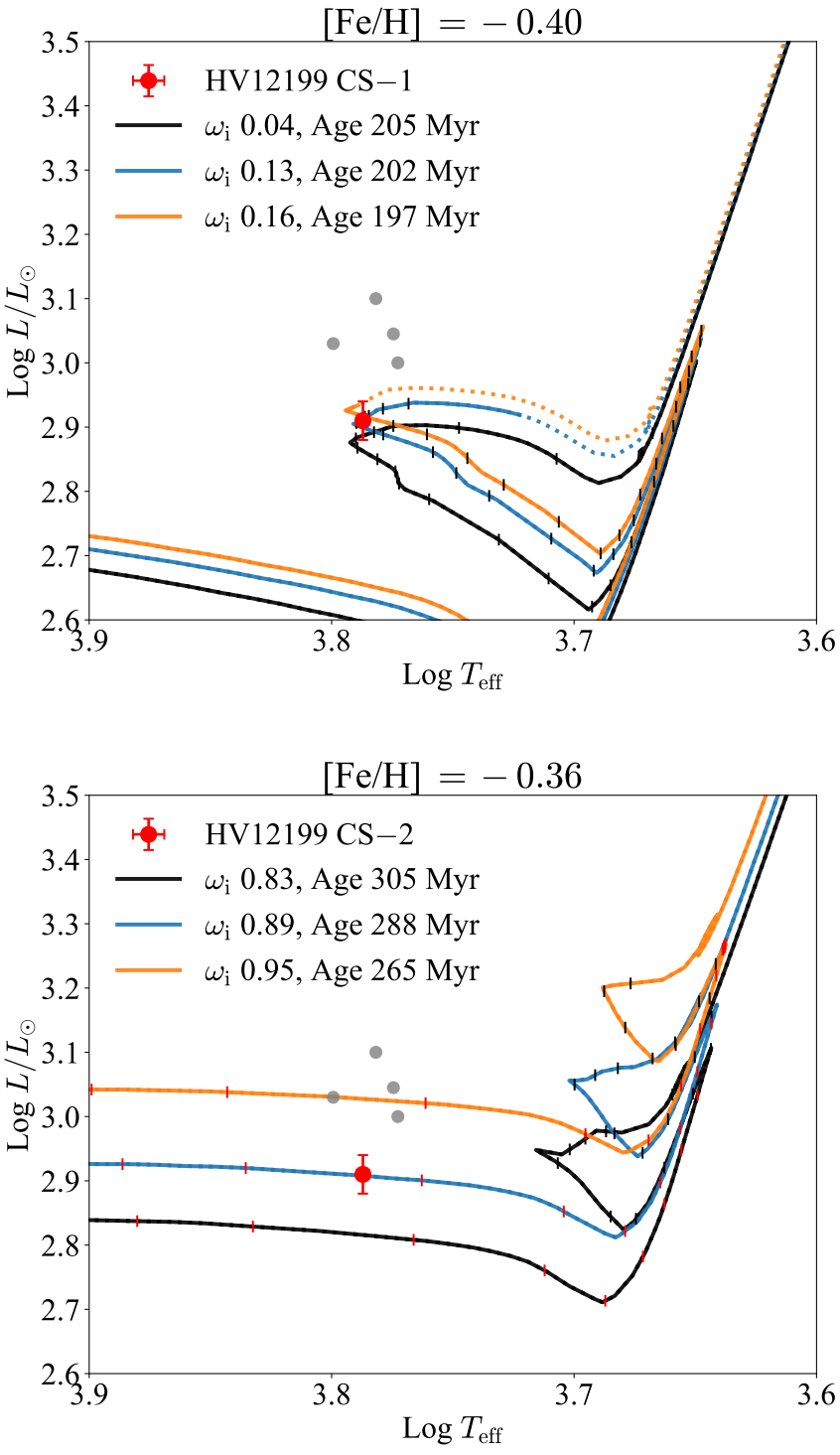

FIGURE 7.14: As in Figure 7.11. In the top panel there is the first class of solution (CS-1), with isochrones with slow initial rotation rates and ages around 202 Myr. The bottom panel shows the second class of solution (CS-2), with isochrones with high rotations and ages around 288 Myr. Values selected from Table 7.2. In the right-hand panel the red vertical markers in the Hertzsprung gap indicate intervals of ΔM = 0.0005 $M_\odot$.

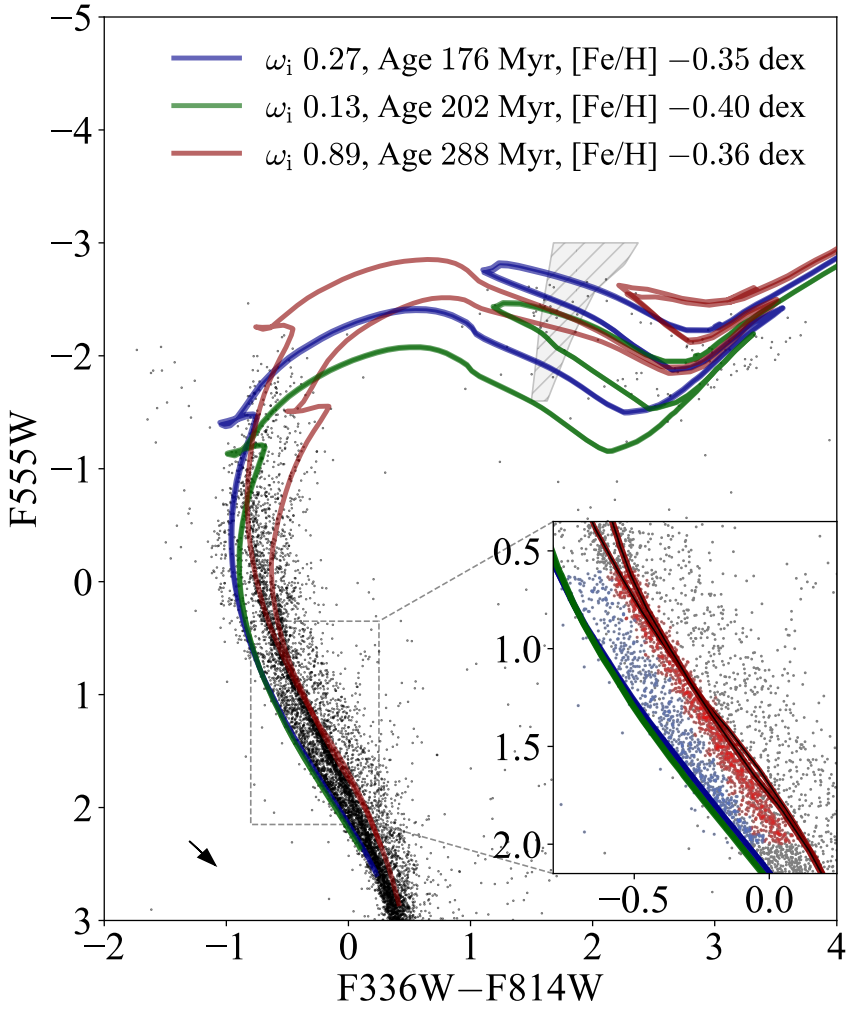

FIGURE 7.15: Comparison between the NGC 1866 cluster data and selected isochrones in the F555W versus F336W - F814W CMD. The data description is the same as in Figure 7.1. The blue isochrone is selected taking the best values found from the common age and metallicity of the four-star combined PDF. The green and red isochrones are the two solutions of HV12199, with low (CS-1) and high initial (CS-2) rotation rates, respectively. All the isochrones are plotted with the effect of gravity darkening. The inclination angles, *i*, of are 0° (pole on) and 90° (edge on) for the most and less bright isochrones, respectively. The shaded area indicates the Cepheids instability strip.

properties, with the CMD of the NGC 1866 cluster. I stress that our comparison is not the result of a best fit procedure to the observed data. Instead, I simply superimpose the selected isochrones to the data adopting distance and reddening as derived by an independent fit performed with PARSEC V1.2s in a previous paper, $(m - M)_0 = 18.43$ mag and $A_V = 0.28$ mag, (Goudfrooij et al., 2018). I use a young population of slowly rotating stars with age of 176 Myr and metallicity [Fe/H] = -0.35, corresponding to the young Cepheid population. The initial rotational velocity is the mean value determined for the four Cepheids, $\omega_{\rm i}$ = 0.27 (see Table 7.2). As for the Cepheid HV12199, I use isochrones corresponding to the CS-1 and CS-2 solutions. For the CS-1 solution I adopt $\omega_{\rm i}$ = 0.13, age of 202 Myr and metallicity [Fe/H] = -0.40. The CS-2 solution is represented by $\omega_{\rm i}$ = 0.89, age of 288 Myr and metallicity [Fe/H] = -0.36. In all cases the isochrone are plotted for two extreme values of the inclination angles, $i = 0°$, $i = 90°$. However, as shown in Figure 7.8, the effects of the gravity-darkening below a rotation rate of 0.6 are almost negligible, hence even though these effects are taken into account and plotted in Figure 7.15, they produce indistinguishable results in the slow rotating isochrones.

Figure 7.15 shows the comparison of the above selected isochrones with the observed data in the CMD of NGC 1866. As can be seen from the figure, the isochrones representing the young Cepheid population (176 Myr, [Fe/H] = -0.35, $i = 0°$, $i = 90°$, blue colour) nicely reproduces the bluest part of the MS. I also see that the bluest part of the MS may be well reproduced by the isochrone that corresponds to the CS-1 solution. I note that, as expected, the CS-1 isochrone does not reproduce the location of the other fours Cepheids simultaneously. The isochrone selected from the CS-2 solution reproduces very well the turn-off of the cluster and the red MS but, as it can be seen from the inset, the lower red MS is not reproduced perfectly.

In summary, I have shown in this Section that, using stellar populations with parameters determined by the Bayesian analysis of well-studied Cepheids in NGC 1866, I can nicely reproduce the main features of its CMD. Better fits could be likely achieved by using isochrones parameters that represent a range of $\omega_{\rm i}$ and/or [Fe/H] values selected within the entire CIs of the solution. This will be done in a future investigation together with full CMD simulations.

7.5 Discussion and Conclusions

In this Chapter, I analyze the evolutionary properties of five Cepheids in the young cluster NGC 1866 with extensively studied pulsational properties. A Bayesian analysis based on new grids of evolutionary tracks shows that it is very unlikely that all the five Cepheids belong to the same stellar population. The age distribution of HV12199 obtained with normal single star evolutionary models is clearly differentiated from that of the other four Cepheids. In order to bring HV12199 in agreement with the other four Cepheids it should have lost about 0.5-0.7 $M_{\odot}$. The mass lost is too large in the case of single stellar evolution, as shown by the other four stars. In the case of binary evolution, since the the external envelope

of a 4 $M_{\odot}$ is of about 3 $M_{\odot}$, the lost mass would require a fine tuning of the binary parameters. These considerations led us to the conclusion that the two group of Cepheids are representative of two different populations harbored by NGC 1866. I find that four Cepheids are likely descendant of a population of initially slow rotating stars (with $\omega_{\rm i} \leq 0.4$), an age of 176^{+4}_{-6} Myr and a [Fe/H] = $-\ 0.35^{+0.01}_{-0.02}$. Instead, for HV12199 I find that possible solutions are either a 202^{+3}_{-5} Myr old slowly rotating population with [Fe/H] = $-\ 0.40^{+0.01}_{-0.03}$, or a 288^{+17}_{-23} Myr old and initially fast rotating ($\omega_{\rm i} \sim 0.90$) population, with [Fe/H] = $-\ 0.36^{+0.02}_{-0.04}$, named CS-1 and CS-2, respectively.

The existence of such a range of ages for NGC 1866 Cepheids is not new. In fact, while Musella et al. (2016) favor a single population with an average age of 140 Myr, significant age differences have been already reported in literature. Lemasle et al. (2017), using the period-age relations of non-rotating (Bono et al., 2005) models find ages between 95 Myr and 115 Myr while, using rotating models (Anderson et al., 2016), find ages between 180 Myr to 250 Myr. This differences may be due to the various prescriptions adopted for the non-rotating models (in their case without the core overshooting), and for the rotating ones (they adopted a velocity of $\omega_{\rm i} = 0.5$). Interestingly I note that, the age found in their work for HV12198 (about 184 Myr) adopting $\omega_{\rm i} = 0.5$, is very close the common age (176^{+4}_{-6} Myr) I have adopted in this work for our four slowly rotating Cepheids.

Remarkably, the observed CMD has clear signatures of multiple stellar populations. The presence of at least two different stellar populations in NGC 1866 with different rotational properties has been already suggested e.g. by Milone, Marino, D'Antona, Bedin, Piotto, et al. (2017) and Goudfrooij et al. (2018), seen in Chapter 6, and corroborated even by direct spectroscopic observations of the stars in the eMSTO (Dupree et al., 2017). Here, I find that the isochrone corresponding to the slowly rotating young Cepheids population reproduces almost perfectly the blue main sequence of NGC 1866. The isochrone corresponding to the fast rotating population derived for HV12199 (CS-2) reproduces very well the observed red main sequence in the CMD. Near the cluster turn-off this sequence widens into a strip that is nicely fitted by taking into account the gravity darkening effects caused entirely by the relative inclination of the rotation axis with respect to the line of sight. The alternative case of a slow initial rotation for HV12199 (CS-1) corresponds to an isochrone which is almost superimposed to the blue sequence. I stress once again that the isochrones shown in Figure 7.15 are not best fits to observed sequences but simple plots of the best solutions found for the Cepheids.

A striking feature in the CMD of NGC 1866 is that the red main sequence becomes bluer than the model isochrone at decreasing luminosity. Since these stars are not significantly evolved the differences between non rotating and fast rotating models must originate from the geometrical effects alone. This could be an indication that these effects are not yet properly modelled or, on the contrary, that the initial rotational properties depend on the stellar mass (Goudfrooij et al., 2018).

Concerning the inclination angles of fast rotators in NGC 1866, I remind that, in a recent analysis of the two open clusters NGC 6791 and

NGC 6819, Corsaro et al. (2017) found a strong alignment between the cluster rotation axes and the stars rotation axes thus claiming that this could have been a general feature in star clusters. However this was not confirmed by more recent asteroseismic studies of the same clusters (performed by Mosser et al., 2018) where, instead, a stochastic dispersion of the stellar inclination angles has been found. I have seen in this work that the eMSTO of NGC 1866 is very well explained by different inclinations of the old fast rotating stars, in agreement with what found by Mosser et al. (2018).

The Bayesian analysis shows that, at maximum, only one over five Cepheid studied descends from initially fast rotating stars. It is interesting to see whether this is in contrast with the claim that about 2/3 of the MS stars in NGC 1866 are fast rotators with $\omega_{\rm i} = 0.90$ (Milone, Marino, D'Antona, Bedin, Piotto, et al., 2017). To this purpose I need to properly account for the evolutionary time spent by the stars within the instability strip. In fact, at turn-off masses typical of NGC 1866, evolutionary tracks with high initial rotations have much less extended blue loops and are not able to cross the Cepheids instability strip during central He-burning (see Figure 7.5). In this case the tracks cross the instability strip only during the Hertzsprung Gap in timescales that are much shorter than those of the CHeB phases, disfavouring the Cepheids phase. To better clarify this point I have quickly estimated the relative number of Cepheids expected from two stellar populations corresponding to the ones highlighted by our analysis. I use the two isochrones representative of the slow rotating young population (with a $\omega_{\rm i} = 0.27$ and with an age of 176 Myr) and of the the fast rotating old population (the CS-2 solution, with $\omega_{\rm i} = 0.89$ and 288 Myr). The number of stars in a the Cepheid phase can be expressed as

$$N \sim \sum_{j=1}^{K} \int_{\Delta M_J} \Phi(M_i)\ \delta M_i \tag{7.1}$$

where K is the number of times that the isochrone crosses the instability strip, ΔM_J is the interval of mass within the strip for each cross, $\Phi(M_i)$ is the initial mass function (IMF), and M_i is the initial stellar mass. Using a Salpeter (1955) IMF and taking into account that, following Milone, Marino, D'Antona, Bedin, Piotto, et al. (2017) the ratio between the two populations in the MS is 1/2, I find that the ratio between the fast initially rotating and the slow rotating Cepheids expected in NGC 1866 is $N_{\rm fast}/N_{\rm slow} \sim 1/20$, thus showing that initially non rotating Cepheids are by far more likely to be observed. Thus the paucity of initially fast rotating Cepheids with respect to the non rotating ones (1/5) I have found, is not in contrast with the results of Milone, Marino, D'Antona, Bedin, Piotto, et al. (2017), once proper accounting is done of the evolutionary time spent within the instability strip.

I have already anticipated that the distance modulus adopted in this work, obtained by a fitting procedure on more recent *HST* photometry of the cluster, is about 0.13 mag smaller than the one obtained by Marconi, Molinaro, et al. (2013). However, both distance modulus agree within their total errors, i.e. within the sum of the systematic and the statistic errors

provided. I remind that the errors adopted in our Bayesian analysis correspond to three times the statistic errors provided by Marconi, Molinaro, et al. (2013) for the structural parameters of the Cepheids and, from our analysis, I obtain ages that consistently fit the MS-split and eMSTO adopting the shorter distance modulus (see Fig. 7.15). It is also worth recalling that the mass difference between the Cepheid HV12199 and the others, is independent on the distance modulus obtained by Marconi, Molinaro, et al. (2013).

I stress here that in order to be fully consistent, the pulsational analysis should be performed using the same input physics adopted in our evolutionary models, which however is beyond the goal of this work. Anyway, to get a first order estimation of the possible effects due to the adoption of different models for the pulsational analysis, I make use of the period-mass-luminosity-effective temperature ($PMLT_{\rm eff}$) relation by C. Chiosi, Wood, and Capitanio (1993, their equation 4). By differentiating such relation and assuming that the uncertainties in the period and the $T_{\rm eff}$ are negligible (see Tables 1 and 2 of Marconi, Molinaro, et al., 2013), I obtain that $\frac{\delta \log M}{\delta \log L} \sim 1$. For example, a variation of the luminosity of say, the 10 per cent, due to different input physics such as a different adopted mixing scheme, different opacities, etc., should correspond to a mass estimation that differs of the same order. I also remind here that, in our Bayesian analysis I adopt an uncertainty on the observed quantities which is three times the standard deviation given by Marconi, Molinaro, et al. (2013).

As a final consideration I note that from a Bayesian analysis of Cepheids data based on a large grid of stellar models with varying initial masses, rotational velocities and metallicities, I are able to obtain the ages of the two main populations of NGC 1866 that clearly stand out in its CMD. The older population is composed of fast rotating stars while the younger population is made by slowly rotating stars. Their metallicity is almost identical. First of all this finding shows that, in agreement with Milone, Marino, D'Antona, Bedin, Piotto, et al. (2017) and Dupree et al. (2017), the observed properties of NGC 1866, and likely of similar clusters, results from a complex mixture of physical effects that include both rotation and age dispersion. A combination of these two effects seems to be a necessary ingredient to correctly interpret the clusters formation and evolution. Second, the characteristics of the main stellar populations suggest a well defined evolutionary scenario for the cluster. A first burst generated the older population that inherited the initial angular momentum from the progenitor clouds, and now hosts the biggest fraction of the initial global angular momentum content. After about 130 Myr another generation of stars forms out of the gas that has already lost memory of the initial angular momentum. The stars of this younger generation are thus mainly slow rotators. The metallicity remain almost unchanged as can be derived from the [Fe/H] content of the two populations. A similar scenario has been already suggested by Dupree et al. (2017), however with a significant difference in the age of the older population that in their case is of about 200 Myr instead of 290 Myr that I have found. It is also interesting to note that this scenario has similarities with the one suggested for the formation of multiple populations in old globular clusters by Decressin

et al. (2007) and Charbonnel et al. (2013). In short, these authors suggest that the anomalies presently observed in the low-mass stars of old GCs, result from the ejecta enriched in H-burning products, of a first generation of fast-rotating massive stars. Indeed, a similar population of fast-rotating massive stars could also have been present in NGC 1866, but what remains at the present age is just its related population of intermediate-mass stars, with ages clearly older than the non-rotating population. Such a first generation of fast-rotating stars, if confirmed in more clusters, could provide an interesting avenue for the interpretation of multiple populations as a whole, including the old globular clusters.

To improve our analysis a first step would be to enlarge the sample of well studied Cepheids in NGC 1866 possibly exploiting the full population of about 24 objects. Furthermore, given the age differences found by different authors for the stellar populations in NGC 1866, it should be also important to compare the different models and check whether these differences can be ascribed only to models or also to some different initial assumptions, e.g. the amount of convective overshooting, the efficiency of the rotational mixing or the possible presence of the magnetic braking.

At the same time it could be worthy to perform a full analysis of the CMD of this and other similar clusters in an attempt to better constrain the distributions of initial rotational velocities, stars spin alignments, ages, and metallicities in these clusters.

All those considerations call for further efforts from both the observational and the theoretical sides.

Chapter 8

Conclusion

In summary, my work has been developed in a few steps/parts. In the first one I implemented the main rotation effects into our 1D stellar evolutionary code PARSEC. With this new version of PARSEC I can follow the evolution of rotating stars with a range of masses from 1.5 $M_{\odot}$ to about 350 $M_{\odot}$, and with initial rotation rates up to $\omega_{\rm i} = 0.99$. In Chapter 3, I discussed how the geometrical distortion due to the centrifugal forces is included in the stellar structure equations and the stellar surface equations. In Chapter 4, I described how the transport of angular momentum and the extra mixing of the chemical elements induced by rotation are included in the code. The transport of momentum is solved adopting a fully-implicit diffusive scheme, and the diffusive coefficient is computed taking into account for the two main rotation instabilities, that is the meridional circulation and the shear friction instability. Another important effect included in the code is the mass loss enhancement. Since rotation lowers the surface gravity, the mass loss of a rotating star is higher with respect to its correspondent non rotating star. The efficiency of the rotation mixing is controlled trough two parameters, that has been calibrated using the results of Brott, de Mink, et al. (2011). Such calibration is a fundamental step since different combinations of the two parameters can significantly change the evolution of a rotating star with the same initial parameters, as shown in Section 4.5.

In Chapter 5, I investigated on double-line eclipsing binaries (DLEBs) that have been recently used to constrain the amount of central mixing as a function of stellar mass, with contrasting results. In this project, I reanalyzed the DLEB sample by Antonio Claret and Guillermo Torres (2018), using a Bayesian method and new PARSEC tracks that account for both convective core overshooting and rotational mixing. Using overshooting alone I obtained that, for masses larger than about 1.9 $M_{\odot}$, the distribution of the overshooting parameter, $\lambda_{\rm ov}$, has a wide dispersion between 0.3 and 0.8, with essentially no values below $\lambda_{\rm ov} = 0.3 - 0.4$. While the lower limit supports a mild convective overshooting efficiency, the large dispersion derived is difficult to explain in the framework of current models of that process, which leave little room for large randomness. I suggested that a simple interpretation of our results can be rotational mixing: different initial rotational velocities, in addition to a fixed amount of overshooting, could reproduce the high dispersion derived for intermediate-mass

stars. After a reanalysis of the data, I found a good agreement with models computed with a fixed overshooting parameter, $\lambda_{ov} = 0.4$, and initial rotational rates, ω, uniformly distributed in a wide range between 0 and 0.8 times the break-up value, at varying initial mass. I also found that our best-fitting models for the components of α Aurigae and TZ Fornacis, agree with their observed rotational velocities, thus providing independent support to our hypothesis. I concluded that a constant efficiency of overshooting in concurrence with a star-to-star variation in the rotational mixing might be crucial in the interpretation of such data.

In Chapter 6, I studied how the rotation changes the interpretation of colour-magnitude and colour-colour diagrams of young and intermediate-age star clusters in the Magellanic Clouds and in the Milky Way. Taking into account the geometrical distortion induced by rotation, that is the gravity darkening, we derived new tables of bolometric corrections as a function of $T_{\rm eff}$, $\log g$, [Fe/H], $\omega_{\rm i}$ and the inclination angle, i. These tables are then integrated into the TRILEGAL code, to compute isochrones and synthetic populations, in different photometric systems. We tried to interpret the photometry of the Large Magellanic Cloud star cluster NGC 1866. The small dispersion in the CCDs suggests that the fast rotators of the cluster either have $\omega_{\rm i} < 0.95$, or are all observed pole on. Such geometric colour-colour effects, although small, might be potentially detectable in the huge, high-quality photometric samples in the post-Gaia era, in addition to the evolutionary effects caused by rotation-induced mixing.

In Chapter 7, I studied the LMC star cluster NGC 1866 with a new approach. I combined statistical Bayesian analysis of a sample of well-studied Cepheids of the cluster, with the analysis of its CMD features. I computed new sets of rotating tracks up to $\omega_{\rm i} = 0.95$, with various metallic content, with a mass range from 1.5 $M_{\odot}$ to 7 $M_{\odot}$. From the Bayesian analysis, I found that four of the five Cepheids belong to an initially slowly rotating young population (of 176 ± 5 Myr), while the fifth one is significantly older, either 288 ± 20 Myr for models with high initial rotational velocity ($\omega_{\rm i} \sim 0.9$), or 202 ± 5 Myr for slowly rotating models. The complementary study of the CMD of the cluster, performed by the comparison with selected isochrones with ages, [Fe/H]and $\omega_{\rm i}$ obtained from the statistical analysis, ruled out the latter solution while strongly supported the presence of two distinct populations of $\sim$176 Myr and $\sim$288 Myr, respectively. Moreover, the observed multiple main sequences and the turn-offs indicate that the younger population is mainly made of slowly rotating stars, as is the case of the four younger Cepheids, while the older population is made mainly of initially fast-rotating stars, as is the case of the fifth Cepheid. This work not only reinforces the notion that some young clusters like NGC 1866 harbor multiple populations, but gives also hints that the first population, the older, may have inherited the angular momentum from the parent cloud while stars of the second one, the younger, do not.

Finally, my work opens different intriguing perspectives for future studies. In the following works, I will compute and release new sets of rotating tracks and isochrones. With these new grids and the methods developed in this Thesis, comprehensive studies of MCs and MW star clusters can be performed on large scale, to shed light and add new clues on

the not yet fully understood star cluster formation. Besides, further PARSEC extensions are in the to-do list for the study of different stellar phenomena. Some of these are:

1. the inclusion of the magnetic braking and the coupling of the stellar magnetic field with the stellar wind;

2. the implementation of the sedimentation (microscopic diffusion) in the new mixing scheme, to study rotating low and very low mass stars;

3. the adoption of a new method to model the pre-main sequence, that consists in starting from a star seed of $M_{\rm i} = 0.01\ M_{\odot}$and let it grow up to the desired $M_{\rm i}$ by accretion. This may give new clues on the interpretation of the bottom parts of star clusters CMDs;

4. the inclusion of the rotation in the horizontal branch is a fundamental step to compute the AGB phase of rotating low mass stars.

Appendix A

My contribution to other projects

In this appendix I briefly discuss the projects in which I was involved during my PhD, but that are not part of this Thesis.

A.1 YBC, a bolometric corrections database with variable extinction coefficients: an application to PARSEC isochrones

The description of this project is taken from Y. Chen and L. A. . Girardi (submitted to A&A). In the following a brief description is given.

The `ybc` database of stellar bolometric corrections (BCs) is available at `http://stev.oapd.inaf.it/YBC`. In the database it we homogenize widely used theoretical stellar spectral libraries and provide BCs for many popular photometric systems, including the Gaia filters. The database can be easily extended to additional photometric systems and stellar spectral libraries. The web interface allows users to transform their catalogue of theoretical stellar parameters into magnitudes and colours of selected filter sets. The BC tables can be downloaded or also be implemented into large simulation projects using the interpolation code provided with the database. We compute extinction coefficients on a star-by-star basis, hence taking into account the effects of spectral type and non-linearity dependency on the total extinction. BC tables for rotating stars and tables of limb-darkening coefficients are also provided.

My contribution to this project was principally devoted to test the new database. Moreover, I have used the `ybc` database to colour the new PARSEC rotating isochrones used in Chapter 5 and 6.

A.2 Merging black hole binaries with the SEVN code

The following description is extracted from Spera, Mapelli, Giacobbo, et al. (2019).

In this project we study the formation and evolution of black hole binaries (BHBs), because it is essential for the interpretation of current

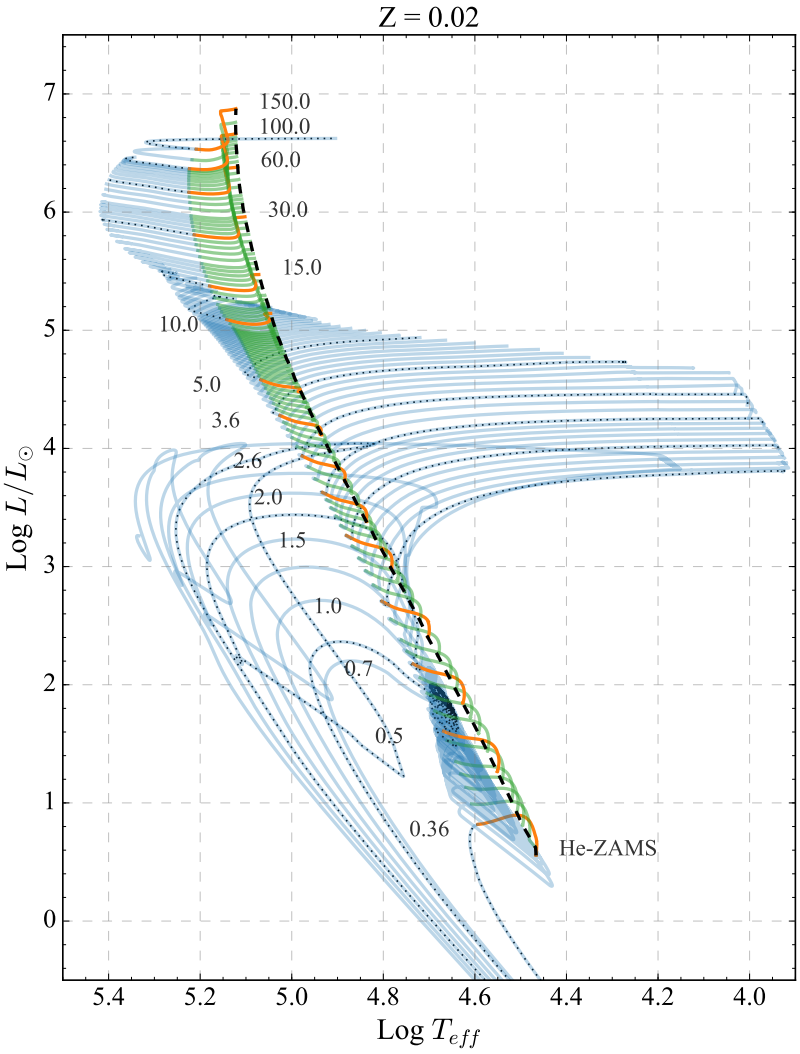

FIGURE A.1: Hertzsprung-Russell diagram of the pure He-star tracks until the end of Carbon burning. In orange and green there are the He-main sequences, in particular the orange correspond to the values of mass in the plot. While in blue the post He-MS.

and forthcoming gravitational wave (GW) detections. We investigate the statistics of BHBs that form from isolated binaries, by means of a new version of the SEVN population-synthesis code. SEVN integrates stellar evolution by interpolation over a grid of stellar evolution tracks. We upgraded SEVN to include binary stellar evolution processes and we used it to evolve a sample of 1.5×10^8 binary systems, with metallicity in the range $[10^{-4}; 4 \times 10^{-2}]$. From our simulations, we find that the mass distribution of black holes (BHs) in double compact-object binaries is remarkably similar to the one obtained considering only single stellar evolution. The maximum BH mass we obtain is ~ 30, 45, and 55 $M_\odot$ at metallicity $Z = 2 \times 10^{-2}$, 6×10^{-3}, and 10^{-4}, respectively. A few massive single BHs may also form (≤ 0.1 per cent of the total number of BHs), with mass up to $\sim$ 65, 90, and 145 $M_\odot$ at $Z = 2 \times 10^{-2}$, 6×10^{-3}, and 10^{-4}, respectively. These BHs fall in the mass gap predicted from pair-instability supernovae. We also show that the most massive BHBs are unlikely to merge within a Hubble time. In our simulations, merging BHs like GW151226 and GW170608, form at all metallicities, the high-mass systems (like GW150914, GW170814, and GW170104) originate from metal-poor ($Z \leq 6 \times 10^{-3}$) progenitors, whereas GW170729-like systems are hard to form, even at $Z = 10^{-4}$. The BHB merger rate in the local Universe obtained from our simulations is $\sim 90\ \mathrm{Gpc^{-3}yr^{-1}}$, consistent with the rate inferred from LIGO–Virgo data.

For this project I computed new sets of non-rotating PARSEC tracks of pure-Helium stars. These tracks are fundamental to follow the binary evolution of a star that loses all its Hydrogen-rich envelope. Figure A.1 shows a set of pure-Helium stars with an initial metallicity of 0.02. Further details on the pure-Helium stars models could be found in (Spera, Mapelli, Giacobbo, et al., 2019).

A.3 Mode classification in fast-rotating stars using a convolutional neural network

This project was developed in collaboration with Mirouh et al., and in the following it is briefly described.

Oscillation modes in fast rotating stars can be split into several subclasses, each with their own properties. To date, seismology of these stars cannot rely on regular pattern analysis and scaling relations. However, recently there has been the promising discovery of large separations observed in spectra of fast-rotating δ Scuti stars; they were attributed to the is land mode subclass, and linked to the stellar mean density through a scaling law. In this work, we investigate the relevance of this scaling relation by computing models of fast-rotating stars and their oscillation spectra. In order to sort the thousands of oscillation modes thus obtained, we train a convolutional neural network isolating the island modes with 96 per cent accuracy. Arguing that the observed large separation is systematically smaller than the asymptotic one, we retrieve the observational $\Delta\nu - \overline{\rho}$ scaling law. This relation will be used to drive forward modelling efforts, and is a first step towards mode identification and inversions for fast-rotating stars.

My contribution to this project was to compute the surface and volume of a model of a 2.5 $M_\odot$ star with different initial rotations, adopting the Roche approximation. Such result was then compared with the more detailed and consistent 2D stellar shape and volume computed with the ESTER code. We found that the Roche model underestimate the stellar volume by 1.6 per cent for low rotation rates and overestimate it up to about 6 per cent for $\omega = 0.9$.

A.4 The Minimum Mass of Rotating Main sequence Stars and its Impact on the Nature of Extended Main sequence Turnoffs in Intermediate age Star Clusters in the Magellanic Clouds

The description of this project is taken from Goudfrooij et al. (2018), and it is given in the following. Extended main-sequence turnoffs (eMSTOs) are a common feature in color–magnitude diagrams (CMDs) of young and intermediate-age star clusters in the Magellanic Clouds. The nature of eMSTOs is still debated. The most popular scenarios are extended star formation and ranges of stellar rotation rates. Here, we study implications of a kink feature in the main sequence (MS) of young star clusters in the Large Magellanic Cloud (LMC). This kink shows up very clearly in new Hubble Space Telescope observations of the 700 Myr old cluster NGC 1831 and is located below the region in the CMD where multiple or wide MSs, which are known to occur in young clusters and thought to be due to varying rotation rates, merge together into a single MS. The kink occurs at an initial stellar mass of $1.45 \pm 0.02\ M_\odot$; we posit that it represents a lower limit to the mass below which the effects of rotation on the energy output of stars are rendered negligible at the metallicity of these clusters. Evaluating the positions of stars with this initial mass in CMDs of massive LMC star clusters with ages of $\sim$1.7 Gyr that feature wide eMSTOs, we find that such stars are located in a region where the eMSTO is already significantly wider than the MS below it. This strongly suggests that stellar rotation cannot fully explain the wide extent of eMSTOs in massive intermediate-age clusters in the Magellanic Clouds. A distribution of stellar ages still seems necessary to explain the eMSTO phenomenon.

A.5 The Predicted Properties of Helium-Enriched Globular Cluster Progenitors at High Redshift

This is a work in preparation by Nataf et al., and it has been submitted in ApJ. A description is given in the following.

Globular cluster progenitors may have been detected by *HST*, and are likely to be observed soon by *JWST* and ground-based *ELT*'s with adaptive optics. This has the potential to elucidate the issue of globular cluster formation and the origins of significantly helium-enriched subpopulations, a problem in Galactic astronomy with no satisfactory theoretical solution. Given this context, we investigate the predicted observables of helium-enriched stellar populations in globular cluster progenitors. We

find that helium-enriched stellar populations similar to those seen in the most massive globular clusters ($\Delta Y = +0.14$), are expected to be 0.28 mag brighter in V, 0.23 mag redder in $(U - V)$, and 0.27 mag redder $(g - r)$ at age $\tau = 20$ Myr, fixed metallicity, and fixed stellar mass. For observations corresponding to wavelengths near $\lambda_0 = 1500$ Å, ignoring the helium enrichment could result in an overestimate of the metallicity corresponding to $\Delta \log(Z) \sim 0.40$ dex. The bolometric corrections for O-star atmospheres are predicted to be nearly insensitive to helium and CNONa abundance variations. The time-integrated increase in ionizing radiation is a negligible ~ 5 %, though we show that the Lyman-α escape fraction could end up higher for helium-enriched stars.

My contribution to this project was to compute tracks with Helium enriched tracks with the PARSEC v1.2. This set has been computed with three different initial Helium compositions Y = 0.26, 0.33 and 0.40, and with masses from 20 to 100 $M_{\odot}$. From this set I computed the correspondent isochrones, and I used the Vega magnitudes system to colour them.

A.6 Hydrodynamic modelling of accretion impacts in classical T Tauri stars: radiative heating of the pre-shock plasma

This work was mainly developed during my master Thesis, but it was completed and published during my first year of PhD. In the following there is a brief description taken from G. Costa et al. (2017).

It is generally accepted that, in Classical T Tauri Stars, the plasma from the circumstellar disc accretes onto the stellar surface with free fall velocity, and the impact generates a shock. The impact region is expected to contribute to emission in different spectral bands; many studies have confirmed that the X-rays arise from the post-shock plasma but, otherwise, there are no studies in the literature investigating the origin of the observed Ultra-Violet emission which is apparently correlated to accretion. We investigated the effect of radiative heating of the infalling material by the post-shock plasma at the base of the accretion stream with the aim to identify in which region a significant part of the UV emission originates. We developed a one dimensional hydrodynamic model describing the impact of an accretion stream onto the stellar surface; the model takes into account the gravity, the radiative cooling of an optically thin plasma, the thermal conduction, and the heating due to absorption of X-ray radiation. The latter term represents the heating of the infalling plasma due to the absorption of X-rays emitted from the post-shock region. We found that the radiative heating of the pre-shock plasma plays a non-negligible role in the accretion phenomenon. In particular, the dense and cold plasma of the pre-shock accretion column is gradually heated up to few 10^5 K due to irradiation of X-rays arising from the shocked plasma at the impact region. This heating mechanism does not affect significantly the dynamics of the post-shock plasma. On the other hand, a region of radiatively heated gas (that we consider a precursor) forms in the un-shocked accretion column and contributes significantly to UV emission. Our model naturally

reproduces the luminosity of UV emission lines correlated to accretion and shows that most of the UV emission originates from the precursor.

Bibliography

Abney, W. De W. (Mar. 1877). "effect of a star's rotation on its spectrum". In: *MNRAS* 37, pp. 278–279. DOI: 10.1093/mnras/37.5.278.

Anderson, R. I. et al. (June 2016). "On the effect of rotation on populations of classical Cepheids. II. Pulsation analysis for metallicities 0.014, 0.006, and 0.002". In: *A&A* 591, A8, A8. DOI: 10.1051/0004-6361/201528031. arXiv: 1604.05691 [astro-ph.SR].

Arnett, W. David et al. (Oct. 2018). "3D simulations and MLT: II. RA-ILES results". In: *arXiv e-prints*, arXiv:1810.04659, arXiv:1810.04659. arXiv: 1810.04659 [astro-ph.SR].

Aufdenberg, J. P. et al. (July 2006). "First Results from the CHARA Array. VII. Long-Baseline Interferometric Measurements of Vega Consistent with a Pole-On, Rapidly Rotating Star". In: *ApJ* 645, pp. 664–675. DOI: 10.1086/504149. eprint: astro-ph/0603327.

Barmina, R., L. Girardi, and C. Chiosi (Apr. 2002). "NGC 1866: A workbench for stellar evolution". In: *A&A* 385, pp. 847–861. DOI: 10.1051/0004-6361:20020197. arXiv: astro-ph/0202128 [astro-ph].

Bastian, N. et al. (Mar. 2017). "A high fraction of Be stars in young massive clusters: evidence for a large population of near-critically rotating stars". In: *MNRAS* 465.4, pp. 4795–4799. DOI: 10.1093/mnras/stw3042. arXiv: 1611.06705 [astro-ph.GA].

Bastian, Nate and Carmela Lardo (Sept. 2018). "Multiple Stellar Populations in Globular Clusters". In: *ARA&A* 56, pp. 83–136. DOI: 10.1146/annurev-astro-081817-051839. arXiv: 1712.01286 [astro-ph.SR].

Bertelli, G. et al. (June 2008). "Scaled solar tracks and isochrones in a large region of the Z-Y plane. I. From the ZAMS to the TP-AGB end for 0.15-2.5 $M_{\odot}$stars". In: *A&A* 484, pp. 815–830. DOI: 10.1051/0004-6361:20079165. arXiv: 0803.1460.

Bethe, H. A. (Mar. 1939). "Energy Production in Stars". In: *Physical Review* 55.5, pp. 434–456. DOI: 10.1103/PhysRev.55.434.

Böhm-Vitense, E. (1958). "{Ü}ber die Wasserstoffkonvektionszone in Sternen verschiedener Effektivtemperaturen und Leuchtkr{ä}fte. Mit 5 Textabbildungen". In: *ZAp* 46, p. 108. ISSN: 1098-6596. DOI: 10.1017/CBO9781107415324.004. arXiv: arXiv:1011.1669v3. URL: https://ui.adsabs.harvard.edu//?bbbRedirect=1%7B%5C#%7Dabs/1958ZA...46..108B/abstract.

Bono, G. et al. (Mar. 2005). "Classical Cepheid Pulsation Models. X. The Period-Age Relation". In: *ApJ* 621.2, pp. 966–977. DOI: 10.1086/427744. arXiv: astro-ph/0411756 [astro-ph].

Bossini, D. et al. (2017). "Kepler red-clump stars in the field and in open clusters: constraints on core mixing". In: *MNRAS* 469, pp. 4718–4725. DOI: 10.1093/mnras/stx1135. arXiv: 1705.03077.

Brandt, T. D. and C. X. Huang (July 2015a). "Bayesian Ages for Early-type Stars from Isochrones Including Rotation, and a Possible Old Age for the Hyades". In: *ApJ* 807, 58, p. 58. DOI: 10.1088/0004-637X/807/1/58. arXiv: 1501.04404 [astro-ph.SR].

— (July 2015b). "Rotating Stellar Models Can Account for the Extended Main-sequence Turnoffs in Intermediate-age Clusters". In: *ApJ* 807, 25, p. 25. DOI: 10.1088/0004-637X/807/1/25. arXiv: 1504.04375 [astro-ph.SR].

Bressan, A. G., C. Chiosi, and G. Bertelli (Sept. 1981). "Mass loss and overshooting in massive stars". In: *A&A* 102, pp. 25–30.

Bressan, A., G. Bertelli, and C. Chiosi (1986). "Evolution of low mass stars with convective overshooting". In: *Mem. Soc. Astron. Italiana* 57, pp. 411–426.

Bressan, A., P. Marigo, et al. (Nov. 2012). "PARSEC: stellar tracks and isochrones with the PAdova and TRieste Stellar Evolution Code". In: *MNRAS* 427, pp. 127–145. DOI: 10.1111/j.1365-2966.2012.21948.x. arXiv: 1208.4498 [astro-ph.SR].

Brocato, E., V. Castellani, and A. M. Piersimoni (Oct. 1994). "Core overshooting and the enigma of NGC 1866." In: *A&A* 290, pp. 59–61.

Brott, I., S. E. de Mink, et al. (June 2011). "Rotating massive main-sequence stars. I. Grids of evolutionary models and isochrones". In: *A&A* 530, A115, A115. DOI: 10.1051/0004-6361/201016113. arXiv: 1102.0530 [astro-ph.SR].

Brott, I., C. J. Evans, et al. (June 2011). "Rotating massive main-sequence stars. II. Simulating a population of LMC early B-type stars as a test of rotational mixing". In: *A&A* 530, A116, A116. DOI: 10.1051/0004-6361/201016114. arXiv: 1102.0766 [astro-ph.SR].

Caffau, E. et al. (Feb. 2011). "Solar Chemical Abundances Determined with a CO5BOLD 3D Model Atmosphere". In: *Sol. Phys.* 268.2, pp. 255–269. ISSN: 00380938. DOI: 10.1007/s11207-010-9541-4. arXiv: 1003.1190. URL: http://link.springer.com/10.1007/s11207-010-9541-4.

Castelli, F. and R. L. Kurucz (2003). "New Grids of ATLAS9 Model Atmospheres". In: IAU Symposium 210. Ed. by N. Piskunov, W. W. Weiss, and D. F. Gray, A20. eprint: astro-ph/0405087.

Charbonnel, Corinne et al. (Sept. 2013). "Why the globular cluster NGC 6752 contains no sodium-rich second-generation AGB stars". In: *Astronomy and Astrophysics* 557, L17, p. L17. DOI: 10.1051/0004-6361/201322422. arXiv: 1309.2073 [astro-ph.SR].

Chen, Y., A. Bressan, et al. (Sept. 2015). "PARSEC evolutionary tracks of massive stars up to 350 $M_\odot$ at metallicities $0.0001 \leq Z \leq 0.04$". In: *MNRAS* 452, pp. 1068–1080. DOI: 10.1093/mnras/stv1281. arXiv: 1506.01681 [astro-ph.SR].

Chen, Y. and L. A. ..... Girardi (submitted to A&A). In: *A&A*.

Chen, Y., L. Girardi, et al. (Nov. 2014). "Improving PARSEC models for very low mass stars". In: *MNRAS* 444, pp. 2525–2543. DOI: 10.1093/mnras/stu1605. arXiv: 1409.0322 [astro-ph.SR].

Chieffi, Alessandro and Marco Limongi (Feb. 2013). "Pre-supernova Evolution of Rotating Solar Metallicity Stars in the Mass Range 13-120 $M_\odot$

and their Explosive Yields". In: *ApJ* 764, 21, p. 21. DOI: 10.1088/0004-637X/764/1/21.

— (Feb. 2017). "The Synthesis of ^{44}Ti and ^{56}Ni in Massive Stars". In: *ApJ* 836, 79, p. 79. DOI: 10.3847/1538-4357/836/1/79. arXiv: 1701.02914 [astro-ph.HE].

Chiosi, C., P. R. Wood, and N. Capitanio (June 1993). "Theoretical Models of Cepheid Variables and Their BVI C Colors and Magnitudes". In: *ApJS* 86, p. 541. DOI: 10.1086/191790.

Choi, Jieun et al. (2016). "MESA ISOCHRONES AND STELLAR TRACKS (MIST). I. SOLAR-SCALED MODELS". In: *ApJ* 823.2, p. 102. ISSN: 1538-4357. DOI: 10.3847/0004-637X/823/2/102. arXiv: 1604.08592. URL: http://iopscience.iop.org/article/10.3847/0004-637X/823/2/102/pdf%20http://arxiv.org/abs/1604.08592%7B%5C%%7D5Cnhttp://dx.doi.org/10.3847/0004-637X/823/2/102%7B%5C%%7D5Cnhttp://stacks.iop.org/0004-637X/823/i=2/a=102?key=crossref.c8bcaff12d2e201377565c78953e3392.

Claret, A. (Apr. 2016). "Theoretical gravity darkening as a function of optical depth. A first approach to fast rotating stars". In: *A&A* 588, A15, A15. DOI: 10.1051/0004-6361/201527336. arXiv: 1606.00834 [astro-ph.SR].

Claret, A. and G. Torres (Nov. 2017). "The Dependence of Convective Core Overshooting on Stellar Mass: A Semi-empirical Determination Using the Diffusive Approach with Two Different Element Mixtures". In: *ApJ* 849, 18, p. 18. DOI: 10.3847/1538-4357/aa8770. arXiv: 1710.08417 [astro-ph.SR].

Claret, Antonio and Guillermo Torres (June 2018). "The Dependence of Convective Core Overshooting on Stellar Mass: Additional Binary Systems and Improved Calibration". In: *ApJ* 859, 100, p. 100. DOI: 10.3847/1538-4357/aabd35. arXiv: 1804.03148 [astro-ph.SR].

Collins II, G. W. and G. H. Sonneborn (May 1977). "Some effects of rotation on the spectra of upper-main-sequence stars." In: *ApJS* 34, pp. 41–94. DOI: 10.1086/190443.

Constantino, Thomas and Isabelle Baraffe (Oct. 2018). "Significant uncertainties from calibrating overshooting with eclipsing binary systems". In: *A&A* 618, A177, A177. DOI: 10.1051/0004-6361/201833568. arXiv: 1808.03523 [astro-ph.SR].

Cordoni, G. et al. (Dec. 2018). "Extended Main-sequence Turnoff as a Common Feature of Milky Way Open Clusters". In: *ApJ* 869, 139, p. 139. DOI: 10.3847/1538-4357/aaedc1. arXiv: 1811.01192 [astro-ph.SR].

Correnti, M. et al. (May 2017). "Dissecting the extended main-sequence turn-off of the young star cluster NGC 1850". In: *MNRAS* 467, pp. 3628–3641. DOI: 10.1093/mnras/stx010. arXiv: 1612.08746 [astro-ph.SR].

Correnti, Matteo et al. (July 2015). "New constraints on the star formation history of the star cluster NGC 1856". In: *MNRAS* 450.3, pp. 3054–3068. DOI: 10.1093/mnras/stv874. arXiv: 1504.03299 [astro-ph.SR].

Corsaro, Enrico et al. (2017). "Spin alignment of stars in old open clusters". In: *Nat. Astron.* 1.March, pp. 1–6. ISSN: 23973366. DOI: 10.1038/s41550-017-0064. arXiv: 1703.05588. URL: http://dx.doi.org/10.1038/s41550-017-0064.

Costa et al., ... (in prep.). In:

Costa, G. et al. (Jan. 2017). "Hydrodynamic modelling of accretion impacts in classical T Tauri stars: radiative heating of the pre-shock plasma". In: *A&A* 597, A1, A1. DOI: 10.1051/0004-6361/201628554. arXiv: 1609.01059 [astro-ph.SR].

Costa, Guglielmo, Léo Girardi, Alessandro Bressan, Yang Chen, et al. (Sept. 2019). "Multiple stellar populations in NGC 1866. New clues from Cepheids and Colour-Magnitude Diagram". In: *arXiv e-prints*, arXiv:1909.01907, arXiv:1909.01907. arXiv: 1909.01907 [astro-ph.SR].

Costa, Guglielmo, Léo Girardi, Alessandro Bressan, Paola Marigo, et al. (June 2019). "Mixing by overshooting and rotation in intermediate-mass stars". In: *MNRAS* 485.4, pp. 4641–4657. DOI: 10.1093/mnras/stz728. arXiv: 1903.04368 [astro-ph.SR].

Cyburt, Richard H. et al. (July 2010). "The JINA REACLIB Database: Its Recent Updates and Impact on Type-I X-ray Bursts". In: *ApJS* 189.1, pp. 240–252. DOI: 10.1088/0067-0049/189/1/240.

D'Antona, F. et al. (Nov. 2015). "The extended main-sequence turn-off cluster NGC 1856: rotational evolution in a coeval stellar ensemble". In: *MNRAS* 453.3, pp. 2637–2643. DOI: 10.1093/mnras/stv1794. arXiv: 1508.01932 [astro-ph.SR].

da Silva, L. et al. (Nov. 2006a). "Basic physical parameters of a selected sample of evolved stars". In: *A&A* 458, pp. 609–623. DOI: 10.1051/0004-6361:20065105. eprint: astro-ph/0608160.

— (Nov. 2006b). "Basic physical parameters of a selected sample of evolved stars". In: *A&A* 458, pp. 609–623. DOI: 10.1051/0004-6361:20065105. eprint: astro-ph/0608160.

de Jager, C., H. Nieuwenhuijzen, and K. A. van der Hucht (Feb. 1988). "Mass loss rates in the Hertzsprung-Russell diagram". In: *A&AS* 72, pp. 259–289.

Decressin, T. et al. (Mar. 2007). "Fast rotating massive stars and the origin of the abundance patterns in galactic globular clusters". In: *Astronomy and Astrophysics* 464.3, pp. 1029–1044. DOI: 10.1051/0004-6361:20066013. arXiv: astro-ph/0611379 [astro-ph].

Demarque, Pierre et al. (Dec. 2004). "Y² Isochrones with an Improved Core Overshoot Treatment". In: *ApJS* 155, pp. 667–674. DOI: 10.1086/424966.

Dewitt, H. E., H. C. Graboske, and M. S. Cooper (Apr. 1973). "Screening Factors for Nuclear Reactions. I. General Theory". In: *ApJ* 181, pp. 439–456. DOI: 10.1086/152061.

Domiciano de Souza, A. et al. (Sept. 2014). "The environment of the fast rotating star Achernar. III. Photospheric parameters revealed by the VLTI". In: *A&A* 569, A10, A10. DOI: 10.1051/0004-6361/201424144.

Dupree, A. K. et al. (2017). "NGC 1866: First Spectroscopic Detection of Fast Rotating Stars in a Young LMC Cluster". In: *Astrophys. J. Lett.* 846.1, p. L1. ISSN: 20418213. DOI: 10.3847/2041-8213/aa85dd. arXiv: 1708.03386. URL: http://arxiv.org/abs/1708.03386%7B%5C%%7D0Ahttp://dx.doi.org/10.3847/2041-8213/aa85dd.

Eddington, A. S. (Nov. 1929). "Internal circulation in rotating stars". In: *MNRAS* 90, p. 54. DOI: 10.1093/mnras/90.1.54.

Eggenberger, P. et al. (Aug. 2008). "The Geneva stellar evolution code". In: *Ap&SS* 316, pp. 43–54. DOI: 10.1007/s10509-007-9511-y.

Ekström, S., C. Georgy, et al. (Jan. 2012). "Grids of stellar models with rotation I. Models from 0.8 to 120 M at solar metallicity (Z = 0.014)". In: *A&A* 537, A146. ISSN: 0004-6361. DOI: 10.1051/0004-6361/201117751. arXiv: 1110.5049. URL: http://www.aanda.org/10.1051/0004-6361/201322178%20http://www.aanda.org/10.1051/0004-6361/201117751.

Ekström, S., G. Meynet, et al. (Feb. 2008). "Evolution towards the critical limit and the origin of Be stars". In: *A&A* 478.2, pp. 467–485. DOI: 10.1051/0004-6361:20078095. arXiv: 0711.1735 [astro-ph].

Emden, R. (Jan. 1902). "Contributions to the Solar Theory". In: *ApJ* 15, p. 38. DOI: 10.1086/140885.

Endal, A. S. and S. Sofia (Nov. 1976). "The evolution of rotating stars. I. Method and exploratory calculations for a 7 M sun star." In: *ApJ* 210, pp. 184–198. DOI: 10.1086/154817.

Espinosa Lara, F. and M. Rieutord (Sept. 2011). "Gravity darkening in rotating stars". In: *A&A* 533, A43, A43. DOI: 10.1051/0004-6361/201117252. arXiv: 1109.3038 [astro-ph.SR].

— (Apr. 2013). "Self-consistent 2D models of fast-rotating early-type stars". In: *A&A* 552, A35, A35. DOI: 10.1051/0004-6361/201220844. arXiv: 1212.0778 [astro-ph.SR].

Frémat, Y. et al. (Sept. 2005). "Effects of gravitational darkening on the determination of fundamental parameters in fast-rotating B-type stars". In: *A&A* 440, pp. 305–320. DOI: 10.1051/0004-6361:20042229. eprint: astro-ph/0503381.

Freytag, B., H. -G. Ludwig, and M. Steffen (Sept. 1996). "Hydrodynamical models of stellar convection. The role of overshoot in DA white dwarfs, A-type stars, and the Sun." In: *A&A* 313, pp. 497–516.

Fu, Xiaoting et al. (2018). "New PARSEC database of alpha-enhanced stellar evolutionary tracks and isochrones I. Calibration with 47 Tuc (NGC104) and the improvement on RGB bump". In: *MNRAS* 16.January, pp. 1–16. DOI: 10.1093/mnras/sty235/4828398. arXiv: 1801.07137.

Gaia Collaboration et al. (Aug. 2018). "Gaia Data Release 2. Observational Hertzsprung-Russell diagrams". In: *Astronomy and Astrophysics* 616, A10, A10. DOI: 10.1051/0004-6361/201832843. arXiv: 1804.09378 [astro-ph.SR].

Gallenne, A. et al. (2016). "The Araucaria Project: High-precision orbital parallax and masses of the eclipsing binary TZ Fornacis". In: *A&A* 586, pp. 1–8. ISSN: 14320746 00046361. DOI: 10.1051/0004-6361/201526764.

Gallet, F. and P. Delorme (June 2019). "Star-planet tidal interaction and the limits of gyrochronology". In: *A&A* 626, A120, A120. DOI: 10.1051/0004-6361/201834898. arXiv: 1905.06070 [astro-ph.EP].

Georgy, C., S. Ekström, et al. (Oct. 2013). "Grids of stellar models with rotation. III. Models from 0.8 to 120 $M_{\odot}$ at a metallicity Z = 0.002". In: *A&A* 558, A103, A103. DOI: 10.1051/0004-6361/201322178. arXiv: 1308.2914 [astro-ph.SR].

Georgy, C., A. Granada, et al. (June 2014). "Populations of rotating stars. III. SYCLIST, the new Geneva population synthesis code". In: *A&A* 566, A21, A21. DOI: 10.1051/0004-6361/201423881. arXiv: 1404.6952 [astro-ph.SR].

Georgy, C., G. Meynet, and A. Maeder (Mar. 2011). "Effects of anisotropic winds on massive star evolution". In: *A&A* 527, A52, A52. DOI: 10.1051/0004-6361/200913797. arXiv: 1011.6581 [astro-ph.SR].

Girardi, L., G. Bertelli, et al. (Aug. 2002). "Theoretical isochrones in several photometric systems. I. Johnson-Cousins-Glass, HST/WFPC2, HST/NICMOS, Washington, and ESO Imaging Survey filter sets". In: *A&A* 391, pp. 195–212. DOI: 10.1051/0004-6361:20020612. eprint: astro-ph/0205080.

Girardi, L., J. Dalcanton, et al. (May 2008). "Revised Bolometric Corrections and Interstellar Extinction Coefficients for the ACS and WFPC2 Photometric Systems". In: *PASP* 120, p. 583. DOI: 10.1086/588526. arXiv: 0804.0498.

Girardi, L., M. A. T. Groenewegen, et al. (June 2005). "Star counts in the Galaxy. Simulating from very deep to very shallow photometric surveys with the TRILEGAL code". In: *A&A* 436, pp. 895–915. DOI: 10.1051/0004-6361:20042352. eprint: astro-ph/0504047.

Girardi, Léo et al. (July 2019). "On the photometric signature of fast rotators". In: *arXiv e-prints*, arXiv:1907.00688, arXiv:1907.00688. arXiv: 1907.00688 [astro-ph.SR].

Gossage, Seth et al. (Aug. 2018). "Age Determinations of the Hyades, Praesepe, and Pleiades via MESA Models with Rotation". In: *ApJ* 863.1, 67, p. 67. DOI: 10.3847/1538-4357/aad0a0. arXiv: 1804.06441 [astro-ph.SR].

Goudfrooij, P. et al. (Sept. 2018). "The Minimum Mass of Rotating Main-sequence Stars and its Impact on the Nature of Extended Main-sequence Turnoffs in Intermediate-age Star Clusters in the Magellanic Clouds". In: *ApJ* 864, L3, p. L3. DOI: 10.3847/2041-8213/aada0f. arXiv: 1807.04737 [astro-ph.SR].

Graboske, H. C. et al. (Apr. 1973). "Screening Factors for Nuclear Reactions. II. Intermediate Screening and Astrophysical Applications". In: *ApJ* 181, pp. 457–474. DOI: 10.1086/152062.

Haffner, Hans and Otto Heckmann (Jan. 1937). "Das Farben-Helligkeits-Diagramm der Praesepe auf Grund neuer Beobachtungen". In: *Veroeffentlichungen der Universitaets-Sternwarte zu Goettingen* 0004, pp. 77–95.

Heger, A. and N. Langer (Dec. 2000). "Presupernova Evolution of Rotating Massive Stars. II. Evolution of the Surface Properties". In: *ApJ* 544, pp. 1016–1035. DOI: 10.1086/317239. arXiv: astro-ph/0005110 [astro-ph].

Heger, A., N. Langer, and S. E. Woosley (Jan. 2000). "Presupernova Evolution of Rotating Massive Stars. I. Numerical Method and Evolution of the Internal Stellar Structure". In: *ApJ* 528, pp. 368–396. DOI: 10.1086/308158. arXiv: astro-ph/9904132 [astro-ph].

Henyey, L. G., J. E. Forbes, and N. L. Gould (Jan. 1964). "A New Method of Automatic Computation of Stellar Evolution." In: *ApJ* 139, p. 306. DOI: 10.1086/147754.

Henyey, L. G., L. Wilets, et al. (May 1959). "A Method for Automatic Computation of Stellar Evolution." In: *ApJ* 129, p. 628. DOI: 10.1086/146661.

Hertzsprung, Ejnar (Jan. 1911). "Ueber die Verwendung photographischer effektiver Wellenlaengen zur Bestimmung von Farbenaequivalenten". In: *Publikationen des Astrophysikalischen Observatoriums zu Potsdam* 63.

Hidalgo, Sebastian L. et al. (Apr. 2018). "The Updated BaSTI Stellar Evolution Models and Isochrones. I. Solar-scaled Calculations". In: *ApJ* 856, 125, p. 125. DOI: 10.3847/1538-4357/aab158. arXiv: 1802.07319 [astro-ph.GA].

Higl, J. and A. Weiss (Dec. 2017). "Testing stellar evolution models with detached eclipsing binaries". In: *A&A* 608, A62, A62. DOI: 10.1051/0004-6361/201731008.

Higl, J et al. (Sept. 2018). "An analysis of the TZ Fornacis binary system". In: *A&A* 617, A36. ISSN: 0004-6361. DOI: 10.1051/0004-6361/201833112. URL: https://www.aanda.org/10.1051/0004-6361/201833112.

Hunter, I. et al. (Mar. 2009). "The VLT-FLAMES survey of massive stars: constraints on stellar evolution from the chemical compositions of rapidly rotating Galactic and Magellanic Cloud B-type stars". In: *Astronomy and Astrophysics* 496.3, pp. 841–853. DOI: 10.1051/0004-6361/200809925. arXiv: 0901.3853 [astro-ph.SR].

Iglesias, Carlos A. and Forrest J. Rogers (June 1996). "Updated Opal Opacities". In: *ApJ* 464, p. 943. DOI: 10.1086/177381.

Irwin, Alan W. (Nov. 2012). *FreeEOS: Equation of State for stellar interiors calculations*. ascl: 1211.002.

Itoh, Naoki et al. (Apr. 2008). "The Second Born Corrections to the Electrical and Thermal Conductivities of Dense Matter in the Liquid Metal Phase". In: *ApJ* 677.1, pp. 495–502. DOI: 10.1086/529367. arXiv: 0708.2967 [astro-ph].

Keller, S. C. and P. R. Wood (May 2006). "Bump Cepheids in the Magellanic Clouds: Metallicities, the Distances to the LMC and SMC, and the Pulsation-Evolution Mass Discrepancy". In: *ApJ* 642, pp. 834–841. DOI: 10.1086/501115. eprint: astro-ph/0601225.

Kippenhahn, R. and H. -C. Thomas (Jan. 1970). "A Simple Method for the Solution of the Stellar Structure Equations Including Rotation and Tidal Forces". In: *IAU Colloq. 4: Stellar Rotation*. Ed. by Arne Slettebak, p. 20.

Kippenhahn, R., A. Weigert, and Emmi Hofmeister (Jan. 1967). "Methods for Calculating Stellar Evolution". In: *Methods in Computational Physics* 7, pp. 129–190.

Kippenhahn, Rudolf, Alfred Weigert, and Achim Weiss (2012). *Stellar Structure and Evolution*. Stellar Structure, Evolution: , Astronomy, and Astrophysics Library. ISBN 978-3-642-30255-8. Springer-Verlag Berlin Heidelberg, 2012. DOI: 10.1007/978-3-642-30304-3.

Kroupa, Pavel (Jan. 2002). "The Initial Mass Function of Stars: Evidence for Uniformity in Variable Systems". In: *Science* 295, pp. 82–91. DOI: 10.1126/science.1067524. arXiv: astro-ph/0201098 [astro-ph].

Lemasle, B. et al. (Dec. 2017). "Detailed chemical composition of classical Cepheids in the LMC cluster NGC 1866 and in the field of the SMC". In: *A&A* 608, A85, A85. DOI: 10.1051/0004-6361/201731370. arXiv: 1709.03083 [astro-ph.GA].

Limongi, Marco (2017). "Supernovae from Massive Stars". In: *Handbook of Supernovae, ISBN 978-3-319-21845-8. Springer International Publishing AG, 2017, p. 513*, p. 513. DOI: 10.1007/978-3-319-21846-5_119.

Limongi, Marco and Alessandro Chieffi (July 2018). "Presupernova Evolution and Explosive Nucleosynthesis of Rotating Massive Stars in the Metallicity Range -3 $\leq$ [Fe/H] $\leq$ 0". In: *The Astrophysical Journal Supplement Series* 237, 13, p. 13. DOI: 10.3847/1538-4365/aacb24. arXiv: 1805.09640 [astro-ph.SR].

Lovekin, C. C., R. G. Deupree, and C. I. Short (May 2006). "Surface Temperature and Synthetic Spectral Energy Distributions for Rotationally Deformed Stars". In: *ApJ* 643, pp. 460–470. DOI: 10.1086/501492. eprint: astro-ph/0602084.

Maeder, A. (May 1975). "Stellar evolution III: the overshooting from convective cores." In: *A&A* 40, pp. 303–310.

— (2009). *Physics, Formation and Evolution of Rotating Stars*. DOI: 10.1007/978-3-540-76949-1.

Maeder, A. and G. Meynet (Sept. 2000). "Stellar evolution with rotation. VI. The Eddington and Omega -limits, the rotational mass loss for OB and LBV stars". In: *A&A* 361, pp. 159–166. arXiv: astro-ph/0006405 [astro-ph].

Maeder, A., G. Meynet, et al. (May 2013). "The thermohaline, Richardson, Rayleigh-Taylor, Solberg-Høiland, and GSF criteria in rotating stars". In: *A&A* 553, A1, A1. DOI: 10.1051/0004-6361/201220936. arXiv: 1303.3230 [astro-ph.SR].

Maeder, A. and E. Peytremann (Nov. 1972). "Uniformly Rotating Stars with Hydrogen- and Metallic-Line Blanketed Model Atmospheres". In: *A&A* 21, p. 279.

Maeder, Andre and Jean-Paul Zahn (1998). "Stellar Evolution With Rotation. III. Meridional Circulation With u-gradients and non-Stationarity". In: *A&A* 1006, pp. 1000–1006. ISSN: <null>. URL: http://adsabs.harvard.edu/abs/1998A%7B%5C&%7DA...334.1000M.

Magic, Zazralt, Achim Weiss, and Martin Asplund (Jan. 2015). "The Stagger-grid: A grid of 3D stellar atmosphere models - III. The relation to mixing-length convection theory". In: *A&A* 573, A89. DOI: 10.1051/0004-6361/201423760. arXiv: 1403.1062. URL: http://arxiv.org/abs/1403.1062%7B%5C%%7D0Ahttp://dx.doi.org/10.1051/0004-6361/201423760.

Maldonado, J., L. Affer, et al. (May 2015). "Stellar parameters of early-M dwarfs from ratios of spectral features at optical wavelengths". In: *A&A* 577, A132, A132. DOI: 10.1051/0004-6361/201525797. arXiv: 1503.03010 [astro-ph.SR].

Maldonado, J., E. Villaver, et al. (Apr. 2019). "Connecting substellar and stellar formation: the role of the host star's metallicity". In: *A&A* 624, A94, A94. DOI: 10.1051/0004-6361/201833827. arXiv: 1903.01141 [astro-ph.SR].

Marconi, M., G. Fiorentino, and F. Caputo (Apr. 2004). "Updated pulsation models for anomalous Cepheids". In: *A&A* 417, pp. 1101–1114. DOI: 10.1051/0004-6361:20040020. arXiv: astro-ph/0401332 [astro-ph].

Marconi, M., R. Molinaro, et al. (2013). "Theoretical fit of Cepheid light a radial velocity curves in the Large Magellanic Cloud cluster NGC 1866". In: *Mon. Not. R. Astron. Soc.* 428.3, pp. 2185–2197. ISSN: 00358711. DOI: 10.1093/mnras/sts197. arXiv: arXiv:1210.4343v1.

Marigo, P. and B. Aringer (Dec. 2009). "Low-temperature gas opacity. ÆSOPUS: a versatile and quick computational tool". In: *A&A* 508, pp. 1539–1569. DOI: 10.1051/0004-6361/200912598. arXiv: 0907.3248 [astro-ph.SR].

Marigo, P., L. Girardi, A. Bressan, et al. (Jan. 2017). "A New Generation of PARSEC-COLIBRI Stellar Isochrones Including the TP-AGB Phase". In: *ApJ* 835, 77, p. 77. DOI: 10.3847/1538-4357/835/1/77. arXiv: 1701.08510 [astro-ph.SR].

Marigo, P., L. Girardi, C. Chiosi, et al. (May 2001). "Zero-metallicity stars. I. Evolution at constant mass". In: *A&A* 371, pp. 152–173. DOI: 10.1051/0004-6361:20010309. arXiv: astro-ph/0102253 [astro-ph].

Marino, A. F., A. P. Milone, et al. (Aug. 2018). "Discovery of Extended Main Sequence Turnoffs in Galactic Open Clusters". In: *ApJ* 863, L33, p. L33. DOI: 10.3847/2041-8213/aad868. arXiv: 1807.05888 [astro-ph.SR].

Marino, A. F., N. Przybilla, et al. (Sept. 2018). "Different Stellar Rotations in the Two Main Sequences of the Young Globular Cluster NGC 1818: The First Direct Spectroscopic Evidence". In: *AJ* 156, 116, p. 116. DOI: 10.3847/1538-3881/aad3cd. arXiv: 1807.04493 [astro-ph.SR].

Martocchia, S. et al. (July 2018). "The search for multiple populations in Magellanic Cloud clusters - IV. Coeval multiple stellar populations in the young star cluster NGC 1978". In: *MNRAS* 477.4, pp. 4696–4705. DOI: 10.1093/mnras/sty916. arXiv: 1804.04141 [astro-ph.SR].

Meynet, G. and A. Maeder (May 1997). "Stellar evolution with rotation. I. The computational method and the inhibiting effect of the μ-gradient." In: *A&A* 321, pp. 465–476.

— (Aug. 2002). "Stellar evolution with rotation. VIII. Models at Z = 10^{-5} and CNO yields for early galactic evolution". In: *A&A* 390, pp. 561–583. DOI: 10.1051/0004-6361:20020755. arXiv: astro-ph/0205370 [astro-ph].

Milone, A. P., A. F. Marino, F. D'Antona, L. R. Bedin, G. S. Da Costa, et al. (June 2016). "Multiple stellar populations in Magellanic Cloud clusters - IV. The double main sequence of the young cluster NGC 1755". In: *MNRAS* 458.4, pp. 4368–4382. DOI: 10.1093/mnras/stw608. arXiv: 1603.03493 [astro-ph.SR].

Milone, A. P., A. F. Marino, F. D'Antona, L. R. Bedin, G. Piotto, et al. (Mar. 2017). "Multiple stellar populations in Magellanic Cloud clusters - V. The split main sequence of the young cluster NGC 1866". In: *MNRAS* 465, pp. 4363–4374. DOI: 10.1093/mnras/stw2965. arXiv: 1611.06725 [astro-ph.SR].

Milone, A. P., A. F. Marino, M. Di Criscienzo, et al. (June 2018). "Multiple stellar populations in Magellanic Cloud clusters - VI. A survey of multiple sequences and Be stars in young clusters". In: *MNRAS* 477, pp. 2640–2663. DOI: 10.1093/mnras/sty661. arXiv: 1802.10538 [astro-ph.SR].

Mirouh, Giovanni M. et al. (Feb. 2019). "Mode classification in fast-rotating stars using a convolutional neural network: model-based regular patterns in δ Scuti stars". In: *MNRAS* 483.1, pp. L28–L32. DOI: 10.1093/mnrasl/sly212. arXiv: 1811.05769 [astro-ph.SR].

Mokiem, M. R., A. de Koter, C. J. Evans, et al. (Sept. 2006). "The VLT-FLAMES survey of massive stars: mass loss and rotation of early-type stars in the SMC". In: *Astronomy and Astrophysics* 456.3, pp. 1131–1151. DOI: 10.1051/0004-6361:20064995. arXiv: astro-ph/0606403 [astro-ph].

Mokiem, M. R., A. de Koter, J. S. Vink, et al. (Oct. 2007). "The empirical metallicity dependence of the mass-loss rate of O- and early B-type stars". In: *Astronomy and Astrophysics* 473.2, pp. 603–614. DOI: 10.1051/0004-6361:20077545. arXiv: 0708.2042 [astro-ph].

Moravveji, E. et al. (2015). "Tight asteroseismic constraints on core overshooting and diffusive mixing in the slowly rotating pulsating B8.3V star KIC 10526294". In: *A&A* 580, A27, A27. DOI: 10.1051/0004-6361/201425290. arXiv: 1505.06902 [astro-ph.SR].

Mosser, B. et al. (Oct. 2018). "Period spacings in red giants IV. Toward a complete description of the mixed-mode pattern". In: *A&A* 618, A109, A109. DOI: 10.1051/0004-6361/201832777.

Mowlavi, N. et al. (May 2012). "Stellar mass and age determinations . I. GMowlavi2012rids of stellar models from Z = 0.006 to 0.04 and M = 0.5 to 3.5 $M_{\odot}$". In: *A&A* 541, A41, A41. DOI: 10.1051/0004-6361/201117749. arXiv: 1201.3628.

Mucciarelli, A. et al. (2011). "NGC 1866: A milestone for understanding the chemical evolution of stellar populations in the Large Magellanic Cloud". In: *Mon. Not. R. Astron. Soc.* 413.2, pp. 837–851. ISSN: 00358711. DOI: 10.1111/j.1365-2966.2010.18167.x. arXiv: 1012.1476 [astro-ph.SR].

Musella, I. et al. (2016). "The Cepheids of NGC 1866: A precise benchmark for the extragalactic distance scale and stellar evolution from modern UBVI photometry". In: *Mon. Not. R. Astron. Soc.* 457.3, pp. 3084–3095. ISSN: 13652966. DOI: 10.1093/mnras/stw151. arXiv: 1601.06628.

Nanni, Ambra et al. (July 2019). "The mass-loss, expansion velocities, and dust production rates of carbon stars in the Magellanic Clouds". In: *MNRAS* 487.1, pp. 502–521. DOI: 10.1093/mnras/stz1255. arXiv: 1904.06702 [astro-ph.SR].

Niederhofer, F. et al. (Mar. 2017). "The search for multiple populations in Magellanic Cloud clusters - II. The detection of multiple populations in three intermediate-age SMC clusters". In: *MNRAS* 465.4, pp. 4159–4165. DOI: 10.1093/mnras/stw3084. arXiv: 1612.00400 [astro-ph.SR].

Nugis, T. and H. J. G. L. M. Lamers (Aug. 2000). "Mass-loss rates of Wolf-Rayet stars as a function of stellar parameters". In: *Astronomy and Astrophysics* 360, pp. 227–244.

Paxton, Bill, Lars Bildsten, et al. (Jan. 2011). "Modules for Experiments in Stellar Astrophysics (MESA)". In: *The Astrophysical Journal Supplement Series* 192, 3, p. 3. DOI: 10.1088/0067-0049/192/1/3. arXiv: 1009.1622 [astro-ph.SR].

Paxton, Bill, Matteo Cantiello, et al. (Sept. 2013). "Modules for Experiments in Stellar Astrophysics (MESA): Planets, Oscillations, Rotation,

and Massive Stars". In: *The Astrophysical Journal Supplement Series* 208, 4, p. 4. DOI: 10.1088/0067-0049/208/1/4. arXiv: 1301.0319 [astro-ph.SR].

Paxton, Bill, Pablo Marchant, et al. (Sept. 2015). "Modules for Experiments in Stellar Astrophysics (MESA): Binaries, Pulsations, and Explosions". In: *The Astrophysical Journal Supplement Series* 220, 15, p. 15. DOI: 10.1088/0067-0049/220/1/15. arXiv: 1506.03146 [astro-ph.SR].

Paxton, Bill, Josiah Schwab, et al. (Feb. 2018). "Modules for Experiments in Stellar Astrophysics (MESA): Convective Boundaries, Element Diffusion, and Massive Star Explosions". In: *The Astrophysical Journal Supplement Series* 234, 34, p. 34. DOI: 10.3847/1538-4365/aaa5a8. arXiv: 1710.08424 [astro-ph.SR].

Paxton, Bill, R. Smolec, et al. (Mar. 2019). "Modules for Experiments in Stellar Astrophysics (MESA): Pulsating Variable Stars, Rotation, Convective Boundaries, and Energy Conservation". In: *arXiv e-prints*, arXiv:1903.01426, arXiv:1903.01426. arXiv: 1903.01426 [astro-ph.SR].

Pérez Hernández, F. et al. (June 1999). "Photometric parameters for rotating models of A- and F-type stars". In: *A&A* 346, pp. 586–598.

Petrovic, J et al. (2005). "Which massive stars are gamma-ray burst progenitors?" In: *A&A* 435.1, pp. 247–259. ISSN: 0004-6361. DOI: 10.1051/0004-6361:20042545. arXiv: 0504175 [astro-ph]. URL: https://www.aanda.org/articles/aa/pdf/2005/44/aa4030-05.pdf%20http://www.aanda.org/10.1051/0004-6361:20054030%20http://www.aanda.org/10.1051/0004-6361:20042545.

Pietrinferni, Adriano et al. (Sept. 2004). "A Large Stellar Evolution Database for Population Synthesis Studies. I. Scaled Solar Models and Isochrones". In: *ApJ* 612, pp. 168–190. DOI: 10.1086/422498.

Potter, Adrian T, Christopher A Tout, and John J Eldridge (2012). "Towards a unified model of stellar rotation". In: *MNRAS* 419.1, pp. 748–759. ISSN: 00358711. DOI: 10.1111/j.1365-2966.2011.19737.x. arXiv: arXiv:1109.0993v1.

Rodrigues, T. S. et al. (Dec. 2014a). "Bayesian distances and extinctions for giants observed by Kepler and APOGEE". In: *MNRAS* 445, pp. 2758–2776. DOI: 10.1093/mnras/stu1907. arXiv: 1410.1350 [astro-ph.SR].

— (Dec. 2014b). "Bayesian distances and extinctions for giants observed by Kepler and APOGEE". In: *MNRAS* 445, pp. 2758–2776. DOI: 10.1093/mnras/stu1907. arXiv: 1410.1350 [astro-ph.SR].

Rodrigues, Thaíse S. et al. (May 2017). "Determining stellar parameters of asteroseismic targets: going beyond the use of scaling relations". In: *MNRAS* 467.2, pp. 1433–1448. DOI: 10.1093/mnras/stx120. arXiv: 1701.04791 [astro-ph.SR].

Rosenfield, P. et al. (June 2017). "A New Approach to Convective Core Overshooting: Probabilistic Constraints from Color-Magnitude Diagrams of LMC Clusters". In: *ApJ* 841, 69, p. 69. DOI: 10.3847/1538-4357/aa70a2. arXiv: 1705.00618 [astro-ph.SR].

Royer, F. (2009). "On the Rotation of A-Type Stars". In: *The Rotation of Sun and Stars*. Vol. 765. Lecture Notes in Physics, Berlin Springer Verlag, pp. 207–230. DOI: 10.1007/978-3-540-87831-5_9.

Russell, H. N. (May 1914). "Relations Between the Spectra and Other Characteristics of the Stars". In: *Popular Astronomy* 22, pp. 275–294.

Sackmann, I. -J., R. L. Smith, and K. H. Despain (Feb. 1974). "Carbon and eruptive stars: surface enrichment of lithium, carbon, nitrogen, and ^{13}C by deep mixing." In: *ApJ* 187, pp. 555–574. DOI: 10.1086/152666.

Salasnich, Bernardo, Alessandro Bressan, and Cesare Chiosi (Feb. 1999). "Evolution of massive stars under new mass-loss rates for RSG: is the mystery of the missing blue gap solved?" In: *A&A* 342, pp. 131–152.

Salpeter, E. E. (Jan. 1955). "The Luminosity Function and Stellar Evolution." In: *ApJ* 121, p. 161. DOI: 10.1086/145971.

Schwarzschild, M., R. Howard, and R. Härm (Jan. 1957). "Inhomogeneous Stellar Models. V. a. Solar Model with Convective Envelope and Inhomogeneous Interior." In: *ApJ* 125, p. 233. DOI: 10.1086/146297.

Schwarzschild, Martin (1958). *Structure and evolution of the stars*. Princeton, Princeton University Press, 1958.

Shajn, G. and O. Struve (Jan. 1929). "On the rotation of the stars". In: *MNRAS* 89, pp. 222–239. DOI: 10.1093/mnras/89.3.222.

Slettebak, A., T. J. Kuzma, and G. W. Collins II (Nov. 1980). "Effects of stellar rotation on spectral classification". In: *ApJ* 242, pp. 171–187. DOI: 10.1086/158453.

Spada, F et al. (2017). "The Yale-Potsdam Stellar Isochrones (YaPSI)". In: *ApJ*. ISSN: 15384357. DOI: 10.3847/1538-4357/aa661d. arXiv: 1703.03975. URL: http://iopscience.iop.org/article/10.3847/1538-4357/aa661d/pdf%20http://arxiv.org/abs/1703.03975%7B%5C%%7D0Ahttp://dx.doi.org/10.3847/1538-4357/aa661d.

Spera, Mario, Michela Mapelli, and Alessandro Bressan (Aug. 2015). "The mass spectrum of compact remnants from the PARSEC stellar evolution tracks". In: *MNRAS* 451.4, pp. 4086–4103. DOI: 10.1093/mnras/stv1161. arXiv: 1505.05201 [astro-ph.SR].

Spera, Mario, Michela Mapelli, Nicola Giacobbo, et al. (May 2019). "Merging black hole binaries with the SEVN code". In: *MNRAS* 485.1, pp. 889–907. DOI: 10.1093/mnras/stz359. arXiv: 1809.04605 [astro-ph.HE].

Stancliffe, R. J. et al. (Mar. 2015). "Confronting uncertainties in stellar physics: calibrating convective overshooting with eclipsing binaries". In: *A&A* 575, A117, A117. DOI: 10.1051/0004-6361/201425126. arXiv: 1501.05322 [astro-ph.SR].

— (Feb. 2016). "Confronting uncertainties in stellar physics. II. Exploring differences in main-sequence stellar evolution tracks". In: *A&A* 586, A119, A119. DOI: 10.1051/0004-6361/201527099. arXiv: 1601.03054 [astro-ph.SR].

Sweet, P. A. (Jan. 1950). "The importance of rotation in stellar evolution". In: *MNRAS* 110, p. 548. DOI: 10.1093/mnras/110.6.548.

Talon, Suzanne and Jean-Paul Zahn (1997). "Anisotropic diffusion and shear instabilities." In: *A&A* 317.1, p. 749. arXiv: 9609010 [astro-ph]. URL: http://adsabs.harvard.edu/abs/1997A%7B%5C&%7DA...317..749T.

Tang, J. et al. (Dec. 2014). "New PARSEC evolutionary tracks of massive stars at low metallicity: testing canonical stellar evolution in nearby star-forming dwarf galaxies". In: *MNRAS* 445, pp. 4287–4305. DOI: 10.1093/mnras/stu2029. arXiv: 1410.1745 [astro-ph.SR].

Testa, Vincenzo et al. (Dec. 1999). "The Large Magellanic Cloud Globular Cluster NGC 1866: New Data, New Models, New Analysis". In: *AJ* 118.6, pp. 2839–2864. DOI: 10.1086/301148. arXiv: astro-ph/9909417 [astro-ph].

Thoul, Anne A., John N. Bahcall, and Abraham Loeb (Feb. 1994). "Element Diffusion in the Solar Interior". In: *ApJ* 421, p. 828. DOI: 10.1086/173695. arXiv: astro-ph/9304005 [astro-ph].

Torres, G., J. Andersen, and A. Giménez (2010). "Accurate masses and radii of normal stars: Modern results and applications". In: *A&A Rev.* 18.1-2, pp. 67–126. ISSN: 09354956. DOI: 10.1007/s00159-009-0025-1. arXiv: 0908.2624.

Torres, Guillermo et al. (2015). "CAPELLA (α AURIGAE) REVISITED: NEW BINARY ORBIT, PHYSICAL PROPERTIES, AND EVOLUTIONARY STATE". In: *ApJ* 807.1, p. 26. ISSN: 1538-4357. DOI: 10.1088/0004-637X/807/1/26. URL: http://stacks.iop.org/0004-637X/807/i=1/a=26?key=crossref.10407c75838131bf36868755ceb48892.

Valle, G et al. (2016). "Calibrating convective-core overshooting with eclipsing binary systems". In: *A&A* 587, A16. ISSN: 0004-6361. DOI: 10.1051/0004-6361/201527389. arXiv: 1601.01535. URL: https://www.aanda.org/articles/aa/pdf/2016/03/aa27389-15.pdf%20http://www.aanda.org/10.1051/0004-6361/201527389.

— (2017). "Statistical errors and systematic biases in the calibration of the convective core overshooting with eclipsing binaries". In: *A&A* 600, A41. ISSN: 0004-6361. DOI: 10.1051/0004-6361/201628240. arXiv: 1612.07066. URL: https://www.aanda.org/articles/aa/pdf/2017/04/aa28240-16.pdf%20http://arxiv.org/abs/1612.07066%7B%5C%%7D0Ahttp://www.aanda.org/10.1051/0004-6361/201628240.

van Belle, G. T. (Mar. 2012). "Interferometric observations of rapidly rotating stars". In: *A&A Rev.* 20, 51, p. 51. DOI: 10.1007/s00159-012-0051-2. arXiv: 1204.2572 [astro-ph.SR].

Vink, J. S., A. de Koter, and H. J. G. L. M. Lamers (Oct. 2000). "New theoretical mass-loss rates of O and B stars". In: *Astronomy and Astrophysics* 362, pp. 295–309. arXiv: astro-ph/0008183 [astro-ph].

Vink, Jorick S., A. de Koter, and H. J. G. L. M. Lamers (Apr. 2001). "Mass-loss predictions for O and B stars as a function of metallicity". In: *Astronomy and Astrophysics* 369, pp. 574–588. DOI: 10.1051/0004-6361:20010127. arXiv: astro-ph/0101509 [astro-ph].

von Zeipel, H. (June 1924). "The radiative equilibrium of a rotating system of gaseous masses". In: *MNRAS* 84, pp. 665–683. DOI: 10.1093/mnras/84.9.665.

Weiss, Achim and Helmut Schlattl (Aug. 2008). "GARSTEC—the Garching Stellar Evolution Code. The direct descendant of the legendary Kippenhahn code". In: *Ap&SS* 316, pp. 99–106. DOI: 10.1007/s10509-007-9606-5.

Woo, J.-H. et al. (2003). "Testing Intermediate-Age Stellar Evolution Models with VLT Photometry of Large Magellanic Cloud Clusters. II. Analysis with the Yale Models". In: *AJ* 125, pp. 754–769. DOI: 10.1086/345959. eprint: astro-ph/0208142.

Yoon, S.-C and N Langer (2005). "Evolution of rapidly rotating metal-poor massive stars towards gamma-ray bursts". In: *A&A* 443.2, pp. 643–648. ISSN: 0004-6361. DOI: 10.1051/0004-6361:20054030. arXiv: 0508242 [astro-ph]. URL: https://www.aanda.org/articles/aa/pdf/2005/44/aa4030-05.pdf%20http://www.aanda.org/10.1051/0004-6361:20054030.

Zahn, J.-P. (Nov. 1992). "Circulation and turbulence in rotating stars." In: *A&A* 265, pp. 115–132.